Photodynamics of upconversion nanoparticles : a combined investigation at ensemble and single particle levels

Ali Eftekhari

Université de Lille

Ecole doctorale Sciences de la Matière, du Rayonnement et de l'Environnement

LAboratoire de Spectroscopie pour les Interactions, la Réactivité et l'Environnement

Thèse préparée pour obtenir le grade de

Docteur de l'Université de Lille

Discipline : Chimie théorique, physique, analytique

Ali Eftekhari

Photodynamics of upconversion nanoparticles:

a combined investigation at ensemble and single particle levels

Soutenance publique le *19 Décembre 2022*

Rapporteurs :

Pr. Pascal Didier	Professeur des Universités, Université de Strasbourg
Dr. Aline Nonat	Chargée de recherche CNRS, Université de Strasbourg

Examinateurs :

Pr. Rachel Méallet-Renault	Professeur des Universités, Université Paris-Saclay
Dr. Hervé Vezin	Directeur de recherche CNRS, Université de Lille

Directeur de thèse :

Dr. Michel Sliwa	Directeur de recherche CNRS, Université de Lille

Co-encadrante de thèse :

Dr. Aude Bouchet	Maître de conférences, Université de Lille

Université de Lille

Ecole doctorale Sciences de la Matière, du Rayonnement et de l'Environnement

LAboratoire de Spectroscopie pour les Interactions, la Réactivité et l'Environnement

Thèse préparée pour obtenir le grade de

Docteur de l'Université de Lille

Discipline : Chimie théorique, physique, analytique

Ali Eftekhari

Photodynamique de nanoparticules up-conversion:

étude couplée en solution et particules uniques

Soutenance publique le *19 Décembre 2022*

Rapporteurs :

Pr. Pascal Didier	Professeur des Universités, Université de Strasbourg
Dr. Aline Nonat	Chargée de recherche CNRS, Université de Strasbourg

Examinateurs :

Pr. Rachel Méallet-Renault	Professeur des Universités, Université Paris-Saclay
Dr. Hervé Vezin	Directeur de recherche CNRS, Université de Lille

Directeur de thèse :

Dr. Michel Sliwa	Directeur de recherche CNRS, Université de Lille

Co-encadrante de thèse :

Dr. Aude Bouchet	Maître de conférences, Université de Lille

Acknowledgements

I deeply thank Dr. Hervé Vezin for welcoming me in LASIRE for 3 years and accepting to be the president of the jury. It is my great pleasure to thank Dr. Aline Nonat and Dr. Pascal Didier to accept to be my thesis jury. I know you are very busy and I really appreciate your time. I thank Dr. Rachel Méallet-Renault and Dr. Pascal Didier for their precious advice and support each year as members of the CST of my thesis and for guiding me to find essential steps and advances in the project. I deeply appreciate for accepting to be the jury members of my thesis.

I would like to thank the region Hauts-de-France and Lille University for their financial support.

I would like to express my sincere gratitude to my supervisors Dr. Aude Bouchet and Dr. Michel Sliwa for having me as one of their students and allowing me to enhance my research at the University of Lille. They have always been the most positive, supportive, and inspiring supervisors to me. They have insights to foresee the trend of our research field and have great ideas of a wide research area related with photonics and electric devices. When I arrived in France, I was quite unfamiliar with the research field and Aude taught me everything from basic to advance. It was always a pleasure to speak with them. Sometimes I had long discussions with Michel, who, despite his busy schedule, stayed and answered all of my questions (Scientific and personal). I record some of them in my notebook as the precious gift of my future life. Their strong leadership also is a module that influences my life. And now, I feel very fortunate and blessed to have worked with them for the past three years.

There is no doubt that my relationship with my supervisors is very close, and our relationship goes far beyond that of a leader and a student. Actually, we are close friends and I am very lucky person to have them.

Greatly, I would like to thank Professor Christophe Coudret for his support and and supervision for our UCNPs project. Christophe is a master of synthesis of ultra-small UCNPs. Through my research, I learned a lot of knowledge from him. And Also, I would like to thank to Peter Dedecker for hosting me in his lab for two months and I had this chance to learn a lot about the biological samples. I want to thank Baptiste Amouroux for helping me a lot when I was in Leuven.

From LASIRE, I would like to thank Dr. Cyril Ruckebusch for his support and advice (especially our daily talk early in the morning). And also, I would like to deeply thank my friends Raffaele Vitale and Lucas Martinez Uriarte. The one person I always turn to for my chemometric questions is Rafa, who has always been able to assist me in understanding them. My learning of coding with Python was guided by Lucas, and I have to admit that I would not have been able to do so without his guidance. In addition, I would like to thank Julien Dubois, our nice lab engineer, for his support and kindness during these three years. I would not want to forget all the PhD students and members of the LASIRE lab that had helped me and accompanied me all over the past years.

Next, I would like to thank our colleagues and collaborators. Dr. Clément Roux and Dr. Jean-Claude Micheau, and Dr. Qilin Zou from university of Toulouse. Thank you for a lot of beneficial discussions and helps. I want to thank Dr. Christoph Gimmler and Dr. Rajesh Komban from Fraunhofer-Zentrum für Angewandte Nanotechnologie CAN for providing us various UCNPs samples. I would like to Thank Dr. Syoji Ito from Osaka university for providing us PDI sample and having such valuable meetings. And also, I want to thank Ahmed Addad for his precious help about recognising particles with SEM. He has welcomed me all the time for my samples.

I would like to Thank my M.Sc. supervisor , Dr. Hadi Parastar, for his endless support all the time and introducing this position to me.

In Addition, I would like to thank my dear friends, Soheil, Franak, Amin, Ensie, Danial, Bahar, Sanaz, Mahsa, and Dominikus (our passionate discussions) for their continued supports.

I would like to thank my family, especially my mother and brother, for their support, love, and unwavering belief in me Although my lovely father and sister are no longer on earth, they remain in my heart all the time.

As a final note, I wish to thank my wife Shahla from the bottom of my heart. Of course, she is my rock, my inspiration, my world: without my wife, Shahla , none of this would ever have been possible. At the darkest part of my, when I lost my father and sister, her love saved me like a miracle. To have a woman of such infinite talent and dynamism put her own professional career on hold to support the dreams of the man she’s married is a powerful thing, and I have striven every day to live up to that. But most of all, thank you for being my best friend. I owe you everything.

توانا بود هر که دانا بود "

"زدانش دل پیر برنا بود

حکیم ابوالقاسم فردوسی

Abstract

The unique photoluminescent properties of upconversion nanoparticles (UCNPs), which emit visible light while being illuminated by near infrared (NIR) radiation, have sparked the interest of researchers worldwide and inspired many bioanalytical applications. Their anti-Stokes emission, long luminescence lifetime, narrow and multiple absorption and emission bands, and excellent photostability enable background-free and multiplexed detection in thick biological objects. Emission is controlled by a balance of numerous radiative and non-radiative pathways, including energy transfers between sensitizers and activators and quenching effects due to the host matrix and surface. Altogether, these processes account for the highly nonlinear response of the emissions to the excitation power. However, despite numerous studies in this field, rationalizing the dynamics of these energy transfers within these nanoparticles still remains a challenge, albeit it controls their time-dependent luminescence (rise and decay) and their emission yield. The purpose of this thesis is thus to investigate the photodynamics taking place in different types of UCNPs in order to disentangle the complex energy pathways driving their emission properties at ensemble and single particle levels.

First, small (5 nm) and ultrasmall (< 3 nm) UCNPs doped with Ytterbium (Yb, sensitizer) and Thulium (Tm, activator) were considered. These particles, due to their small size, have a limited luminescence. We have therefore studied the effect of adding a fluoride shell to a 5 nm oxysulfide core on the photophysical properties of these heterostructures. Moreover, the reduced number of activators present in these small UCNPs allows to select the number of processes controlling their emission: thanks to a limited probability of cross-relaxation between the activators, the dynamics of energy redistribution in the kinetic network of activators is greatly simplified. Thus, a minute examination of a batch of ultra-small (< 3 nm) UCNPs in solution was thus possible using different irradiation schemes (continuous wave, nanosecond pulse, pulse square, sensitizer-mediated or direct activator excitations). In particular, the α-to-β phase transition occurring during the synthesis procedure could be evidenced by the sudden increase of the $^3H_4$ excited state lifetime. Additionally, we also addressed the influence of Yb concentration and surface coating with a shell on the emission dynamics of the different Tm excited states.

To study the emission at the single particle level, we have developed a new confocal microscope based on a millisecond-square pulse NIR excitation and a detection with an intensified gated CCD camera in order to measure space- and time-resolved emission spectra. We discuss here two applications of this new tool: (i) we first investigated the emission properties of Tm core and core-shell UCNPs assemblies. According to the nanometric spatial arrangement of the particles, we could demonstrate that the emission dynamics of single particles, 2D monolayers or 3D aggregates differ in terms of power-dependent emission band ratios and lifetimes. (ii) We examined hybrid systems composed of single UCNPs (Erbium, Er and Tm) and perylenediimide (PDI)-based organic films deposited on UCNPs in terms of emission spectra and lifetimes for UCNPs in order to study the nature of the energy transfers from the UCNP to PDI films according to the nature of the emitter (Er and Tm) and its excited states.

Résumé

Les propriétés exceptionnelles de photoluminescence des nanoparticules up-conversion (UCNP), qui émettent de la lumière visible tout en étant éclairées par un rayonnement proche infrarouge (NIR), ont suscité l'intérêt des chercheurs du monde entier et inspiré de nombreuses applications bioanalytiques. Leur émission anti-Stokes, leur longue durée de vie de luminescence, les bandes d'absorption et d'émission étroites et multiples et leur excellente photostabilité permettent une détection multiplexée et sans bruit de fond dans des objets biologiques épais. L'émission est contrôlée par un équilibre subtil entre de nombreuses voies radiatives et non radiatives, comprenant les transferts d'énergie entre les sensibilisateurs et les activateurs et les effets d'extinction dus à la matrice hôte et à la surface. L'ensemble de ces processus explique la réponse hautement non linéaire des émissions en fonction de la puissance d'excitation. Cependant, malgré de nombreuses études dans ce domaine, la rationalisation de la dynamique de ces transferts d'énergie au sein de ces nanoparticules reste encore un défi, alors qu'elle contrôle leurs temps de vie de luminescence (montée et déclin) et leur rendement d'émission. L'objectif de cette thèse est donc d'étudier la photo-dynamique qui a lieu dans différents types d'UCNPs afin de décrire les voies énergétiques complexes qui régissent leurs propriétés d'émission en solution et au niveau de la particule unique.

Tout d'abord, des UCNPs petites (5 nm) et ultra-petites (< 3 nm) dopées par de l'Ytterbium (Yb, sensibilisateur) et du Thulium (Tm, activateur) ont été considérées. Ces particules, par leur petite taille, possèdent une luminescence limitée. Nous avons donc étudié dans un premier temps l'effet de l'ajout d'une coquille fluorure à un cœur de 5 nm à base d'oxysulfure sur les propriétés photophysiques de ces hétérostructures. De plus, le nombre réduit d'activateurs présent dans ces UCNP de petite taille permet de sélectionner le nombre de processus contrôlant leur émission : grâce à une probabilité limitée de relaxation croisée entre les activateurs, la dynamique de la redistribution de l'énergie dans le réseau cinétique des activateurs est grandement simplifiée. Ainsi, un examen minutieux d'un lot d'UCNP ultra-petites (< 3 nm) en solution a donc été possible en utilisant différents schémas d'irradiation (continue, impulsion nanoseconde, impulsion ms carrée, excitations médiées par le sensibilisateur ou directes par l'activateur). En particulier, la transition de phase α-β se produisant pendant la procédure de synthèse a pu être mise en évidence par l'augmentation soudaine de la durée de vie de l'état excité $^3H_4$. En outre, nous avons également abordé l'influence de la concentration d'Yb et du revêtement de surface avec une coquille sur la dynamique d'émission des différents états excités du Tm.

Pour étudier l'émission au niveau de la particule unique, nous avons développé un nouveau microscope confocal basé sur une excitation NIR à impulsions carrées de l'ordre de la milliseconde et une détection avec une caméra CCD intensifiée afin de mesurer des spectres résolus dans l'espace et dans le temps. Nous discutons ici de deux applications de ce nouvel outil : (i) nous avons d'abord étudié les propriétés d'émission des assemblages de UCNPs à base de Thulium (cœur et cœur-coquille). Selon l'arrangement spatial des particules à l'échelle nanométrique, nous avons pu démontrer que la dynamique d'émission des particules uniques, des monocouches 2D ou des agrégats 3D diffère en termes de rapports de bandes d'émission dépendants de la puissance et de durées de vie. (ii) Nous avons examiné des systèmes hybrides composés d'UCNP uniques et de films organiques à base de pérylène en termes de spectres d'émission et de durées de vie afin d'étudier la nature des transferts d'énergie de l'UCNP vers la partie organique en fonction de la nature de l'état excité de l'émetteur.

Glossary and Abbreviations

APD: Avalanche Photodiode

C: Core

CCD: Charged-Coupled Device

CR: Cross-Relaxation

CS: Coreshell

CSU: Cooperative Sensitization Upconversion

CW: Continuous wave

DE: Direct Excitation

DG: Delay Generator

ED: Electric Dipole

Em: Emission

EM CCD: Electron Multiplying Charged-Coupled Device

EMU: Energy Migration-Mediated Upconversion

EQ: Electric Quadrupole

Er: Erbium

ESA: Excited State Absorption

ET: Energy Transfer

ETU: Upconversion Energy Transfer

Ex: Excitation

FEG: Field Electron Gun

FRET: Förster Resonance Energy Transfer

FWHM: Full Width at Half Maximum

Gd: Gadolinium

GSA: Ground State Absorption

HSM: Hyper Spectral Microscopy

ICCD: Intensified Charged-Coupled Device

ICP-OES: Inductively Coupled Plasma – Optical Emission Spectroscopy

IRF: Instrumental Response Function

MCP-PMT: Microchannel Plate-Based Photomultiplier Tubes

MD: Magnetic Dipole

ms: Millisecond

NA: Numerical Aperture

Nd:YAG: Neodymium-Doped Yttrium Aluminium Garnet

NIR: Near-infrared

NPs: Nanoparticles

nr: Non-radiative

OPO: Optical Parametric Oscillator

PA: Photon Avalanche

PAA: Poly(Acrylic Acid)

PC: Principal Component

PCA: Principal Component Analysis

PDI: Perylene-bis(dicarboximides)

PMT: Photon Multiplayer Tube

PSD: Particle Size Distribution

RE: Rare-Earth Elements

SEM: Scanning Electron Microscopy

SHG: Second Harmonic Generation

SP: Short Pass

SQ: Surface Quenching

TCSPC: Time-Correlated Single Photon Counting

Tm: Thulium

TPA: Two-photon absorption

UC: Upconversion

UCNPs: Upconversion Nanoparticles

UCL: Upconversion Luminescence

UV: Ultraviolet

XRD: X-ray Diffraction

Yb: Ytterbium

µs: Microsecond

Table of Contents

1

Introduction

Upconversion (UC) refers to nonlinear optical processes characterized by the absorption of two or more photons and leads to the emission of a single photon at shorter wavelength.[1] The phenomenon has been known since the 1960s,[2, 3] but the use of the upconversion effect has been limited to bulk glass or crystalline materials, which have been utilized for the development of some effective optical devices, including infrared quantum counter detectors, temperature sensors, and solid-state lasers.[4-11] Until the late 1990s, nanoscience and nanotechnology experienced a rapid growth. Due to appropriate small size (which allows them to pass into and out of biological hosts, such as cytoplasms, and so on) and unique optical properties, upconversion nanoparticles (UCNPs) have found wide applications in the field of bioimaging.[12-14] The unique optical properties of UCNPs consist of nonlinear power dependent emission, low autofluorescence background for an improved signal-to-noise ratio, large anti-Stokes shifts allowing to easily separate the photoluminescence (PL) from the excitation wavelength, narrow emission bandwidths that allow an easy multiplexing of images, as well as the ability to resist to photobleaching, making them suitable for long-term repetitive imaging applications.[15] Furthermore, UCNPs are also non-blinking, less light scattering, and allow deep tissue penetration because their excitation occurs in the near-infrared (NIR) region, which is within the optical transparency window (800 nm - 1000 nm). Moreover, a new direction for theranostic UCNPs utilizes hierarchically built nanostructures to combine upconversion luminescence (UCL) imaging with other imaging modalities such as magnetic resonance imaging (MRI),[16] computed tomography (CT),[17] single-photon emission tomography (SPECT),[18] positron emission tomography (PET).[19] Additionally, tumour targeting is a prerequisite for improving imaging and therapeutic efficacy; the targeting markers specialized for diseased areas are particularly excellent for cancer treatment that selectively kills cancer cells by loading indocyanine green (ICG) molecules on the surface of drug carrier.[20, 21] Molecular targeting is becoming more efficient and less toxic with the use of new targeting techniques for attaching biomolecules to imaging agents. The unique optical properties of UCNP have made them widely used in actively targeted tumour imaging. In this aim, a targeted imaging system was developed by Xiong et al. using special receptors (Figure 1).[22] They linked these receptors to the surface of UCNPs coated with polyethylene glycol (PEG), to form UCNP-receptors and found that the nanoparticles could efficiently target U87MG tumours cells. Excitation with 980 nm light produced a strong UCL signal in the left hind leg; however, no notable UCL signal was observed in

the other legs. It has been hence demonstrated that UCNP can serve as molecularly targeted probes for *in vivo* cancer diagnosis based on the recognition of the receptors.

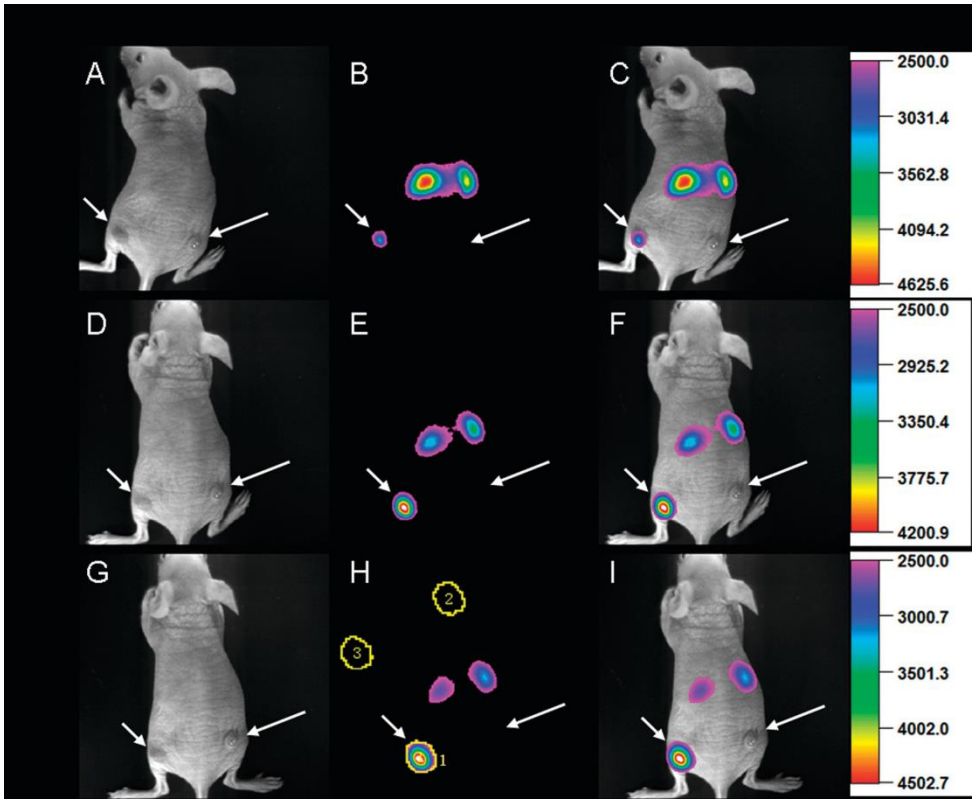

Figure 1. Time-dependent *in vivo* upconversion luminescence imaging of subcutaneous U87MG tumor (left hind leg, indicated by short arrows) and MCF-7 tumor (right hind leg, indicated by long arrows) borne by athymic nude mice after intravenous injection of UCNP-receptors over a 24 h period. Reprinted with permission from publication [22] copyright ACS 2009.

Each UCNP is considered an actuator, i.e., as an UCNP is a nanolamp. These nanolamps are used to produce visible to UV light locally in deep-tissue, upon NIR excitation. Due to this, usual photoreactive systems, such as photodynamic therapy (PDT),[23] photothermal therapy (PTT),[24] drug-release or optogenetics,[25] are transposed using UCNPs. As an example of PDT application, we can point out that human infectious diseases are caused by bacterial biofilms. Biofilms can effectively protect bacteria and produce antibiotic resistance. The emergence of super-resistant bacteria and the growth of bacterial biofilms have seriously hindered the development of biomaterials. Despite the excellent antibacterial properties of inorganic materials such as Ag^{+} and Cu^{+}, excessive use can result in high costs and toxicity. It is essential to perform simultaneous

biofilm removal and sterilization in a synergistic manner. PDT drug delivery systems based on UCNPs have gradually emerged in the field. As shown in Figure 2, Qi et al. constructed an PDT using $NaYF_4$: Yb^{3+}, Tm^{3+}@TiO_2 core shell nanoparticles.[26] Under 980-nm excitation, UCNPs can emit strong UV light, which triggers the PDT function of shell TiO_2 through energy transfer, thereby achieving significant antibacterial effects on three periodontitis-related pathogens and biofilms.

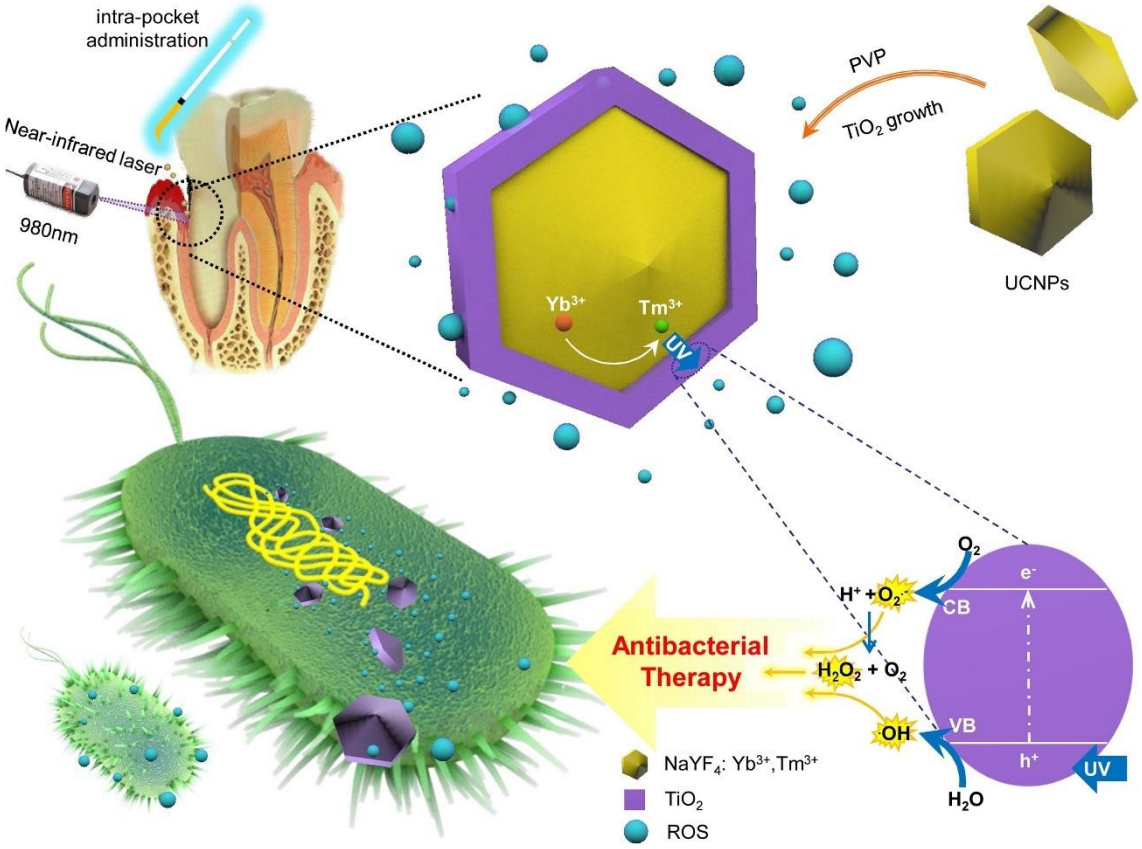

Figure 2. Synthesis of $NaYF_4$:Yb^{3+},Tm^{3+}@TiO_2 and mechanism of aPDT under NIR irradiation. Upon NIR irradiation, the UCNP nucleus converts NIR light into ultraviolet (UV) light and the UV light in turn excites TiO2 to generate active oxygen, which eventually causes oxidative damage against the microorganisms. Reprinted with permission from publication [26] copyright Elsevier 2019.

As mentioned previously, generating ultraviolet light from NIR excitation can enhance medical applications of UV light. It is also possible to activate a substrate by a non-radiative process such as FRET. As shown in Figure 3a, by increasing the excitation pulse width, the intensity of the UV emission increases non-linearly. However, the intensity of NIR emission stays constant. This feature was used to activate a fluorescence probe, 9,10-

diphenylanthracene (DPA), by FRET process with excitation at 360 nm, as shown in Figure 3b.

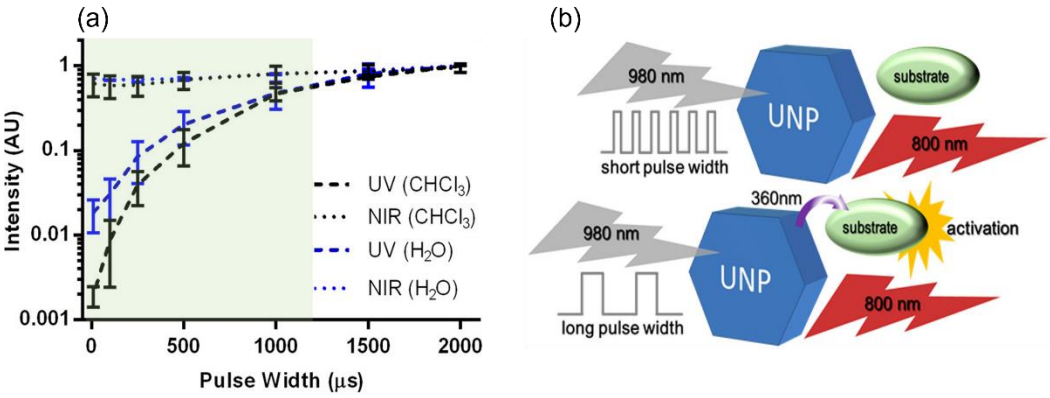

Figure 3. (a) Representing the effect of excitation pulse width on the UV and NIR emission intensity of Tm based UCNPs. (b) Showing the activation of a substrate in 2 ms excitation pulse width due to the activation of UV emission. Reprinted with permission from publication [27] copyright 2018 ACS

Furthermore, UCNPs can also be used in solar cells. Alkahtani et al. [28] electrodeposited lithium-based UC thin films, $LiYF_4:Yb^{3+},Er^{3+}$ on fluorene-doped tin oxide (FTO) glass for solar cell applications. They fabricated a complete perovskite solar cell (PSC) on top of FTO glass coated with UC thin film. The UCNPs thin film in PSCs will work as a spectral converter to harvest the near-infrared (NIR) solar photons from sunlight and convert them to absorbable visible light photons by the perovskite light-harvesting active layer. The photovoltaic performance of the fabricated PSC on the UC thin film demonstrated an increase in PCE of 24 % in comparison to pristine PSC devices.

In spite of the numerous unique photophysical properties of UCNPs, their low UCL efficiency (emission quantum yield) is still the most serious limitation for their applications. Indeed, the increase of their quantum yield emission needs a thorough understanding of the parameters that control their complex non-linear power dependent emission dynamics. In UCNPs, one type of Ln^{3+} dopant serves as a sensitizer ion that absorbs NIR light and, after multiple energy transfer steps between neighboring sensitizer ions, transfers the excitation energy to a neighboring activator ion in sequential steps which is called energy transfer upconversion (ETU).[29] An individual particle contains several dopant ions (sensitizers, emitters, host matrix ions), which can interact with one

another and create a complex network of energy transfers that can affect the efficiency of ETU by energy migration (EM) among sensitizers , cross-relaxation (CR) between emitters, or surface quenching .[30] This complex network of energy transfers between sensitizers, emitters (and host matrix ions) consist of numerous radiative and non-radiative pathways which control the emission of UCNPs, and are mediated by the size and surface coating. Therefore, deep and precise understanding of the dynamic interaction of dopants in UCNPs should be considered as an important milestone for the development of optimized UCNPs. The purpose of my thesis is thus to investigate the photodynamics at ensemble and single particle levels taking place in different types of UCNPs in order to uncover the complex energy pathways driving their emission properties.

To precisely understand the challenges about the rationalizing of emission UCNPs and the situation in the literature, in chapter 2, I will review the bibliography on the photo-dynamics of upconversion nanoparticles. I will show that challenges are on small (< 10 nm) and ultrasmall (< 3 nm) UCNPs and in the understanding of energy transfers with different receptors (other UCNPs or dyes attached to them).

This chapter is then followed (Chapter 3) by the study at the ensemble level of two small and ultrasmall UCNPs designed by our collaborators in Toulouse (Dr. C. Roux and C. Coudret, B. Amouroux, Q. Zhou). In this chapter, I will describe in detail setups that I developed. I developed ns pulse setup (excitation at 976 nm and 355 nm) equipped with different detection systems (intensified time gated camera and PMT) and ms square pulse setup to study the photodynamics of small particles at ensemble level.

In our first work which was a collaboration with Dr. Cément Roux in Toulouse, we measured steady state spectra using cw at 976 nm and time-resolved luminescence of Yb^{3+}/Tm^{3+}-doped core-only (5 nm) and core-shell heterostructured (9 nm) UCNPs under ns pulse excitation at 976 nm with a gated intensified CCD camera. We could demonstrate dramatic increase of steady state spectra and lifetimes after adding shell (these results have been published in ACSnano). [31]

Then, we moved toward even smaller UCNPs (less than 3 nm), which were developed by Baptiste Amouroux et al.[32] based on an original synthesis procedure relying on the use of a microwave heating sequence. Therefore, we decided to investigate the influence of the number of heating cycles used for the synthesis on size and emission properties. Indeed, the question raised is to know how much it is possible to decrease the size of the

particle while preserving β-crystal phase that ensures the emission properties. In this aim, investigation of the emission properties as a function of the number of heating cycles for Tm-based UCNPs has been carried out using steady state, time-resolved spectroscopy and compared to the crystal phase structure measured by XRD. Average lifetimes of the 800 nm ($^3H_4$ excited state) emission decays (under ms square pulse irradiation) show a meaningful step increase that is assigned to the apparition of β-crystal phase. Accordingly, we could precisely characterize the emergence of the emissive phase in such ultrasmall UCNPs by measuring steady state spectra and luminescence lifetimes. In addition, to analyze the dynamics of the dopant ions in nanometric nanoparticles, we concentrated on 4 representative samples which differ from the number of dopant ions and size. Decreasing the size of UCNP down to less than 10 nm inevitably brings strong quenching effects coming from high surface-to-volume ratios but also from enhanced activator cross-relaxation (CR) quenching. We demonstrated these quenching effects are strongly dependent on the emission bands considered. Ultrasmall core particles, due to their size (<3nm), have a reduced number of activators (average less than 2), and cross relaxation is thus less efficient and on the other hand, reducing the size of the particle entails an increased influence of surface quenching. However, cross-relaxation plays a major role in bigger particles (< 8 nm), which have a high activator concentration quenching. We characterize radiative and non-radiative decay rates (k_r and k_{nr}, respectively) by using various steady state emission bands under cw irradiation at 976 nm and luminescence decays with direct excitation of activators at 355 nm and excitation of sensitizers at 976 nm.

In the fourth chapter (chapter 4), my interest was to investigate the energy transfers occurring between UCNPs when they are organized with various spatial arrangements, and to characterize their heterogeneous emission at single particle level. To achieve such studies, I have developed a new confocal microscope based on a millisecond-square pulse NIR excitation and an intensified gated CCD camera detection in order to measure space- and time-resolved emission spectra at single particle level. Using this new confocal setup, we show the heterogeneity in single, 2D monolayer and 3D aggregate UCNPs. I measured steady state spectra (in cw excitation at 976 nm) and time resolved profiles (in square pulse irradiation at 976 nm) for the same pixel at various power density for core-shell and core Tm particles (β-$NaYF_4$:20% Yb^{3+}, 2% Tm^{3+} and β-$NaYF_4$:20% Yb^{3+}, 2% Tm^{3+}/$NaYF_4$) spincoated on a clean coverslip. These findings exhibited various measured

dynamic efficiency of UCNPs when they are in single particle level, monolayer structure, and in a 3D aggregate structure. In addition, for better revealing the heterogeneity among steady state spectra of UCNPs in the three mentioned arrangements, I utilized principal component analysis (PCA) to analyse the emission dependence with power densities.

In the fifth chapter, using the new confocal setup I designed to study UCNPs emission at single particle level, I investigated the energy transfer process between specific excited states of UCNPs (doped with Tm and Er emitters) and perylene diimide (PDI) molecules by measuring steady state spectra and luminescence lifetimes before and after depositing PDI molecules (PDI film). The reason that encouraged us for using two emitters is that first they have different emission spectral overlap with absorption of PDI, and secondly, in contrast to Tm, change of spin multiplicity for Er emission is different (change of spin multiplicity for some Tm emissions, no change for Er ones). Furthermore, PDI molecules were not directly attached to the surfaces of UCNPs. Instead, two usual methods, spincoating and dropcasting, were employed. Based on the obtained results, the efficiency of energy transfer depends on the sample preparation and the type of emitter (Er or Tm). Moreover, we could show that it is possible to transfer excited-state energy through a Förster-type mechanism without conserving the spin angular momentum in Tm particles.

Finally, in chapter 6, we could clarify photodynamic emission of UCNPs by investigation of ultrasmall single emitter particles with various developed spectroscopic techniques. In addition, we could investigate interparticle interaction in UCNPs and resonance energy transfer from different emitters (Tm and Er) to PDI molecules with new microscopy system. These findings also open the doors to future research.

During my PhD, I also spent two months in Dr. Peter Dedecker laboratory in KU Leuven in order to produce photoswitchable proteins, such as Dronpa, for modulation of UCNPs emission. In this period, I could also learn about transformation, transfection, DNA purification, cell culture, and super resolution optical fluctuation imaging (SOFI) microscopy. Another highlight of my experience was to participate in time-resolved microscopy and correlation spectroscopy courses at PicoQuant in Berlin. Additionally, I was lucky to present my work in 6 conferences during my PhD period and I could obtain two prizes (one for my poster in upconversion conference and another for my oral presentation in French-Swiss photochemistry symposium).

In addition, I also focused on learning Python coding. By writing some Python code, I was able to automate the time-consuming data analysis process. Furthermore, I was trying to utilize my chemometric skills in order to extract more information from hyperspectral data obtained through our microscopy setup. Finally, in an attempt to gain unprecedented insights into complex systems such as UCNPs, I tried to combine characterization approaches with advanced data analysis techniques.

1.1 References

1. IUPAC, I., *Compendium of chemical terminology*. the "Gold Book." Blackwell Scientific Publications Oxford, 1997.
2. Auzel, F., *Upconversion and anti-stokes processes with f and d ions in solids.* Chemical reviews, 2004. **104**(1): p. 139-174.
3. Leverenz, H.W. and F. Urbach, *Introduction to the Luminescence of Solids*. Physics Today, 1950. **3**(9): p. 32.
4. Gandrud, W. and H. Moos, *Improved rare-earth trichloride infrared quantum counter sensitivity*. IEEE Journal of Quantum Electronics, 1968. **4**(5): p. 249-252.
5. Pandey, A. and V.K. Rai, *Rare earth doped materials for temperature sensors.* Spectroscopic techniques for security forensic and environmental applications, 2014: p. 279-92.
6. Smirnov, V. and I. Shcherbakov, *Rare-earth scandium chromium garnets as active media for solid-state lasers.* IEEE journal of quantum electronics, 1988. **24**(6): p. 949-959.
7. Oomen, E., *Up-conversion of red light into blue light in thulium doped fluorozirconate glasses*. Journal of luminescence, 1992. **50**(6): p. 317-332.
8. Pacheco, E.M. and C.B. De Araujo, *Frequency up-conversion in a borate glass doped with Pr3+*. Chemical physics letters, 1988. **148**(4): p. 334-336.
9. Chamarro, M. and R. Cases, *Energy up-conversion in (Yb, Ho) and (Yb, Tm) doped fluorohafnate glasses*. Journal of luminescence, 1988. **42**(5): p. 267-274.
10. Yeh, D., W. Sibley, and M. Suscavage, *Efficient frequency upconversion of Tm3+ ions in Yb3+ doped barium-thorium fluoride glass.* Journal of applied physics, 1988. **63**(9): p. 4644-4650.
11. Kamma, I., et al., *Spectroscopic characterization of erbium doped glass ceramic*. Optical Materials Express, 2013. **3**(6): p. 884-892.
12. Alivisatos, A.P., *Semiconductor clusters, nanocrystals, and quantum dots*. science, 1996. **271**(5251): p. 933-937.
13. Armstrong, A.R. and P.G. Bruce, *Synthesis of layered LiMnO2 as an electrode for rechargeable lithium batteries.* Nature, 1996. **381**(6582): p. 499-500.
14. Choi, J.-s., et al., *Biocompatible heterostructured nanoparticles for multimodal biological detection*. Journal of the American Chemical Society, 2006. **128**(50): p. 15982-15983.
15. Li, X., F. Zhang, and D. Zhao, *Lab on upconversion nanoparticles: optical properties and applications engineering via designed nanostructure.* Chem Soc Rev, 2015. **44**(6): p. 1346-78.
16. Kumar, R., et al., *Combined optical and MR bioimaging using rare earth ion doped NaYF4 nanocrystals.* Advanced Functional Materials, 2009. **19**(6): p. 853-859.
17. Xing, H., et al., *Multifunctional nanoprobes for upconversion fluorescence, MR and CT trimodal imaging.* Biomaterials, 2012. **33**(4): p. 1079-1089.
18. Yang, Y., et al., *Hydrothermal synthesis of NaLuF4: 153Sm, Yb, Tm nanoparticles and their application in dual-modality upconversion luminescence and SPECT bioimaging.* Biomaterials, 2013. **34**(3): p. 774-783.
19. Sun, Y., et al., *Fluorine-18 labeled rare-earth nanoparticles for positron emission tomography (PET) imaging of sentinel lymph node.* Biomaterials, 2011. **32**(11): p. 2999-3007.
20. Liu, B., et al., *Multifunctional UCNPs@ PDA-ICG nanocomposites for upconversion imaging and combined photothermal/photodynamic therapy with enhanced antitumor efficacy*. Journal of Materials Chemistry B, 2016. **4**(28): p. 4884-4894.
21. He, J., et al., *Tumor targeting strategies of smart fluorescent nanoparticles and their applications in cancer diagnosis and treatment.* Advanced Materials, 2019. **31**(40): p. 1902409.
22. Xiong, L., et al., *High contrast upconversion luminescence targeted imaging in vivo using peptide-labeled nanophosphors.* Analytical chemistry, 2009. **81**(21): p. 8687-8694.

23. Idris, N.M., et al., *In vivo photodynamic therapy using upconversion nanoparticles as remote-controlled nanotransducers.* Nature medicine, 2012. **18**(10): p. 1580-1585.
24. Cheng, L., et al., *Facile preparation of multifunctional upconversion nanoprobes for multimodal imaging and dual-targeted photothermal therapy.* Angewandte Chemie, 2011. **123**(32): p. 7523-7528.
25. Wang, C., L. Cheng, and Z. Liu, *Drug delivery with upconversion nanoparticles for multi-functional targeted cancer cell imaging and therapy.* Biomaterials, 2011. **32**(4): p. 1110-1120.
26. Qi, M., et al., *Novel nanotechnology and near-infrared photodynamic therapy to kill periodontitis-related biofilm pathogens and protect the periodontium.* Dental Materials, 2019. **35**(11): p. 1665-1681.
27. Dawson, P. and M. Romanowski, *Excitation Modulation of Upconversion Nanoparticles for Switch-like Control of Ultraviolet Luminescence.* J Am Chem Soc, 2018. **140**(17): p. 5714-5718.
28. Alkahtani, M., et al., *Electrodeposition of lithium-based upconversion nanoparticle thin films for efficient perovskite solar cells.* Nanomaterials, 2022. **12**(12): p. 2115.
29. Resch-Genger, U. and H.H. Gorris, *Perspectives and challenges of photon-upconversion nanoparticles-Part I: routes to brighter particles and quantitative spectroscopic studies.* Analytical and bioanalytical chemistry, 2017. **409**(25): p. 5855-5874.
30. Chan, E.M., E.S. Levy, and B.E. Cohen, *Rationally Designed Energy Transfer in Upconverting Nanoparticles.* Adv Mater, 2015. **27**(38): p. 5753-61.
31. Zou, Q., et al., *Heterogeneous Oxysulfide@ Fluoride Core/Shell Nanocrystals for Upconversion-Based Nanothermometry.* ACS nano, 2022. **16**(8): p. 12107-12117.
32. Amouroux, B., et al., *Importance of the Mixing and High-Temperature Heating Steps in the Controlled Thermal Coprecipitation Synthesis of Sub-5-nm Na (Gd–Yb) F4: Tm.* Inorganic Chemistry, 2019. **58**(8): p. 5082-5088.

2

State of the art on the photodynamics of upconversion nanoparticles and goal of the thesis

2.1 Definitions

Upconversion nanoparticles (UCNPs) are a class of luminescence nanomaterials which are characterized by their anti-Stokes emission and non-linear irradiation power dependent behavior. These luminescent materials, which include a host matrix and dopants, are frequently referred to as phosphors, which literally means "light bearer." Lanthanide elements, which have the most intricate electronic structures due to the abundance of incomplete 4f energy levels, are mostly incorporated into the host matrix in these components.[1]

2.1.1 Anti-stokes emission

Spectroscopy is concerned with the interaction of electromagnetic radiation with matter. It provides information on the wavelengths of electromagnetic radiation.[1] Optical spectroscopy stands out among the different spectroscopy techniques because it enables to obtain detailed information about the absorbing and emitting atoms, ions, molecules, defects, as well as their local surroundings, etc.[2] Aspects of optical spectroscopy can be categorized into four groups: absorption, luminescence, reflection, and scattering.[3] In the presence of photons of the appropriate frequency, a matter might transit upward to a higher state and return to the ground state by different processes (stimulated radiation, radiative emission, and non-radiative relaxation etc.).[3] The phenomenon of luminescence caused by excitation of light is known as photoluminescence. The luminescent materials can be divided into Stokes- and anti-Stokes-types luminescent materials based on the energy of the excitation and emission bands. Through the use of proper ultraviolet (UV) or near-infrared (NIR) excitations, the photoluminescent materials can emit visible emissions. When the energy of emitted photon exceeds the energy of absorbed photon, this is known as an anti-Stokes emission.[2, 3] In the anti-Stokes emission process, three processes are involved: two-photon absorption (TPA), second harmonic generation (SHG), and upconversion (UC) as shown in Figure 1.[4, 5] Maria Goeppert-Mayar anticipated TPA in 1931, which was experimentally verified by the laser following its discovery.[6] The simultaneous absorption of two photons of the same or different frequencies by an atom, ion, or molecule is known as TPA.[7] The electron is promoted from a low energy level, or ground state, to an excited level during this process, and the energy of the emission transition is equal to the sum of the two-photon energies.

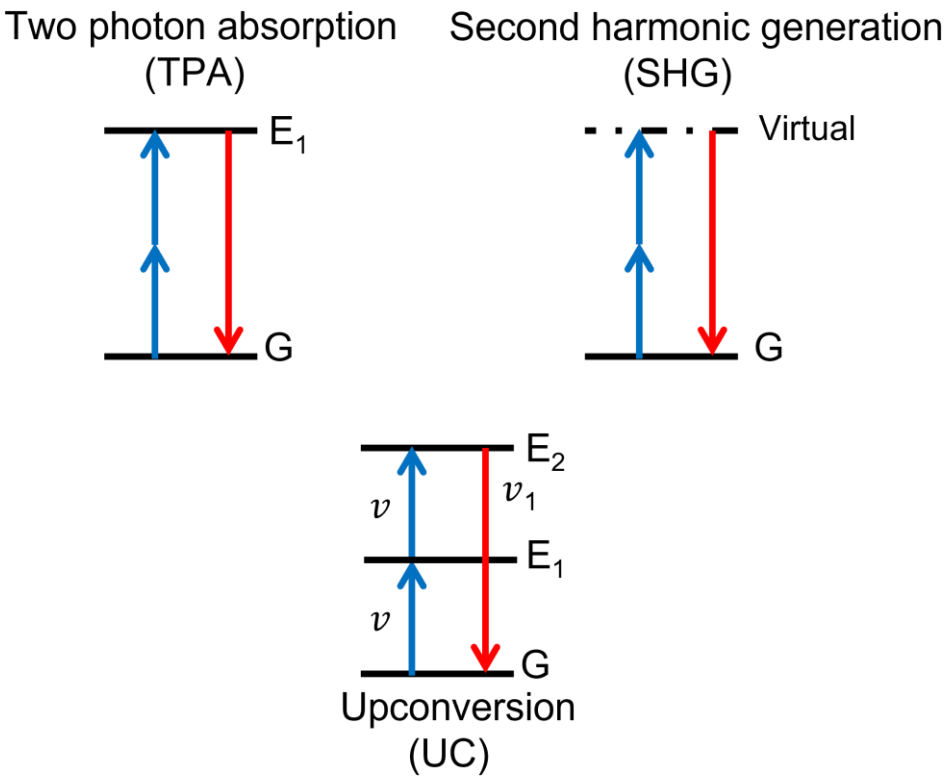

Figure 1. Representing basic energy level diagrams of anti-stoked processes (two-photon absorption, second harmonic generation, and upconversion).

On the other hand, SHG, "an optical nonlinear process," occurs from a virtual state in a medium having second-order nonlinear susceptibility. As mentioned in Figure 1, SHG occurs when two photons of the same frequency interact with a nonlinear medium and give rise to a new photon of double the frequency or energy of the incident photon.[8] Franken et al. made this known and experimentally demonstrated it in 1961. When the quartz crystal was exposed to a powerful 6943 Å beam from the ruby laser, they were able to identify the second harmonic light.[9]

Additionally, UC, which is a stepwise absorption process involving intermediate states, is an anti-Stokes mechanism that transforms low-energy photons into high-energy photons as demonstrated in Figure 1, such as converting infrared light into visible or ultraviolet light. In general, SHG and TPA require a pulsed beam (femtosecond for TPA) as well as a very high excitation beam intensity, while the UC process happens even with cw laser beam intensities due to the presence of actual long lifetime intermediate states.[10, 11] It is known that upconverting materials are those that exhibit UC properties. In general, the UC phenomena seen in these materials is not as straightforward

as shown in Figure 1, and in the following chapter we will discuss numerous processes that are responsible for the UC mechanisms. Before going through various UC mechanisms, let's introduce lanthanides, the key elements for UCNPs, and their photophysical characteristics.

2.1.2 Lanthanides and their photophysical properties

The 15 chemical elements that make up the lanthanides have atomic numbers that range from 57 to 71 in the sixth period of the periodic table, and these 15 lanthanide elements are commonly named as lanthanum (La), cerium (Ce), praseodymium (Pr), neodymium (Nd), promethium (Pm), samarium (Sm), europium (Eu), gadolinium (Gd), terbium (Tb), dysprosium (Dy), holmium (Ho), erbium (Er), thulium (Tm), ytterbium (Yb), and lutetium (Lu). They are grouped together as rare earth (RE) elements together with the elements yttrium (Y) and scandium (Sc).[12] RE elements are used in most lasers, phosphors, amplifiers, etc. The elements ytterbium, yttrium, erbium, and terbium were later called after the Swedish settlement of Ytterby, where Carl Axel Arrhenius originally found the lanthanides (Lns) in a black, heavy material in 1787.[13] RE elements can either be trivalent or divalent and are incorporated into a variety of host materials. In divalent and trivalent RE ions, the configurations are $5d^m\ 4f^n\ 5s^2\ 5p^6$ and $4f^n\ 5s^2\ 5p^6$, where n (which varies from 0 to 14) indicates how many electrons are available in the unfilled 4f shell and are responsible for the spectroscopic transitions. The divalent RE ions Eu (+2), Yb (+2), and Sm (+2) contain one additional electron than the trivalent ions, which gives them different optical features and different treatment - which is not the scope of this thesis.[14, 15] These elements lose their 5d and 6s orbital electrons in the triply ionized state, as shown in table 1, but because the 5s and 5p orbitals have greater radii than the 4f orbital, the 4f electrons remain protected. Due to the shielding effect of RE ions when they are absorbed into a solid host, the 4f electrons are very minimally disrupted, in contrast to transition metals where the outer 3d electrons are severely influenced by the crystal field effect. As a result of this shielding effect, the 4f energy levels in RE ions do not differ very much between hosts and show sharp absorption and emission spectra (line-like), which are characteristic of each metal.[16, 17]

Table 1. Electronic configuration of trivalent Lanthanide ions.[18]

Ion	atomic number	Electronic configuration	$S = \sum s$	$L = \sum l$	$J = L - S$ ($n < 7$) $J = L + S$ ($n \geq 7$)	Ground state
La^{+3}	57	$[Xe]4f^0$	0	0	0	$^1S_0$
Ce^{+3}	58	$[Xe]4f^1$	1/2	3	5/2	$^2F_{5/2}$
Pr^{+3}	59	$[Xe]4f^2$	1	5	4	$^3H_4$
Nd^{+3}	60	$[Xe]4f^3$	3/2	6	9/2	$^4I_{9/2}$
Pm^{+3}	61	$[Xe]4f^4$	2	6	4	$^5I_4$
Sm^{+3}	62	$[Xe]4f^5$	5/2	5	5/2	$^6H_{5/2}$
Eu^{+3}	63	$[Xe]4f^6$	3	3	0	$^7F_0$
Gd^{+3}	64	$[Xe]4f^7$	7/2	0	7/2	$^8S_{7/2}$
Tb^{+3}	65	$[Xe]4f^8$	3	3	6	$^7F_6$
Dy^{+3}	66	$[Xe]4f^9$	5/2	5	15/2	$^6H_{15/2}$
Ho^{+3}	67	$[Xe]4f^{10}$	2	6	8	$^5I_8$
Er^{+3}	68	$[Xe]4f^{11}$	3/2	6	15/2	$^4I_{15/2}$
Tm^{+3}	69	$[Xe]4f^{12}$	1	5	6	$^3H_6$
Yb^{+3}	70	$[Xe]4f^{13}$	1/2	3	7/2	$^5F_{7/2}$
Lu^{+3}	71	$[Xe]4f^{14}$	0	0	0	$^1S_0$

Different perturbations cause the 4f energy levels to split, including electron-electron interactions (coulombic interactions), spin-orbit coupling, and ligand field effects as illustrated in Figure 2. The effects of these interactions are different for 3d and 4f ions. In contrast to d electrons, the 4f electrons are mostly concentrated in the inner shell, making the effects of the ligand-field on the electronic structure far less significant. In addition, the spin-orbit coupling of lanthanides are much stronger than that of 3d-block ions. As a consequence, these effects make various characteristics in 4f ions.[19, 20]

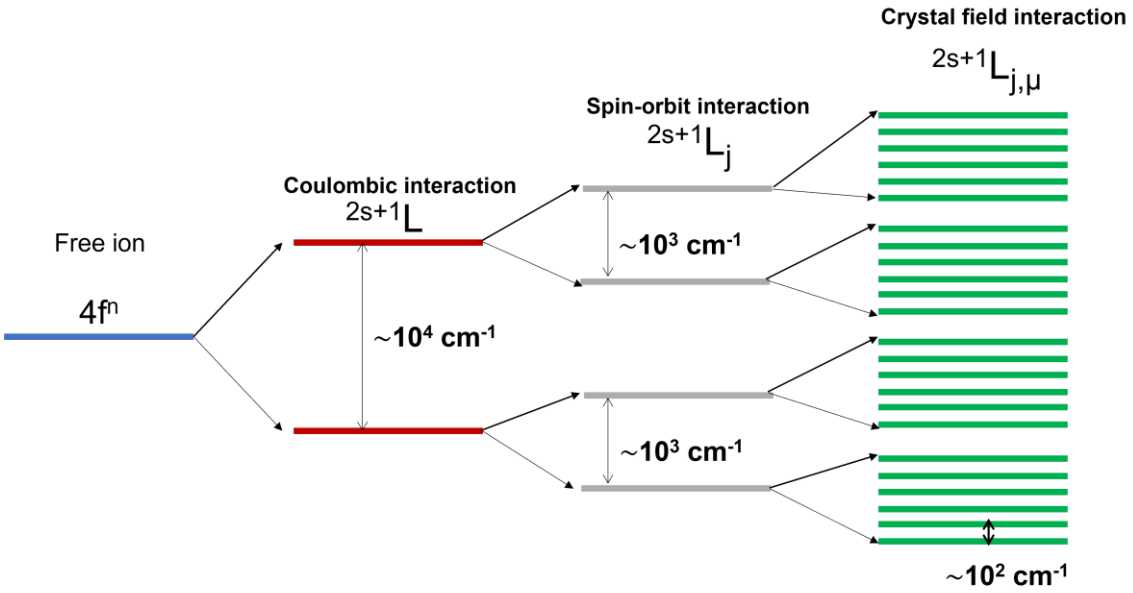

Figure 2. Energy levels in 4f of lanthanide ion electronic structures. From left to right, electron-electron interactions, spin-orbit coupling, and crystal field interactions.

Indeed, coulombic interaction, which denotes the repulsion between 4f valence electrons in the RE ions, is the strongest of the three interactions (as mentioned in Figure 2, the energy separation is in the order of 10^4 cm^{-1}). Due to the coulombic interaction, the individual electrons' orbital angular momentum (l_i) and spin angular momentum (s_i) couple together to generate total orbital angular momentum (L) and total spin angular momentum (S). The energy levels of all RE ions are separated into ^{2S+1}L folds as a result of this interaction. In spin-orbit interaction, the total angular momentum term (J) is produced as a result of the spin and orbital angular momentum coupling and the splitted levels are represented as $^{2S+1}L_J$ levels.[21, 22] Depending on how differently orbitals are filled, the value of J varies (L-S for less than half-filled and L+S for more than half-filled). In some cases, when doping RE ions are into host materials, a strong crystal field can be occasionally formed. When this happens, the RE ions $^{2S+1}L_J$ levels once more exhibit additive splitting, or Stark splitting. The degeneracy of $^{2S+1}L_J$ level becomes 2J+1 for fold in the case of even number of electrons in 4f and J+1/2 fold for odd values of valence electrons. As a result, $^{2S+1}L_{J,\mu}$ (μ demonstrates number of Stark sublevels) is the general representation of the energy level of dopant ions for Stark splitting. Accordingly, due to the weak crystal field effect in RE-doped host materials (often referred to as phosphors), the spin-orbit interaction typically predominates (as shown in Figure 2, it is 10 times

more).[22] Figure 3 illustrates all the energy level structures of lanthanide ions, which is known as Dieke diagram.[23]

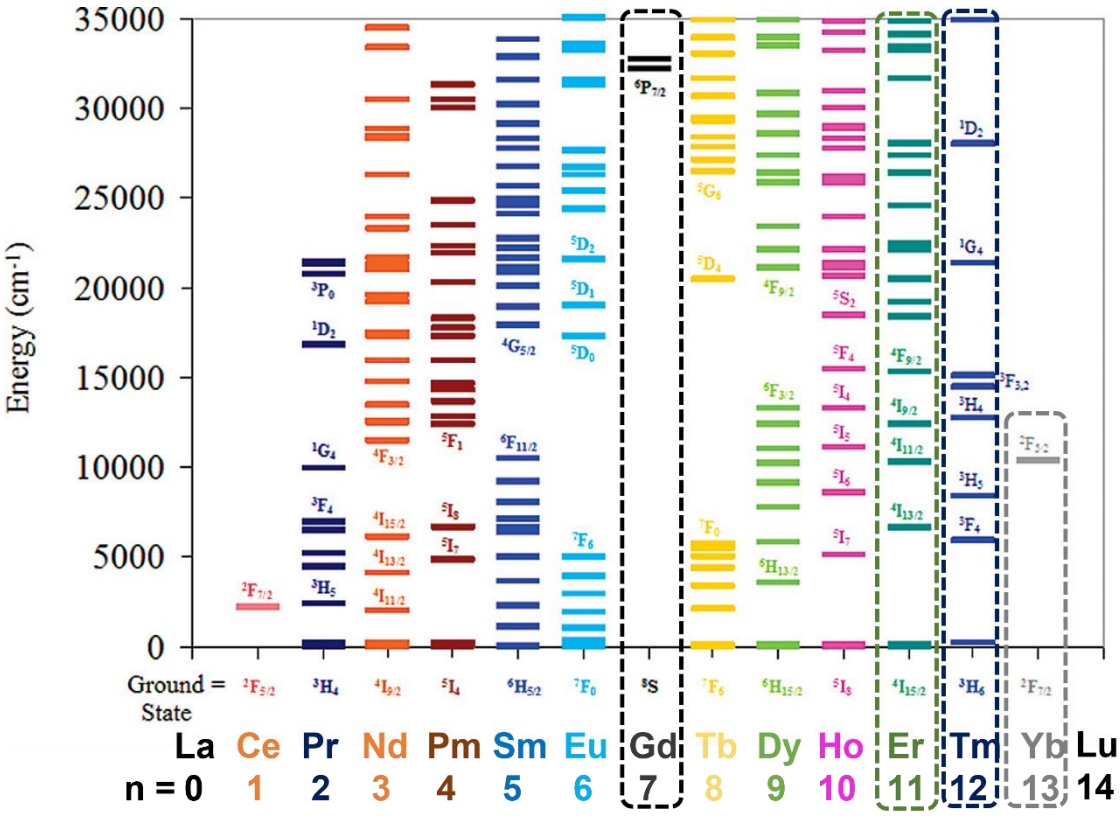

Figure 3. Dieke diagram representing a summary of electronic ground and excited state energy levels the Ln (III) series.

Optical electromagnetic radiation (light) process uses oscillating electric dipoles (ED), magnetic dipoles (MD), electric quadrupoles (EQ) as its sources of radiation. As a result of the selection rules, Laporte rules,[24] that need to be followed, not all possible transitions are permitted. In fact, the interaction of the lanthanide ion with the oscillating magnetic field component of light leads to magnetic dipole transitions.[24, 25] The Laporte selection rule completely permits these transitions, although they have a low transition probability. When a lanthanide ion is positioned in several host lattices, the strength of MD transitions is essentially unaffected by the local environment.

An electric dipole transition occurs when a lanthanide ion interacts with an oscillating electric field component of light. For a free ion, ED transitions between states of the same configuration (for example f-f transition) are strictly parity forbidden (since the parity of

the initial and final state does not change). However, the wave functions of the 4f and 5d orbitals mix in the presence of the crystal field (Stark effect), 4f-4f transitions in RE-doped phosphor materials that were previously parity prohibited are now allowed. Increasing the mixing degree means deviating further from inversion symmetry and reducing the energy difference between states of opposite parity. Then, higher ED transition probabilities are the result of improved mixing. Because of this, the local environment of the lanthanide ion has a significant impact on the intensity of ED transitions. [26, 27] [28]

Although MD and EQ are parity-allowed, they are much weaker than the ED transitions. The cause is that ED is partly allowed because initial and final states in the presence of a crystal field will have different parities. (based on the selection rules which are listed in Table 2).[29-31]

Table 2. Selection rules for f-f transitions between spectroscopic levels. J = 0 to J' = 0 transitions are always forbidden.

Operator	Parity	ΔS	ΔL	ΔJ
EQ	Same	0	0, ±1, ±2	0, ±1, ±2
MD	Same	0	0	0, ±1
ED	Opposite	0	≤6	≤6(2,4,6 if J or J'=0)

The phrases "forbidden" and "allowed" transitions should not be interpreted too strictly because the selection rules are generated under a number of hypotheses that are not always fully met in reality. It would be much more accurate to say that a forbidden transition is less likely to occur with a long characteristic time constant, and an allowed transition is highly likely. [32]

2.1.3 Different upconversion processes

The materials with the UC characteristics are referred to be upconverting materials. As soon as upconversion materials absorb photons, several processes are accountable for UC mechanisms as follow (Figure 4).

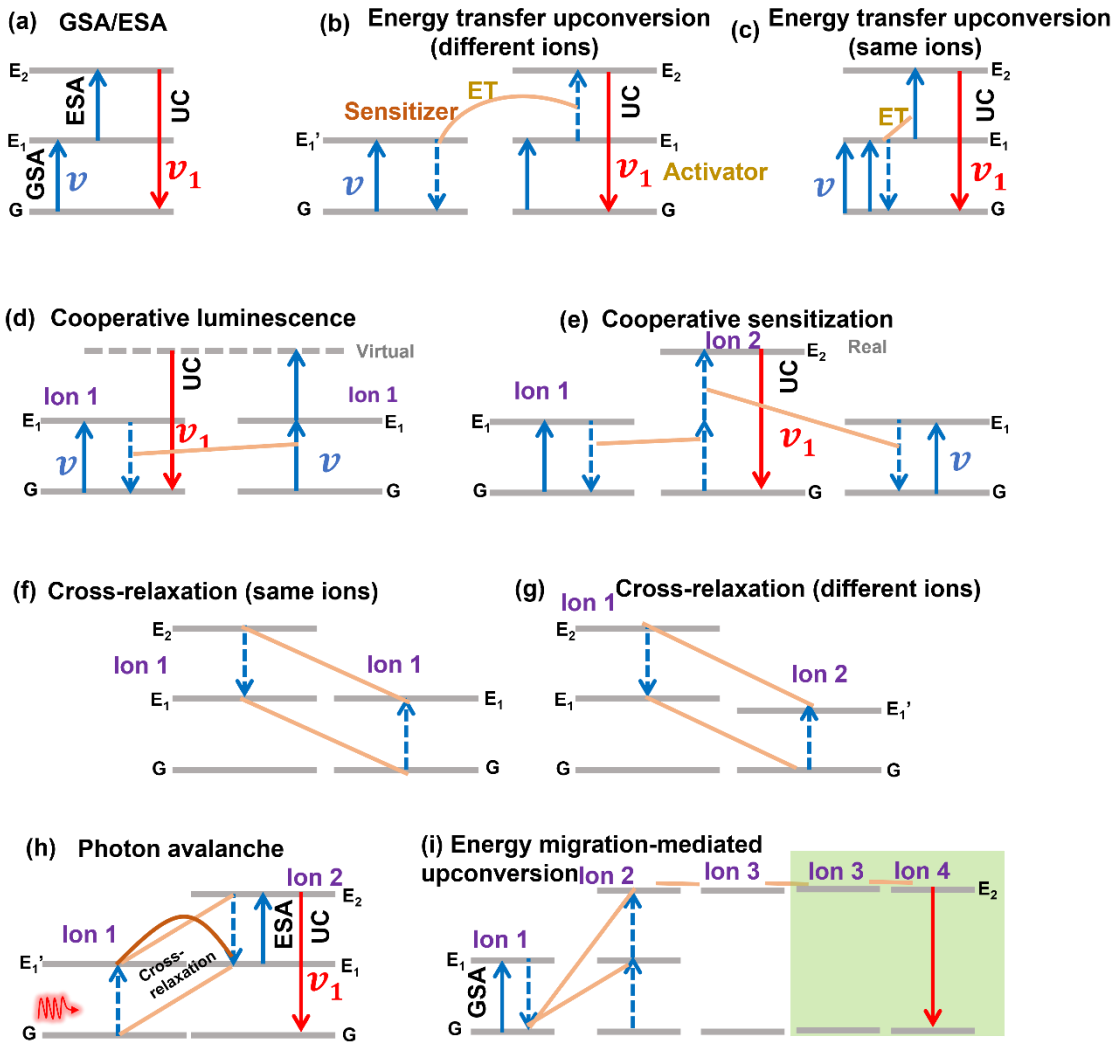

Figure 4. Schematic representation of possible UC mechanisms. (a) Ground State Absorption (GSA) and Excited State Absorption (ESA); (b and c) Energy Transfer Upconversion (ETU); (d) cooperative luminescence; (e) cooperative sensitization; (f and g) Cross Relaxation (CR); (h) Photon Avalanche (PA) processes. (i) Energy migration upconversion in the presence of four different ions. Four types of luminescent centers are incorporated into separate layers with precisely defined concentrations of sensitizer, accumulator, migrator and activator.[1]

2.1.3.1 Ground/excited state absorption (GSA/ESA)

One of the trivial photo-induced process UC is ground-state absorption (GSA). The GSA is the process by which the ground-state ions, having obtained the necessary energy from the pump photons, are elevated to the first intermediate level. The ESA process is independent of the dopant concentration because, as Figure 4a illustrates, it takes place within a single ion. Ions constantly absorbed low energy photons, allowing them to attain a metastable excited state and then higher excited levels. UC emission happens when an ion radiatively decays from an excited state (E_2) to its ground state (G). A ladder-like energy-level arrangement in the ions is necessary to achieve efficient UC emission through the ESA procedure. Only a few numbers of lanthanide ions, such as Nd^{3+}, Er^{3+}, and Tm^{3+}, have this arrangement of energy levels and a well-matched excitation wavelength of 975 and/or 808 nm.[32, 33]

2.1.3.2 Energy transfer upconversion (ETU)

Energy transfer upconversion (ETU), which is distinct from ESA, is shown in Figure 4b and c. ETU requires the involvement of two nearby ions, one of which is a sensitizer and the other an activator. The pump photons are absorbed by the sensitizer as they go from the ground state to the E_1 energy level, and it constantly transmits the harvested photons to the excited state E_1 of the activator. Eventually, the activator reaches its maximum emission level E_2, while the sensitizer relaxes back into its ground state G. The efficiency of the ETU process relies on the distance between the sensitizer and activator as well as the ion concentration. To understand upconversion luminescence (UCL) mechanism in UCNPs, ETU procedure is crucial because UCNP is doped with Yb^{3+}/Er^{3+}, Yb^{3+}/Ho^{3+}, and Yb^{3+}/Tm^{3+} ion pairs (sensitizers and activators) for excitation at 980 nm.

2.1.3.3 Cooperative luminescence and cooperative sensitization upconversion (CSU)

Two ions are involved in UC emission through a cooperative energy transfer mechanism (one performs the role of a donor, while the other acts as an acceptor).[34, 35] As depicted in Figure 4d, two ions absorb the pump photons sequentially in the cooperative luminescence process to reach the higher (intermediate) state E_1. These two ions transfer their energy at this intermediate level in such a way that the donor returns to the ground

state while the acceptor obtains excitation energy (G). The acceptor ascends to a higher energy level, "which is a virtual state," after receiving the donor's excitation energy. In this case, the lifetime of virtual state will be short. For example, Knighton et al. mearsured nanosecond (ns) lifetime range for virtual state in $RuYb_3$ system. [36] The cooperative energy state is another name for this virtual state. It relaxes radiatively from this virtual state to the ground state (G) by producing a photon with an energy greater than the incident photon energy as demonstrated in Figure 4d. Conversely, at least three ion centers would be involved in the cooperative sensitization upconversion process (CSU). According to Figure 4e, ions 1 and 3 typically belong to the same element, and after absorbing pump photons, both of them are excited to the appropriate excited states. Subsequently, ion 2 is concurrently interacted with by both excited ions, and they cooperate together to transmit the absorbed energy to excite it to greater levels. The upconverted radiate energy is released by the excited ion 2 so that it may relax back into ground state. As they transfer the absorbed energy to ion 2, ions 1 and 3 are regarded as sensitizers in this instance. The upconverted photons are generated by ion 2, which acts as an activator and absorbs the activation from both excited ions. In general, UC mechanism is described based on CSU process for various Ln-ion pairings, including Yb^{3+}/Eu^{3+}, Yb^{3+}/Pr^{3+}, and Yb^{3+}/Tb^{3+}. As an example, Charbonnier et al. reported cooperative sensitization upconversion of lanthanide complexes in solution.[37] In their study, molecular solution-state cooperative luminescence (CL) upconversion arising from an Yb excited state is explored and the mechanistic origin behind cooperative sensitisation (CS) upconversion in Yb/Tb systems (Tb_xYb_y) is investigated.

2.1.3.4 Cross-relaxation (CR)

Ion-ion interaction is the main cause of the energy transfer process known as cross relaxation between two ions. As shown in Figure 4f, self-quenching occurs as a result of the cross-relaxation of two similar ions or molecules. The intermediate states of both ions (ion 1) in the self-quenching process have the same energy (E_1). When two different ions cross-relax, the first ion shares some of its excitation energy with the second ion through the mechanism E_2 (ion 1) + G (ion 2) → E_1 (ion 1) + E_1' (ion 2) as demonstrated in Figure 4g. In this process, a portion of the excitation energy from the first ion (ion 1), which is originally present in the excited state (E_2), is transferred to the second ion (ion 2), which is initially present in the ground state (G). In this manner, the energy of the first ion (ion

1) decreases by an amount equal to the energy of the second ion increases. As a consequence, both ions or molecules change to the excited state (E_1 and E_1') at the same time.[28, 38] It worth mentioning that the CR process is low in low concentration of activator in UCNPs (usually below 2 mol %). Wei et al. reported a systematic investigation of CR in Tm based UNCPs with heavy activator doping. [39] They showed 100% red emission output in visible region through CR effect rely solely on Tm interactions. Their strategy based on CR effect is not only successful in achieving pure red 696 or 660 nm UC emission but could also act as an alternative approach for precise UC colour tuning and provide further insight into the UC mechanism. In addition, Figure 6b demonstrates some examples of CR processes among Tm^{3+} ions.

2.1.3.5 Photon Avalanche (PA)

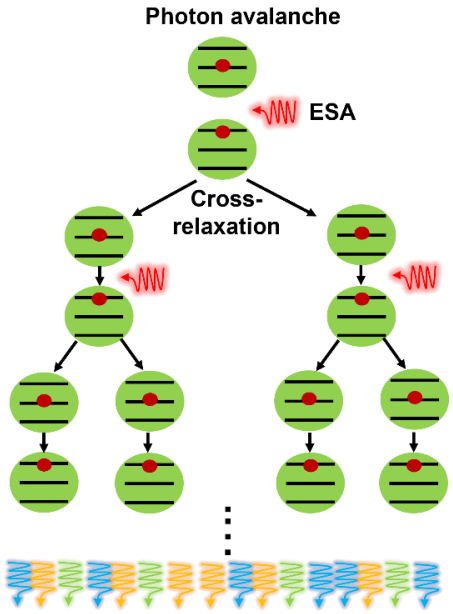

Figure 5. Schematic representation of photon avalanche mechanism illustrates that the efficient cross-relaxation and ESA procedures are looped.

Photon avalanche (PA), which was first discovered experimentally in Pr^{3+}-doped infrared quantum counters by Chivian (in 1979), is one of UC processes (it is known as absorption avalanche as well).[40] This PA process typically starts when the excitation energy goes beyond its threshold limit. Upon exceeding this threshold, the intensity of UCL can be seen to increase dramatically with increasing power of excitation; below the threshold, very slight upconversion luminescence (UCL) occurs. As depicted in Figure 4h, the

intermediate level and the higher excited level are first populated by the GSA, ESA, and ETU processes in order for the PA process to occur. Two ions are produced at the intermediate level E_1 by the CR process between these upper excited levels and the ground state of a nearby ion. Two ions are now accessible for the ESA process in the intermediate stage. The result is an increase in the quantity of ions in the intermediate level and substantial UC emission as a function of the simultaneous feedback looping of ESA and CR processes (Figure 5).

In PA process, the higher excited state E_2 of ion 2 and state E_1' of ion 1 are in resonance with the frequency of the incident photon. Therefore, it could result in considerable UC emission from the intermediate state (E_1) of ion 2 without any resonant GSA from the ground state (G).

2.1.3.6 Energy migration-mediated upconversion (EMU)

The EMU process is more complex than other UC processes and can only be found in core-shell structures (we will go through this structure in more details following this chapter). Sensitizer (ion-1), accumulator (ion-2), migrater (ion-3), and activator (ion-4) are the four kinds of ions that participate in this process. Sensitizer is initially excited by incident light, and the energy then moves to an accumulator ion. Afterward, the migrator ion receives the accumulated energy from the accumulator ion and the excitation energy migrates through the migrator ion through the core-shell sub-lattice. Finally, the activator ion receives the migratory energy to release upconverted energy.[41]

According to Auzel,[32] the ETU process is the most effective of all of them when evaluating the magnitude of each process' quantum efficiency in comparison to all of the other mechanisms. It's interesting to note that upconversion phenomena exceeds the typical non-linear processes enabled by coherent photon absorption (two photon or second order harmonic generation SHG). Compared to other lanthanides, Yb^{3+} and Nd^{3+} (whose Dieke diagram is particularly simple) have a higher absorption cross section that makes them an ideal option for sensitizer (sometimes it is called antenna). The sensitizer and activator are selected in accordance with the application under consideration. For example, Yb^{3+} ion requires the wavelength of the irradiation to be adjusted to 976 nm. On the other hand, the irradiation wavelength should be set at 800 nm when Nd^{3+} is present. Likewise, the activator (emitter) ions are selected in accordance with the

application (favourable wavelength). For instance, Tm^{3+} and Er^{3+} ions are two famous emitters, which have recently been used in many applications and are known as blue and green emitters, respectively, based on their maximum intensity peak. Figure 6 shows the ETU scheme and CR for upconversion nanoparticles under different excitation wavelength, which can have multiple emissions based on the emitter ions.[42]

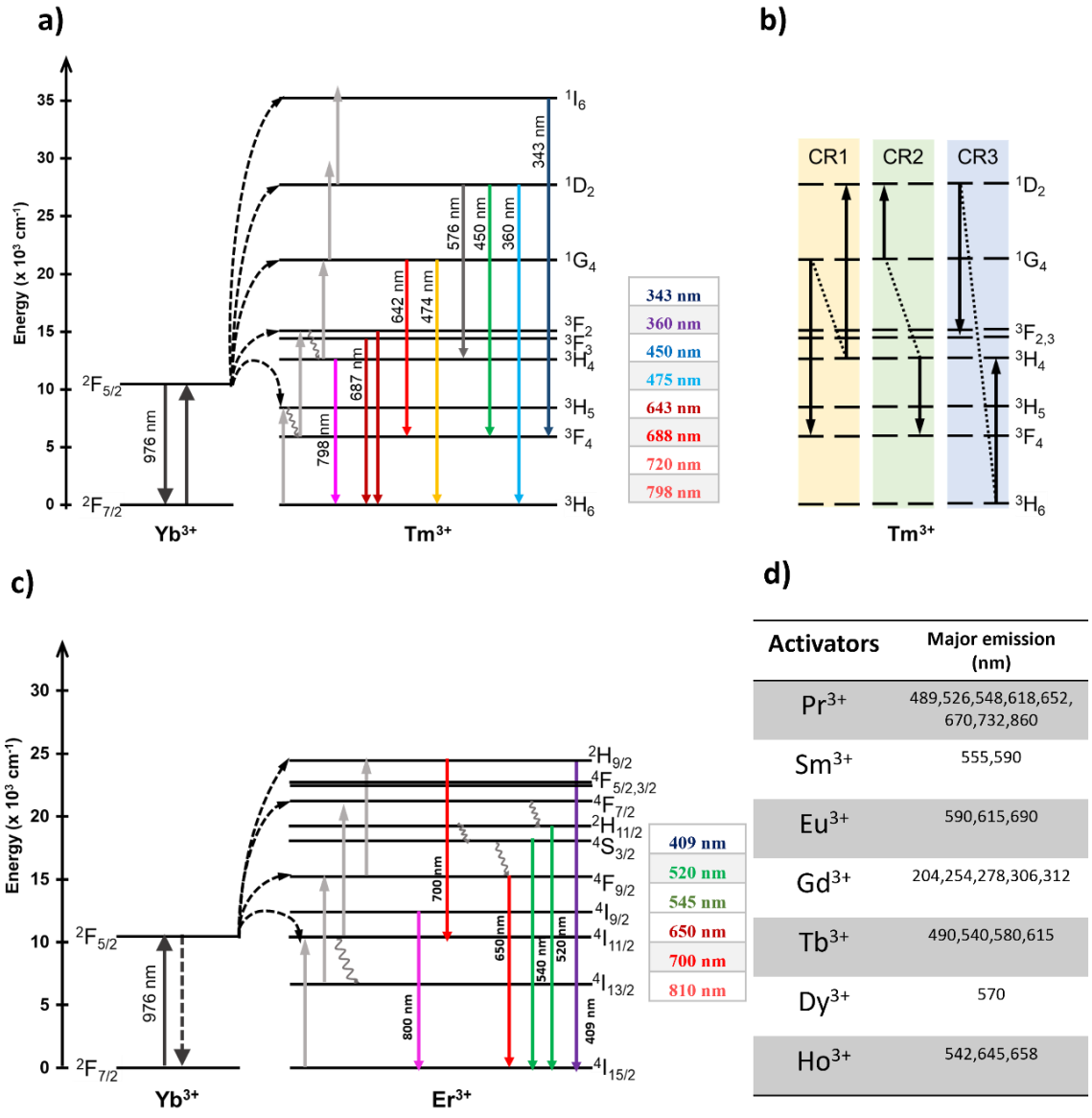

Figure 6. (a) Energy level diagram of Yb^{3+},Tm^{3+}. (b) Possible cross-relation process for Tm ions. (c) Energy level diagram of Yb^{3+},Er^{3+}.(d) Other activators with their major emission bands.

2.1.3.7 Temporal response of UCNPs

As previously mentioned, since the majority of UCNPs are doped with ion pairs, following equations can be used for describing the ETU process between sensitizer and activator (Figure 4):

$$\frac{dn_{E'1}}{dt} = \rho_{exc}\sigma n_{Gs} - W_0 n_{E'1} n_{Ga} - W_1 n_{E'1} n_{E1} - A_{E'1} n_{E'1} \qquad (1)$$

$$\frac{dn_{E1}}{dt} = W_0 n_{E'1} n_{Ga} - W_1 n_{E'1} n_{E1} - A_{E1} n_{E1} \qquad (2)$$

$$\frac{dn_{E2}}{dt} = W_1 n_{E'1} n_{E1} - A_{E2} n_{E2} \qquad (3)$$

where n_{Gs} , $n_{E'1}$, n_{Ga}, n_{E1}, n_{E2} are the populations of each of the energy levels of the sensitizer and acceptor respectively, ρ_{exc} is the laser photon number density, σ is the absorption cross section of the sensitizer ion, W_1 and W_2 are the energy transfer coefficients from the $n_{E'1}$ level to the n_{Ga} and n_{E1} levels, respectively, and $A_{E'1}$ and $A_{E1,E2}$ are the decay rates of the corresponding energy levels (Figure 6).

According to the previous statement, the emission of upconversion is a non-linear process. The link between excitation power density P (under cw irradiation) and upconversion emission intensity I, that is $I \propto P^n$ under low power density, was predicted by Pollnau et al. in the year 2000 which is call log-log plot (or power density plot).[4] The value of n shows how many NIR excitation photons are necessary to produce one upconversion photon. Based on a simplified upconversion model and the low-density excitation assumption, this well-known and distinctive description is generated. Because of the impacts of nonlinearity, UCNPs with various n frequently have dissimilar responses to the power density. It worth mentioning that by increasing the excitation power, n gradually becomes one, regardless of the number of energy transfer steps involved, and UCL saturation appears. This saturation is due to the saturated absorption of the sensitizers (Yb^{3+}). In other words, at high power, the saturated sensitizer keeps the activator (Tm^{3+} or Er^{3+}) in the excited state rather than in the ground state and only one subsequent energy transfer is required to bring it to emitting states. In addition, when n is smaller than one, the UCL quenching is due to the thermal effects.[43, 44] Additionally, the main reason that sometimes n is not precisely an integer number is due to the presence of the ‘‘real’’ intermediate states from which competing decay channels other than upconversion are available.[28]

Measuring power dependent plot under cw excitation can be informative about the dynamics of ETU process. For example, Shan et al. [43] compared the slope of power dependence plots for showing the surface effect in various particle's shapes. They demonstrated that by decreasing the surface to volume ratio the slope factor decreased due to the increasing of surface defect.

Moreover, the temporal response of UCNPs is a crucial component of their optical characteristics since they are kinetic systems.[45] A kinetic system's temporal response is fundamentally characterized by its impulse response function, i.e., the time trace in response to short-pulsed excitation (ideally a δ(t) function). Different upconversion systems can exhibit distinct impulse response functions depending on the processes. In a GSA/ESA mechanism, the upper emitting state is populated only during laser pulses. As shown in Figure 7a, a short-pulsed excitation causes instantaneous luminescence that decays at the same rate as that seen with direct excitation to the emitting state. The time profile of the upconversion luminescence signal following short-pulsed excitation, on the other hand, for a GSA/ETU mechanism (Figure 4b) exhibits both rise and decay behaviour with a delayed maximum (Figure 7b), denoting that the upper emitting state population does not occur during the laser pulse but rather occurs after the laser pulse. According to phenomenology, upconversion luminescence exhibits the following impulse response function [46, 47]:

$$I(t) = A \qquad (4)$$

where A is a scaling factor, and τ_d and τ_r are the decay and rising time constants. In the literature, these time constants, particularly the decay time constant, are frequently regarded as the intrinsic radiative properties of the emitting energy state. However, it should be made clear that such an interpretation is incorrect because the theoretical analyses carried out by Gamelin et al.[48] reveal that these observed time constants typically refer to the temporal response of the entire upconversion system rather than to the characteristics of any specific energy state. It means that both the rise and decay times are impacted by the lifetimes of the involved energy states and also by the energy transfer between the sensitizers and activators. Therefore, for accurate intrinsic lifetime measurements (as shown in Figure 8), direct light excitation to the specific energy states should be used (especially for activator) rather than an indirect upconversion excitation mechanism.[5]

On the other hand, under square-wave excitation, the response of a kinetic system in the time domain to an excitation function can be calculated by convolution of the excitation function with the impulse response function of the system. Therefore, the response to the rise part of a square-wave excitation can be written as:

$$S_d(t) = 1 - exp\left(\frac{t}{\tau}\right) \qquad (5)$$

This rise part response features an exponential rise. This apparent "rise" time is frequently mistaken for the luminescence's rise time, although it is actually the decay time constant (Figure 7c). The rise-edge response of upconversion systems to a square wave also contains information about the decay time constant of the system. Therefore, the time constant sought after, fitting with experimentally obtained rise curve data, cannot be interpreted as the rise time. A more appropriate explanation could be the amount of time needed to reach the steady state.[45]

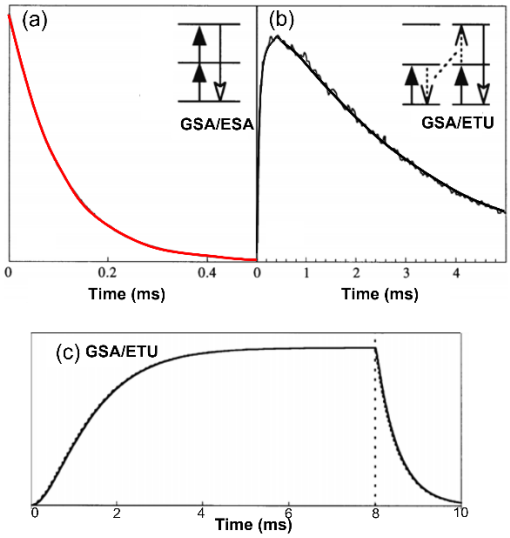

Figure 7. Temporal response of a kinetic system which depends on the mechanism of the system. (a) Temporal impulse response function for a GSA/ESA system under short pulse irradiation. (b) Temporal impulse response function for a GSA/ETU system under short pulse irradiation. (c) Illustrating the response of a kinetic system (GSA/ETU) to a square-wave excitation function. Reprinted with permission from publication [48] copyright 2001 Springer.

Since in any case the rise and decay times are the temporal response of the whole upconversion system to the excitation function and are fundamentally governed by the relative significance of different population and depopulation terms, they could vary

under different excitation conditions. Almost all upconversion emissions using cw laser excitation are controlled by steady state processes, where the rates of energy transfer and excitation energy deactivation are equal. Only a very short laser pulse can produce non-steady state upconversion emission, which is characterized by inequalities in the rates of excited state decay and energy transfer upconversion. The system does not have enough time to reach the equilibrium condition when the pulse width is short; this condition can only be reached by long pulse excitation which is mentioned in the following example.[49]

UCNPs have demonstrated a unique sensitivity to pulsed excitation, particularly to pulse lengths in the microsecond to millisecond range. Based on these new findings, excitation modulation offers a promising post-preparation method of controlling luminescence.[50] For instance, according to a study by Dawson et al. [51], Tm-based UCNPs have significantly varied emission responses to irradiation pulse widths between 10 µs and 2000 µs for their UV and NIR emission intensities. By increasing the excitation pulse width, the intensity of the UV emission increases non-linearly. However, the intensity of NIR emission stays constant.

2.2 Control of the UCL in Tm^{3+} and Er^{3+} UCNPs

The absorption cross-section of lanthanide ions is essential for the analysis of the lanthanide upconversion system. There are several reasons for using Yb^{3+} ions inside UCNPs as a sensitizer, including their higher absorption cross section when compared to activators (Tm^{3+} or Er^{3+}). Table 3 shows the some photophysical and chemical properties (absorption cross section of specific states, lifetimes, and composition of glass) of Yb^{3+}, Er^{3+} and Tm^{3+} in crystal. In accordance with their absorption cross sections, it is possible to mention that Yb^{3+} has an absorption cross section that is 10 times greater than Er^{3+} and Tm^{3+}.

Table 3. Photophysical and chemical properties of Yb^{3+}, Er^{3+}, and Tm^{+3} ions.

	Yb^{3+}	**Er^{3+}**	**Tm^{3+}**
State (emission wavelength)	$^3F_{5/2}$ (976 nm)	$^4F_{9/2}$ (650 nm)	$^1G_4$(475 nm)
Lifetime (ms)	1.2	0.66	0.07
Absorption cross section ($\times 10^{-20}$ cm^2)	3	0.3	0.2
Composition of glass	Yb:QX phosphate glass 1.2 um	Er: $NaYF_4$ crystal 1.5 um	Tm: $LiYF_4$ Crystal
Reference	[52, 53]	[54, 55]	[56, 57]

It is possible to carefully control the upconversion emission of lanthanide-doped nanocrystals in terms of emission colour, lifetime, and intensity for both cutting-edge research and a range of real-world uses. As shown in Figure 8, there are different ET pathways in a UCNP. Therefore, besides excitation profile there are three fundamental ways to tune and investigate upconversion process and its efficiency: (1) host matrix, (2) concentration of dopant ions, and (3) size and shell effect[58]

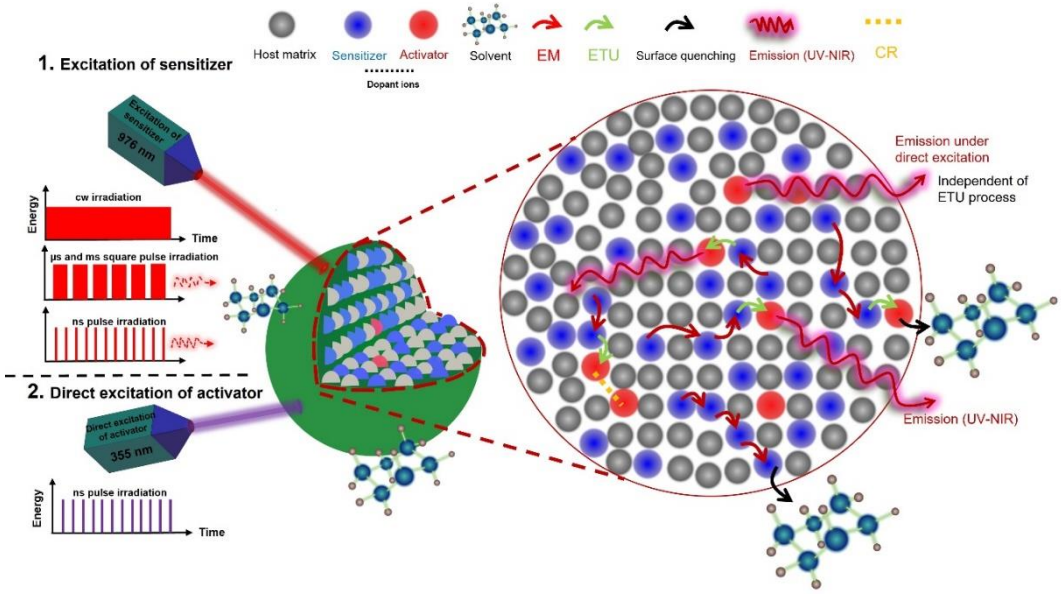

Figure 8. Schematic view on important photo-physical parameters which affect the emission of UCNPs.

2.2.1 Host matrix

The distance between dopant ions, their relative spatial location, their coordination numbers, and the kind of anions surrounding the dopant are all influenced by the host lattice chosen. Therefore, the host lattice's characteristics and interactions with dopant ions strongly affect the upconversion process.[59] Additionally, close lattice matching with dopant ions and low phonon energies are most necessary for the host materials (avoiding non-radiative energy relaxation). Indeed, crucial element that controls the population of intermediate and emission levels and, consequently, the effectiveness of the UC process is the non-radiative multiphonon relaxation (phonon energy) rate between energy levels. For 4f levels of lanthanide ions, the multiphonon relaxation rate constant k_{nr} is defined as:

$$k_{nr} \propto exp\left(-\beta \frac{\Delta E}{h\omega_{max}}\right) \qquad (6)$$

where β is an empirical constant of the host, ΔE is the energy gap between the populated level and the next lower-lying energy level of a lanthanide ion, and $h\omega_{max}$ is the highest energy vibrational mode of the host lattice. [60-62] According to the energy gap law, the multiphonon relaxation rate constant falls down exponentially as the energy gap increses. Er^{3+} and Tm^{3+} have very large energy gaps, as illustrated in Figure 6, and hence have lower probability of non-radiative transitions between their different excited states. As a result, multiphonon relaxation decay is significantly slowed down in lattices with low phonon energy, decreasing non-radiative losses and significantly increasing the efficiency of UC luminescence. The inorganic compounds of trivalent rare earth ions are excellent host materials for upconverting lanthanide dopant ions because they all have comparable ionic sizes and chemical properties. Additionally, several transition metal ions (Zr^{4+} and Ti^{4+}) and alkaline earth ions (Ca^{2+}, Sr^{2+}, and Ba^{2+}) have similar ionic sizes to lanthanide ions.[63] Accordingly, inorganic substances that contain these ions are commonly used as host materials for UC activities. In spite of this, lanthanide doping is always associated with the formation of crystal defects such as interstitial anions and cation vacancies that maintain charge neutrality in these nanocrystals. The dopant concentration must be carefully controlled to keep the host in a single crystal phase for effective UC. Because of the significant ionic size discrepancy between the host and dopant ions, it is currently unclear whether the lanthanide ions in these nanocrystals are mostly distributed on the outermost layer of the nanocrystals or uniformly incorporated into the host lattice. As

point out previously, in order to minimize non-radiative loss and maximize radiative emission, ideal host materials should also have low lattice phonon energies. The phonon energies of heavy halides such chlorides, bromides, and iodides are typically less than 300 cm^{-1}. Nevertheless, they have a limited utility and are hygroscopic. Oxides have remarkable chemical stability, but because of the stretching vibration of the host lattice, their phonon energies are often more than 500 cm^{-1}. As a result, fluorides are frequently utilized as the host materials for UC since they typically display low phonon energies (350 cm^{-1}) and high chemical stability. The common and ideal cations for using with fluorides are Na^{+} and Y^{3+} due to ionic radii close to those of the lanthanide dopant ions prevent the formation of crystal defects and lattice stress. Table 4 illustrates some of the materials that are commonly used in host matrixes and their phonon energy values.

Table 4. The highest phonon lattice energy of the commonly used matrices for rare-earth ions.[64]

Material	High phonon energy (cm^{-1})
phosphate glass	1200
silica glass	1100
fluoride glass	550
chalcogenide glass	400
$LaPO_4$	1050
YAG[a]	860
YVO_4	600
LaF_3	300
$LaCl_3$	240

[a] YAG: yttrium aluminium garnet.

In Figure 9, it is obvious that for Fluoride $MREF_4$ (M is for alkali and RE is for Rare Earth) matrix, which represents the most commonly used matrix, two kinds of crystal phases can occur: a cubic crystal (α- $MREF_4$) and a hexagonal crystal (β- $MREF_4$). The multiple crystal-fields around trivalent lanthanide ions in matrices of different symmetries are directly responsible for the phase-dependent optical characteristic. Compared to their

high symmetry counterparts, low symmetry hosts often impose a crystal-field around the dopant ions that has more uneven components.[65] Uneven components improve the f-f transition probabilities of the dopant ions by enhancing the electronic coupling between 4f energy levels and higher electronic configuration. Additionally, the decrease in the host's cation size (or unit-cell volume) may result in a stronger crystal field around the dopant ions (more Stark effect and less forbidden), which would improve UC effectiveness. Lanthanide ions exhibit a higher degree of symmetry (Oh symmetry) in the cubic phase than they do in the hexagonal phase (C3h symmetry). Therefore, because of the reduced symmetry and "less" forbidden transitions, it is expected that the hexagonal phase would exhibit a better upconversion efficiency. This was confirmed experimentally, i.e. the hexagonal phase produces NPs that are at least an order of magnitude brighter (total number of emitted photon) than the cubic phase.[66]

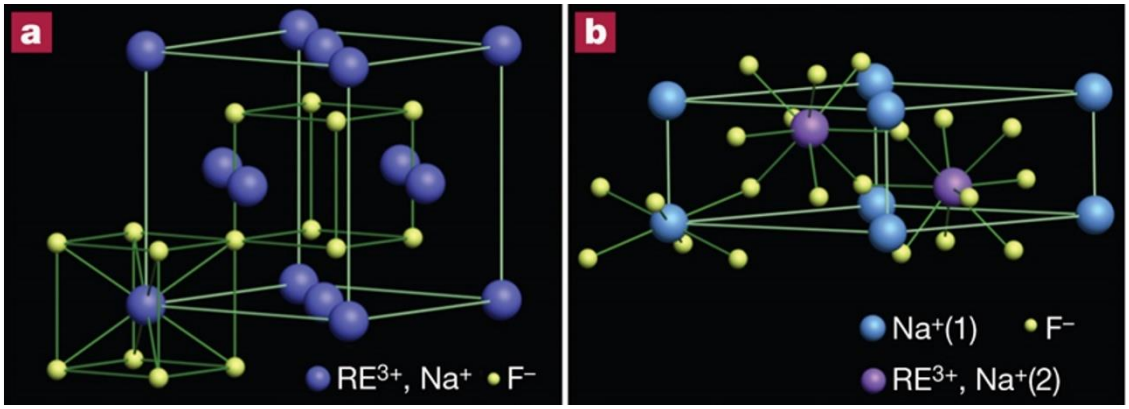

Figure 9. Schematic view of the two various phases for Fluoride $NaREF_4$. Reprinted with permission from publication [63] copyright 2010 Springer.

However, it should be noticed that phonon energy is not always a negative parameter. The low phonon energy of the host also limits the multiphonon relaxation processes of the high-energy emission states. This significantly boosts the intensity of green UC emission ($^2H_{11/2}$, $^4S_{3/2} \rightarrow {}^4I_{15/2}$, Figure 6c) in comparison to red emission ($^4F_{9/2} \rightarrow {}^4I_{15/2}$) in Er-based materials, for instance. The reason is explained by the fact that the phonon assistance needed to fill the gaps ($^2H_{11/2}$, $^4S_{3/2} \rightarrow {}^4F_{9/2}$) required for the feeding of the $^4F_{9/2}$ state that results in red emission is on the order of several thousand cm^{-1}, which is less effective for low energy host lattices.[66]

Furthermore, the solubility of UCNPs host matrix is another essential parameter that should be taken into consideration. Most commonly, high-boiling organic solvents are used to create highly monodisperse UCNPs of homogeneous size and shape. Oleic acid, for instance, acts as a solvent and controls the growth of crystals by coordinating with the surface of nanoparticles and forming a hydrophobic layer of surface ligands. There is, however, a requirement for UCNPs to exhibit high dispersibility and stability in aqueous media when they are used in biological environments. Therefore, these UCNPs must undergo further surface modification to provide a hydrophilic surface composition before being used in bioanalytical applications. There are consequently several techniques that have been published in recent years to change the hydrophobic surface of UCNPs to a more hydrophilic one so that they can be dispersed in aqueous environments. A few of these methods will be briefly discussed in this section. These methods include: (A) chemical modification of the hydrophobic (typically oleate) ligand on the surface, (B) addition of the extra layer, (C) addition of a thin shell on top of the UCNP, and (D) complete replacement of the original ligand by another one.[67]

Chemical modification (A) produces particles with terminal oxygen functionalities by oxidizing the oleate or oleylamine. This technique is less often utilized since only a small number of functional groups can be added, solutions of the resultant UCNPs in water have poor colloidal stability, procedures are time-consuming and frequently provide low yields. In methods B and C, UCNPs are coated with amphiphiles or have shells composed of titanium oxide, silica oxide, metallic gold, or silver. These techniques are extremely adaptable in terms of potential modifications, such as adding more cross-links or using thiol-gold chemistry. It is possible to divide Method D into subgroups based on either (1) direct (single step) replacement of the native ligand with a new ligand or (2) two-step protocols using nitrosyltetrafluoroborate ($NOBF_4$) or strong acids as reagents to produce ligand-free UCNPs before the attachment of a new ligand. These techniques are straightforward and adaptable, and they allow for precise control of the distance between the new ligand and the luminescent particle. This distance is one of the important elements for some applications of UCNPs that we will discuss in following section.[68]

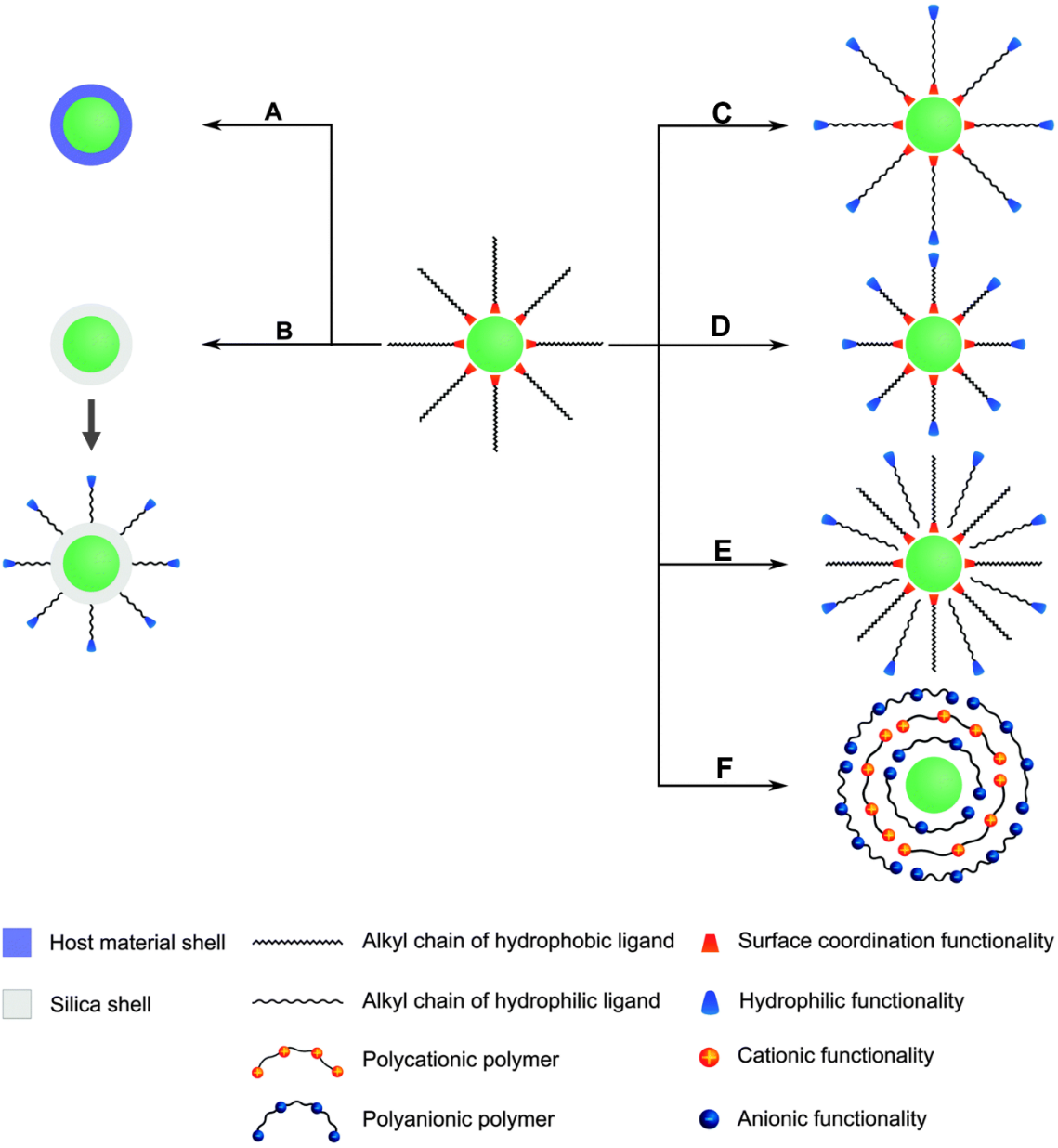

Figure 10. Illustration of some surface modification of oleic acid- coated UCNPs in order to solubilize it in aqueous solution. (A) uncapped UCNPs (containing an inert shell). (B) The silica shell provides a dispersible surface to the water and is chemically inert. In addition, the growth of a silica shell creates an easily accessible platform for introducing various functional groups via silanization. As an example, the binding of gold or silver nanoparticles on the UCNP surface (Through silanization) can enhance the upconversion emission intensity by localized plasmon resonance and also provides an anchoring site for thiol-containing ligands. Oleic acid can be substituted by a ligand exchange reaction (C) or oxidized (D) to yield a hydrophilic surface functionalization. (E) Utilizing ligand interactions, additional layers of ligands are added on the surface of UCNPs. (F) By using the layer-by-layer (LbL) method, polyanions and polycations can be deposited on the surface of the UCNP.[69]

Recent studies indicate that even though many efforts have been made to solubilize and stabilize UNCPs in aqueous solutions, UCNPs are still dissolving when suspended in aqueous solutions. Lahtinen et al.[69] reported that due to the dissolution of the UCNPs (coated with poly(acrylic acid) (PAA), thin silica shell, or thick silica shell), active Yb^{3+} and Er^{3+} ions were lost, resulting in a decrease in upconversion luminescence since the ions were no longer close to each other. Additionally, when nanoparticle coatings decompose, additional surface defects are created, which exposes the particle core to stronger luminescence quenching mechanisms such water's OH vibrations. In accordance with the equation that is mentioned below, until a solubility equilibrium was reached, the ions dissociated from the $NaYF_4$:Yb^{3+},Er^{3+} nanoparticles.

$$NaREF_4 \leftrightarrow Na^{++R^{3+}+4F^-} \quad K_{sp}(NaREF_4) \approx 10^{-26} \qquad (7)$$

As a result, the destruction of the nanoparticles depends on their concentration, and in concentrated UCNP suspensions, just a little amount of decomposition per nanoparticle is required to bring about ionic equilibrium. Nevertheless, at diluted UCNP suspensions most of the particles must be almost completely decomposed before the equilibrium is reached. Therefore, according to the solubility product, the fluoride ion plays a significant part in the decomposition of nanoparticles.[69] Moreover, addition of KF to the UCNPs solution can prevent (or reduce) their decomposition, but further research is needed to determine whether KF can be used in bioanalytical procedures (Fluoride may cause cell death, hence KF cannot be used to image living cells). In addition, since utilizing a thick silica shell slowed down the dissolution of the nanoparticles, it is possible that using an even thicker silica shell or another polymer shell with total coverage may stop the dissolution of the UCNPs for a period. There is, however, also the possibility of OH groups being present in silica shells, which might produce a quenching effect. On the other hand, using a thick shell might prevent the decomposition but have also a negative effect for FRET applications, i.e. on the efficiency of resonant energy transfer from UCNPs to another species near the surface due to the fact that there is a long distance (more than FRET distance) between an emitter that is near the surface and an acceptor.

2.2.2 Concentration of dopant ions effect

The ETU process includes ion mutual interactions, which are often categorized as dipole-dipole, dipole-quadrupole, or quadrupole-quadrupole interactions and are consequently sensitive to the operating distance. Because the doping concentration controls both the spacing between the dopant ions and the quantity of dopant ions in a nanoparticle, it has a major impact on both the energy transfer mechanism and the optical characteristics of UCNPs (changing the amplitude and pattern of the upconversion emission spectrum).[58] Based on the doping concentration of the sensitizer and the acceptor, the following equation approximates the average distance between a sensitizer and an acceptor, which is determined by the size of the unit cell and evolved from the known lattice parameters when ignoring the lattice distortion caused by doping [8]:

$$d_{\beta-NaYF_4} = \left(\frac{a^2 c\sqrt{3}/2}{1.5(x+y)}\right)^{1/3} \qquad (8)$$

which x and y represent the doping concentrations of the sensitizer and acceptor, respectively, while a and c are the lattice parameters of the hexagonal unit cells.

It is possible to enhance the upconversion emission to some amount by increasing the doping concentration of Ln^{3+} ions (either sensitizer or activator) in the nanoparticles. In high dope concentration, the excitation energy migrates more easily from one ion to another, which is called energy migration, increasing the probability for the energy to be trapped by the defects inside and/or at the surface of the nanoparticles. There is usually energy migration between sensitizers when they interact with each other in high concentration. As mentioned previously, the hexagonal-phase alkaline rare-earth fluoride nanocrystal is known as one of the most efficient host materials for upconversion and typically uses relatively low concentrations of sensitizers (typically around 20-40% mol percent) and activators (below 2 mol %) to proceed with an efficient upconversion. In UCNPs, the process of the energy extraction from a sensitizer to an activator usually takes place via a non-radiative exchange or/and a multipolar interaction.[8, 32, 70]

Considering the fact that most lanthanides have abundant excited states, there is a high likelihood that they will couple with one another (in high concentration) through multipolar interaction with matching energy gaps, which is known as CR (Figure 4f,g, Figure 6b). These cross-relaxations lead to concentration quenching (in some bands) because neighbouring ions, one in the excited state and the other in the ground state,

exchange energy non-radiatively, resulting in phonon relaxation. Shorter lifetimes and a drop in luminescence intensity are signs of the cross-relaxation process. It is important to note that CR relaxation has mutual effects. It increases the population of some bands while reducing the population of others (as mentioned in section 1.3.4, Figure 6b).[58, 71]

It is important to note that despite the fact that concentration quenching phenomenon severely can suppress the emission of activators, there are several ways to mitigate this effect. The first strategy is to select a proper host matrix. In addition to the well-known $NaYF_4$, a number of alternative host materials have also been investigated with the purpose of shortening the energy transfer operating distance. For instance, it is discovered that Na_xScF_{3+x} is a host that facilitates the red upconversion emission of Er^{3+} (660 nm), which is attributed to the short radius of Sc^{3+}. The Er^{3+} and Yb^{3+} cation pairs are closer together than they are in a $NaYF_4$ host when Yb^{3+} replaces Sc^{3+}.[72] Although shortening the distance between a sensitizer and an emitter can increase the efficiency of the upconversion process, it may also increase the probability of back energy transfer from a sensitizer to an emitter, which can negatively impact the efficiency of the upconversion process. Wang et al. reported the supressed population in excited levels of $^2H_{9/2}$, $^2H_{11/2}$, and $^4S_{3/2}$, resulting in the decrease of blue and green light emission, due to the back energy transfer from Er^{3+} to Yb^{3+} as the concentration of Yb^{3+} increased.[73]

In addition, Wang et al. typically created a more comprehensive "dopant ions spatial separation" structure at the sub-lattice level using a KYb_2F_7 host material.[74] As presented in Figure 11, the Yb^{3+} ions are separated as arrays of distinct clusters at the sub-lattice level, and the average distance between the ionic clusters is significantly greater than the ionic distance inside the clusters. This is a unique feature of the KYb_2F_7 crystal structure. The excitation energy that the Yb^{3+} ions absorb in this configuration is more likely to be contained inside the cluster as opposed to traveling far to reach neighboring clusters. Therefore, this unique arrangement enables the preservation of excitation energy within the sublattice domain and effectively minimize the migration of excitation energy to defect even at high Yb content (Figure 11).

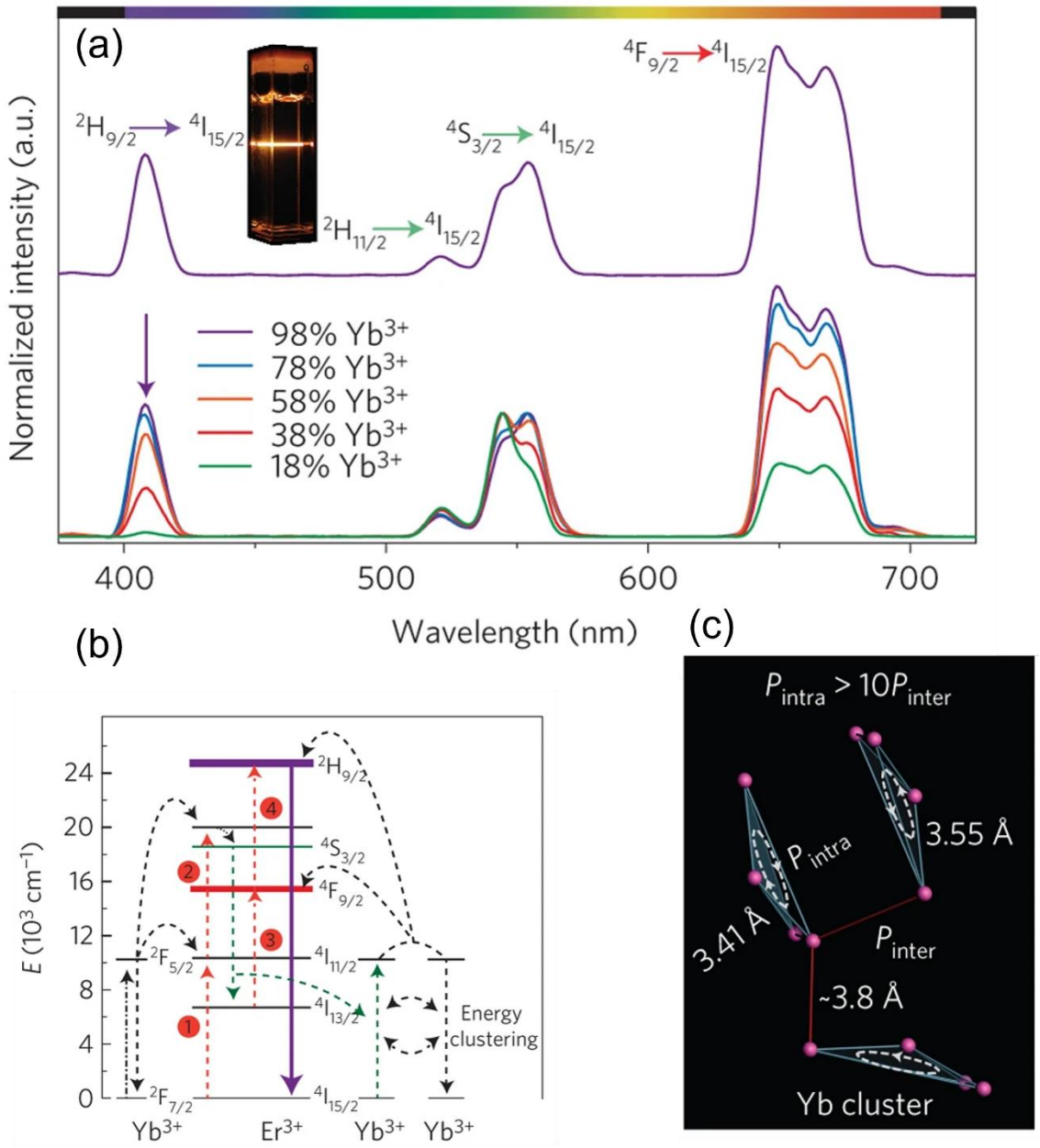

Figure 11. Effect of KYb_2F_7 host material. (a) Intensity enhancement of Er^{+3} emission in all bands by increasing amount of sensitizer (up to 98%) (b) upconversion mechanism in KYb_2F_7:2%Er^{3+} nanocrystals. (c) excitation energy in Yb tetrad clusters of KYb_2F_7. Reprinted with permission from publication [74] copyright 2014 Springer.

2.2.3 Size and shell effects

The size of nanocrystals has been found to have a significant effect on upconversion emission and it has been demonstrated that smaller nanocrystals are more suitable for various imaging applications. As a result of reducing the size of the nanoparticles, besides the fact that the number of sensitizers and emitters is reduced, the majority of lanthanide ions tend to be located near the surface of the nanosystems (due to the higher surface to

volume ratio), since nanosystems have a high surface-to-volume ratio, which results in quenching. This is ascribed to the presence of high vibrational frequencies of surface defects, unknown impurities, passivating ligands, and solvent molecules (-OH,-CH, C=O) which provide thermal energy necessary to populate or depopulate various excited states. Therefore, surface properties are an important aspect of nanotechnology that should not be overlooked. By assuming that NPs have a spherical closed pack structure and that the surface atoms are those on the top layer, the rare earth ions in the outer spherical shell have a molar concentration ratio (MCR) to the total nanosphere [66]:

$$MCR = \frac{\left[\frac{4}{3}\pi r^3 - \frac{4}{3}\pi(r-2d)^3\right]}{\frac{4}{3}\pi r^3} = 1 - \left(1 - \frac{2d}{r}\right)^3 \qquad (9)$$

where r is radius of the NPs, and d is the radius of ions of dopant or the host material (in which they have the same radius). It has been found that the values of MCR increase rapidly with the decrease in nanoparticle size, and that most of the dopants are located near or on the surfaces of the nanoparticles, which results in the weak fluorescence of the UCNPs. On the other hand, the surface-related losses become significant when particles are smaller than 20 nm. As shown in Figure 12, it is established that surface impacts have a certain direct interaction distance (1.5–5 nm which is called dark site).[75, 76]

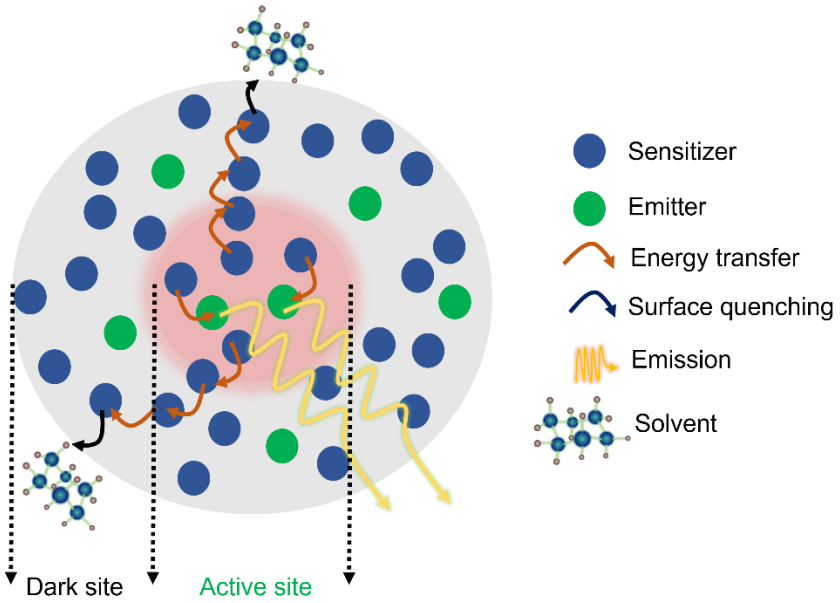

Figure 12. Representing two areas in core UCNPs: 1) active site which acts as a luminescence core and 2) dark site represents a surface quenched region.[77]

Even at the longest surface effect distance (5 nm), there is still 12.5 percent of a 20 nm (diameter) sized nanoparticle that is inert to surface effects. This suggests that the maximum factor of luminescence enhancement caused by shell coating should be about 8. This factor, however, was reportedly greater than 20 or even close to two orders of magnitude when the shell thickness was just around 1-2 nm.[64] These findings suggest that the surface quenching interact with deep dopant ions deep within the nanoparticle in addition to those within the direct interaction distance. Therefore, intercalating an inert spacer thick enough to protect the surface from molecules at the surface is the preferred method for overcoming surface quenching. Moreover, as mentioned in previous section, increasing the amount of Yb^{3+} in the host lattice improves upconversion luminescence by increasing the density of optical centers that can absorb and maintain the energy of the excitation light. Nevertheless, the Yb-Yb interatomic distance would be reduced and energy hopping in the Yb sublattice would be facilitated by a high Yb^{3+} concentration in the $NaYF_4$ host lattice.[78] The excitation energy should then be transferred from the inside of the nanoparticle to the outside area by energy hopping, which will have a greater surface-quenching impact. According to the findings by Sun et al, by adding an inert shell,[79] the Er emission intensity of the nanoparticles increases as a function of Yb^{3+} concentration in the 8-40 mole% range which is in contrast with the reported results for core nanoparticles (as shown in Figure 13b). An inert protective shell therefore recovers more excitation energy from the naked-core equivalents with greater Yb^{3+} concentrations, leading to bigger emission enhancement factors. Figure 13c illustrates a massive decrease in the Yb^{3+} lifetime when the Yb^{3+}-dopant concentration in the core nanoparticles (with size of around 30 nm) increased from 8 to 38 mol percent, indicating the Yb-sublattice-mediated luminescence-quenching mechanism. As presented in Figure 13d, all core-shell nanoparticles showed much longer decay times after surface coating, which confirmed that the protection shell shields the luminescent lanthanide dopant ions. The optimum condition of a nanoparticle surface is also determined by the application in which the nanoparticle is used. It is preferred that a relatively thick shell is used for luminescence imaging in order to achieve the strongest emission. However, for FRET-relevant applications, the shell thickness will reduce energy transfer between an emitter to other particles on the surface (it will be discussed in 2.4 section).

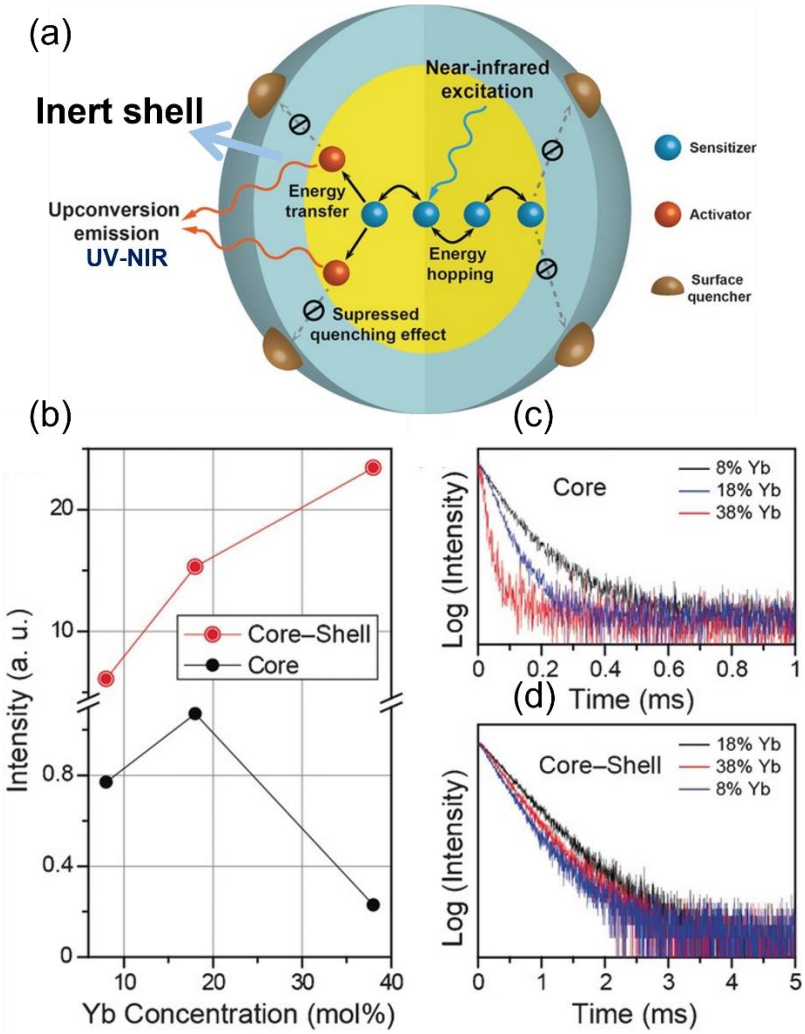

Figure 13. (a) Schematic illustration of surface coating for eliminating luminescence quenching. (b) Effect of adding a shell on the upconversion emission intensity as a function of Yb^{3+} concentration under 976 nm irradiation at 1 W for $NaYF_4$:Yb/Er and $NaYF_4$:Yb/Er@$NaYF_4$ particles. (c) and (d) Decay profiles upon addition of shell. Reprinted with permission from publication [79] copyright 2015 Wiley.

2.3 Toward ultrasmall UCNPs

While dark site could prevent to consider UCNPs below 5 nm, it can be highly desirable to dispose of ultrasmall (< 5nm), Yb-sensitized UCNPs with a much-reduced number of activators and with improved biological properties due to their size (super-resolution), good transport properties through cellular membranes and global excretability for large organisms (< 3nm).[80, 81] Furthermore the dynamics of the energy redistribution among the activator kinetic network is expected to be greatly simplified. Indeed, thanks to a limited probability of CR (null for one activator), a small number of processes controls

the activator's emission. In particular, the direct excitation at high energy of the activator should bring some useful information about its highly excited levels independently of the ETU processes. Remarkably, some molecular Ln complexes can display the upconversion phenomenon. In particular, ETU can take place in heteronuclear assembly of a handful of Ln ions with a defined arrangement between sensitizers and activators.[82-85] Thus, as far as size is concerned, the chemical "bottom limit" to upconversion is to have only one emitting activator ion, on the other hand, no UCNPs with one activator are reported. While very efficient preparations of 10 to 40 nm UCNPs are now available, [80, 81] little is known for ultrasmall sizes (<10nm), and even less for sizes smaller than 3nm. In addition, Table 5 indicates that there hasn't been any fundamental research on ultrasmall UCNPs (under 3 nm) with a limited number of activators by comprehensive spectroscopic methods in order to uncover the energy distribution pathways. Therefore, this subject is one of the main purposes of this thesis that will be explained in the following chapters.

Table 5. Representative literature for sub-8 nm UCNPs with focus on photophysical type of studies (ensemble or single particles)

Host:Dopant	Size (nm)	Phase	Measured photophysical properties	Ensemble/ Single particles studies	Reference
$NaYF_4:Yb^{3+},Er^{3+}$	7	α	Steady state spectra (cw)	Ensemble	[86]
$NaYF_4:Yb^{3+},Er^{3+}$	5.4	β	Steady state spectra (cw)	Single	[87]
$NaYF_4:Yb^{3+},Er^{3+}$	5.3	β	Steady state spectra (cw)	Ensemble	[88]
$NaYF_4:Yb^{3+},Er^{3+}$	5.4	β	Steady state spectra (cw)	Ensemble	[89]
$KGdF4:Tm^{3+},Yb^{3+}$	3.7	β	Steady state spectra (cw)	Ensemble	[90]
$Na(Yb-Gd)F4:Tm^{3+}$	4.6	β	Steady state spectra (cw)	Ensemble	[91]
$NaYF_4:Yb^{3+},Er^{3+}$	8	β	Steady state spectra (cw), Lifetime (ns pulse)	Single	[77]

Besides comprehensive spectroscopy study of ultrasmall UCNPs in ensemble condition, which is vital for understanding the ET process in UCNPs, single particle spectroscopy

study of UNCPs is also significant for revealing some unique behaviour of these particles which are beyond the ensemble studies. Hence, in the following, we will discuss the importance of single particle study of UCNPs with mentioning some fundamental examples.

2.3.1 Single particle spectroscopy insights: Beyond ensemble spectroscopy

Ensemble spectroscopy of UCNPs is only capable of measuring the photophysical behaviour (lifetimes and steady state spectra) in average effect, ignoring the heterogeneity of the nanoparticles. In addition to the fact that UCNP exhibits a complex energy network, as well as the presence of ligands and surface defects, the photophysical behaviour of doped lanthanides is also highly complex. Therefore, the single nanoparticle spectroscopy provides clear insight into the interaction of intrinsic and extrinsic influences and then provides guidelines for understanding behaviour of UCNPs. Using confocal scanning microscopy setups for this purpose, we can obtain both high resolution spatial and spectroscopic information at single particle levels.[92]

In addition, using proper detection approaches and sample preparation methods for single UCNP are vital tasks. In this aim, atomic force microscopy (AFM), transmission electron microscopy (TEM), or scanning electron microscopy (SEM) are common methods for ensuring that we are working at the single particle level. For sample preparation in single particle level, employment of surface treatment agent on top of the coverslip may be helpful to avoid agglomeration of nanoparticles during evaporation of solvent. In the following , we discuss some further significant fundamental advances in the upconversion luminescence characteristics of single nanoparticles which has been done by advanced single particle characterization.

For example, Frenzel et al. [93] used a confocal microscopy setup (power-density ranging from 1kW/cm^2 to 2.6 MW/cm^2, 1 ms irradiation) for single particle studies in order to demonstrate how high-power density can activate higher energy levels by multiphotonic processes which can affect decay kinetics and compare it with ensemble measurements which were measured at low power-density. They accomplished this using two core and core-shell UCNPs doped with 20% Yb^{3+} and 1%–3% Er^{3+} (with 5 nm shell size). As shown in Figure 14a and b, in core particles, green Er^{3+} emission express shorter lifetimes in ensemble than in single particles while for the core-shell the opposite trend was

observed. Accordingly, it can be concluded that contributions from higher energy transitions excited at high power-density lead to effective accelerations in the decay kinetics of luminescence. On the other hand, increasing the amount of Er^{3+} in core particles decreases lifetime of these particles. However, for core-shell particles in single particle measurements, lifetimes stay almost constant. Moreover, the very small difference in single particle air and cyclohexane is due to the influence of solvent in high power-density range.

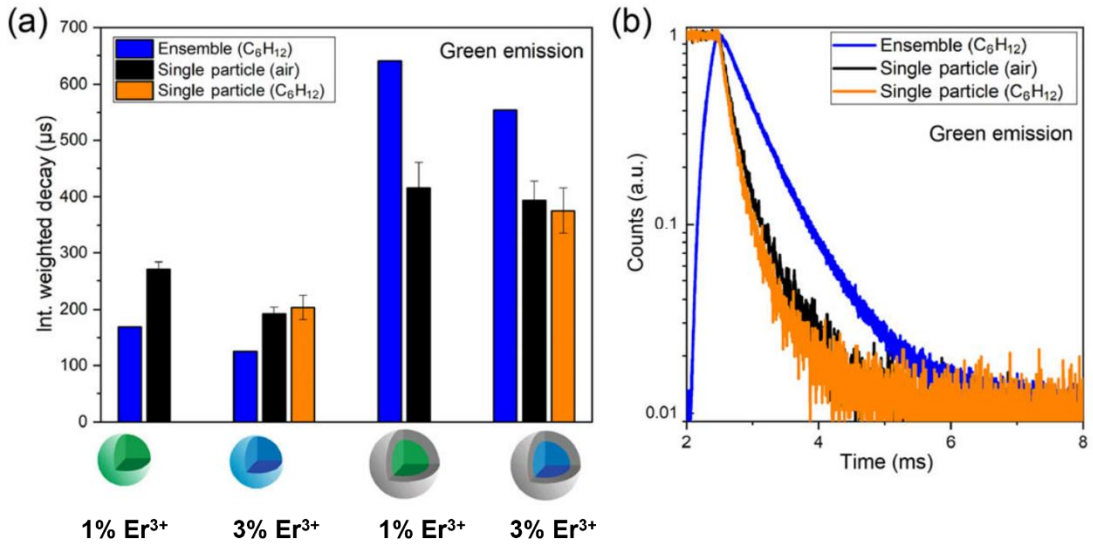

Figure 14. Time-resolved luminescence study of core and core-shell UCNPs doped with 20% Yb^{3+} and 1% or 3% Er3+ in single particle and ensemble measurements. (a) Intensity weighted lifetimes of green emission. (b) Decay curves of green emission in various environments. Sample was first dried on glass and then re-dispersed in cyclohexane to determine the impact of the various UCNP conditions (orange). [93]

Nonblinking and nonbleaching luminescence of UCNPs should also be mentioned. A common characteristic of molecular emitters seen in single quantum dots and fluorophores is photoluminescence blinking, which is the random switching between high (ON) and low (OFF) emissivities. Additionally, single Eu^{3+} ions embedded in Y_2O_3 nanoparticles have been seen to blink on a variable time scale ranging from several hundred milliseconds to several seconds. [94] However, single nanoparticles containing a large number of lanthanides do not exhibit this effect. The answer to the issue of whether the lanthanide-activated UCNPs blink or not has been established by single particle characterisation utilizing confocal or wide-field microscopy. According to Figure 15, Cohen et al. reported the first graphic demonstration of nonblinking behavior and zero photobleaching or photodamage after one hour of continuous laser illumination of a single

(-$NaYF_4$) nanoparticle doped with 20 % Yb^{3+} and 2 % Er^{3+}, which was subsequently thought to be the most suitable material for single molecule imaging.[94]

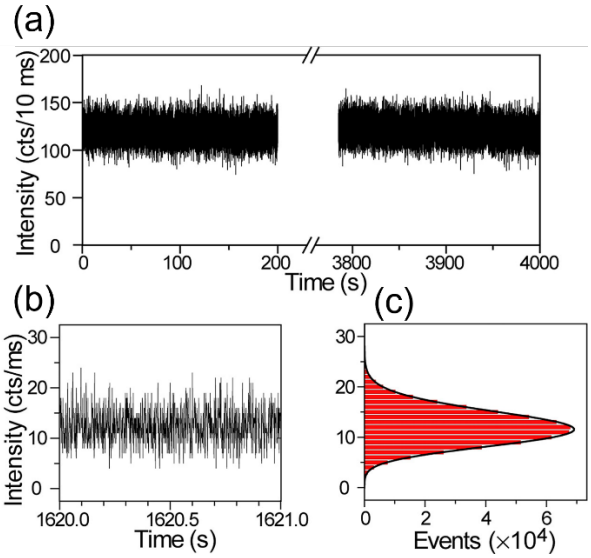

Figure 15. Photostability and non-blinking behaviour of single UC nanoparticles. (a) The temporal trace of an individual UC nanoparticle's emission intensity during more than an hour of continuous laser irradiation. (b) and (c) The zoomed-in time trace and emission intensity histogram indicate no on/off or blinking behavior. [94]

In addition, nanoparticles that are synthesized through wet chemical methods with various kinds of surfactants are usually capped at the surface via chemical bonding. Surface ligands, such as oleic acid molecules etc. , accompanying with the crystal defects will affect the precision spectroscopy of each nanoparticle. Figure 16 shows typical heterogeneous high-resolution spectra, for 4 particles, with particle-to-particle variations in peak intensities at 541 nm and 557 nm, which was a pioneering discovery by Gargas et al.[76] This heterogeneity is eliminated when undoped $NaYF_4$ shells are added to the nanoparticles (Figure 16a, bottom trace), which points to an area within the nanoparticles where the lanthanides may be emissive but are energetically connected to the surface. These observed spectrum discrepancies may result from variations in surface defects, surface reconstruction, or faceting, as well as variations in lanthanide distributions between nanoparticles.

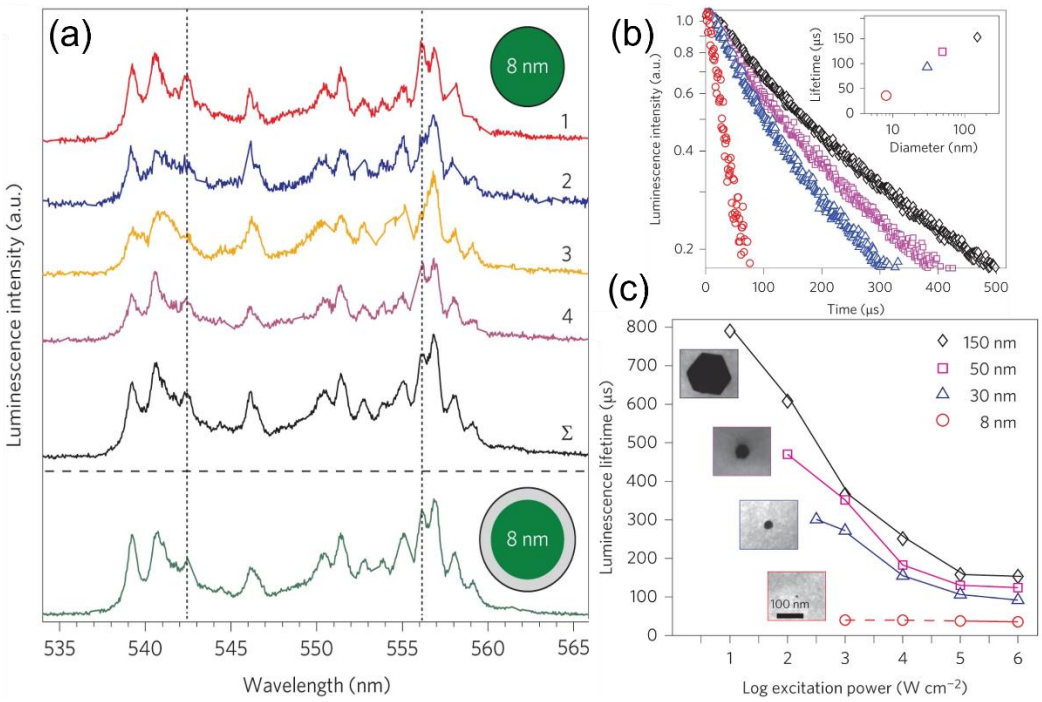

Figure 16. (a) Fine spectra of the green emission bands collected from four single 8-nm UCNPs (curves 1–4) and their averaged spectra (curve Σ). Vertical dotted lines highlight peaks exhibiting heterogeneity between individual UCNPs. The green emission spectrum of an 8 nm UCNP with epitaxial 1.8 nm undoped shell is shown below the horizontal dashed line. (b) Normalized luminescence decay for as a function of UCNPs diameter (c) Single UCNP luminescence lifetime as a function of particle size and excitation power. Reprinted with permission from publication [77] copyright 2014 Nature.

Moreover, for single particle study of UCNPs with a diameter greater than 30 nm, Gargas et al. reported a significant decay lifetime dependency on the excitation power density (Figure 16b and c). The luminescence lifetime for sub-10-nm UCNPs, however, remained constant regardless of excitation power, indicating that surface-related recombination dominates in these UCNPs.

In addition, they showed that (Figure 17a) at low excitation power density (3×10^4 W cm^{-2}), the conventional upconversion nanoparticles (β-$NaYF_4$ with 20% Yb^{3+} and 2% Er^{3+}) are brighter than the Er^{3+}-rich upconversion nanoparticles (20% Yb^{3+}, 25% Gd^{3+}, and 20% Er^{3+}). The Er^{3+}-rich upconversion nanoparticles get brighter as the excitation power density rises, eventually outshining the traditional upconversion nanoparticles when the power density exceeds 3×10^6 W cm^{-2} (Figure 17 b-c). In order to provide a framework for the proposed physical picture, the authors have given an initial distribution of the excited state population in the nanoparticles. There is a significant increase in excited Yb^{3+} ions in the nanoparticles due to the higher density excitation, and the critical

step in upconversion emission is transferring the excited state energy from Yb^{3+} to the activator (Tm^{3+} or Er^{3+}) during the upconversion emission. If there are not enough activators, they will quickly get saturated while absorbing excitation energy from the sensitizers. According to this concept, larger doping levels of the activator should encourage the usage of the excitation energy stored in the sensitizers and improve upconversion emission under high density excitation.

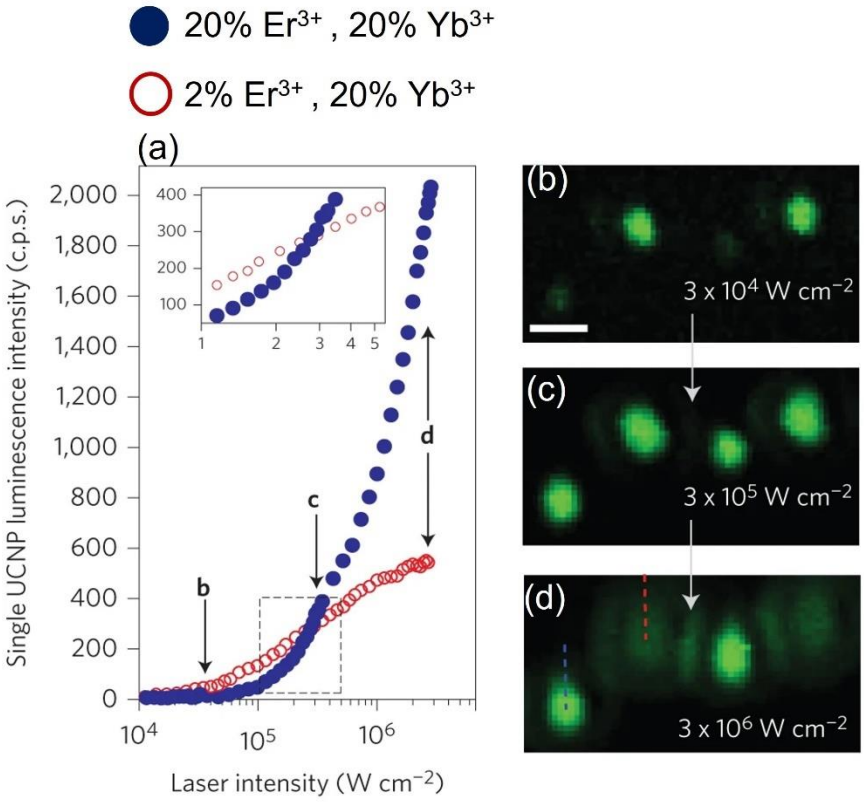

Figure 17. Power density effect in single particle UCNPs emission (a) Excitation density vs. integrated upconversion luminescence intensity (400-850 nm) for a series of Er^{3+} doped nanoparticles. (b) UCNPs with 20 percent Er^{3+} (blue circles) and 2 percent Er^{3+} (red circles) excitation density dependence in terms of luminescence intensities. (c-e) Confocal luminescence images of single UCNPs containing a mixture of 2% (dashed red line) and 20% (dashed blue line) Er^{3+} under different excitation densities. Reprinted with permission from publication [77] copyright 2014 Nature.

2.4 Förster resonance energy transfer (FRET) to modulate emission of UCNPs

A classical way to modulate the emission of UCNPs is to use FRET between UCNP (donor) and an organic dye (acceptor) to develop new UCNPs .[67] Förster, who first treated such a case theoretically by quantum-mechanical theory, considered the dipole-dipole interaction. He assumed that the interaction is strongest if electric-dipole transitions are permitted for both transitions. Therefore, FRET is based on classical dipole–dipole interactions between the transition dipoles of the donor (D) and acceptor (A). As mentioned in the following equation, the rate of the energy transfer (K_T) decreases with the D–A distance, R, falling off at a rate of $1/R^6$.

$$K_T = \frac{1}{\tau_D}\left(\frac{R_0}{R}\right)^6 \qquad (10)$$

$$R_0^6 = \frac{9(ln10)k^2\varphi_D J}{128\pi^5 n^4 N_A} \qquad (11)$$

$$J = f_D(\lambda)\varepsilon_A(A)\lambda^4 d\lambda \qquad (12)$$

R = distance of donor-accepter

R_0 = Forster radius at which the energy transfer efficiency between D and A falls to 50% and the Forster radius is the distance at which the energy transfer rate is equal to radiative rate of the sensitizer ions in the absence of activators

N_A = Avogadro constant

n = refractive index of the medium

τ_D = lifetime of donor in excited state (in the absence of acceptor)

k^2 = orientation factor (usually fix at 2/3 for randomly oriented systems)

Φ_D= quantum yield of the donor

J = peak overlap factor

$f_D(\lambda)$ = emission intensity of donor at λ, normalized to 1 over the spectral windows concerned

$\varepsilon_A(A)$ = molar extinction coefficient of the accepter as a function of wavelength

Equation (9) indicate that the energy transfer rate is proportional to an inverse power of the distance R (as R^{-6}) and it rapidly decreases when $R > R_0$. Considering a random distribution of ions, R may be taken as the average distance between sensitizer ions and activator ions.

Additionally, the efficiency of energy transfer between donor and an acceptor can defined as follow:

$$E = \frac{R_0^6}{R_0^6 + R_{DA}^6} \qquad (13)$$

When $R_0 > R_{DA}$ then the energy transfer efficiency is more than 50% between a donor and an acceptor (as shown in Figure 18): in the other words, more than half of all the donor's relaxation processes are accounted for RET process. [95, 96]

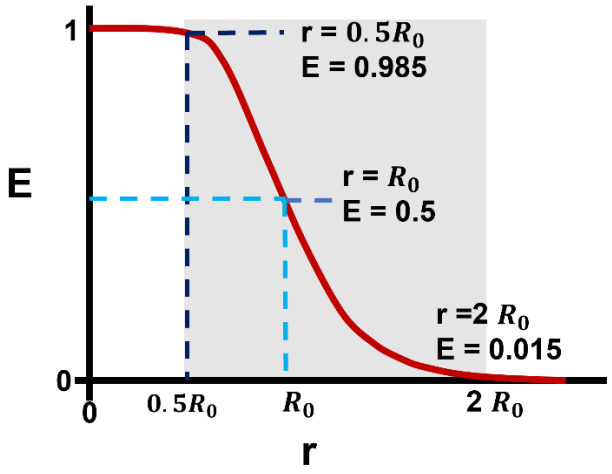

Figure 18. FRET efficiency (E) as a function of donor and acceptor. The efficiency of energy transfer change dramatically by changing the distance between donor and acceptor.

Contrary to conventional donor-acceptor pairings, these particles include a large number of emitting lanthanide ions and a large number of acceptor molecules (dyes, biological molecules) spaced at varying distances, dramatically altering with particle diameter. Therefore, it is possible to categorize different parameters for having efficient energy transfer between UCNPs and acceptor molecules as follows [97, 98]:

1) Structure of nanoparticles: it consists of the size of the UCNPs and the way in which emitter ions are distributed inside the UCNPs. Considering the UCNP, it is important to

keep in mind that it is composed of a large number of individual emitters, such as Tm^{3+} or Er^{3+} ions, operating in different environments. Based on the assumption that particles with diameters more than 15 nm include a significant portion of donor ions in the UCNP center that are outside of the effective Förster distance, which is around 5 nm, and are therefore unable to participate in an effective FRET process. Consequently, it is anticipated that the particle size will have a considerable impact on the FRET efficiency. Furthermore, the surface of the UCNPs can bind several FRET acceptors to different donor lanthanide ions at various distances. This distance varies in core and core-shell structure due to the shell thickness (Figure 19). In comparison to the 1:1 stoichiometry in pairs of organic emitters, this results in a condition that is significantly different. In addition, UCNP-based FRET systems stand out from many other multichromophoric donor-acceptor systems because the upconversion process depends on intraparticle energy transfer cascades between the many emitting lanthanide ions, which compete with nonradiative deactivation pathways (e.g., conventional dye-doped polymer particles).

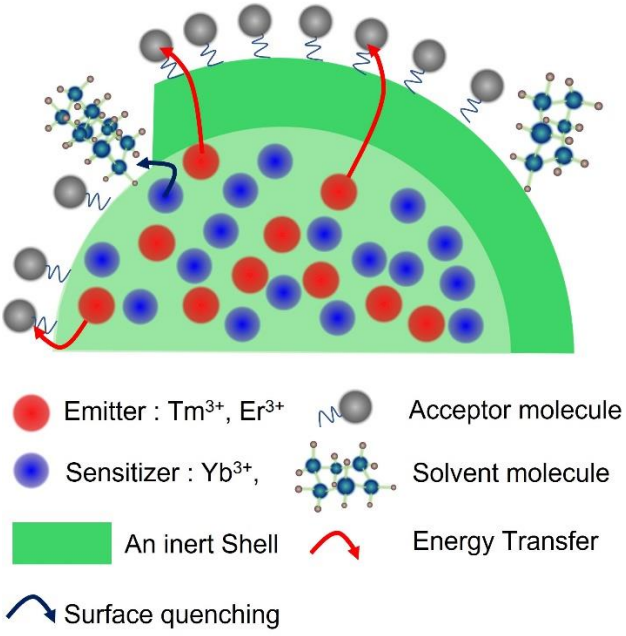

Figure 19. Representation of the various distances between emitters and acceptor molecules. Emitters that are near to the surface have more chance to transfer energy to the acceptors. Due of the large distance, emitters located in the core of UCNPs rarely contribute to the energy transfer process Although the presence of shell reduces the quenching effect, it causes a larger distance between an emitter and an acceptor. This means that the thickness of the shell should be able to be accurately estimated .

2) Spectral overlap between donor emission spectrum and the acceptor absorption spectrum: according to equations (9), (10), and (11), a larger value of spectral overlap

results in a higher R_o, which ultimately results in a better efficiency of energy transfer. Therefore, it is extremely important to choose the right acceptor in order to achieve the highest energy transfer quantum yield.

3) Donor and acceptor should have high molar extinction coefficients and high emission quantum yields, respectively: choosing an acceptor with a high molar extinction coefficient is essential when considering the fact that UCNPs have a low molar extinction coefficient. Additionally, using a proper UCNP with the highest concentration of emitter near the surface and, in parallel, the lowest quenching effect is highly substantial. Table 6 is showing different types of UCNPs with significant structural variations function as donors paired with various types of acceptors.

Table 6. Representative literature on different UCNPs structures paired with various acceptors.

Donor	Acceptor	Surface	Target
$NaYF_4$:Yb^{3+},Er^{3+} 50 nm [99]	graphene oxide	polyacrylic acid (PAA)	Glucose
$NaYF_4$:Yb^{3+},Er^{3+} 47 nm [96]	graphene oxide	SiO_2-COOH	DNA
$BaGdF_5$: Yb^{3+},Er^{3+} 16 nm [100]	*gold nanoparticles*	poly(ethylenimine)	Virus gene
$NaYF_4$:Yb^{3+},Er^{3+} 26 nm [101]	QDs	streptavidin	Biotin (vitamin H)
$NaYF_4$:Yb^{3+},Er^{3+} 36 nm [102]	pHrodo red	silica shell	HeLa cell
$NaYF_4$:Yb^{3+},Tm^{3+} 19 nm [103]	fluorescein	silica shell	HeLa cell
$NaYF_4$:Yb^{3+},Tm^{3+} 49 nm [104]	xylenol orange	silica shell	HeLa cell
$NaYF_4$:Yb^{3+},Er^{3+} 27 nm [105]	pHrodo red	poly(ethylenimine)	MDA-MB-231
$NaYF_4$:Yb^{3+},Tm^{3+} 22 nm [106]	fluorescein	poly(ethylenimine)	QBC939
$NaYF_4$: Yb^{3+}, Er^{3+}, Tm^{3+} 40 nm [107]	GSH-sensitive dye	amino carboxyl poly(ethylene glycol)-2000	Glutathione
β-$NaYF_4$: Yb^{3+}/Er^{3+} 22 nm [108]	Ring-opened rhodamine	a-cyclodextrin	Cysteine

Even if all the requirements for an effective energy transfer are obvious, it is still required to evaluate these factors in an actual experiment (due to the complexity of UCNPs). There

are some fundamental efforts in order to rationalize the design of efficient FRET sensors based on UCNPs. As an example, Muhr et al [98] evaluate the efficiency of FRET from 20% Yb^{3+}, 2% Er^{3+} doped UCNPs with sizes ranging from 10 to 43 nm to the organic dyes rose bengal and sulforhodamine B, acting as model FRET acceptors for the green emission of Er^{3+} by the means of steady state and time-resolved fluorometry. The changes in the lifetime of green emission band at 540 nm were measured before and after dye attachment in order to determination of FRET efficiency of different dye-capped UCNPs as follow:

$$E = 1 - \frac{\tau_{DA}}{\tau_D} \qquad (14)$$

where τ_{DA} and τ_D represent the lifetime of donor in the presence and the absence of acceptor respectively. Therefore, by the means of this equation, it is possible to assert that the FRET efficiency increases as the difference between lifetime in the presence and absence of the acceptor increases. Due to the significant impact of surface deactivation on luminescence lifetimes, Figure 20a illustrates how the lifetime of green emission of particles depends on the surface area of the UCNPs. In addition, there is a linear dependence on the surface area of the nanoparticles in the absence of acceptor dyes. As presented in Figure 20b, for the 21 nm sized nanoparticles, both particle-dye systems demonstrated the maximum efficiency, while bigger ones have a larger number of donors to acceptors ratio (Table 7).

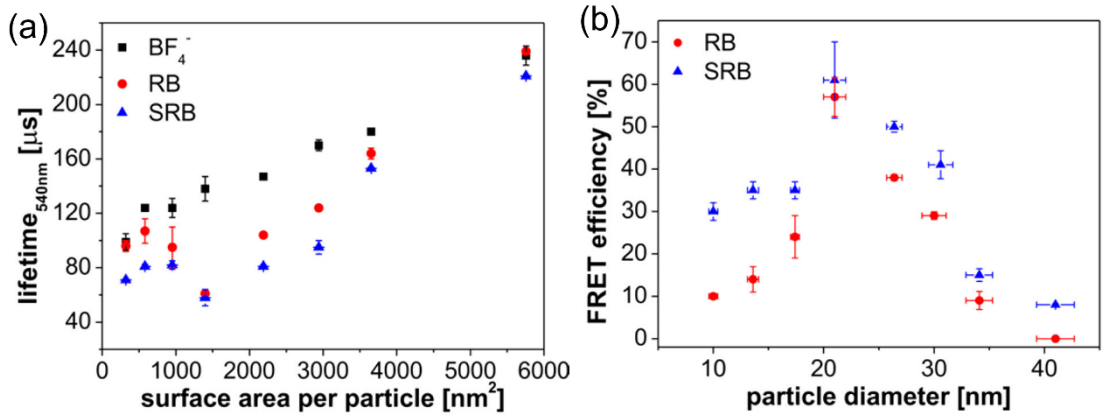

Figure 20. (a) Trend of lifetime changes by surface area for three various UCNPs (BF_4^-: Bare UNCPs surrounded by BF_4^- , RB: UCNPs capped by rose bengal dye, and SRB: UCNPs capped by sulforhodamine B dye). (b) Change of FRET efficiency as particle size varies. Particles with 21 nm size show the highest FRET efficiency. Reprinted with permission from publication [109] copyright 2018 ACS.

Table 7. The ratio of donors to acceptors (rose bengal and sulforhodamine B) and how it varies with particle size.

Diameter of UCNPs (nm)	$N_{donor}/N_{acceptor}$
10.1	11
13.6	15
17.4	19
21.1	23
26.4	29
30.7	34
34.1	37
42.8	47

Accordingly, these results show that adjusting a suitable particle size (not number of acceptor or donor) is the first crucial parameter to reach the maximum FRET efficiency. Furthermore, as shown as Figure 21a for particles less than 17 nm, a thin shell with a thickness of less than 1 nm led to an increase in FRET quantum yield efficiency. This emphasizes the significant impact of surface deactivation mechanisms on the luminescence of small-diameter UCNPs. Nevertheless, for larger UCNPs, a shell with a tiny thickness decreases the FRET efficiency. As demonstrated in Figure 21 b, a thicker shell of 4 nm resulted in a sharp decline in the FRET efficiency to barely 20% for both dyes. These results show that for UCNP-based FRET systems the size of UCNPs plays a vital role due to the distance between the donor and acceptor which is a crucial parameter.

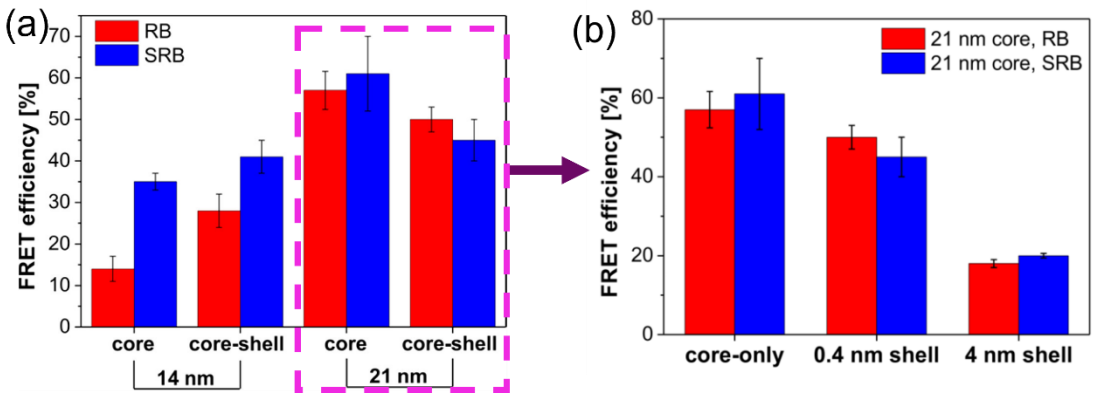

Figure 21. Effect of shell on FRET efficiency for various particle sizes. Reprinted with permission from publication [108] copyright 2018 ACS.

2.5 Challenging in UCNPs and goal of the thesis

Despite numerous studies on upconversion dynamics, rationalizing the dynamics of energy transfers within these nanoparticles still remains a challenge. For a precise understanding of the interactions between doping ions, such as ETU, CR, etc., a comprehensive photophysical study of ultrasmall UNCPs that have a limited number of sensitizers and emitters, is interesting as it allows the selection of the number of processes controlling the emission. This is the results of chapter 3, a comprehensive ensemble photophysical investigation for 5 nm (published article in ACS nano) and < 3 nm UCNPs by measuring time-resolved luminescence of activators under ETU process and direct excitation. Since the measured lifetime under ETU process is informative about the whole UC process, nevertheless, lifetime of activators is only limited to interaction of activator ions. As we already demonstrated in section 1.4.3.1, there are a few photophysical investigations based on ultrasmall UCNPs (sub 8 nm). It is certain that in all mentioned research, there is no comprehensive photophysical investigation on ultrasmall UCNPs with limited number of activators (< 3nm).

In chapter 3, we first studied 5 nm UNCPs developed by our collaborators in Toulouse. We demonstrated a great enhancement of upconversion luminescence due to the reduction of surface quenching upon addition of inert shell β-$NaREF_4$ (around 4 nm) to 5 nm Gd_2O_2S:20%Yb,1%Tm by using steady state spectra and time-resolved emission with ns pulse setup equipped with time-gated CCD camera.

Then, we investigated the photophysical properties of sub 3 nm of core UCNPs synthesized by our collaborators in Toulouse during the phase transition from α to β form by measuring their luminescence emission (under cw irradiation at 976 nm) and time-resolved luminescence emission (under ms pulse square excitation at 976 nm). Additionally, we could address the influence of Yb concentration and surface coating with a shell on the emission dynamics of the different Tm excited states by measuring their time-resolved luminescence (under ns pulse excitation at 976 nm) and direct excitation of Tm^{3+} (under ns pulse excitation at 355 nm).

Furthermore, for better understanding of UCNPs dynamics, single particle study is an interesting method. Therefore, the purpose of this thesis in chapter 4 and 5 is the investigation at the single particle level the photo-dynamics and energy transfer taking

place in different types of UCNPs in order to disentangle the complex energy pathways driving their emission properties at ensemble and single particle levels.

In the fourth chapter, we study the dynamics of assemblies of UCNPs (ET among UCNPs) using a unique developed new confocal microscope based on a millisecond-square pulse NIR excitation and an intensified gated CCD camera in order to measure space- and time-resolved emission spectra. We investigated the emission properties of Tm-based core and core-shell UCNPs assemblies. According to the nanometric spatial arrangement of the particles, we could demonstrate that the emission dynamics of single particles, 2D monolayers or 3D aggregates differ in terms of power-dependent emission band ratios and lifetimes.

In the fifth chapter of this thesis, by utilizing our confocal microscopy setup, we investigated the energy transfer process between specific emission bands of UCNPs (with Tm and Er emitters) and PDI molecules by measuring steady state spectra and luminescence lifetimes before and after adding PDI molecules. PDI molecules were not directly attached to the surfaces of UCNPs. Instead, two usual methods, spincoating and dropcasting, were employed. Based on the obtained results, the efficiency of energy transfer depends on the sample preparation and the type of emitter (Er or Tm). Moreover, we could show that it is possible to transfer excited-state energy through the Förster mechanism without conserving the spin angular momentum in Tm particles.

In chapter 6, we could clarify photodynamic emission of UCNPs by investigation of ultrasmall single emitter particles with various developed spectroscopic techniques. In addition, we could investigate interparticle interaction in UCNPs and resonance energy transfer from different emitters (Tm and Er) to PDI molecules with new microscopy system. These findings also open the doors to future research with some preliminary results.

2.6 References

1. Mondal, M. and V.K. Rai, *Introduction to Upconversion and Upconverting Nanoparticles.* Upconverting Nanoparticles: From Fundamentals to Applications, 2022: p. 1-30.
2. Huang, X., et al., *Enhancing solar cell efficiency: the search for luminescent materials as spectral converters.* Chemical Society Reviews, 2013. **42**(1): p. 173-201.
3. Loo, J.F.-C., et al., *Upconversion and downconversion nanoparticles for biophotonics and nanomedicine.* Coordination Chemistry Reviews, 2019. **400**: p. 213042.
4. Pollnau, M., et al., *Power dependence of upconversion luminescence in lanthanide and transition-metal-ion systems.* Physical Review B, 2000. **61**(5): p. 3337.
5. Gamelin, D.R. and H.U. Güdel, *Design of luminescent inorganic materials: new photophysical processes studied by optical spectroscopy.* Accounts of chemical research, 2000. **33**(4): p. 235-242.
6. Grzybowski, A. and K. Pietrzak, *Maria Goeppert-Mayer (1906–1972): two-photon effect on dermatology.* Clinics in dermatology, 2013. **31**(2): p. 221-225.
7. Ronda, C.R., *Luminescence: from theory to applications*. 2007: John Wiley & Sons.
8. Nadort, A., J. Zhao, and E.M. Goldys, *Lanthanide upconversion luminescence at the nanoscale: fundamentals and optical properties.* Nanoscale, 2016. **8**(27): p. 13099-13130.
9. Franken, P., et al., *Generation of optical harmonics.* Physical Review Letters, 1961. **7**(4): p. 118.
10. Auzel, F., *Quantum counter by transfer of energy between two rare earth ions in mixture of tungstate and glass.* CR Acad. Sci.(Paris), 1966. **262**: p. 1016.
11. Ovsyakin, V. and P. Feofilov, *Cooperative sensitization of luminescence in crystals activated with rare earth ions.* Soviet Journal of Experimental and Theoretical Physics Letters, 1966. **4**: p. 317.
12. Aguilar, M. and G. García-Solé, *Trivalent europium in x-irradiated NaCl: Eu.* Physical Review B, 1982. **26**(8): p. 4507.
13. Davy, H., *1.2 The Puzzle of Rare Earth Elements and the Discovery of Yttrium.* Biochemistry of Scandium and Yttrium, Part 1: Physical and Chemical Fundamentals: p. 2.
14. Bünzli, J.-C.G., *Lanthanide coordination chemistry: from old concepts to coordination polymers.* Journal of Coordination Chemistry, 2014. **67**(23-24): p. 3706-3733.
15. Bünzli, J.-C.G., *Lanthanide luminescence for biomedical analyses and imaging.* Chemical reviews, 2010. **110**(5): p. 2729-2755.
16. Rivera, V., F. Ferri, and E. Marega Jr, *Localized surface plasmon resonances: noble metal nanoparticle interaction with rare-earth ions.* Plasmonics-Principles and Applications, 2012: p. 283-312.
17. Newman, D.J. and B. Ng, *Crystal field handbook*. Vol. 43. 2000: Cambridge University Press Cambridge.
18. Shionoya, S., W.M. Yen, and H. Yamamoto, *Phosphor handbook*. 2018: CRC press.
19. Hehlen, M.P., M.G. Brik, and K.W. Krämer, *50th anniversary of the Judd–Ofelt theory: An experimentalist's view of the formalism and its application.* Journal of Luminescence, 2013. **136**: p. 221-239.
20. Liu, G. and B. Jacquier, *Spectroscopic properties of rare earths in optical materials*. Vol. 83. 2006: Springer Science & Business Media.
21. Liu, G., *Advances in the theoretical understanding of photon upconversion in rare-earth activated nanophosphors.* Chemical Society Reviews, 2015. **44**(6): p. 1635-1652.
22. Gao, S. and M. Affronte, *Molecular nanomagnets and related phenomena*. 2015: Springer.
23. Moore, E.G., A.P. Samuel, and K.N. Raymond, *From antenna to assay: lessons learned in lanthanide luminescence.* Accounts of chemical research, 2009. **42**(4): p. 542-552.
24. Henderson, B. and G.F. Imbusch, *Optical spectroscopy of inorganic solids*. Vol. 44. 2006: Oxford University Press.

25. Binnemans, K., *Interpretation of europium (III) spectra.* Coordination Chemistry Reviews, 2015. **295**: p. 1-45.
26. Chen, W., et al., *Energy structure and fluorescence of Eu 2+ in ZnS: Eu nanoparticles.* Physical Review B, 2000. **61**(16): p. 11021.
27. Chen, W., et al., *Upconversion luminescence of Eu 3+ and Mn 2+ in ZnS: Mn 2+, Eu 3+ codoped nanoparticles.* Journal of Applied physics, 2004. **95**(2): p. 667-672.
28. Chen, G., et al., *Upconversion nanoparticles: design, nanochemistry, and applications in theranostics.* Chemical reviews, 2014. **114**(10): p. 5161-5214.
29. Ofelt, G., *Intensities of crystal spectra of rare-earth ions.* The journal of chemical physics, 1962. **37**(3): p. 511-520.
30. Judd, B., *Optical absorptionintensities of lanthanides ions.* Phys Rev, 1962. **127**: p. 504.
31. CK, J., *rgensen and BR Judd.* Mol. Phys, 1964. **8**: p. 281.
32. Auzel, F., *Upconversion and anti-stokes processes with f and d ions in solids.* Chemical reviews, 2004. **104**(1): p. 139-174.
33. Lingeshwar Reddy, K., et al., *Lanthanide doped near infrared active upconversion nanophosphors: fundamental concepts, synthesis strategies, and technological applications.* Small, 2018. **14**(37): p. 1801304.
34. Diaz-Torres, L., et al., *Enhanced cooperative absorption and upconversion in Yb3+ doped YAG nanophosphors.* Optical Materials, 2005. **27**(7): p. 1305-1310.
35. Maciel, G., et al., *Blue cooperative upconversion in Yb 3+-doped multicomponent sol-gel-processed silica glass for three-dimensional display.* Applied Physics Letters, 2000. **76**(15): p. 1978-1980.
36. Knighton, R.C., et al., *Upconversion in ad–f [RuYb3] Supramolecular Assembly.* Journal of the American Chemical Society, 2022. **144**(29): p. 13356-13365.
37. Knighton, R.C., et al., *Cooperative Luminescence and Cooperative Sensitisation Upconversion of Lanthanide Complexes in Solution.* Angewandte Chemie, 2022. **134**(4): p. e202113114.
38. Pattnaik, S. and V.K. Rai, *Impact of charge compensation on optical and thermometric behaviour of titanate phosphors.* Materials Research Bulletin, 2020. **125**: p. 110761.
39. Wei, W., et al., *Cross relaxation induced pure red upconversion in activator-and sensitizer-rich lanthanide nanoparticles.* Chemistry of Materials, 2014. **26**(18): p. 5183-5186.
40. Chivian, J.S., W. Case, and D. Eden, *The photon avalanche: a new phenomenon in Pr3+-based infrared quantum counters.* Applied Physics Letters, 1979. **35**(2): p. 124-125.
41. Wang, F., et al., *Tuning upconversion through energy migration in core–shell nanoparticles.* Nature materials, 2011. **10**(12): p. 968-973.
42. Dong, H., L.-D. Sun, and C.-H. Yan, *Energy transfer in lanthanide upconversion studies for extended optical applications.* Chemical Society Reviews, 2015. **44**(6): p. 1608-1634.
43. Shan, J., et al., *The hidden effects of particle shape and criteria for evaluating the upconversion luminescence of the lanthanide doped nanophosphors.* The Journal of Physical Chemistry C, 2010. **114**(6): p. 2452-2461.
44. Jung, T., et al., *The preferred upconversion pathway for the red emission of lanthanide-doped upconverting nanoparticles, NaYF 4: Yb 3+, Er 3+*. Physical Chemistry Chemical Physics, 2015. **17**(20): p. 13201-13205.
45. Liu, H., et al., *Photon upconversion kinetic nanosystems and their optical response*. Laser & Photonics Reviews, 2018. **12**(1): p. 1700144.
46. Hong-Wei, S., et al., *Upconversion luminescence dynamics in Er3+/Yb3+ codoped nanocrystalline yttria.* Chinese Physics Letters, 2006. **23**(2): p. 474.
47. Lin, C., et al., *Highly luminescent NIR-to-visible upconversion thin films and monoliths requiring no high-temperature treatment.* Chemistry of Materials, 2009. **21**(14): p. 3406-3413.
48. Gamelin, D.R. and H.U. Gudel, *Upconversion processes in transition metal and rare earth metal systems.* Transition metal and rare earth compounds, 2001: p. 1-56.
49. Cho, Y., et al., *Statistical Time-Resolved Spectroscopic Study on Upconversion Luminescence*. The Journal of Physical Chemistry C, 2019. **124**(4): p. 2680-2688.

50. May, P.S. and M. Berry, *Tutorial on the acquisition, analysis, and interpretation of upconversion luminescence data.* Methods and applications in fluorescence, 2019. **7**(2): p. 023001.
51. Dawson, P. and M. Romanowski, *Excitation Modulation of Upconversion Nanoparticles for Switch-like Control of Ultraviolet Luminescence.* J Am Chem Soc, 2018. **140**(17): p. 5714-5718.
52. Zou, X. and H. Toratani, *Evaluation of spectroscopic properties of Yb 3+-doped glasses.* Physical review B, 1995. **52**(22): p. 15889.
53. Brown, D.C., N.S. Tomasello, and C.L. Hancock, *Absorption and emission cross-sections, Stark energy levels, and temperature dependent gain of Yb: QX phosphate glass.* Optics Express, 2021. **29**(21): p. 33818-33835.
54. Payne, S.A., et al., *Infrared cross-section measurements for crystals doped with Er/sup 3+/, Tm/sup 3+/, and Ho/sup 3+*. IEEE Journal of Quantum Electronics, 1992. **28**(11): p. 2619-2630.
55. Fu, L., Y. Wu, and T. Fu, *Determination of absorption cross-section of RE3+ in upconversion powder materials: Application to β-NaYF4: Er3+*. Journal of Luminescence, 2022. **245**: p. 118758.
56. Kıbrıslı, O., et al., *Instantaneous color tuning of upconversion emission in a novel lanthanide-doped monolithic glass via excitation modulation.* The Journal of Physical Chemistry C, 2020. **124**(19): p. 10687-10695.
57. Walsh, B.M., N.P. Barnes, and B. Di Bartolo, *Branching ratios, cross sections, and radiative lifetimes of rare earth ions in solids: application to Tm 3+ and Ho 3+ ions in LiYF 4.* Journal of applied physics, 1998. **83**(5): p. 2772-2787.
58. Wen, S., et al., *Advances in highly doped upconversion nanoparticles.* Nature communications, 2018. **9**(1): p. 1-12.
59. Gnach, A. and A. Bednarkiewicz, *Lanthanide-doped up-converting nanoparticles: merits and challenges.* Nano Today, 2012. **7**(6): p. 532-563.
60. Chan, E.M., et al., *Concentrating and recycling energy in lanthanide codopants for efficient and spectrally pure emission: the case of NaYF4:Er3+/Tm3+ upconverting nanocrystals.* J Phys Chem B, 2012. **116**(35): p. 10561-70.
61. Yu, D., J. Ballato, and R.E. Riman, *The Temperature-Dependence of Multiphonon Relaxation of Rare-Earth Ions in Solid-State Hosts.* J Phys Chem C Nanomater Interfaces, 2016. **120**(18): p. 9958-9964.
62. Wang, F. and X. Liu, *Recent advances in the chemistry of lanthanide-doped upconversion nanocrystals.* Chem Soc Rev, 2009. **38**(4): p. 976-89.
63. Wang, F., et al., *Simultaneous phase and size control of upconversion nanocrystals through lanthanide doping.* Nature, 2010. **463**(7284): p. 1061-5.
64. Haase, M. and H. Schafer, *Upconverting nanoparticles.* Angew Chem Int Ed Engl, 2011. **50**(26): p. 5808-29.
65. Krämer, K.W., et al., *Hexagonal sodium yttrium fluoride based green and blue emitting upconversion phosphors.* Chemistry of materials, 2004. **16**(7): p. 1244-1251.
66. Yan, C., et al., *Lanthanide Ion Doped Upconverting Nanoparticles: Synthesis, Structure and Properties.* Small, 2016. **12**(29): p. 3888-907.
67. Muhr, V., et al., *Upconversion nanoparticles: from hydrophobic to hydrophilic surfaces.* Acc Chem Res, 2014. **47**(12): p. 3481-93.
68. Sedlmeier, A. and H.H. Gorris, *Surface modification and characterization of photon-upconverting nanoparticles for bioanalytical applications.* Chem Soc Rev, 2015. **44**(6): p. 1526-60.
69. Lahtinen, S., et al., *Disintegration of Hexagonal NaYF4:Yb3+,Er3+ Upconverting Nanoparticles in Aqueous Media: The Role of Fluoride in Solubility Equilibrium.* The Journal of Physical Chemistry C, 2016. **121**(1): p. 656-665.
70. Chen, G., et al., *Energy-cascaded upconversion in an organic dye-sensitized core/shell fluoride nanocrystal.* Nano letters, 2015. **15**(11): p. 7400-7407.

71. Hossan, M.Y., et al., *Explaining the Nanoscale Effect in the Upconversion Dynamics of β-NaYF4:Yb3+, Er3+ Core and Core–Shell Nanocrystals.* The Journal of Physical Chemistry C, 2017. **121**(30): p. 16592-16606.
72. Teng, X., et al., *Lanthanide-doped Na x ScF3+ x nanocrystals: crystal structure evolution and multicolor tuning.* Journal of the American Chemical Society, 2012. **134**(20): p. 8340-8343.
73. Wang, F. and X. Liu, *Upconversion multicolor fine-tuning: visible to near-infrared emission from lanthanide-doped NaYF4 nanoparticles.* Journal of the American Chemical Society, 2008. **130**(17): p. 5642-5643.
74. Wang, J., et al., *Enhancing multiphoton upconversion through energy clustering at sublattice level.* Nat Mater, 2014. **13**(2): p. 157-62.
75. Zhao, J., et al., *Upconversion luminescence with tunable lifetime in NaYF 4: Yb, Er nanocrystals: role of nanocrystal size.* Nanoscale, 2013. **5**(3): p. 944-952.
76. Gargas, D.J., et al., *Engineering bright sub-10-nm upconverting nanocrystals for single-molecule imaging.* Nat Nanotechnol, 2014. **9**(4): p. 300-5.
77. Gargas, D.J., et al., *Engineering bright sub-10-nm upconverting nanocrystals for single-molecule imaging.* Nature nanotechnology, 2014. **9**(4): p. 300-305.
78. Tu, L., et al., *Excitation energy migration dynamics in upconversion nanomaterials.* Chemical Society Reviews, 2015. **44**(6): p. 1331-1345.
79. Sun, T., et al., *Shielding Upconversion by Surface Coating: A Study of the Emission Enhancement Factor.* Chemphyschem, 2016. **17**(5): p. 766-70.
80. Lohse, S.E. and C.J. Murphy, *Applications of colloidal inorganic nanoparticles: from medicine to energy.* Journal of the American Chemical Society, 2012. **134**(38): p. 15607-15620.
81. Zarschler, K., et al., *Ultrasmall inorganic nanoparticles: State-of-the-art and perspectives for biomedical applications.* Nanomedicine: Nanotechnology, Biology and Medicine, 2016. **12**(6): p. 1663-1701.
82. Golesorkhi, B., et al., *Deciphering and quantifying linear light upconversion in molecular erbium complexes.* Chemical science, 2019. **10**(28): p. 6876-6885.
83. Knighton, R.C., et al., *Upconversion in molecular hetero-nonanuclear lanthanide complexes in solution.* Chemical Communications, 2021. **57**(1): p. 53-56.
84. Nonat, A.M. and L.J. Charbonnière, *Upconversion of light with molecular and supramolecular lanthanide complexes.* Coordination Chemistry Reviews, 2020. **409**: p. 213192.
85. Suffren, Y., et al., *Taming lanthanide-centered upconversion at the molecular level.* Inorganic chemistry, 2016. **55**(20): p. 9964-9972.
86. Niu, W., S. Wu, and S. Zhang, *Utilizing the amidation reaction to address the "cooperative effect" of carboxylic acid/amine on the size, shape, and multicolor output of fluoride upconversion nanoparticles.* Journal of Materials Chemistry, 2011. **21**(29): p. 10894-10902.
87. Ostrowski, A.D., et al., *Controlled synthesis and single-particle imaging of bright, sub-10 nm lanthanide-doped upconverting nanocrystals.* ACS nano, 2012. **6**(3): p. 2686-2692.
88. Rinkel, T., et al., *Synthesis of 10 nm β-NaYF4: Yb, Er/NaYF4 core/shell upconversion nanocrystals with 5 nm particle cores.* Angewandte Chemie International Edition, 2016. **55**(3): p. 1164-1167.
89. Li, H., L. Xu, and G. Chen, *Controlled synthesis of monodisperse hexagonal NaYF4: Yb/Er nanocrystals with ultrasmall size and enhanced upconversion luminescence.* Molecules, 2017. **22**(12): p. 2113.
90. Wong, H.-T., et al., *Water dispersible ultra-small multifunctional KGdF 4: Tm 3+, Yb 3+ nanoparticles with near-infrared to near-infrared upconversion.* Journal of Materials Chemistry, 2011. **21**(41): p. 16589-16596.
91. Amouroux, B., et al., *Importance of the Mixing and High-Temperature Heating Steps in the Controlled Thermal Coprecipitation Synthesis of Sub-5-nm Na (Gd–Yb) F4: Tm.* Inorganic Chemistry, 2019. **58**(8): p. 5082-5088.

92. Liu, R.-S., *Phosphors, up conversion nano particles, quantum dots and their applications*. Vol. 1. 2017: Springer.
93. Frenzel, F., et al., *Multiband emission from single β-NaYF4(Yb,Er) nanoparticles at high excitation power densities and comparison to ensemble studies.* Nano Research, 2021. **14**(11): p. 4107-4115.
94. Wu, S., et al., *Non-blinking and photostable upconverted luminescence from single lanthanide-doped nanocrystals.* Proceedings of the National Academy of Sciences, 2009. **106**(27): p. 10917-10921.
95. Andresen, E., U. Resch-Genger, and M. Schaferling, *Surface Modifications for Photon-Upconversion-Based Energy-Transfer Nanoprobes.* Langmuir, 2019. **35**(15): p. 5093-5113.
96. Alonso-Cristobal, P., et al., *Highly Sensitive DNA Sensor Based on Upconversion Nanoparticles and Graphene Oxide.* ACS Appl Mater Interfaces, 2015. **7**(23): p. 12422-9.
97. Su, Q., et al., *Resonance Energy Transfer in Upconversion Nanoplatforms for Selective Biodetection.* Acc Chem Res, 2017. **50**(1): p. 32-40.
98. Muhr, V., et al., *Particle-size-dependent Forster resonance energy transfer from upconversion nanoparticles to organic dyes.* Analytical chemistry, 2017. **89**(9): p. 4868-4874.
99. Zhang, C., et al., *Biosensing platform based on fluorescence resonance energy transfer from upconverting nanocrystals to graphene oxide.* Angew Chem Int Ed Engl, 2011. **50**(30): p. 6851-4.
100. Ye, W.W., et al., *Upconversion luminescence resonance energy transfer (LRET)-based biosensor for rapid and ultrasensitive detection of avian influenza virus H7 subtype.* Small, 2014. **10**(12): p. 2390-7.
101. Mattsson, L., et al., *Upconverting nanoparticle to quantum dot FRET for homogeneous double-nano biosensors.* RSC Advances, 2015. **5**(18): p. 13270-13277.
102. Arppe, R., et al., *Photon upconversion sensitized nanoprobes for sensing and imaging of pH.* Nanoscale, 2014. **6**(12): p. 6837-43.
103. Wu, Y.X., et al., *Quench-Shield Ratiometric Upconversion Luminescence Nanoplatform for Biosensing.* Anal Chem, 2016. **88**(3): p. 1639-46.
104. Ma, T., et al., *Dye-conjugated upconversion nanoparticles for ratiometric imaging of intracellular pH values.* Journal of Materials Chemistry C, 2015. **3**(26): p. 6616-6620.
105. Nareoja, T., et al., *Ratiometric Sensing and Imaging of Intracellular pH Using Polyethylenimine-Coated Photon Upconversion Nanoprobes.* Anal Chem, 2017. **89**(3): p. 1501-1508.
106. Li, C., et al., *Accurate Quantitative Sensing of Intracellular pH based on Self-ratiometric Upconversion Luminescent Nanoprobe.* Sci Rep, 2016. **6**: p. 38617.
107. Zheng, J., et al., *Synchronous detection of glutathione/hydrogen peroxide for monitoring redox status in vivo with a ratiometric upconverting nanoprobe.* Nano Research, 2019. **12**(4): p. 931-938.
108. Ni, J., et al., *Assembling of a functional cyclodextrin-decorated upconversion luminescence nanoplatform for cysteine-sensing.* Chem Commun (Camb), 2015. **51**(74): p. 14054-6.
109. Kraft, M., et al., *Particle-size-dependent upconversion luminescence of NaYF4: Yb, Er nanoparticles in organic solvents and water at different excitation power densities.* Nano Research, 2018. **11**(12): p. 6360-6374.

3

Investigation of small and ultrasmall UCNPs photodynamics at ensemble level

3.1 Introduction

In terms of photokinetics, the highly nonlinear response to the excitation energy of the UC phenomenon reflects the interplay of several energy redistribution processes between all energy levels involved: the usual unimolecular ones (non-radiative and radiative decays) and some bimolecular ones (ETU, energy migration, and cross-relaxation (CR)).

Nanometric (sub-10 nm and smaller) inorganic nanoparticles are convenient reporters and tags for bioimaging applications as their size can be close to biological structures, e.g. enabling good transport properties through cellular membranes, and because of the potentiality of multimodal applications.[1, 2] However, for a finite size crystal, the surface plays a prominent role through luminescence quenching by ligands and molecules containing groups with high energy vibrations and surface defects.[3-5] Thus, decreasing the size of UC crystals inevitably leads to a reduction in brightness due to a low number of absorbing and emissive dopant ions and surface quenching.

Interestingly, ETU has been also reported for molecular poly-heteronuclear complexes with a defined arrangement between sensitizers and activators of few lanthanide ions.[6-9] Thanks to a careful tailoring of inter-metallic distances (typically less than 0.5 nm) and to the optimization of the first ligand shell to prevent vibration-induced relaxation, the classical upconversion mechanisms (ESA and ETU) were observed despite the proximity of efficient quenchers similar to those observed in small UCNPs.[10] Thus, as far as size is concerned, there is no apparent bottom limit for this phenomenon.

The objective of this chapter is therefore to characterize small (< 10 nm) and ultrasmall (< 3 nm) UCNPs whose synthesis procedure has been optimized by our collaborators in Toulouse to ensure good emission properties despite their small size.

First, a common strategy to ensure a relatively high luminescence of small UCNPs is to add an insulating shell in order to reduce surface-based non-radiative processes.[11] To this end, fluoride@fluoride homogeneous core/shell structures have been extensively studied because fluoride host matrices are normally recognized as the most efficient family of host materials with low phonon energies for achieving highly efficient UCL.[12] Construction of heterogeneous core/shell structures by combining two different materials is much more challenging from the synthesis point of view but is at the same time expected to provide very advantageous emission properties. Our collaborators Q.

Zou and C. Roux from IMRCP laboratory in Toulouse developed a synthetic pathway for unique Ln^{3+}-doped oxysulfide@fluoride core/shell heterostructures published in ACS Nano.[13] The first part of this chapter thus describes the enhancement of upconversion luminescence of 5 nm Gd_2O_2S:20%Yb,1%Tm UCNPs upon addition of an inert shell of $NaREF_4$ (around 4 nm) by measuring steady state spectra and time-resolved luminescence.

Secondly, we were interested in understanding the upconversion process in ultrasmall UCNPs containing a limited number of emitters, for which the dynamics of the energy redistribution among the activator kinetic network is expected to be greatly simplified. This work is the result of a collaboration with our Toulouse colleagues of the IMRCP laboratory (Baptiste Amouroux, Christophe Coudret) who developed an original synthetic pathway based on a cycled microwave heating procedure to produce sub-3 nm Tm-doped UCNP. The second part of this chapter is dedicated to the study of the of the α-to-β phase transition occurring during the synthesis procedure of these ultrasmall UCNPs. Then, we concentrated on 4 samples that have a limited number of emitters (from a single emitter to 8 emitters) to analyze the emission dynamics arising from the interplay between emitters in these ultrasmall nanoparticles.

In order to perform all of the photodynamic investigation of UCNPs structures, we introduced various spectroscopy setups. These setups consist of various excitation temporal profiles, from nanosecond (ns) pulse excitation to millisecond (ms) square pulse excitation, with different detection systems such as photomultiplier tube (PMT) and intensified time-gated CCD camera. Moreover, in order to investigate the dynamics of emitter ions independent of sensitizers, we employed direct excitation at 355 nm in our ns pulse setup. Detailed explanations of utilized setups will be provided in the following section.

3.2 Developed experimental setups for UCNPs

3.2.1 Absorbance measurements

Due to the low UCNPs cross section and the colloid structure of the material, they have an extremely low electronic absorption (high scattering and limited colloidal stability at high concentrations). We used a sensitive double beam Cary 3500 absorption spectrometer (spectral bandwidth of 1 nm and one point every 1 nm) to scan from 1100 nm until 800 nm in order to measure Yb^{3+} absorbance spectrum for UCNPs suspensions (cyclohexane and toluene spectroscopic grade Sigma-Aldrich).

3.2.2 Steady state emission measurements

The non-linear nature of UCNPs necessitates a spectroscopic setup with a unique excitation and detection channel.[14] A well-defined beam profile, as well as a high wavelength and intensity stability at excitation wavelength that matches the narrow Yb^{3+} absorption band around 980 nm, are all part of this process. Measuring UCNP emission spectra not only provides information about emission profiles at various wavelengths, but also show the various types of relationships between excitation power density and emission spectra.[15] In order to measure steady state emission spectra and power dependent curves, we used the setup in Figure 1.

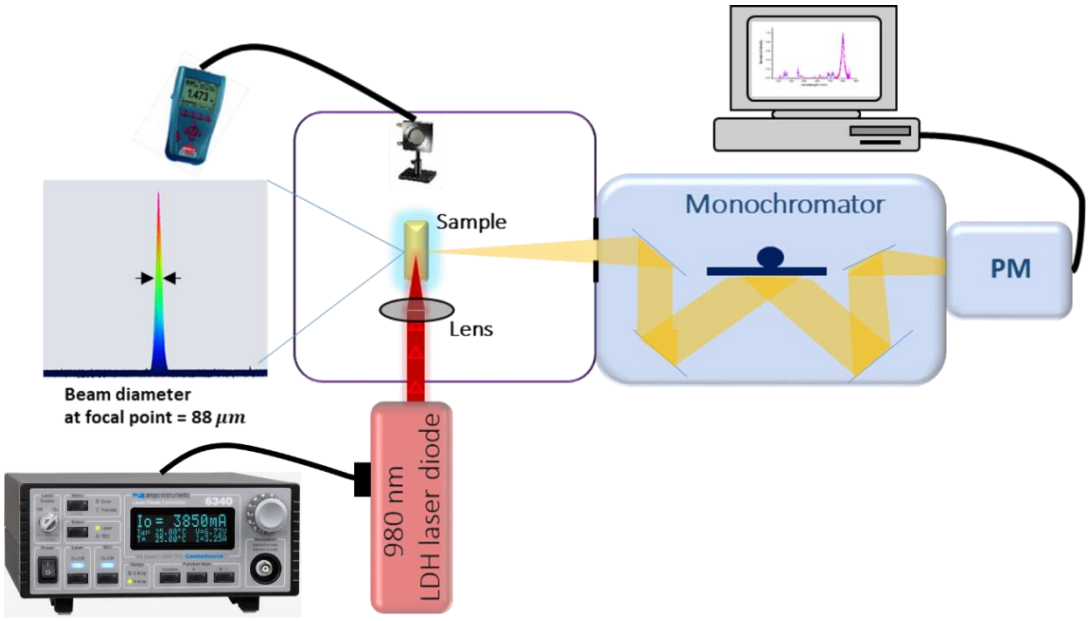

Figure 1. Schematic representation of the commercial fluorimeter (Fluoromax-3, Horiba Jobin Yvon) combined with 980 nm diode laser in order to measuring steady state spectra.

In this setup, the laser diode equipped with a fiber-Bragg-grating 976 nm stabilized laser diode (Thorlabs, 900 mW) was controlled by an Arroyo instrument diode controller (series 6300, model 6340) which is a high-accuracy laser driver combined with a 60W temperature controller and a voltage range from 100 mA to 4000 mA. The beam was usually focalized into a 4x10 mm quartz cuvette without stirring by a convergent lens (focal length 5.2 mm), providing a gaussian intensity shape at the focal point as shown in Figure 1. The shape of the beam was measured by a Gentec (Beamage 3.0) camera, and the diameter of the beam with and without lens was 30 μm and 1130 μm at full width at half maximum (FWHM), respectively. In order to calculate the power density, the diameter of the excitation beam was measured at the focal point of the sample (or it was calculated from the diameter of the excitation beam in the sample without a lens). This amount of power density varies from a few W/cm^2 until kW/cm^2 which allow covering different emission region of UCNPs. Moreover, the excitation power was continuously measured by NOVA II OPHIR laser power meter.

For all measurements the emission spectra were recorded between 300 and 850 nm and using the appropriate wavelength increment is essential. In a wavelength scan, the increment is the distance between adjacent data points in nanometers. The resolution of the spectrum is affected by the spacing between data points, as does the overall acquisition time. Most fluorescence samples have broad-band emissions with a Lorentzian distribution, therefore tiny increment is not required. UCNPs, on the other hand, have a narrow emission band and have a high photostability. Therefore, the proper increment that we chose was 0.5 second.

Selecting the appropriate bandpass affects the resolution of the spectra. The amount of fluorescence captured by the detector is controlled by the emission spectrometer slits. The square of the slit width is proportional to the signal intensity as mentioned below:

$$\text{Signal level} \propto (\text{slit width})^2 \qquad (1)$$

And the formula for calculating bandpass is as follows:

$$\text{Bandpass (nm)} = \text{slit width (mm)} \times \text{dispersion (nm/mm)} \qquad (2)$$

The mentioned fluorimeter has a single grating monochromator and 1200 grooves/mm gratings with a dispersion of 4.25 nm/mm. In our measurements, we use a 5 nm bandpass for the emission slit size.

It is critical to collect correct information on a sample's emission, therefore data must be corrected (correction file) by the response properties of gratings, detectors, and other spectrometer components as they vary as a function of wavelength. Moreover, beside correction function provided by the instrument manufacturer, an additional baseline correction was carried out by subtracting the solvent signal (cyclohexane or toluene). In order to calculate the upconversion luminescence intensities, the corrected emission spectra (corrected by instrument correction function and baseline correction) were subdivided into the several emission bands.

For the automated computation of integration in each emission band, a Python program was written (By me!). In addition, for visualization of the data that produced by Python, Originlab.

3.2.3 Time-resolved measurements

For a comprehensive study of energy transfer processes within UCNPs, rising and decay parameters of UCNPs excited states were investigated with different irradiation schemes and setups as follow:

1. Nanosecond pulse setup under 976 nm excitation and nanosecond transient absorption scheme equipped with intensified time-gated CCD camera.

2. Millisecond square pulse setup under 976 nm excitation and single photon counting detection scheme.

3. Nanosecond pulse setup under 976 nm and 355 nm excitation and nanosecond transient absorption detection scheme with a PMT.

1. The nanosecond pulse setup, equipped with time-gated CCD camera, is used to characterize Ln^{3+}-doped Gd_2O_2S@$NaREF_4$ heterogeneous core/shell structures. As shown in Figure 2, time-resolved luminescence measurements were performed using a nanosecond 976 nm excitation (fwhm 7-8 ns, 2.5 mJ, 2 Hz) provided by a 10-Hz Nd:YAG laser (Continuum Surelite II) coupled to an OPO (Continuum Panther EX OPO) and focused to the cuvette by a focal lens with 5 cm focal length. Samples were introduced in a quartz cell (4 × 10 mm) and the emitted light was collected at 90°,

dispersed by a monochromator (Horiba Jobin-Yvon, iHR320, bandpass 10 nm) and analyzed with a gated intensified CCD camera (1024 x 256 pixels, PI-MAX 4, Princeton Instruments) triggered by a photodiode. Time-resolved spectra between 400 and 900 nm can be recorded with constant gates width for UCNPs samples. The first gate time was set to start at 26 ns (insertion delay of the camera) and number of gates / spectra are defined to get time-resolved spectra of UCNPs samples.

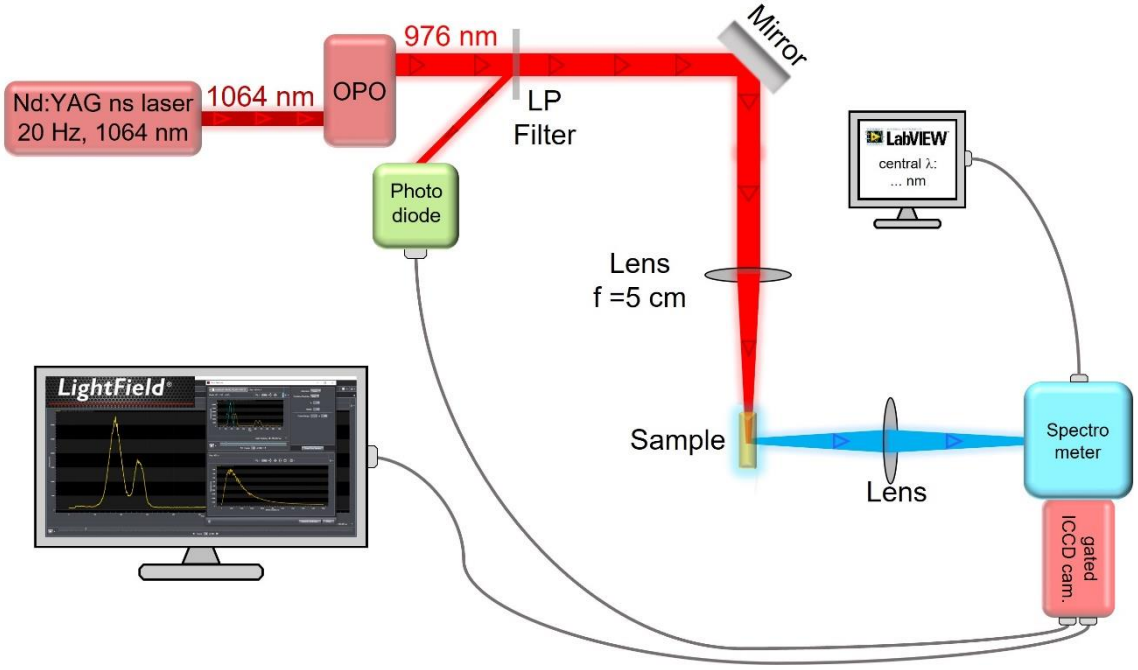

Figure 2. Schematic representation of the nanosecond pulse experimental setup equipped with time gated ICCD camera detection to investigate UCNPs lifetime.

2. The millisecond square pulse setup was used to measure the lifetime of ultrasmall UCNPs (< 3 nm) during the phase transition and is shown in Figure 3. The most common technique to compare steady state properties and lifetime for UCNPs consists of exciting the sample with a square ms pulse to reach the photo-stationary steady state. The rising time kinetic contains the contributions of all the ETU processes that can happen in the UCNP, i.e. photon absorption, energy transfers between the different ions and photon emission. The emission kinetics observed when the irradiation square pulse stops give a measure of the activator's averaged lifetime at the photo-stationary state. Here a pulse square of 3 milliseconds affords reaching the photo-stationary emission of the 798 nm emission for Tm^{3+} in cycled particles. It was achieved using LDH laser head at 976 nm operated in the cw mode with the Taiko PDL M1 controller (Picoquant) and a delay generator (SRS, model DG535) allowing

the generation of square pulses with variable length. The experiments were performed with 3 milliseconds square pulses at 200 Hz, i.e., the UCNPs were irradiated every 5 ms by a 3 ms square pulse at 980 nm. The choice of the pulse length was guided by the time necessary to reach the photo-stationary state. The laser beam was focalized into a 4 x 10 mm quartz cell placed in the chamber of a fluorescence lifetime spectrometer where solutions were stirred (FluoTime200, Picoquant). The emitted photons were collected through a monochromator (band pass 16 nm) and detected by a MCP-PMT detector (Hamamatsu). The arrival time of the photons was measured using a photon counting card working in the multichannel scaling mode, in long range mode (TimeHarp260pico). The laser power density was estimated to be 100 W/cm² at the sample, i.e., ca. 0.13 mJ per pulse. The bin time resolution was set at 1.6 µs.

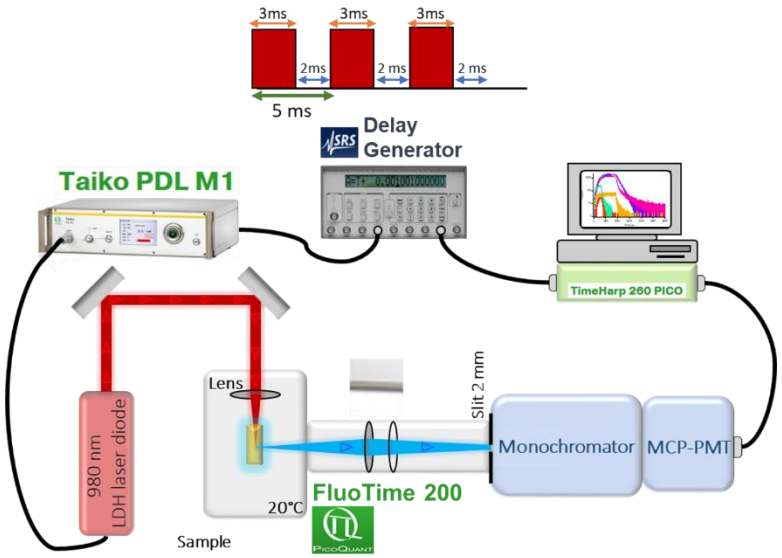

Figure 3. Schematic representation of the millisecond pulse square experimental setup afforded to reach photo-stationary emission of Tm^{3+} in different states.

3. The third setup, shown in Figure 5, is used to study the photodynamics of ultrasmall UCNPs. It is equipped with a ns pulsed laser system operating at two different excitation wavelengths to probe Tm^{3+} directly excited to the $^1D_2$ state (at 355 nm) or to probe Tm^{3+} upconversion process by exciting Yb^{3+} ions at 976 nm. Figure 4 shows the energy scheme of Tm^{3+} ion excited either by energy transfers from excited Yb^{3+} at 976 nm (UC) or directly excited at 355 nm (DE).

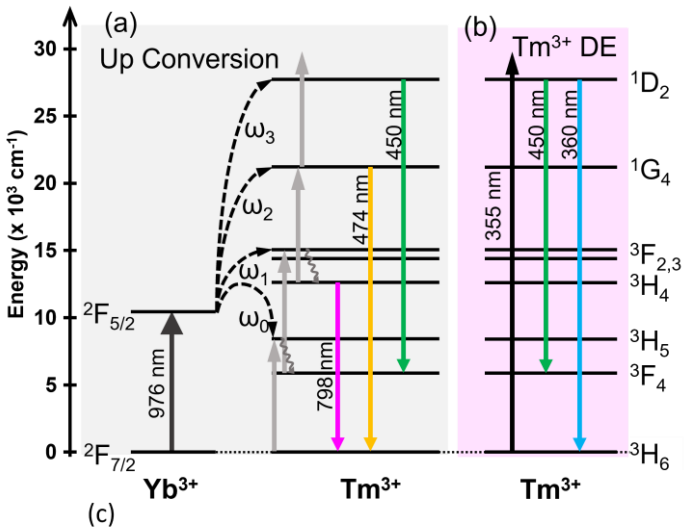

(c)

UC/DE	Electronic transition	λ_{Ex}[nm]	λ_{Em}[nm]
UC	$^3H_4 \rightarrow {}^3H_6$	976 nm	800 nm
UC	$^1G_4 \rightarrow {}^3H_6$	976 nm	475 nm
UC	$^1D_2 \rightarrow {}^3F_4$	976 nm	450 nm
DE	$^1G_4 \rightarrow {}^3F_4$	355 nm	450nm
DE	$^1D_2 \rightarrow {}^3H_6$	355 nm	360 nm

Figure 4. a) Excitation of Yb^{3+} at 976 nm for investigating Tm emission states at 800 nm, 475nm, and 450nm. b) Direct excitation of Tm^{3+} at 355 nm for probing dynamics of $^1D_2$ state. c) Electronic transition, excitation and emission wavelengths that were used in this work for upconversion (Yb^{3+}) and direct excitation (Tm^{3+}).

To probe the upconversion processes, nanosecond pulses at 976 nm (fwhm 7-8 ns, 1 mJ, 2 Hz) were provided by a 10-Hz Nd:YAG laser (Continuum Surelite II) coupled to an OPO (Continuum Panther EX OPO) and SH05 shutter (Thorlabs) as presented in Figure 5. UNCPs are irradiated by 8 ns pulse every 0.5 seconds. The emitted light was collected at 90°, dispersed by a monochromator (Horiba Jobin-Yvon, iHR320, bandpass 10 nm) and analyzed with a photomultiplier (R1477-06, Hamamatsu) coupled to a digital oscilloscope (LeCroy 454, 500 MHz). Samples were stirred in a quartz cell (4 × 10 mm). A resistance of 4.7 kΩ was used to multiply the detected signal.

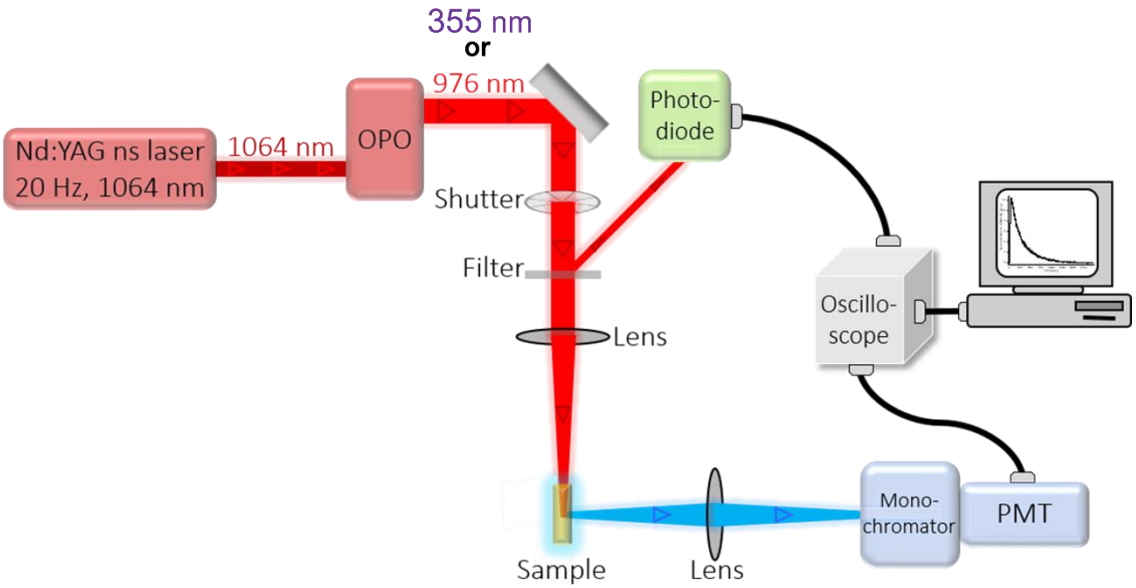

Figure 5. Schematic representation of the nanosecond pulse experimental setup used to probe upconversion process and direct excitation of ultrasmall UCNPs at 976 nm and 355 nm, respectively.

The instrumental response function (IRF) was then determined to be about 2 µs (decay of laser scattering signal, Figure 6a). For each emission wavelength (360, 450, 474 and 798 nm), the recorded traces were averaged for 64 pulses. In addition, Tm^{3+} direct excitation was carried out using the 355 nm light resulting from the tripled Nd:YAG laser emission. The emitted light was collected at 450 nm. In this case, no resistance was used and , the IRF was a decay of 200 ns using laser scattering signal. The energies used in these experiments reached 2 mJ /pulse at 976 nm and 2.5 mJ/pulse at 355 nm. Samples were stirred in a quartz cell (4 × 10 mm).

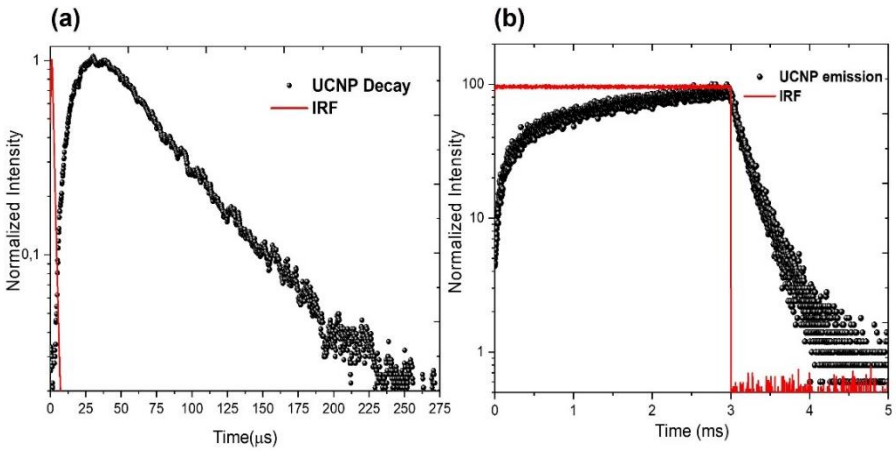

Figure 6. Representing instrumental response function (IRF) in different setups and compare with UCNPs emission. (A) IRF and UCNPs emission in nanosecond pulse setup. (B) IRF and UCNPs emission in square pulse setup.

3.3 Upconversion luminescence enhancement in oxysulfide heterostructured 5 nm UCNPs

Lanthanide (Ln^{3+})-doped upconversion nanoparticles (UCNPs) often suffer from weak luminescence, especially when their size is small (less than 10 nm). Enhancing the upconversion luminescence (UCL) efficiency of small UCNPs has remained a challenge that must be undertaken if any practical applications are to be envisaged. Our collaborators introduced new oxysulfide heterostructures by combining hexagonal rare earth oxysulfide and sodium rare earth fluorides which have a good stability in solution (figure 7).[13] By measuring steady state spectra and time-resolved luminescence, we could demonstrate a great increase of upconversion luminescence upon addition of the inert shell β-$NaREF_4$ (around 4 nm) to a 5 nm Gd_2O_2S:20%Yb,1%Tm core.

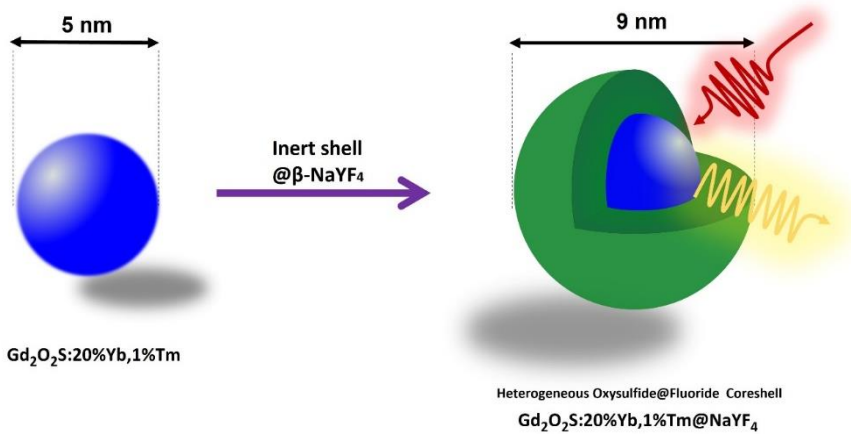

Figure 7. Enhancement upconversion luminescence upon addition of inert shell $NaREF_4$.

As shown in Figure 8a, under illumination with a 976 nm continuous wave laser, Gd_2O_2S:20%Yb,1%Tm core-only and Gd_2O_2S:20%Yb,1%Tm@β-$NaYF_4$ core-shell UCNPs exhibit emission bands at 469, 640, and 803 nm ascribed to the $^1G_4 \rightarrow {}^3H_6$, $^1G_4 \rightarrow {}^3F_4$, and $^3H_4 \rightarrow {}^3H_6$ transitions of Tm^{3+} respectively. We observed an 836-fold enhancement in overall emission for Tm-doped UCNPs after $NaYF_4$ coating. Furthermore, we measured time-resolved luminescence of both Yb^{3+}/Tm^{3+}-doped core-only and core-shell UCNPs under ns pulse excitation at 976 nm with a gated intensified CCD camera (as shown in Figure 3). The lifetimes of the 469 and 803 nm emission decays were increased from 8 and 5 µs for the core-only (Figure 8b) to 789 and 898 µs for the

core/shell (Figure 8c), respectively, displaying approximately 100- to 180-fold longer lifetimes. The dramatic increase of the characteristic decay times in the core/shell particles might be attributed to light trapping inside the particle due to refractive index mismatches between the Gd_2O_2S core and the $NaYF_4$ shell. Therefore, we will have less leak of energy through the shell and favor the energy migration within the core, resulting in the striking lengthening of the decay times. In addition, the real concentration of Tm has been confirmed to be 0.68% via ICP measurements for the core/shell UCNPs, which is lower than the theoretical concentration of 1%. Low Tm concentration is known to induce long lifetimes of $^1G_4$ and $^3H_4$ excited states because of a reduced cross relaxation between Tm^{3+} ions.[16] In core particles, it is not noticeable because the emission arising from $^1G_4$ and $^3H_4$ are strongly quenched at the surface of the particle. However, in core/shell particles, the synergy of light trapping and low cross relaxation induces the very long observed lifetimes.

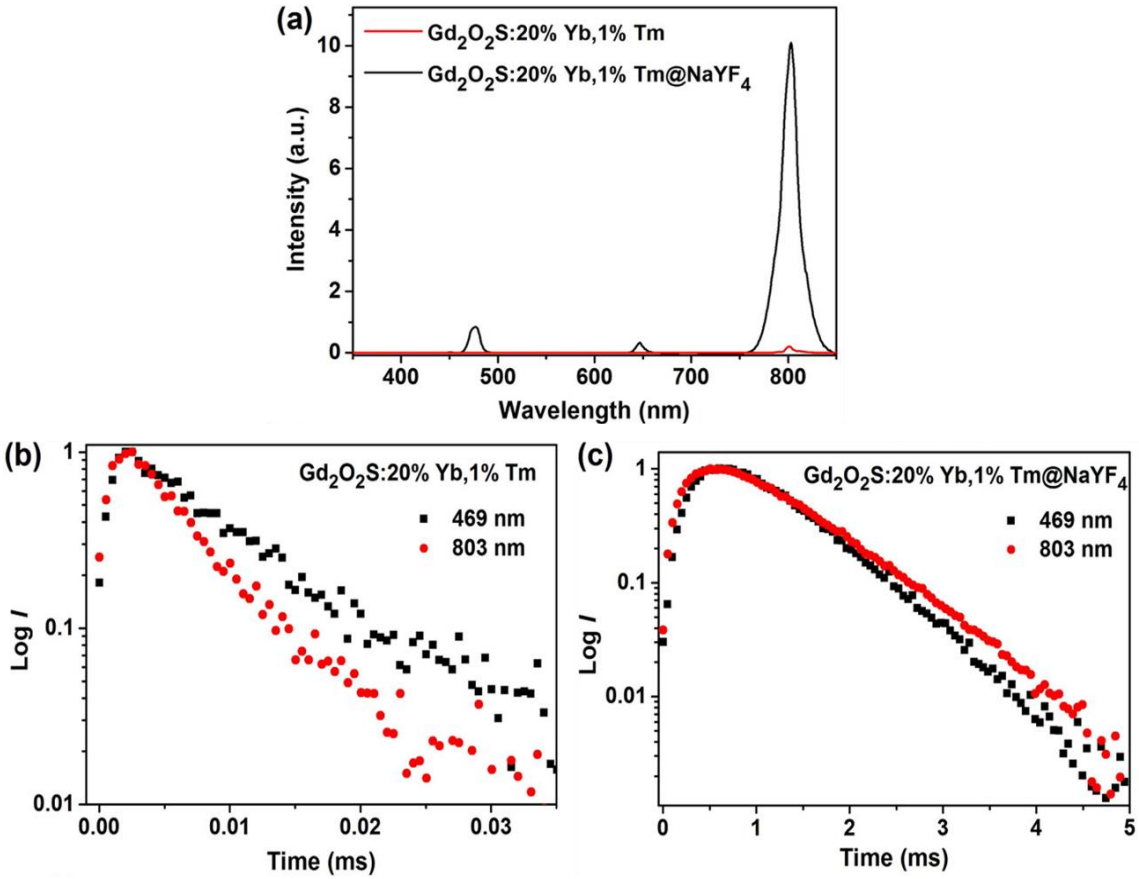

Figure 8. (a) UCL spectra of Gd_2O_2S:20%Yb,1%Tm 5 nm core-only and Gd_2O_2S:20%Yb,1%Tm@ β-$NaYF_4$ 9 nm core-shell UCNPs under 976 nm laser excitation. (b, c) UCL decays of core-only and core/shell UCNPs under ns pulse irradiation at 976 nm.

Concerning luminescence reabsorption, we consider that radiative reabsorption is mostly ineffective in lanthanide-based nanoparticles [17] because of the narrow absorption bands and low molar extinction coefficients of the majority of lanthanide acceptors.

This study shows a significant step toward bright sub-10 nm UCNPs by introducing a heterogenous core/shell structure. There is, however, the possibility of going even smaller. A reduction in the size of such a complex system allows for a reduced number of dopants ions and, consequently, a reduced number of interactions between them. As a result of simplifying a complex system, precise photodynamic phenomena are revealed among the dopant ions.

3.4 Photodynamic investigation in ultrasmall UNCPs (< 3 nm)

One can wonder if upconversion would still be observable for nanocrystals containing only one emitting activator ion. For an ultrasmall UCNP using a standard activator composition of 1% of all RE ions and a typical $NaREF_4$ unit-cell volume of 0.1 nm^3, such a one-emitter particle with a concentration of 20% Yb should have a diameter of less than 3 nm. It should be stressed here that a small variation in size can induce a large variation in sensitizer and activator concentrations, i.e., an increase of 0.5 nm will lead to 2 activators per UCNP and an increase of Yb concentration ratio. However, this drawback can be seen as an advantage in the study of cross relaxation processes. Indeed, for a single activator particle, cross-relaxation processes are eliminated while they can become predominant for few activators. Therefore, a great care should be taken at the control of particle mean diameter, and particle size distribution (PSD).

For $NaREF_4$, the synthesis, in organic solvents, is challenged by the possible transient presence of various inorganic phases: the two $NaREF_4$ polymorphs α and β, and possibly NaF. As predicted by the group of Haase, the narrowest β-phase PSD should therefore be found right after the α-phase has vanished [18]. By the using of a gadolinium-rich matrix [19-21], not only can this metal lead to the β-phase directly, but it also facilitates the formation of nanocrystals of less than 10 nm [22] over a large range of concentrations [23, 24].

To reach sub-3 nm UNCPs, temperature cycling variations of temperature during the crystallization, strategy was used by our colleagues.[25] Indeed, a fast warming up of a suspension of microcrystals induces the dissolution of the smallest ones, while subsequent fast cooling allows the remaining ones to grow from the supersaturated solution [26]. This approach has been identified to cause crystal coarsening in various media (from food processing [27] to geochemistry [28]), and has become a powerful tool to control the size and size-distribution of micro- to macrocrystals of proteins or pharmaceutical compounds [29-31]. However, temperature cycling is scarcely used for the preparation of nanocrystals. Noticeably, a related approach has been developed for the preparation of upconverting nanoparticles by Li et al.[32].

In this study, two steps structured our work. First, our colleagues showed that by using additional temperature cycles, it is possible to prepare highly monodisperse homogeneous, β-phase nanometric UCNPs with a limited number of one to few emitting ions but with a variable amount of sensitizers (< 3 nm). Therefore, the influence of the number of heating cycles on size and emission properties needs to be examined in order to determine how much it is possible to decrease the size of the particle while preserving the β-crystal phase that ensures proper emission properties. In this aim, steady state and time-resolved spectroscopy were employed to investigate the emission properties of these Tm^{3+}-based UCNPs as a function of the number of heating cycles used for the synthesis and compared to the crystal phase structure measured by XRD.

Second, we also addressed the influence of Yb concentration and particle coating with a shell of $NaGdF_4$ using steady state and time-resolved spectroscopy as shown in Figure 9. Moreover, impact of activator concentration on emission dynamics was tackled by exciting the particle either from sensitizer side at 976 nm or from direct excitation of the activator at 355 nm in order to understand the mechanisms of the energy transfers occurring in these sophisticated nanoparticles.

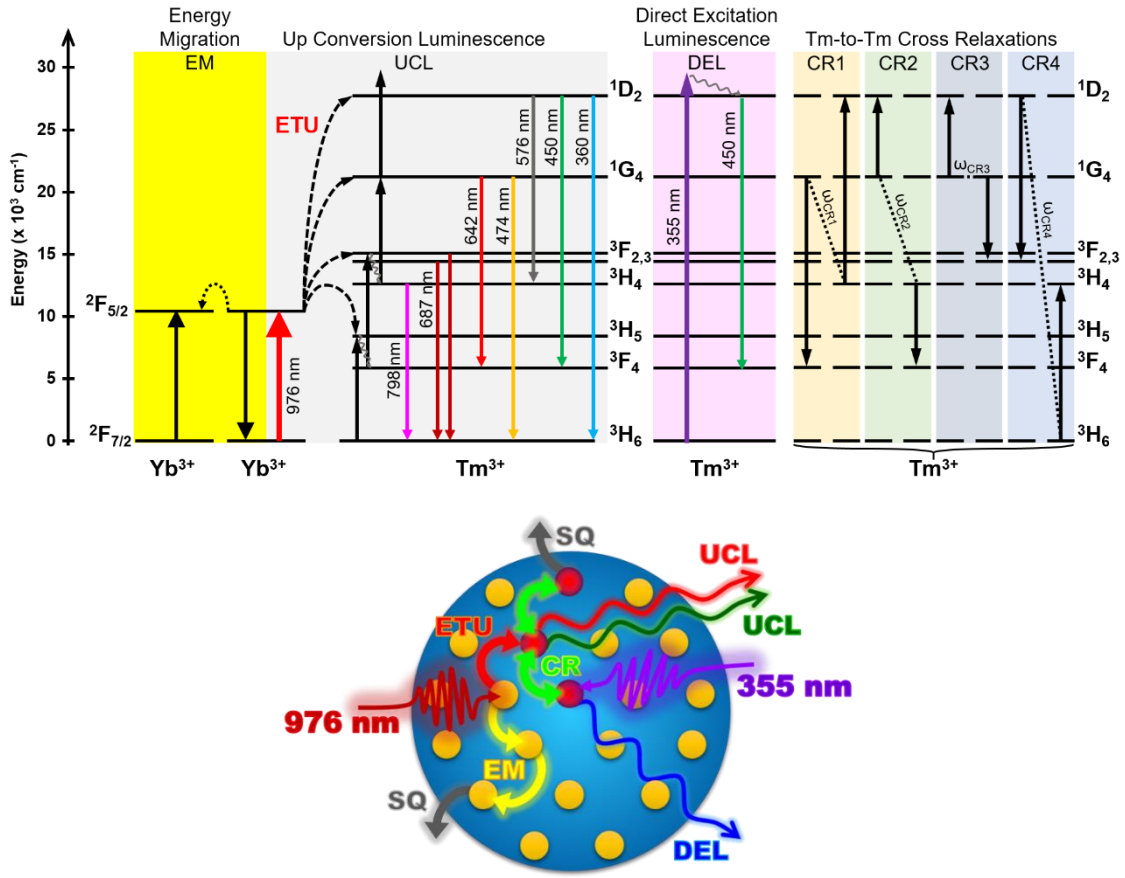

Figure 9. Most characteristic energy processes encountered within UCNPs upon NIR irradiation (UCL) or activator direct UV excitation (DEL).

3.4.1 First step: photophysical properties of ultra-small UCNPs in various temperature cycles

3.4.1.1 Absorbance measurements

As shown in Figure 10, Yb absorbance is broad due to the convolution of the different transitions in the 4f stark sub-levels [33]. To compare the emission spectra of different samples without having to worry about their concentration, we wanted to utilize these amounts for correction of emission spectra (which is mentioned in the following section). Our preference, however, was to compare them by their relative intensity due to the low signal, which was achieved by normalizing them at 798 nm as demonstrated in Figure 12.

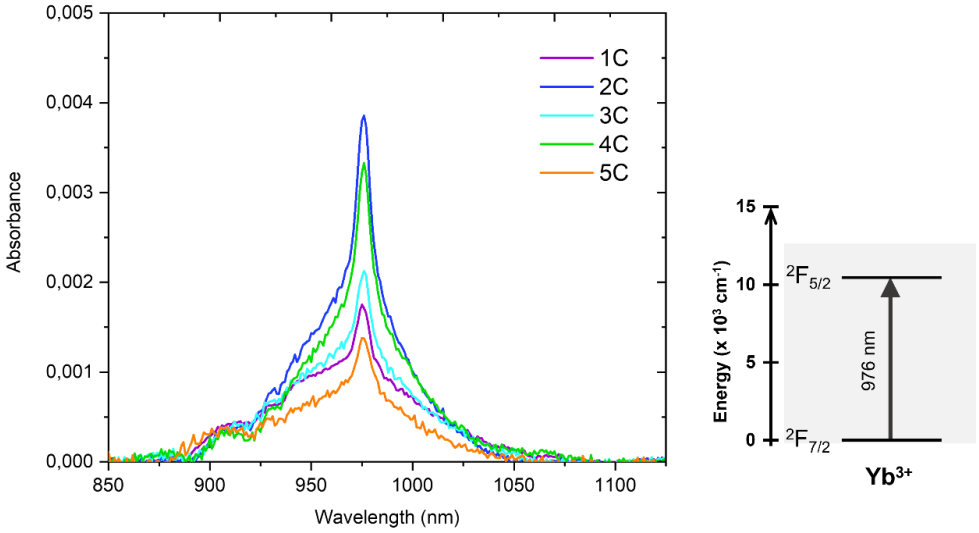

Figure 10. Absorption spectra of Yb^{3+} in UCNPs in cycled samples.

3.4.1.2 Steady state emission measurements

As shown in Figure 11, a microwave heating sequence composed of a number of cycles varying from 1 to 6 was performed for the synthesis of ultrasmall UCNPs. Such numbers were chosen in accordance with the apparatus limitations (30 min max in the range 280-300°C). The progress of the transformation was examined by TEM for the quality of the PSD, by XRD on powder (Figure 11) to monitor the onset of the hexagonal phase upon increasing the number of cycles, and by luminescence measurements on the as-prepared colloidal suspension after purification (Figure 12) to assess the relative evolution of each emission line (intensities and lifetimes). TEM analyses showed that the average diameter obtained was always smaller (between 2 and 3.5 nm) than for the original protocol [25] demonstrating the impact of the temperature cycling. However, while the PSD was found to remain extremely narrow (σ <0.65), the evolution of this average size with the number of cycles was found to be limited, therefore other criteria beside the morphological one had to be found to select the optimal number of cycles.

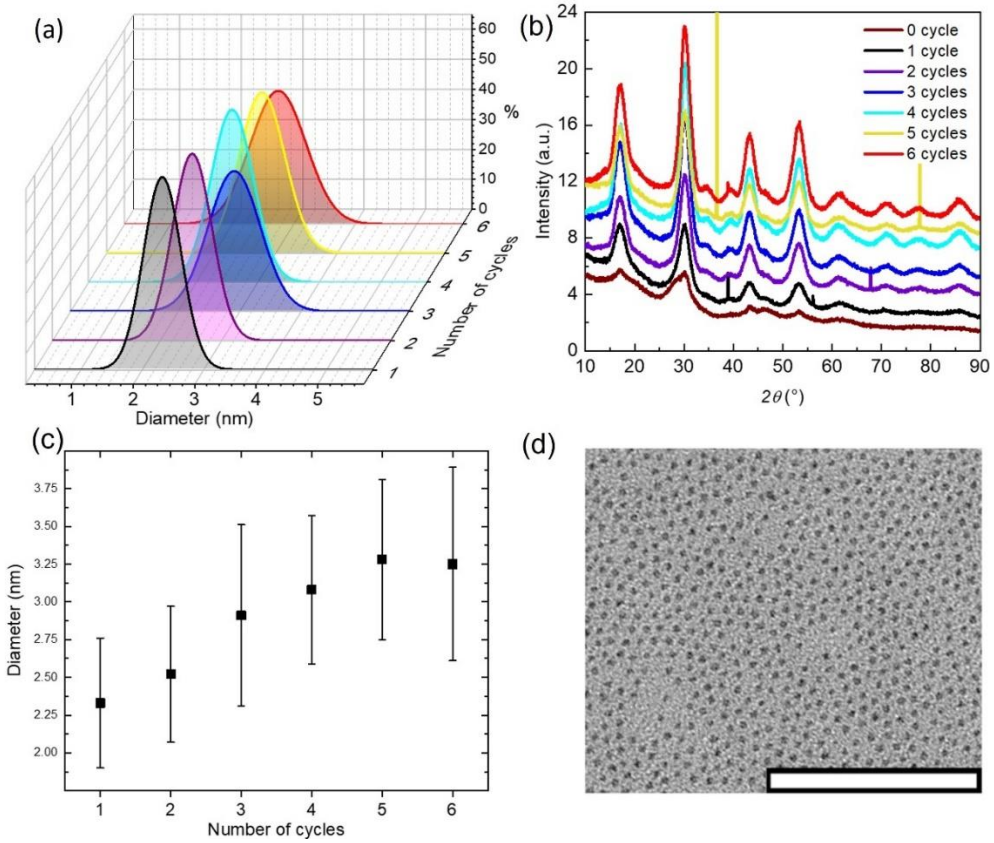

Figure 11. (A) and (B) PSD and XRD obtained for 6 cycles heating sequence.(C) Diameter (nm) and standard deviation of particles prepared with 1 to 6 heating steps. (D) Electron micrograph of the 6-cycle nanoparticles. The scale bar is 100 nm

First, we looked at the chemical homogeneity of the particles by XRD analyses (Figure 11b). No α/β crystalline material was detected in the reaction mixture prior to the starting of the heating cycles supporting the necessity of a high temperature step. After the first cycle, the hexagonal β polymorph was identified as the main component present along with a detectable amount of sodium fluoride. This composition rapidly simplified as the synthesis progressed and the analyzed particles were found to be composed of solely the β-phase as soon as for the 3rd cycle, the subsequent ripening implying thus only one polymorph.

The intrinsic sensibility of X-ray analysis (i.e. within 10%) limits the discussion on α-to-β phase transition. Thus, the steady state emission properties upon cw 976 irradiation of particles prepared with 1 to 5 microwave-heating cycles were monitored in order to investigate their changes along the synthesis steps (Figure 9). A detailed analysis shows that the four intensity ratios of the Tm^{3+} emission bands arising from the high energy states ($^1I_6 \rightarrow {}^3F_4$ (343 nm), $^1D_2 \rightarrow {}^3H_6$ (360 nm), $^1D_2 \rightarrow {}^3F_4$ (450 nm), $^1D_2 \rightarrow {}^3H_4$ (576

nm), i.e., absorption of 4 and 5 photons) to the red emission (798 nm) exhibit a plateau for 1 to 3 cycles particles before sharply increasing for particles obtained for cycles 4 and 5 (Figure 13). In other words, the presence of pure β-phase UCNP induces an increase of the contribution of the UV-emission bands to the steady state spectrum as previously reported for hexagonal NaYF4:Yb^{3+}/Tm^{3+} microcrystals in comparison to their cubic counterparts.[34] This is in line with the actual growth of the luminescent β-phase after the third heating cycle and the disappearance of the cubic phase suggested by XRD analysis.

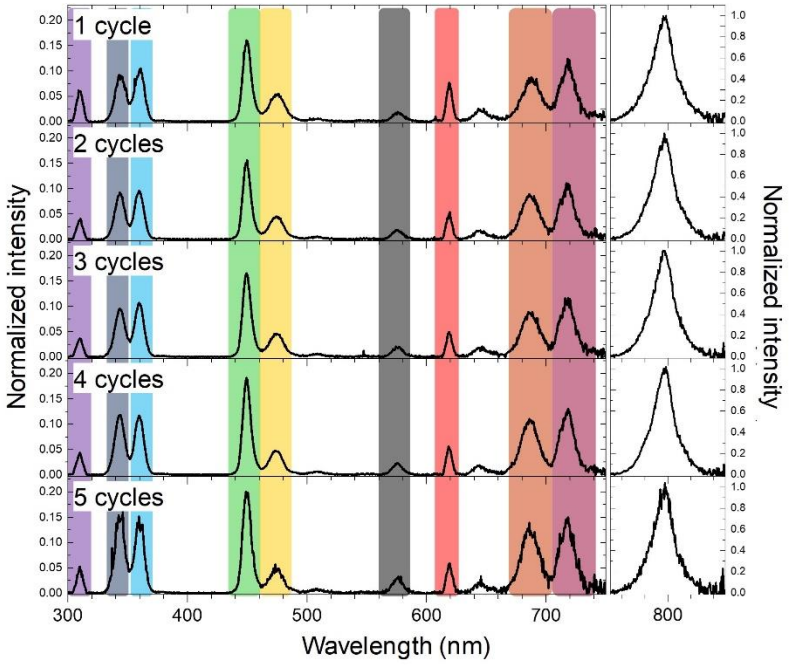

Figure 12. Steady state spectra for cycle particles ranging from 300 nm to 850 nm.

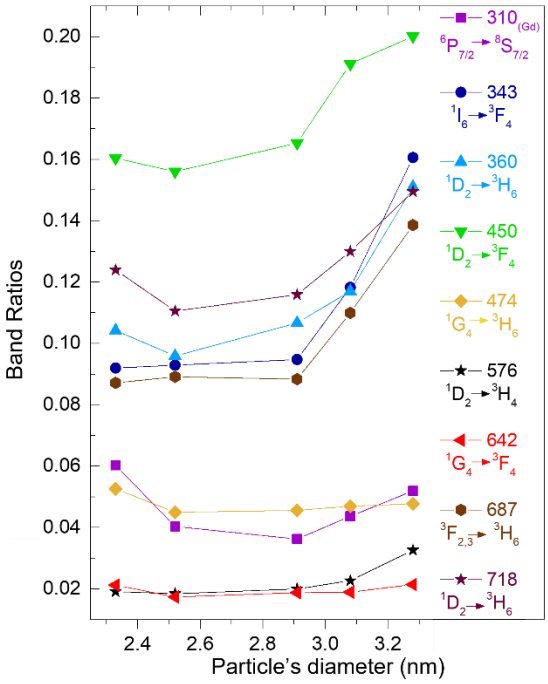

Figure 13. Band ratios calculated for each transition of the steady state spectra between 310 and 720 nm to the intensity of the 798 nm band. Changing intensity ratios after third cycle demonstrates the actual growth of the luminescent β-phase.

3.4.1.3 Time-resolved measurements of cycled particles

For a comprehensive study of energy transfer processes of cycled particles, decay parameters of UCNPs excited state were investigated with millisecond square pulse setup as demonstrated in Figure 3.

Luminescence decays at 798 nm of the particles prepared after 1 to 6 microwave heating cycles are shown in Figure 14. Emission amplitude-averaged lifetimes were calculated from the biexponential fit of the decay curve (3 to 5 ms):

$$\langle \tau \rangle_a = \frac{\sum_{i=1}^{2} \alpha_i \tau_i}{\sum_{i=1}^{2} \alpha_i} \qquad (3)$$

where α_i and τ_i are the pre-exponential factors and decay times of each exponential, respectively.

The analysis of amplitude-averaged lifetimes as a function of the number of heating cycles (Figure 14) clearly shows a threshold after cycle 2. The average lifetime ranges from 165 µs for cycle 1 to about 215 µs ± 12 µs for cycle 6 (Table 1). After cycle 2, the average lifetime increases linearly with the size. This result shows that the completion of the α-to-β phase transition is achieved already at the second heating cycle. After that

stage, the particle has reached a fully β-crystal phase and the lengthening of the lifetime with the increase of UCNP size is due to the decrease of the surface-to-volume ratio and thus to the decrease of the surface quenching. For demonstration the consistency among lifetimes and steady state results, steady state spectra of cycle particles were measured at 798 nm (purple square dots in Figure 14) by the fluorometer setup as shown in Figure 1 . This luminescence corresponds to the $^3H_4 \rightarrow {}^3H_6$ emissive state of Tm^{3+} that is populated through 2 energy transfers from Yb^{3+} to Tm^{3+} ($^3H_6 \rightarrow {}^3H_5$, non-radiative relaxation to $^3F_4$, $^3F_4 \rightarrow {}^3F_2$, non-radiative relaxation to $^3H_4$, Figure 12a). The weak luminescence observed after 1 cycle is appropriate in the line with their lifetimes which is due to the small size of the particle and the existence of α-phase. It seems that a threshold exists after cycle 2 and a strong increase is obtained from the third cycle; it then remains constant from 4 to 5 cycles. Such an enhancement of luminescence matches with the disappearance of the cubic phase observed by XRD (Figure 11b).

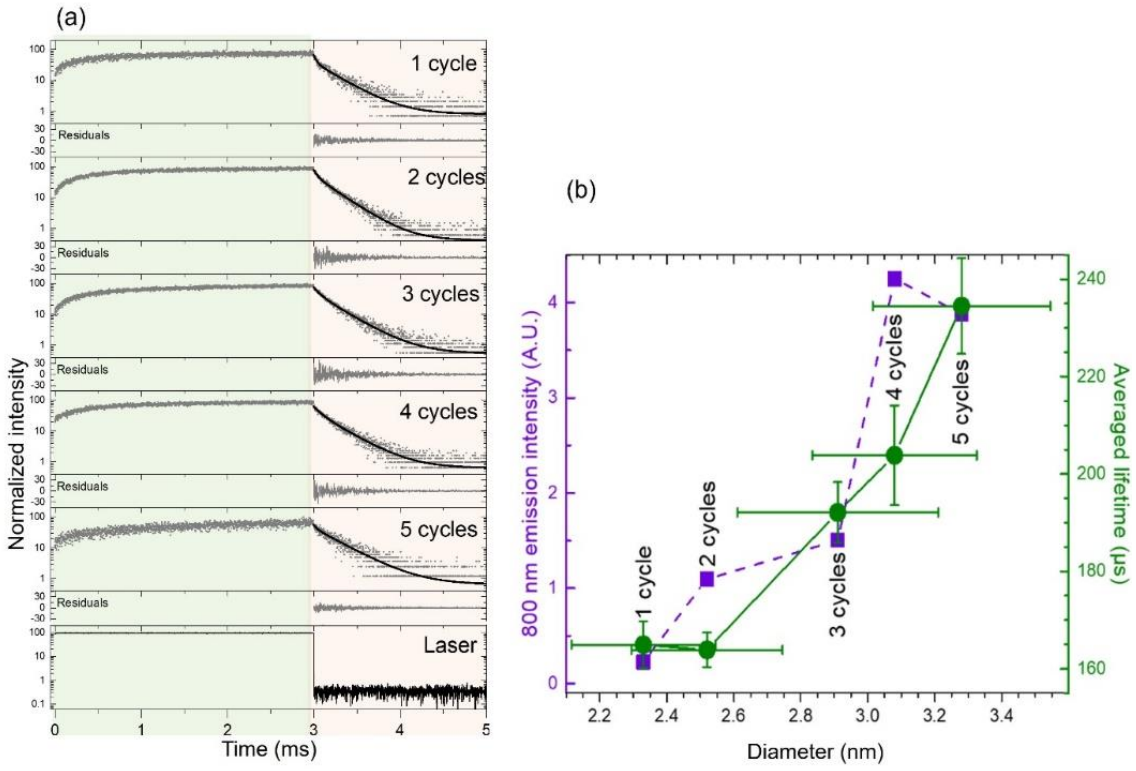

Figure 14. (a) Time-resolved 798 nm luminescence of the particles prepared after 1 to 6 microwave heating cycles and instrumental response function (IRF) measured with a 3 ms square pulse. (b) 798 nm steady state luminescence intensity of particles prepared after 1 to 6 microwave heating cycles (2.33 to 3.28 nm). Average lifetimes calculated from the amplitude weighted sum of the time constants obtained from biexponential fitting of the decays (3 to 5 ms). Decays are measured during the 2 ms that laser is off. Biexponential fitting curves of the decays along with residuals are also reported.

Table 1. Time constants (in µs) and their contributions (in %) obtained from biexponential fitting of the decays presented in A (3 to 5 ms) for five cycled particles. Intensity- ($\langle\tau\rangle_f$) and amplitude-averaged ($\langle\tau\rangle_a$) are also reported.

Number of cycles	Diameter nm	τ_1 (µs)	$\%\tau_1$	τ_2 (µs)	$\%\tau_2$	$\langle\tau\rangle_f$ (µs)	$\langle\tau\rangle_a$ (µs)
1	2.33	33.0 ± 2.9	41.8	259.8 ± 7.2	58.2	240.8 ± 5.8	164.9 ± 4.8
2	2.52	44.8 ± 2.8	35.8	230.2 ± 4.2	64.2	212.1 ± 3.7	163.9 ±3.5
3	2.91	70.1 ± 5.4	35.6	259.6 ± 7.0	64.4	235.0 ± 6.3	192.1 ± 6.2
4	3.08	78.0 ± 9.9	32.3	264.0 ± 10.6	67.7	241.0 ± 10.3	203.8 ± 10.3
6	3.25	117.5 ± 9.6	44.5	293.3 ± 15.0	78.9	250.5 ± 12.9	215.1 ± 12.4
5	3.28	38.8 ± 10.2	21.1	286.8 ± 9.5	55.5	278.1 ± 9.9	234.5 ± 9.8

The conclusion that can be drawn is that, by interpretation of steady state spectra and time-resolved luminescence data, it is possible to follow the phase transition from α to β in such ultra-small particles. Furthermore, these findings are significant enough to be used as a demonstration of how many cycles are needed to produce ultra-small and bright particles.

3.4.2 Second step: towards the determination of ultra-small UCNPs emissivity parameters

The successful synthesis of ca 3 nm luminescent UCNPs with 57% Yb encouraged us to carry on with our strategy. As it has been reported that a substantial variability of the average UCNPs diameter could be observed for a defined synthetic protocol, we simply repeated the above-mentionned synthesis of Na(Yb57%-Gd42%)F_4:Tm1% and Na(Yb20%-Gd79%)F_4:Tm1%. While the PSD remained constant thanks to our new heating method, we could achieve the preparation of ultrasmall UCNPs ranging from 3.86 nm down to 2.36 nm diameter, the target size for single Tm UCNPs. Importantly, the observed narrow size distribution translates into a rather limited range of activator ions per particles. We applied a Poisson distribution description in order to describe the dispersal of thulium among all the particles. Experimentally, the PSD, suitably binned, gives the frequencies of sizes $\{f_i\}$. For a given size i, the parameter of the distribution is

the average number of thulium ions per particle N_i. In a given batch, the proportion of particles containing one thulium independently of their size is the sum over all i of the probability of finding one Tm for a given size i weighted by the i-particle frequency f_i :

$$P(Tm = k) = \sum_{i=0}^{\infty} f_i \frac{1}{k!} (N_i)^k e^{-N_i} \qquad (4)$$

Table 2. Composition, size, and Poisson distributions of the number of Tm ions per particles in the two prepared core particles with 57 and 20% of Yb sensitizer.

	%Gd	%Yb	%Tm	diameter {Å}	Average number Yb/NP	Average number Tm/NP	0 Tm / NP	1 Tm / NP	2 Tm / NP	> 2 Tm / NP
$Na(Yb_{20\%}Gd_{79\%})F_4:Tm_{1\%}$	75.5%	23.1%	1.4%	23.6	21.0	1.2	33%	27%	18%	22%
$Na(Yb_{57\%}Gd_{42\%})F_4:Tm_{1\%}$	40.6%	58.3%	1.1%	28.4	94.6	1.8	19%	27%	23%	31%

Results show that the relative proportions of particles according to their Tm content of the two batches of ultrasmall particles (20% or 57% of Yb) are almost identical (Table 2). Furthermore, they are very close to the ideal "one-emitter particle" distribution that comprises 1/e = 37% of "empty" (activator free) and one-activator particles, $1/e^2$ (ca 18%) of two-activator particles, etc... Consequently, these two batches can be considered as the first example of 1-Tm UCNPs, differing only by their Yb content.

Core-shell nanoparticles were further prepared by growing a photophysically inert shell of $NaGdF_4$ onto the previously prepared 20% Yb^{3+} and 57% Yb^{3+} cores. The protocol described for a $NaYF_4$ shell by Zhai et al has been adapted,[35] and rare earth oleate in association with sodium trifluoroacetate as sole source of sodium and fluoride have been used. This procedure applied to the 2.4 (20%Yb) and 2.8 (57%Yb) nm ultrasmall cores previously described, lead to monodisperse particles of 5.8 nm. Powder XRD confirm the β-phase nature of the NP's material and the crystallite size. ICP-OES analyses confirmed the successful incorporation of the shell material, as the final Yb or Tm/Gd ratio are close to the expected one. However, simple application of the final RE atomic concentrations to the resulting objects indicated that none of the obtained core-shell particles could derive from a single core (Table 2). Two limits scenari can be proposed: (i) A complete core dissolution followed by the crystallization of core + shell material leading to particles

with a homogeneous repartition of all the RE throughout the crystal, (ii) the deposition of a shell onto sintered core particles, thus leading to "core-shell" architecture. Table 3 summarizes important parameters that are numbers of Tm per nanoparticle (rounded to the main population using Poisson distribution, Table A3.1), numbers of Yb per nanoparticle (rounded to the nearest tens unit), surface to volume ratios and average inter-ions distances evaluated using the formula proposed by Eva Goldys et al.[36] 4 ultrasmall UNCPs: core C_1^{20} and C_1^{90}, core-shell CS_8^{120} and CS_7^{400} were obtained. Furthermore, larger (7.3 nm) 20% Yb^{3+} particles (C20-7.5) C_{34}^{570}(std) were also obtained by using standard procedure method reported by the team of Wang[37] as a standard particle for comparison purposes.

Table 3. Size, number of Yb^{3+} and Tm^{3+} ions and inter-ions distances in core (C) and core-shell (CS) particles with 20% or 57% Yb doping. * Standard procedure

	C20	**C57**	**CS20**	**CS57**	**C20***
%Gd	75.53%	40.58%	90.37%	69.81%	77.50%
%Yb	23.12%	58.31%	9.03%	29.64%	21.21%
%Tm	1.35%	1.11%	0.60%	0.55%	1.29%
diameter {Å}	23.56	28.35	57.72	57.68	72.55
radius {Å}	11.78	14.18	28.86	28.84	36.28
Surface {$Å^2$}	1744	2526	10469	10453	16536
Volume {$Å^3$}	6847	11939	100727	100490	199945
S/V	0.255	0.212	0.104	0.104	0.083
Average number RE/NP	90.8	162.3	1332.3	1344.3	2665.6
Average number Gd/NP	68.6	65.9	1204.0	938.4	2065.8
Average number Yb/NP	21.0	94.6	120.3	398.4	565.4
Average number Tm/NP	1.2	1.8	8.0	7.4	34.4
d(Yb-Tm) (Å)	6.35	4.69	8.68	5.91	6.52
d(Yb-Yb) (Å)	6.48	4.72	8.87	5.94	6.65
d(Tm-Tm) (Å)	16.69	17.67	21.89	22.45	16.92
Notation	C_1^{20}	C_1^{90}	CS_8^{120}	CS_7^{400}	$C_{34}^{570}(std)$

It should be stressed that even if the majority of the population of C_1^{20} and C_1^{90} has only one Tm per nanoparticle, 40% of nanoparticles have more than one Tm for C_1^{20} and 54%

for C_1^{90}. Number of CR processes will be minimized for C_1^{20} but not zero. Similarly, to core ultrasmall UCNPs, the Poisson statistics for core-shell CS_8^{120} and CS_7^{400} (Table A3.1) shows that the percentage of particles with 6 to 9 Tm/NP are same and about 9% for each. So, the number of Tm/NP should be considered similar in the following dynamics study. To get better knowledge on the emission dynamics of the ultrasmall core and small core UCNPs (Figure 15), different irradiation and excitation schemes were considered (Figure 9) to unmix the different parameters that control up-conversion emission, i.e. EM and ETU from Yb, CR between Tm and SQ.

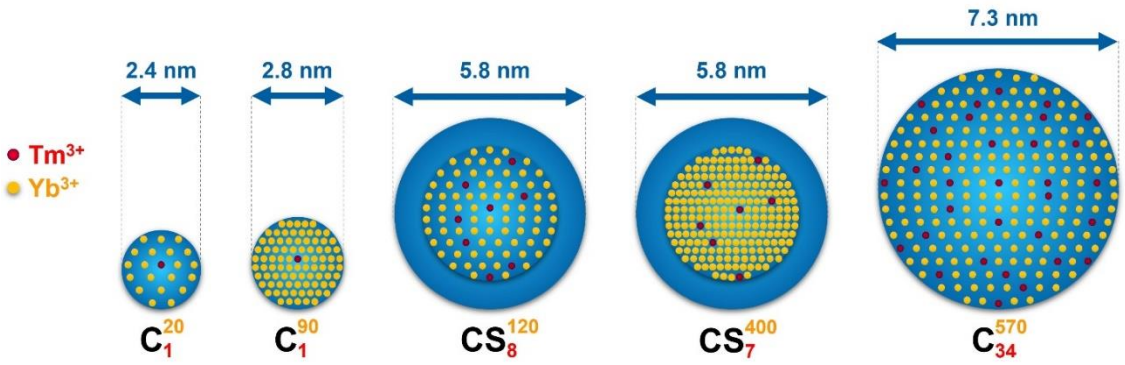

Figure 15. Schematic representation of different UCNPs which used for determination of emissivity parameters. In this figure core and core-shell particles (C and CS) demonstrated with C_x^y (or CS_x^y) which x and y represent number of Tm^{3+} and Yb^{3+} ions, respectively.

3.4.2.1 Absorbance measurements

As shown in Figure 16, the absorbance of these particles was measured as same as cycled particles. In this aim, we used double beam Cary 3500 absorption spectrometer (spectral bandwidth of 1 nm and one point every 1 nm) to scan from 1100 nm until 800 nm in order to measure Yb^{3+} absorbance spectrum.

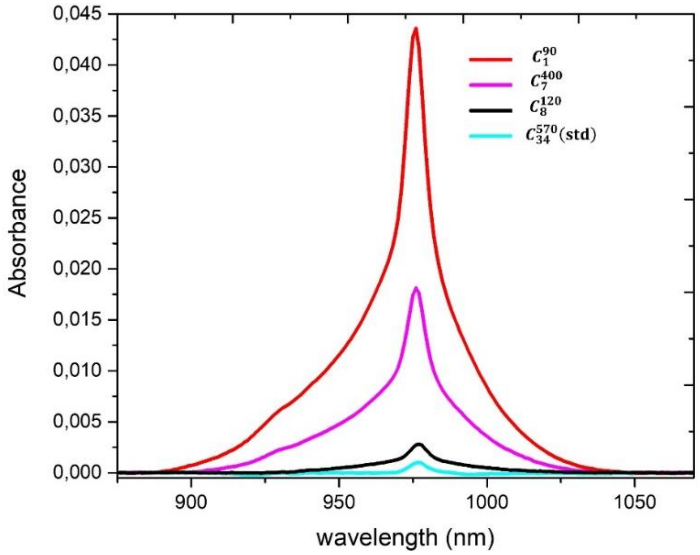

Figure 16. Representing the absorption spectra of Yb^{3+} in UCNPs in ultra-small samples.

3.4.2.2 Steady state emission measurements of ultra-small UCNPs

The first photophysical investigations of the nanometric core UCNPs C_1^{20} and C_1^{90} (C_1^{20}: 2.4 nm and C_1^{90}: 2.8 nm) and their core-shell analogues (CS_8^{120} and CS_7^{400}: 5.5 nm) were performed under steady state conditions using 976 nm irradiation using the same setup as before (Figure 1). Emission spectra between 300 nm and 850 nm are shown in Figure 17 (normalized on the 798 nm band). Despite their small size and number of emitters, all the studied particles displayed the usual Tm^{3+} emission bands between 345 and 800 nm. As illustrated in Table 4, these emissions were used to qualitatively address the effect of the modification of the NPs architecture, i.e., the Yb^{3+} concentration and shell, on the contributions of the different emission bands to the total integrated emission signal. For measuring this contribution, the below equation has been used:

$$\% \text{ of contribution of a band (X1)} = \frac{X1}{\sum X} \times 100 \qquad (5)$$

where the X1 is the area of the considered band and ∑X is the summation of all emission bands.

Emission spectra between 300 nm and 850 nm are shown in Figure 17 (normalized on the 798 nm band). Despite their small size and number of emitters, all the studied particles displayed the usual Tm^{3+} emission bands between 345 and 800 nm. The contributions of the different emission bands to the total integrated emission signal (Table 4) allow to qualitatively address the effect of the modification of the NPs architecture, i.e., the

number of Tm^{3+} vs Yb^{3+} and existence of shell. For C_1^{20} and C_1^{90} core particles, the number of Yb^{3+} sensitizers have a significant impact on the relative spectral distribution of the recorded emission. Thus, an increase of the Yb^{3+} content from 20% to 57% led to a relative increase (13%) of the contribution of the 798 nm emission from $^3H_4$ state (2 ETU) while the contributions of the visible emissions at 450 nm and 474 nm from the $^1D_2$ (4 ETU) and $^1G_4$ states (3 ETU) were reduced by a factor 2 and 3.5, respectively (Table 4). Likewise, these trends were also observed for core-shell particles as the contribution of the 798 nm emission band to the 300 – 850 nm emission was further enhanced by 20% for CS_7^{400} compared to CS_8^{120} and the 474 nm band decreased by a factor 4.7 for CS_7^{400}. We attribute this result to the enhancement of the energy migration in the Yb^{3+} sub-lattice in the 57% Yb^{3+} particles due to higher sensitizer content. It results in an enhanced surface quenching as the migration of the absorbed energy to the particle surface is favored and the possibility of its transfer to Tm3+ ions is reduced, impeding the ETU process. $^1D_2$ and $^1G_4$ states (emission at 450 and 474 nm emission), which are populated by 4 ETU and 3 ETU, have a lower contribution than the $^3H_4$ state emission (emission at 798 nm, 2 ETU) to the steady state emission upon 976 nm irradiation for 57% UCNP in comparison the one with 20% sensitizer.

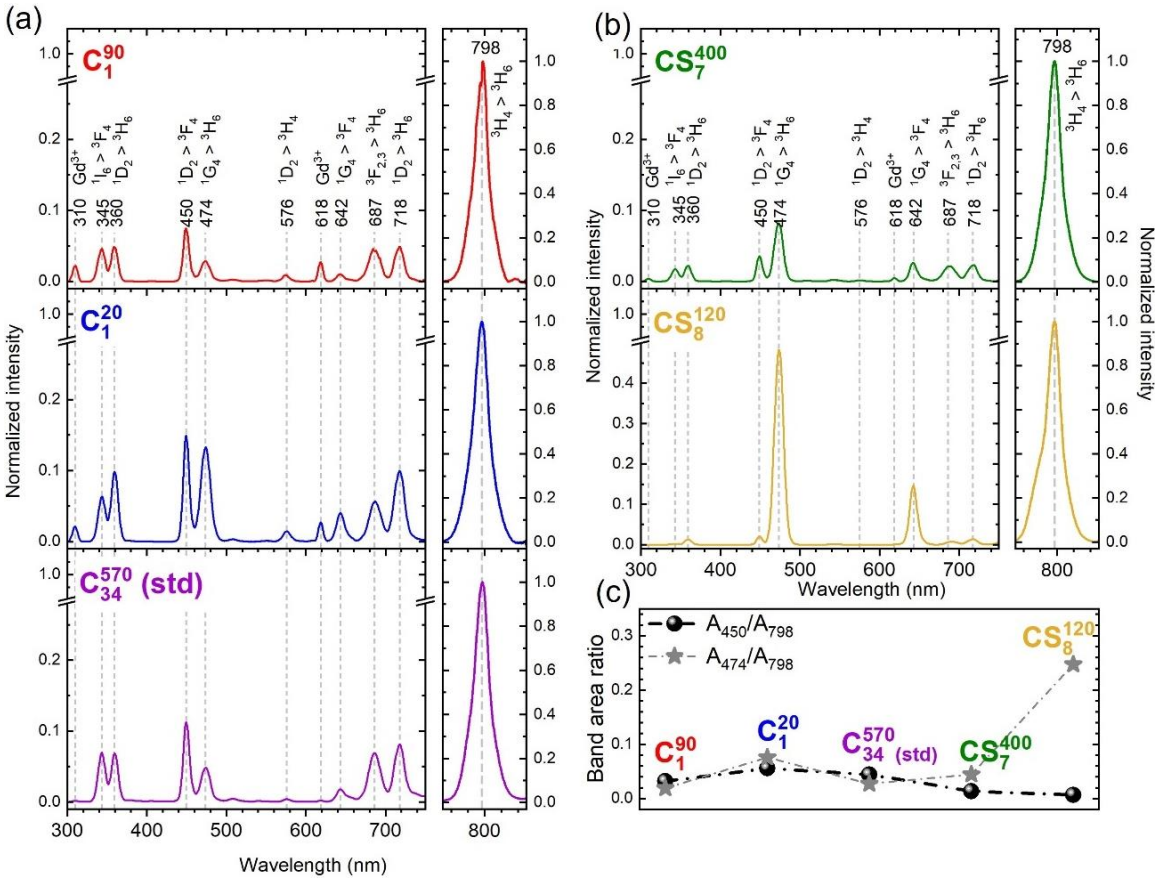

Figure 17. Steady state spectra of core particles (a) and core-shell particles (b) upon cw 976 nm irradiation (6.85 kW/cm²). Spectra are normalized on the 798 nm band. (c) Band area ratio for the different nanoparticles.

Then, as observed by many other research groups,[12] the presence of a surface protecting shell reduces SQ processes and increases the probability of ETU, i.e. the population of excited Tm increases. The alleviation of surface quenching could also be thought partly due to the increase in size from ≈ 2.6 nm diameter for the core UCNPs to 5.8 nm for the core-shell one. However, this would also be the case for the 7.3 nm C_{34}^{570} (std) while its emission is similar to the core one. In fact, the shell induces significant differences for the different emission band compared to the parent core UCNP. The comparison of C_1^{20} and CS_8^{120}indicates that the contribution of the emission bands at 360, 450 and 718 nm arising from the $^1D_2$ state considerably decreases upon surface shielding whereas the contribution of the bands at 474 and 642 nm originating from the $^1G_4$ energy level is significantly enhanced. The decrease of $^1D_2$ state emission for CS_8^{120} and CS_7^{400} can be assigned to the existence of CR4 (Scheme 1, cross relaxation between a Tm^{3+} ion excited and one in the ground state). For the 7.3 nmC_{34}^{570} (std) core nanoparticles, the low contribution of all visible emission band can be explained, as we used high power

irradiation (6.85 kW/cm^2), by the number of excited Tm which favour the existence of different CRs (Figure 9A, CR1-3), and lead to a migration onto the surface (Figure 17b) and surface quenching of excited Tm.

Table 4. Contributions of the different emission bands to total emitted signal (Eq. 5).

		C_1^{90} (C57) (2.4 nm)		**C_1^{20} (C20) (2.8 nm)**		**CS_7^{390} (CS57) (5.8 nm)**		**C_8^{120} (CS20) (5.8 nm)**	
State	Center	Integrated range	%	Integrated range	%	Integrated range	%	Integrated range	%
$^1I_6$	**345**	328-351	1.88	328-351	2.03	328-351	0.67	328-351	0.068
$^1D_2$	**360**	351-374	1.91	351-374	3.03	351-374	0.82	351-374	0.37
$^1D_2$	**450**	428-461	2.67	428-461	4.14	434-457	1.24	434-457	0.51
$^1G_4$	**474**	461-494	1.61	461-494	5.64	457-498	3.97	457-498	18.46
$^1G_4$	**642**	629-663	0.56	628-664	1.59	627-665	1.21	616-671	4.92
$^3F_{2,3}$	**687**	663-703	3.14	664-702	2.99	665-704	1.49	671-704	0.36
$^1D_2$	**718**	703-746	2.75	702-746	4.78	704-746	1.28	704-736	0.57
$^3H_4$	**798**	746-830	83.79	746-830	74.33	746-830	88.94	746-830	74.62

3.4.2.3 Time-resolved measurements of ultra-small UCNPs

More details on the dynamics of the different states are obtained measuring the response of UCNPs upon 976 nm nanosecond pulse (Figure 18). Measured emission are the ones originating from $^1D_2$ (4 ETU, 450 nm), $^1G_4$ (3ETU, 475 nm) and $^3H_4$ (2 ETU, 798 nm) states. There are two regimes: (i) the growing of the signal due to the building of the state through ETU until the disappearance of excited Yb^{3+} and (ii) a multi-exponential decay illustrating the complex interconversion and CR between the different Tm states. As previously mentioned for cw irradiation, reducing the Yb^{3+} content in the core results in a slower energy migration from the core to the surface through the sensitizer lattice and induces an attenuation of the surface quenching.[38] This is seen for all three transitions

by the increase of the growing time (few microseconds from C_1^{20} to C_1^{90}core nanoparticles until a hundred of microseconds from CS_8^{120} to CS_7^{400} core-shell ones) as well as the increase of the average decay times. In the core-only particles C_1^{20} and C_1^{90}, the decay time of the 474 nm emission increases by a factor of four when the concentration is lowered to 20% and the 450 nm transition is enhanced by a factor close to three. This trend is also noticed in a less pronounced manner for the corresponding core-shell particles (Table 5). As observed and detailed in the steady state luminescence studies, the shelling of the core particle caused considerable changes in the emission properties. In particular, the lifetimes were increased compared to the core particles independently of Yb^{3+} content (Table 5). Thus, the lifetimes of the 450 nm and 475 nm emission bands of the UCNP doped with 20% Yb^{3+} increased by about 50% for the core-shell architecture. An even more pronounced effect was found for the UCNP containing 57% Yb^{3+} for which the lifetimes of the different transitions were extended by a factor of two for the 450 nm emission and a factor of four for the 475 nm and 798 nm emission bands.

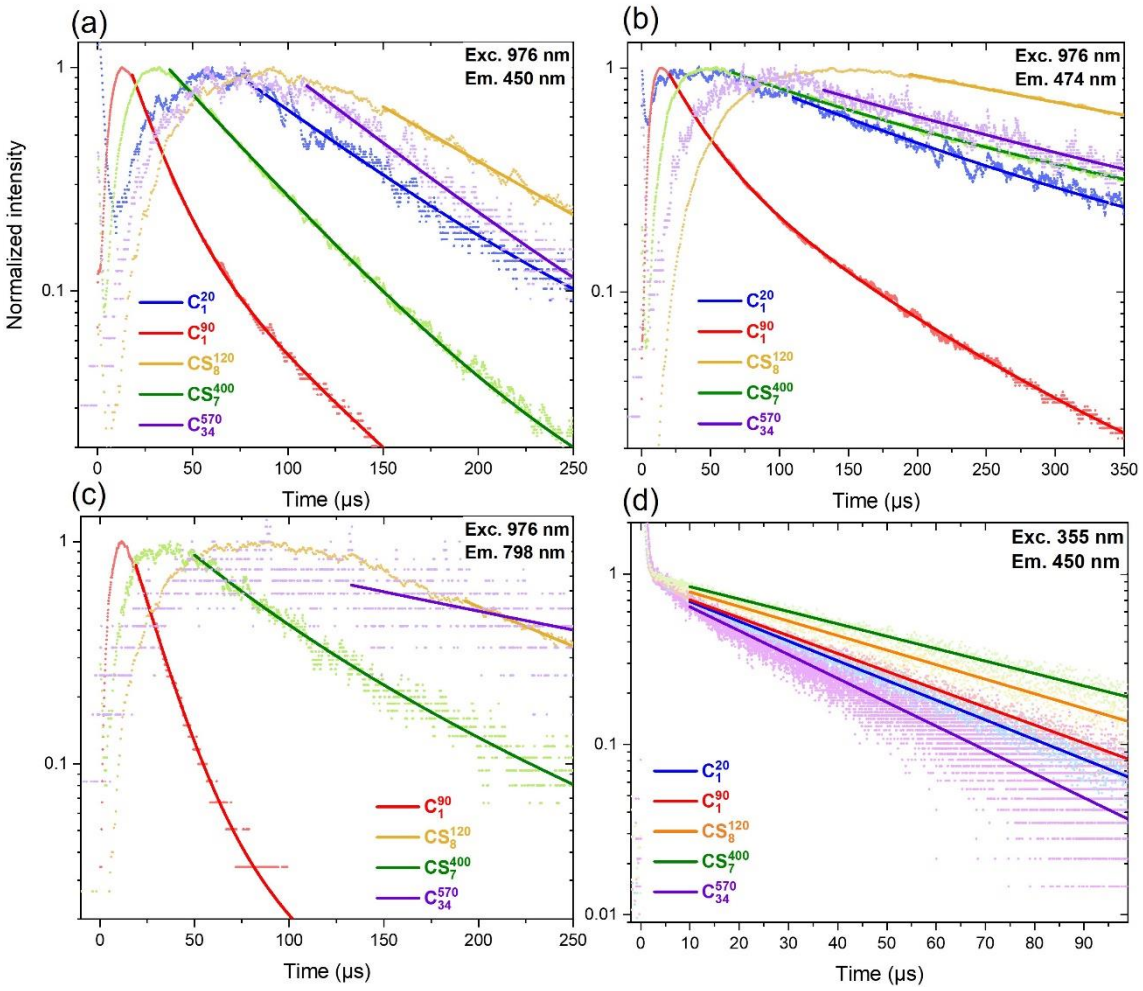

Figure 18: Time-resolved emissions at 450 and 474 nm with nanosecond laser excitation at 976 nm (A and B, respectively) and at 355 nm (C). Bold line is the respective results for bi-exponential fit (A, B) and mono-exponential fit (C). The first short decay observed in panel C is due to laser scattering

The decay time of the $^1D_2 \rightarrow {}^3F_4$ emission at 450 nm is shorter than that of the $^3H_4 \rightarrow {}^3H_6$ emission at 798 nm for particles with high amount of Tm. Indeed, in this case the $^1D_2$ state is likely strongly quenched by CR4 cross-relaxation (Figure 19). For particle with 1 or 2 Tm in average (C_1^{20} and C_1^{90}), Tm^{3+}-to-Tm^{3+} CR4 is unlikely and the 450 nm emission is thus much less diminished than in the other particles of this series which contain in average more Tm^{3+} activators per particle, increasing the likelihood for CR to occur. Moreover, the decay time of the 450 nm emission for the 7.3 diameter core particle C_{34}^{570}(std) ($\langle\tau\rangle_{a,450}$ = 66.3 ± 0.3 µs) is slightly shorter than the lifetime obtained for the ultrasmall 2.4 core particle C_1^{20} ($\langle\tau\rangle_{a,450}$ = 70.1 ± 0.3 µs). This value could be surprising taking solely into account the lower surface-to-volume ratio (Table 5) and thereby the impact of surface quenching. However, the opposite effect is observed, suggesting that

CR is much more likely to occur in the 7.3 nm particles containing 34 Tm^{3+}/particle. Moreover, it also shows that with the excitation power used, only few Tm are excited within one UCNPs and solely CR4 is observed because other CR would increase the lifetime of $^1D_2$ sate (Figure 9a). This is also in line with the increase of lifetime at 798 nm for $^3H_4$ state as CR4 is leading to an increase of $^3H_4$ state (Figure 19). Thus, to conclude, up conversion luminescence for ultrasmall particle size, which implies a low number of activator ions, reduces the probability of CR and its emission is mainly controlled by energy migration of excited Yb and its surface quenching. Furthermore, analysis of $^1D_2$ state emission will be done using direct exaction as $^1D_2$ is a good descriptor to analyse the competition between the different energy transfer processes (ETU, EM) and CR. All pre-exponential factors and times for mono- and bi-exponential fitting are listed in Table A3.2- A3.6.

Table 5. Amplitude-averaged luminescence decay times of core (C) and core-shell (CS) particles with 20% or 57% Yb^{3+} doping. Non radiative decay rate k_{nr} has been estimated using the decay times measured in this work and the radiative decay time reported in Villanueva-Delgado et al for a 0.01% Tm^{3+} β-$NaYF_4$ glass [39]. $\langle\tau\rangle_{(a,798)}$ could not be determined for C20 because of the very poor experimental signal-to-noise ratio

	Exc. @ 976 nm			Exc. @ 355 nm	
	$\langle\tau\rangle_{a,450}$	$\langle\tau\rangle_{a,474}$ (μs)	$\langle\tau\rangle_{a,798}$	τ_{450} (μs)	k_{nr} x10^3 s^{-1}
C_1^{20}	70.1 ±0.3	261.4 ±10.7	*	37.6±0.1	11.8
C_2^{90}	24.5 ±0.1	65.5±12.9	18.2±1.4	41.4±0.1	9.3
C_8^{120}	101.4±18.9	400.3±2.7	131.5±21.	50.9±0.3	4.8
CS_7^{390}	49.9 ±2.5	287.3±0.9	74.9±2.8	59.7±0.2	1.9
C_{33}^{550}	66.3 ±0.3	309.3±51.6	220.3±3.5	31.0±0.1	17.4

Afterwards, we used direct excitation for measuring intrinsic lifetimes of Tm^{3+} ions independent of Yb^{3+} ions in order to uncover the interactions among Tm^{3+} ions. While up conversion excitation is characterized by a growing and a multi-exponential decay, emission dynamics of $^1D_2$ state upon 355 nm nanosecond excitation is characterized by a mono-exponential (Figure 18d), time constants are provided in Table 5. As mentioned above, CR processes can be further clarified by directly probing the $^1D_2$ state of Tm^{3+} by excitation of Tm^{3+} at 355 nm (Figure 19a), indeed the dynamics does not involve ETU

processes and excited Yb^{3+}. From the Diecke diagram (Figure 9a),[16, 39] a general kinetic equation for the decay of the population of the $^1D_2$ state can be derived, neglecting Tm^{3+}-to-Yb^{3+} back energy transfer (this assumption is justified as the increase of number of Yb does not imply a decrease of lifetime, Table 5):

$$\frac{dN_4}{dt} = -\left(k_{4,r} + k_{4,SQ} + \omega_{CR4}N_0\right)N_4 + \left(\omega_{CR1}N_2 + \omega_{CR2}N_2 + \omega_{CR3}N_3\right)N_3 \qquad (6)$$

where N_0 is the number of Tm^{3+} in the $^3H_6$ ground state and N_2, N_3 and N_4 are the number of Tm^{3+} in the $^3H_4$, $^1G_4$ and $^1D_2$ excited states, respectively; $k_{(4,r)}$ is the global first-order depopulation rate of $^1D_2$ state including the radiative processes and the non-radiative relaxation except surface quenching. This equals the decay rate constant for an isolated Tm^{3+} ion in a bulk material. $k_{(4,SQ)}$ is the non-radiative depopulation rate due to surface quenching and ω_{CRi} represent the CR energy transfer coefficients between two Tm^{3+} ions (Figure 9a).

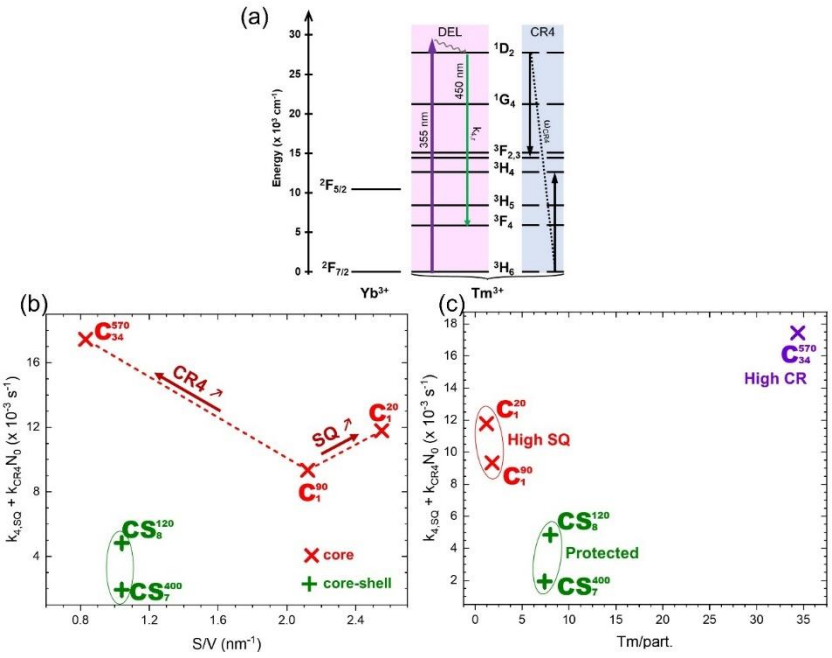

Figure 19. (a) Energy level diagram of NaGdF4:Yb^{3+}:Tm^{3+} UCNPs highlighting the transitions explored or 355 nm (Tm^{3+} direct excitation, DE) light and CR4 process involving excited $^1D_2$ state (Tm#1) and ground $^3H_4$ state (Tm#2). (b, c) Estimated non radiative rate constants of core (red) and core-shell (blue) particles plotted as a function of surface to volume ratio (b) or as function of number of Tm per nanoparticle (c).

After direct $^1D_2$ excitation, the $^3H_4$ and $^1G_4$ states are most likely not populated, because of the low number of Tm^{3+} per particle (<40) and regarding the low absorption cross-section of Tm^{3+}. Therefore, the CR1, CR2 and CR3 processes are not operative (Figure

19a). This reduces equation 6 to its first term leading to a time constant as described by equation 7:

$$\tau = \frac{1}{k_{4,r}+k_{4,SQ}+\omega_{CR4}N_0} \qquad (7)$$

For the core particles C_1^{20} and C_1^{90}, the radiative time constant τ_{450} is slightly shorter for C_1^{20} (τ_{450} = 37.6 µs) than for C_1^{90} (τ_{450} = 41.4 µs) while both nanoparticles contain similar Tm^{3+} per particle. Considering that CR4 has very little chance to happen in both particles that contain less than 2 Tm^{3+}/NP, this result is thus assigned to the larger size of C_1^{90}, revealing a surface to volume ratio of 2.1 nm^{-1} where surface quenching is slightly less severe than in C_1^{20} with a surface to volume ratio of 2.6 nm^{-1}. As $k_{(4,r)}$ presents the decay rate of the $^1D_2$ state in the absence of CR and surface quenching, its value can be approximated to the known $^1D_2$ decay time measured for a 0.01% Tm^{3+} β-$NaYF_4$ glass at 450 nm ($k_{(4,r)} = 1/\tau = 14.8 \times 10^3\ s^{-1}$).[39] This allows unmixing the contributions of surface quenching and cross-relaxation from the experimental rate constant of the global processes defined as $k_{(4,SQ)} + \omega_{CR4}N_0 = 1/\tau$ -14.8 10^3 (Table 5, Figure 19C). In particular, the lifetime measured for the core particles, for which CR4 is unlikely, leads to an estimation of the surface quenching rate constant of 11.3 × 10^3 s^{-1} for particles with an average diameter of 2.4 nm and 9.3 × 10^3 s^{-1} for 2.8 nm average diameter particles. The interplay between CR and surface quenching is illustrated by comparing the 450 nm time-resolved emission of the larger 20%Yb^{3+} 7.3 nm core particle C_{34}^{570} (std) and its ultrasmall counterparts C_1^{20} and C_1^{90}. Despite a lower surface-to-volume ratio (Figure 19B), the lifetime of this large particle is shorter (31.0 µs ≈ 40 µs) and the calculated $k_{4,nr}$ value is found to be the largest one between the 5 UNCPs (17.4 103 s^{-1}, Table 5 and Figure 18d). This illustrates the importance of CR4 in the quenching of the 450 nm Tm^{3+} emission.

For the core/shell particles, the lifetimes were always longer for the CS particles than for the parent core ones, that revealed the lowest k4,nr values of 4.8 103 s^{-1} and 1.9 10^3 s^{-1} for CS_8^{120} and CS_7^{400}, respectively. As the number of Tm/NP is quite similar the different non radiative rate constant can only be explained by a different structure as mentioned in the synthesis section. CS_7^{400} is more likely a core-shell nanoparticles with a protective layer while for CS_8^{120} an intermixing of core and shell should be involved to explain the difference in lifetime

3.5 Conclusion

In this chapter, we utilized our spectroscopic setups with various irradiation wavelengths and temporal excitation profiles to study the photodynamic emission of small and ultrasmall UCNPs.

In the first work, measuring steady state spectra and time-resolved luminescence under ns pulse excitation at 976 nm with a gated intensified CCD camera, we could demonstrate that a great enhancement of upconversion luminescence at 469 nm and 803 nm by coating $NaYF_4$ shell to 5 nm oxysulfide core. This enhancement of upconversion luminescence was attributed to a decreased surface quenching of the core. In addition, due to refractive index mismatches between the Gd_2O_2S core and the $NaYF_4$ shell, energy might be trapped inside the particle which causes the lengthening of the measured lifetimes. Therefore, we will have less leak of energy through the shell and favour the energy migration within the core, resulting in the higher upconversion luminescence.

Concerning the study of ultrasmall Tm-doped core UCNPs, it clearly appears that the application of temperature cycling offers a practical strategy to control the PSD. In this task, steady state spectra and time-resolved measurements (ms-squared pulse setup) enabled to confirm the optimum number of cycles which is needed for having bright enough fully β-phase particles. We have now an idea about when/how phase transformation (from α to β) affects the emissive states which agrees with XRD results. Eventually, these results enabled us to significantly reduce the reaction time as only 5 cycles (25 minutes) are necessary to produce highly monodisperse Gd-rich ultrasmall β-phase UCNPs. Furthermore, it was found to be sufficiently robust to achieve the preparation of ultrasmall UCNPs of similar sizes with a reduced number of activators ions despite a variable percentage of Yb^{3+}. In addition, using such a protocol, nanocrystals with a size as small as 2.5 nm could be obtained. Decreasing the size of UCNP down to less than 3 nm inevitably brings strong quenching effects coming from high surface-to-volume ratios but simultaneously reduces the likelihood for activator concentration quenching by cross-relaxation (CR), as the number of Tm^{3+} ions per UCNP is also automatically reduced. These quenching effects are strongly dependent on the emission bands considered. For the emission stemming from the high energy $^1D_2$ excited state, the activator concentration quenching is high in such small particles as we noticed for the

C_{34}^{570}(std) for which cross-relaxation plays a major role. The luminescence properties of the two ultrasmall core particles with sizes of 2.4 ± 0.9 nm and 2.8 ± 0.6 nm studied here illustrate the balance that has to be found for extremely small UCNP. On the one hand, these two particles contain in average less than 2 Tm^{3+} ions making CR unlikely and on the other hand, reducing the size of the particle entails an increased influence of surface quenching. These competitive effects could be unambiguously evidenced by scrutinizing the emission decay at 450 nm originating from the direct excitation of Tm^{3+} ions into their $^1D_2$ excited state using UV light. However, the 474 nm emission originating from the $^1G_4$ state of Tm^{3+} is mainly populated via ETU and barely affected by CR. Thus, this emission is strongly sensitive to surface quenching favored by for small particles sizes, particularly in the absence of a tight surface shielding shell, and a high Yb^{3+} concentration. Therefore, the 474 nm emission strongly benefits from the coating of the particle by a thin $NaGdF_4$ inert shell.

The purpose of this chapter is to provide an understanding of the critical parameters, such as phase transitions, number of dopant ions, and UCNP structure (size and shell), which have a profound impact on the radiative and non-radiative energy transfer pathways inside the UCNPs. These findings are also of considerable interest for designing brighter UCNPs. It is also important to note, however, that in the following chapters, we attempt to explore how energy is transferred between UCNPs and between a single UNCP and an acceptor in order to gain a better understanding of what is happening out of UCNPs.

3.6 References

1. Lohse, S.E. and C.J. Murphy, *Applications of colloidal inorganic nanoparticles: from medicine to energy*. Journal of the American Chemical Society, 2012. **134**(38): p. 15607-15620.
2. Zarschler, K., et al., *Ultrasmall inorganic nanoparticles: State-of-the-art and perspectives for biomedical applications.* Nanomedicine: Nanotechnology, Biology and Medicine, 2016. **12**(6): p. 1663-1701.
3. Arppe, R., et al., *Quenching of the upconversion luminescence of NaYF 4: Yb 3+, Er 3+ and NaYF 4: Yb 3+, Tm 3+ nanophosphors by water: the role of the sensitizer Yb 3+ in non-radiative relaxation.* Nanoscale, 2015. **7**(27): p. 11746-11757.
4. Zhao, J., et al., *Upconversion luminescence with tunable lifetime in NaYF4:Yb,Er nanocrystals: role of nanocrystal size.* Nanoscale, 2013. **5**(3): p. 944-52.
5. Siefe, C., et al., *Sub-20 nm Core–Shell–Shell Nanoparticles for Bright Upconversion and Enhanced Förster Resonant Energy Transfer*. Journal of the American Chemical Society, 2019. **141**(42): p. 16997-17005.
6. Golesorkhi, B., et al., *Deciphering and quantifying linear light upconversion in molecular erbium complexes.* Chemical science, 2019. **10**(28): p. 6876-6885.
7. Knighton, R.C., et al., *Upconversion in molecular hetero-nonanuclear lanthanide complexes in solution.* Chemical Communications, 2021. **57**(1): p. 53-56.
8. Nonat, A.M. and L.J. Charbonnière, *Upconversion of light with molecular and supramolecular lanthanide complexes.* Coordination Chemistry Reviews, 2020. **409**: p. 213192.
9. Suffren, Y., et al., *Taming lanthanide-centered upconversion at the molecular level.* Inorganic chemistry, 2016. **55**(20): p. 9964-9972.
10. Haase, M. and H. Schafer, *Upconverting nanoparticles.* Angew Chem Int Ed Engl, 2011. **50**(26): p. 5808-29.
11. Wang, Y., *The role of an inert shell in improving energy utilization in lanthanide-doped upconversion nanoparticles.* Nanoscale, 2019. **11**(22): p. 10852-10858.
12. Homann, C., et al., *NaYF4: Yb, Er/NaYF4 core/shell nanocrystals with high upconversion luminescence quantum yield.* Angewandte Chemie International Edition, 2018. **57**(28): p. 8765-8769.
13. Zou, Q., et al., *Heterogeneous Oxysulfide@ Fluoride Core/Shell Nanocrystals for Upconversion-Based Nanothermometry*. ACS nano, 2022. **16**(8): p. 12107-12117.
14. Singh, P., P. Singh, and S. Singh, *Photon Upconversion Spectroscopy*, in *Modern Techniques of Spectroscopy*. 2021, Springer. p. 389-407.
15. Kaiser, M., et al., *Power-dependent upconversion quantum yield of NaYF 4: Yb 3+, Er 3+ nano-and micrometer-sized particles–measurements and simulations.* Nanoscale, 2017. **9**(28): p. 10051-10058.
16. Maurizio, S.L., et al., *BaYF5: Yb3+, Tm3+ upconverting nanoparticles with improved population of the visible and near-infrared emitting states: implications for bioimaging.* ACS applied nano materials, 2021. **4**(5): p. 5301-5308.
17. Chen, X., et al., *Photon upconversion in core–shell nanoparticles.* Chemical Society Reviews, 2015. **44**(6): p. 1318-1330.
18. Voss, B. and M. Haase, *Intrinsic focusing of the particle size distribution in colloids containing nanocrystals of two different crystal phases.* ACS nano, 2013. **7**(12): p. 11242-11254.
19. Damasco, J.A., et al., *Size-tunable and monodisperse Tm3+/Gd3+-doped hexagonal NaYbF4 nanoparticles with engineered efficient near infrared-to-near infrared upconversion for in vivo imaging.* ACS applied materials & interfaces, 2014. **6**(16): p. 13884-13893.
20. Dong, C., et al., *Nonstatistical dopant distribution of Ln3+-doped NaGdF4 nanoparticles.* The Journal of Physical Chemistry C, 2011. **115**(32): p. 15950-15958.
21. Liu, X., et al., *Controllable synthesis of ultrasmall core-shell hexagonal upconversion nanoparticles towards full-color output.* Optik, 2020. **207**: p. 164398.

22. Wang, F., et al., *Simultaneous phase and size control of upconversion nanocrystals through lanthanide doping.* nature, 2010. **463**(7284): p. 1061-1065.
23. Gargas, D.J., et al., *Engineering bright sub-10-nm upconverting nanocrystals for single-molecule imaging.* Nature nanotechnology, 2014. **9**(4): p. 300-305.
24. Liu, J., et al., *Sub-6 nm monodisperse hexagonal core/shell NaGdF 4 nanocrystals with enhanced upconversion photoluminescence.* Nanoscale, 2017. **9**(1): p. 91-98.
25. Amouroux, B., et al., *Importance of the Mixing and High-Temperature Heating Steps in the Controlled Thermal Coprecipitation Synthesis of Sub-5-nm Na (Gd–Yb) F4: Tm.* Inorganic Chemistry, 2019. **58**(8): p. 5082-5088.
26. Wu, Z., S. Yang, and W. Wu, *Application of temperature cycling for crystal quality control during crystallization.* CrystEngComm, 2016. **18**(13): p. 2222-2238.
27. Guo, E., et al., *Synchrotron X-ray tomographic quantification of microstructural evolution in ice cream–a multi-phase soft solid.* Rsc Advances, 2017. **7**(25): p. 15561-15573.
28. Mills, R.D., J.J. Ratner, and A.F. Glazner, *Experimental evidence for crystal coarsening and fabric development during temperature cycling.* Geology, 2011. **39**(12): p. 1139-1142.
29. Kacker, R., M. Radoiu, and H.J. Kramer, *Novel design integrating a microwave applicator into a crystallizer for rapid temperature cycling. A direct nucleation control study.* Crystal Growth & Design, 2017. **17**(7): p. 3766-3774.
30. Kacker, R., et al., *Microwave assisted direct nucleation control for batch crystallization: Crystal size control with reduced batch time.* Crystal Growth & Design, 2016. **16**(1): p. 440-446.
31. Wu, Z., et al., *Control of crystal size distribution using non-isothermal Taylor vortex flow.* Crystal Growth & Design, 2015. **15**(12): p. 5675-5684.
32. Li, D., et al., *Facile synthesis of ultrasmall hexagonal NaYF 4: Yb 3+, Er 3+ upconversion nanocrystals through temperature oscillation.* Inorganic Chemistry Frontiers, 2017. **4**(7): p. 1211-1214.
33. Dzuba, V., et al., *Strongly enhanced effects of Lorentz symmetry violation in entangled Yb+ ions.* Nature Physics, 2016. **12**(5): p. 465-468.
34. Wang, G., et al., *Controlled synthesis and luminescence properties from cubic to hexagonal NaYF4: Ln3+ (Ln= Eu and Yb/Tm) microcrystals.* Journal of alloys and compounds, 2009. **475**(1-2): p. 452-455.
35. Zhai, X., et al., *A Simple Strategy for the Controlled Synthesis of Ultrasmall Hexagonal-Phase NaYF4: Yb, Er Upconversion Nanocrystals.* ChemPhotoChem, 2017. **1**(8): p. 369-375.
36. Nadort, A., J. Zhao, and E.M. Goldys, *Lanthanide upconversion luminescence at the nanoscale: fundamentals and optical properties.* Nanoscale, 2016. **8**(27): p. 13099-13130.
37. Wang, F., R. Deng, and X. Liu, *Preparation of core-shell NaGdF4 nanoparticles doped with luminescent lanthanide ions to be used as upconversion-based probes.* Nature protocols, 2014. **9**(7): p. 1634-1644.
38. Sun, T., et al., *Shielding Upconversion by Surface Coating: A Study of the Emission Enhancement Factor.* Chemphyschem, 2016. **17**(5): p. 766-70.
39. Villanueva-Delgado, P., et al., *Modeling blue to UV upconversion in β-NaYF 4: Tm 3+.* Physical Chemistry Chemical Physics, 2016. **18**(39): p. 27396-27404.

4

Photodynamic investigation of ET between UCNPs: heterogeneous emission of UCNPs in various assemblies at single particle level

4.1 Introduction

As mentioned in chapter one, up-converting nanoparticles (UCNPs) have a multimodal fluorescence emission owing to multiple electronic levels and intrinsic properties of f-f transitions.[1] UCNPs can be excited by near-IR irradiation and emit at higher energies in the UV, visible, or NIR, which can find clear advantages in numerous fields extending from photonics[2-4] and photocatalysis[5, 6] to fluorescence bio-imaging.[7-9] Excellent photostability, lack of blinking, absence of autofluorescence in biological specimens, and low cytotoxicity make UCNPs an attractive alternative for luminescence imaging probes in fluorescence microscopy.[10-12] Additionally, having long lifetime excited states ranging from μs to ms is favourable for time-gated emission to get rid of autofluorescence. [13-15] Following absorption of NIR photons by a sensitizer, there are several feasible energy pathways among dopant ions inside each particle. For instance, this energy can be transferred among sensitizer ions, which is called energy migration (EM), it can be transferred between a sensitizer and an emitter by ETU, which is the most efficient upconversion process among dopants.[11] Moreover, there might be interactions between sensitizers/emitters and the environment at the surface of the nanoparticle, including solvent molecules or other UCNPs.[16, 17] All these interactions can be influenced by the concentration of dopant ions, architecture and size of UCNPs, excitation power density, and surface environment.[17, 18] Deep and precise understanding of the dynamic interaction of dopants in UCNPs can be considered an important milestone for the development of optical properties and optimizing UCNPs emission. Although there are some fundamental studies attempting to unravel these interactions,[16, 19-21] numerous of these studies have been conducted in solution and measure the spectroscopic behaviour of UCNPs only as an average response. That is, these measurements have been done with large collection areas and ignore the heterogeneity of the sample at the nanometric scale. Thereby, even in extremely diluted UCNPs suspensions, the existence of aggregated nanocrystals is inevitable.[22] Different assemblies of UCNPs, from solvated single particles to large aggregates, are expected to provide different spectroscopic response because of the potential interactions that might occur between individual particles and between particles and solvent molecules.[23] As previously mentioned in chapter 2, surface of UCNPs are usually coated with oleic acid which is not suitable for aqueous media. Therefore, surface modification with stable shells (as

discussed in chapter 2) are needed. In addition, even for particles with relatively large shell thickness, energy transfer among them may occur.[24] Therefore, the expected discrepancy of the emission properties (steady state and time-resolved) of single and aggregated particles seems to be unattainable in solution. It is however essential for rationalizing the behaviour of UCNPs, for biological applications, where particles have a higher propensity for agglomeration than in organic solvents, or for photonics film materials.

Single nanoparticle microscopy allows for distinguishing the level of aggregation of the probed UCNPs, and thus to specifically evaluate and uncover the role of various parameters, such as architecture, environmental surroundings, etc. by controlling the contribution of particle-to-particle interactions. To this end, advanced single particle characterization methods, such as hyperspectral microscopy (HSM), are required. HSM is a technique that combines imaging and spectroscopy to collect spectral and spatial information concomitantly.[25, 26] As already mention in chapter 2 (section 2.3.1), there are some fundamental studies revealing the heterogeneous behaviour of a single particle,[23, 27, 28] based on HSM. However, there are still challenges of such studies. As previously discussed, the emission of UCNPs depends on the temporal excitation profile. Therefore, using 976-nm square-wave pulses combined with time-gated spectra is essential for studying of photodynamic emission, which has not yet been reported.

To shed more light on the behaviour of UCNPs, this study introduced a new hyperspectral time-resolved microscope setup able to measure growing and decay times with different pulse width excitations, from a few of µs to ms, at different power densities (0.2-36 kW/cm^2). This setup was used to demonstrate the heterogeneity of steady state and time-resolved luminescence of deposited by spin-coated core and core-shell Tm-based UCNPs according to the level of aggregation, from single UCNP to large 3-dimensions layouts. This heterogeneous behaviour of various regions is essential for intensity- and lifetime-based ratiometric multiplex encoding[29], optical sensing of temperature[30, 31], and all studies based on ratiometric evaluations.

In order to collect enough signal, these particles are no longer ultra-small as in the previous work presented in chapter 2. The investigated core particles (β-$NaYF_4$:20% Yb^{3+}, 2% Tm^{3+}) have a diameter of 12 nm and their core-shell counterparts (β-$NaYF_4$:20% Yb^{3+}, 2% Tm^{3+}@$NaYF_4$) have a diameter of 20 nm, i.e. a shell thickness of

about 4 nm. In particular, two specific emission bands were investigated corresponding to $^1D_2 \rightarrow {}^3F_4$ (450 nm) and $^1G_4 \rightarrow {}^3H_6$ (475 nm) Tm transitions. Three distinct areas were identified: bright spots, carpets, and dark regions, each of them exhibits entirely different properties according to the power.

4.2 Sample preparation and characterization

β-$NaYF_4$:20% Yb^{3+}, 2% Tm^{3+} core and β-$NaYF_4$:20% Yb^{3+}, 2% Tm^{3+}@$NaYF_4$ core-shell UCNPs were provided by Dr. Rajesh Komban and Prof. Christoph Gimmler from the Center for Applied Nanotechnology (CAN) of the Fraunhofer Institute in Hamburg, Germany. The original solution of UCNPs was provided in toluene with a concentration of 10 mg/mL. The solution was diluted 1000 times in toluene (99.5%) and sonicated for 30 minutes. The samples were prepared by spin-casting 8 µL of diluted solution (one minute at 70000 rph) onto a cleaned glass coverslip (22×22 mm). The following procedure was used to clean coverslips: (a) 20 min in acetone with sonication, (b) clean them carefully with HQ water, (c) put them into Hellmanex solution for 20 min, (d) wash carefully with HQ water, (e) 3 times in water with 20 min sonication, (f) dry them with a dryer, and (g) put them in a becher for ozonization (30 min each side). Scanning electron microscopy images were taken at the “Plateforme de Microscopie Electronique de Lille” (UMET – Institut Chevreul) by using a Hitachi SU 5000 scanning electron microscope equipped with a field electron gun (FEG) electron source.

4.3 Experimental setup

4.3.1 Ensemble measurements

Steady state luminescence spectra were measured using a commercial fluorimeter (Fluoromax-3, Horiba Jobin Yvon) equipped with a fiber-Bragg-grating 976 nm stabilized laser diode (Thorlabs, 900 mW) run with a temperature stabilizing controller (Arroyo 6340 ComboSource). For high power density, the beam was focalized into a 4x10 mm quartz cuvette without stirring by a convergent lens (focal length 5.2 mm), providing a gaussian intensity shape at the focal point of 88 µm ($1/e^2$). The emission slit was set to

2 nm bandpass, and the emission spectra were recorded between 300 and 850 nm with 1nm steps. The spectra were corrected for the wavelength dependence of the detector´s spectral sensitivity using the correction function provided by the instrument manufacturer. An additional baseline correction was carried out by subtracting the solvent signal (toluene).

4.3.2 Hyperspectral imaging setup

The confocal images, time-resolved luminescence measurements, and steady state luminescence spectra were measured using the confocal microscopy setup shown in Figure 1. For excitation of UCNPs, an LDH laser head at 976 nm (or 800 nm) operated in the cw mode with the Taiko PDL M1 controller (Picoquant). For the creation of the excitation time gates, the Taiko controller was functioning in the cw / fast gate mode connected to a delay generator (DG, SRS, model DG535). One DG channel was connected to the Taiko to generate the square pulses with variable length (from µs to ms), and another channel sent a trigger signal to the photon counting card and to the gated ICCD camera.

The excitation light was guided using broadband dielectric and gold mirrors and going through a half wave-plate to get a circular polarization. The excitation light was directed into an inverted Olympus IX71 and focused on the sample through a short pass dichroic beamsplitter (670 nm edge BrightLine® multiphoton short-pass dichroic beamsplitter, Semrock) and an oil-immersion objective lens (Olympus, UPLSAPO 60×, NA=1.42).

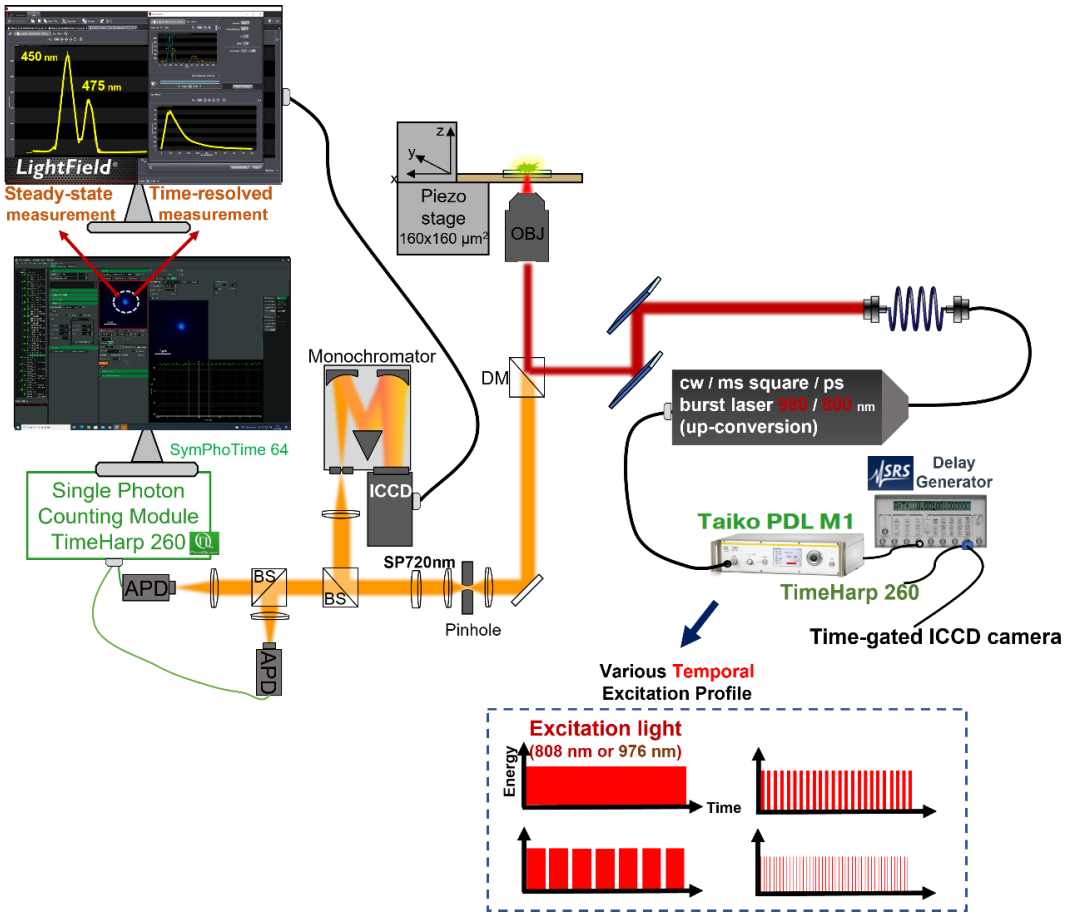

Figure 1. Scheme of the hyperspectral time-resolved microscope.

Emitted light was collected back through the same objective and dichroic beamsplitter, passed through the confocal pinhole (100 µm), and filtered out using a short pass emission filter (720 nm blocking edge BrightLine® multiphoton short-pass emission filter, Semrock) before being redirected to (i) a single-photon counting avalanche diode (SPAD) (MPD, 50 mm, Grade D, <50 cps and IRF of 50 ps) and (ii) a multi-grating versatility monochromator (Princeton Instruments IsoPlane 160 equipped with two gratings 300 g/mm with 300 nm and 750 nm blazing) coupled with intensified CCD camera (1024 × 1024 pixels, PI Max4 Princeton instruments). The beam was split into the two pathways using a 10% / 90% unpolarised beam splitter (10% to the SPAD, 90% to the CCD).

The sample was mounted on a 3D translation stage (E-725, Physik Instrument) which allowed scanning pixel-by-pixel an entire area on the sample of 160 × 160 µm which was controlled via Symphotime 64 software (Picoquant). Photon arrival time for each pixel was obtained using a TimeHarp 260 PICO photon counting card operating in the long range mode.

Point spread function (PSF, which describes the response of an imaging system to a point source or point object [32]) was measured using a single core-shell UCNP (20 nm diameter) under 976 nm irradiation at 36 kW/cm^2 power density. Spatial resolution was determined by the Gaussian fit of the intensity in x and y directions. The full width at half maximum (FWHM) of the Gaussian function provided a spatial resolution of 600 nm in x and y directions (Figure 2).

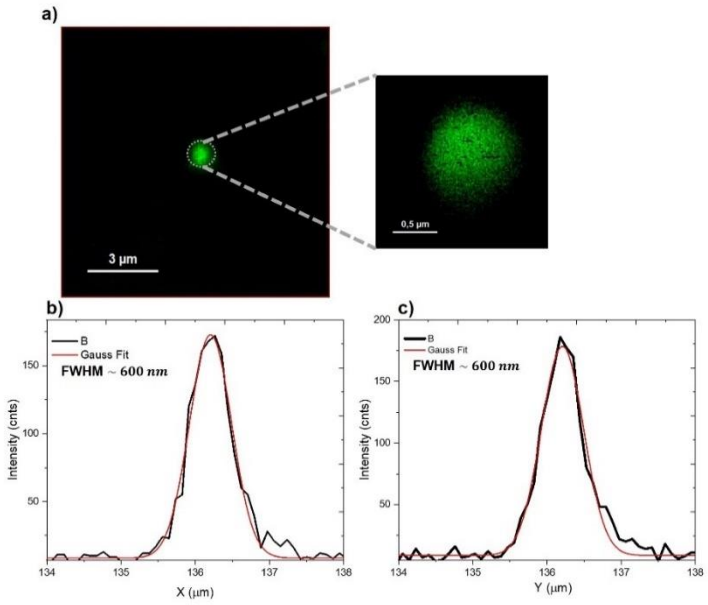

Figure 2. Measurement of PSF with UCNPs under 976 nm irradiation.

Images were first recorded using the 976 nm diode in continuous-wave mode using the APD as detector, and time-resolved luminescence spectra were subsequently performed using a square-wave excitation and the time-gated ICCD camera detection (triggered with the delay generator) in chosen pixels of the confocal image. These measurements were performed in various power densities (3.5 kW/cm^2 to 36 kW/cm^2) and different ranges of excitation duration (700 µs to 8 ms). Both rising and decay parts of UCNPs emissions at various wavelengths could be recorded (Figure 3). Moreover, it was feasible to demonstrate various growing shapes relying on the different temporal excitation profiles as illustrated in Figure 3b. By mean of this setup, time-resolved spectra for various emission bands of Tm^{3+}, $^1D_2 \rightarrow {}^3F_4$ (450 nm) and $^1G_4 \rightarrow {}^3H_6$ (475 nm) bands, were recorded with constant gate width of 50 µs for UCNPs samples. The first gate was set to start at 37 ns (insertion delay of camera) and 240 gates were recorded (37 ns to 12 ms, Figure 3a).

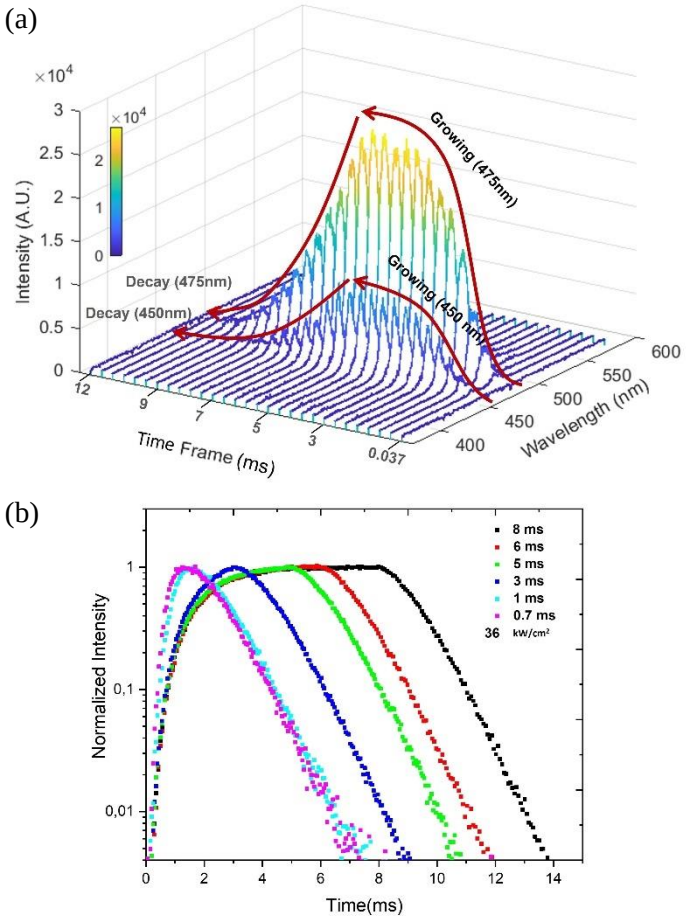

Figure 3. (a) Rising and decaying parts of UCNPs emission at 450 nm and 475 nm in 36 kW/cm^2. (b) Influence of the temporal excitation duration on the rising profile of UCNPs (700 µs to 8 ms cw excitation at 976 nm).

Effective emission lifetimes (τ_{eff}) were calculated from time-resolved luminescence plots as the ratio of the integrated decay area to its maximum, which is functionally equivalent to the amplitude-weighted average lifetime calculated from the exponential fit of the decay curve:[28, 33]

$$\tau_{eff} = \frac{\int_{t=0}^{\infty} I(t)}{I_{max}} = \sum_{i=1}^{n} a_i \tau_i \qquad (1)$$

Where a_i is the fractional amplitude associated to the time constant τ_i of each of the n exponential functions used for the fit.

Moreover, steady state luminescence spectra were performed between 420 and 500 nm using cw 976 nm in different power densities (0.2 kW/cm^2 to 36 kW/cm^2) by ICCD camera. Additionally, all the data acquisition for time-resolved and steady state luminescence spectra were controlled by Lightfield software (Princeton Instrument). The

power was measured after objective lens and cleaned cover slip by a power meter (NOVA II OPHIR). Then, the excitation power densities and FWHM were calculated from the imaged laser spot (Gentec Beamage-4M beam profiling camera).

4.3.2.1 Confocal data analysis

After extraction from Lightfield software, data were imported into OriginLab software for first pre-processing of the data such as background correction, and analysed. All data analysis of steady state spectra for measuring power dependent plots and area band ratios were automatized by a code in Python (section A3.1).

4.4 Results and discussion

Hyperspectral imaging microscopy has a profound potential to demonstrate heterogeneities within the sample.[23] To investigate heterogeneities of spin-coated core-shell β-$NaYF_4$:20% Yb^{3+}, 2% Tm^{3+}@$NaYF_4$ and core nanoparticles β-$NaYF_4$:20% Yb^{3+}, 2% Tm^{3+}, various areas of the coverslip have been scanned. As demonstrated in Figure 4a, by scanning core-shell sample under cw irradiation at 976 nm, mainly two different areas can be observed:

1) high intensity area (resembling a carpet of particles)

2) low intensity area (can be referred as a dark area)

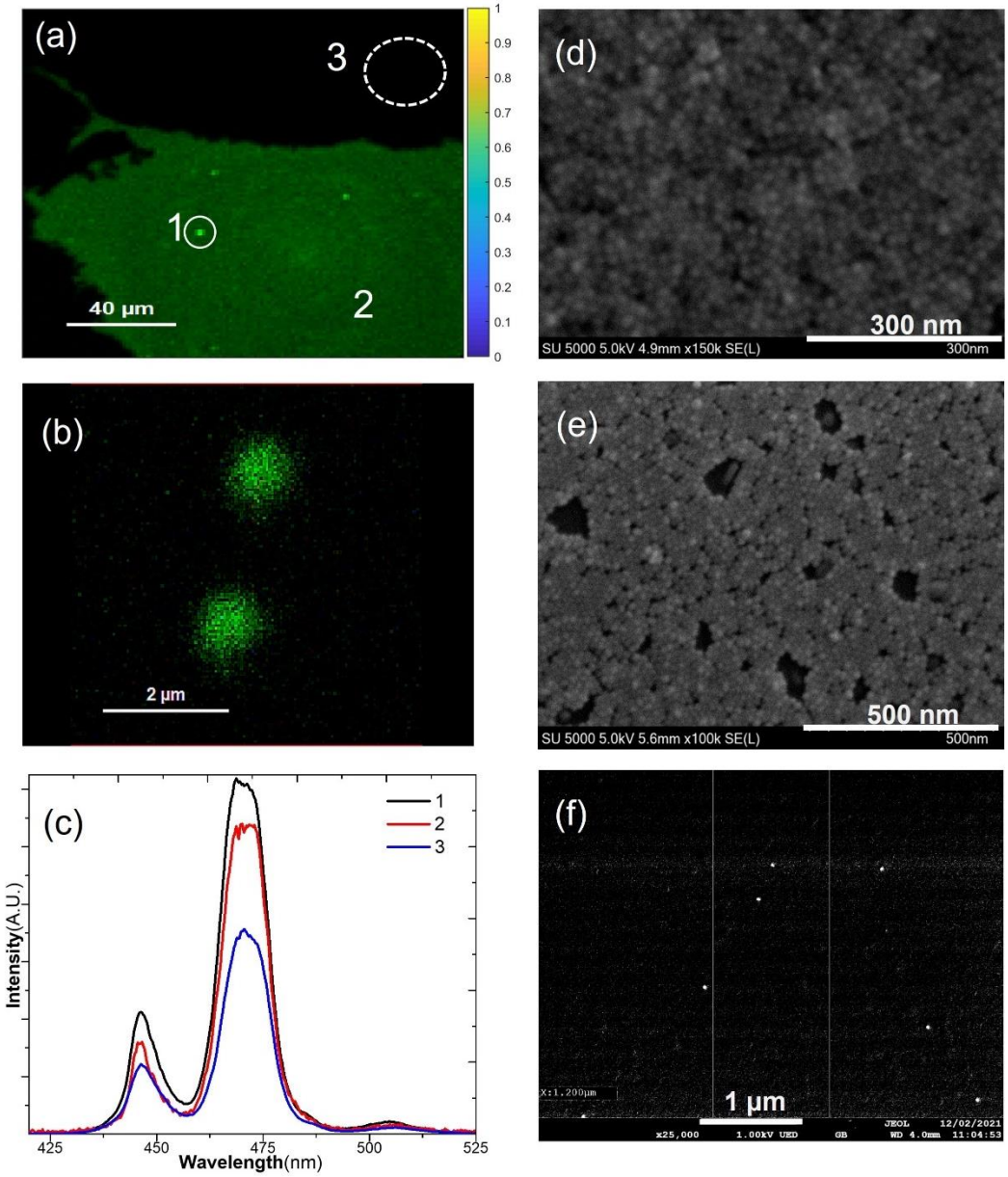

Figure 4. (a) Confocal image of core-shell particles spin-coated on a coverslip irradiated with cw 976 nm light (full range: 160 x 160 µm) with high intensity regions (1 and 2) and a dark region (3). (b) Confocal image of single particles observed in region 3 (6 x 6 µm). (c) Steady state spectra at 450 nm and 470 nm of the three regions (1, 2 and 3) under 976 nm cw excitation (power density 36 kW/cm^2). (d, e, f) SEM images of (d) bright spots arising from the high intensity region 1, (e) 2D layer observed in region 2 and (f) single particles of region 3.

By taking a careful look at high intensity regions of Figure 4a, bright spots which are more intense than the remainder of the carpet can be identified (Figure 4a, region 1). Steady state luminescence spectra for $^1D_2 \rightarrow {}^3F_4$ and $^1G_4 \rightarrow {}^3H_6$ bands, ascribed to 450 nm and 475 nm, respectively, have been measured in these regions. As illustrated in Figure 4c, the emission intensity of bright spots for these two bands are higher than other regions.

For further exploration of these regions, SEM analysis of the identically prepared spin-coated sample has been performed. As shown in Figure 4d, e and f, they clearly reveal that the spatial distribution of UCNPs after spin coating is not homogeneous which is in good agreement with recorded confocal image (Figure 4a). The homogenous area of the high intensity region of Figure 4a (region 2) is related to Figure 4e which indicates a two dimensions monolayer organization of UCNPs. Whereas the bright spots in this carpet arrangement are due to three-dimensional layouts of UCNPs (Figure 4d). By scanning a section of the dark region of Figure 4a (region 3), the confocal image (Figure 4b) reveals well-separated single particles, which have the least steady state emission intensity. Single particles are indeed detected by SEM imaging (Figure 4f).

Similarly, as demonstrated in Figure 5a, two main areas were detected for core particles (β-$NaYF_4$:20% Yb^{3+}, 2% Tm^{3+}) as for core-shell particles. High- and low-intensity domains can be seen in the confocal image (Figure 5a). The high intensity area consists of monolayer arrangements (carpet, region 2) and multilayer structures (bright spots, region 1). Figure 5b shows the scanning of region 2 of Figure 5a (carpet with a monolayer structure) which was confirmed SEM image (Figure 5e). Moreover, Figure 5c shows confocal images of single particles detected in the dark region (3) which is confirmed by SEM (Figure 5f).

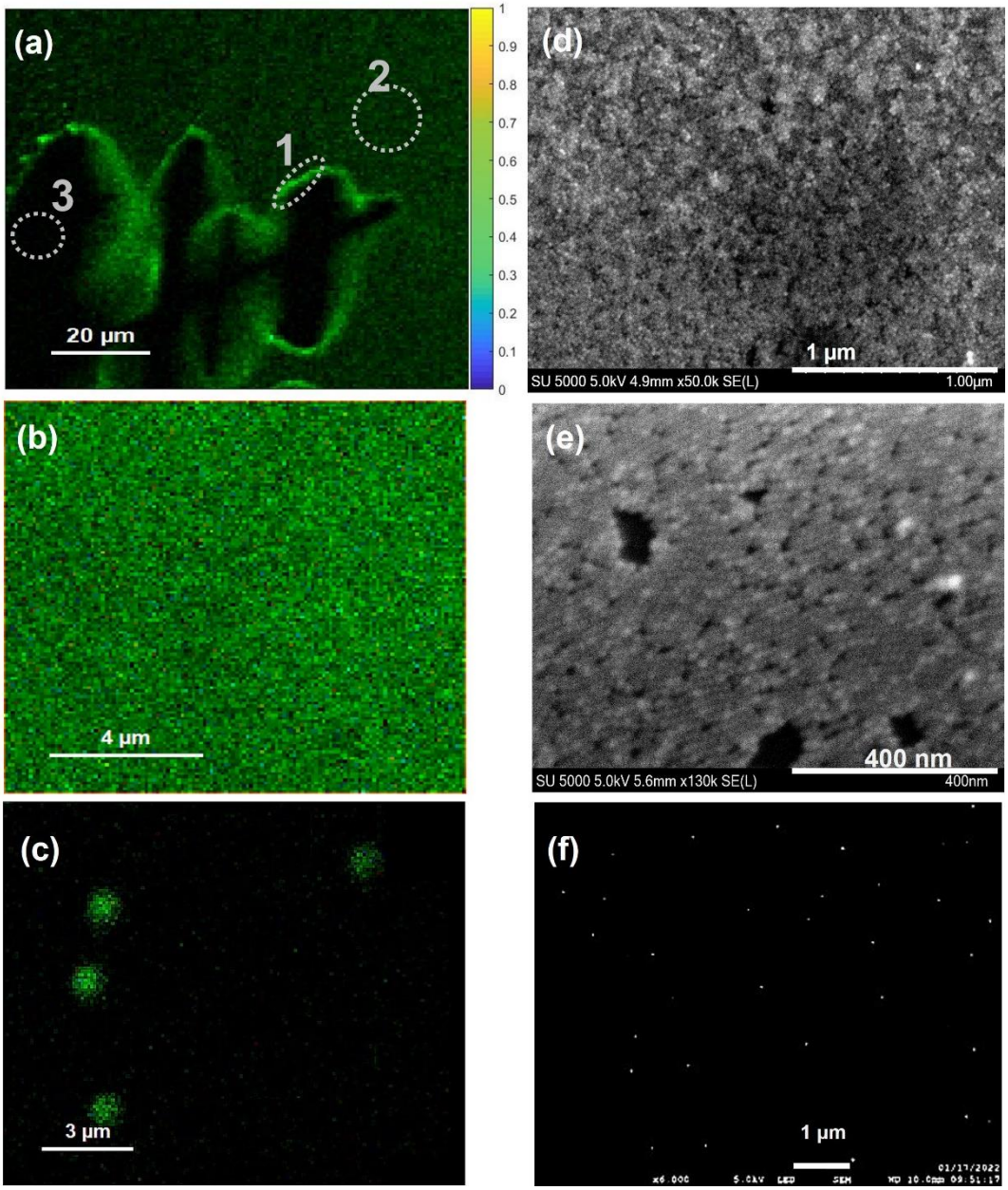

Figure 5. (a) Confocal image of core particles spin-coated on a coverslip irradiated with cw 976 nm light (full range: 160 x 160 µm) with high intensity regions (1 and 2) and a dark region (3). (b,c) 50 x 50 µm confocal images of (b) a 2D layer observed in region 2 and (c) single particles observed in region 3. (d, e, f) SEM images of (d) bright spots arising from the high intensity region 1, (e) 2D layer observed in region 2 and (f) single particles observed in region 3.

Now that three different organisations are well identified and controlled, the aim is to demonstrate how this local arrangement influences the emission properties of core and core-shell UCNPs. First, steady state spectra of the core and core-shell particles were measured in solution to obtain their power-dependence plot under 976 nm cw excitation (Figures 6a and 7a) and to monitor their 475-to-450 nm band ratios in various power

conditions (Figures 6b and 7b). In chapter two, we discussed about the power-dependence plot which was about the link between excitation power P (under cw) and upconversion emission intensity I. In the assumption of low excitation density, the slope of the power-dependence plot (n) is equal to the number of excitation photons required to produce one upconversion photon. For example, as shown in Figure 6e, emitting one photon from 450 nm and 475 nm bands need 4 and 3 excitation photons, respectively. As soon as the power-density increases, n gradually becomes one, regardless of the number of energy transfer steps involved. And upconversion luminescence (UCL) saturation appears. This saturation is due to the saturated absorption of the sensitizers (Yb^{3+}). In other words, at high power-density , the saturated sensitizer keeps the activator (Tm^{3+}) in the excited state rather than in the ground state and only one subsequent energy transfer is required to bring it to emitting states. Furthermore, when n becomes smaller than one, UCL quenching due to thermal effects appears. Therefore, power-dependence plot can be informative about the dynamics of ETU processes. Lie et al. [34] investigated the upconversion luminescence (UCL) of Tm core (25 nm) and core-shell (35 nm) particles in various power densities (in cw excitation). They reported that core-shell nanoparticles (in the same size of core and dopant concentration) reach the saturation regime sooner than core particles due to the shielding effect of the shell.

For core-shell particles, two regimes with distinct area ratios are observed in Figure 6b. The area ratios for low power density (< 100 W/cm^2) dramatically decreases with increasing power density. This corresponds to the emergence of the 450 nm band which is almost non-existent when the power is low. It is worth mentioning that the emission from a high-lying level (450 nm, 4-photon process) happens at a higher excitation power compared to lower levels (chapter 2, section 1.3.7). In addition, the power-dependent plot in the low power range (Figure 6c.) reveals a linear behaviour with a slope of ~ 3 for 475 nm band and ~ 4 for 450 nm band. On the other hand, in the high-power range (> 200 W/cm^2), the band ratio is decreasing by increasing the power density. A saturation regime is about to be reached, as shown in Figure 6d by the breaking in the slope occurring in 0.7 kW/cm^2 and 0.9 kW/cm^2 at 475 nm and 450 nm , respectively.

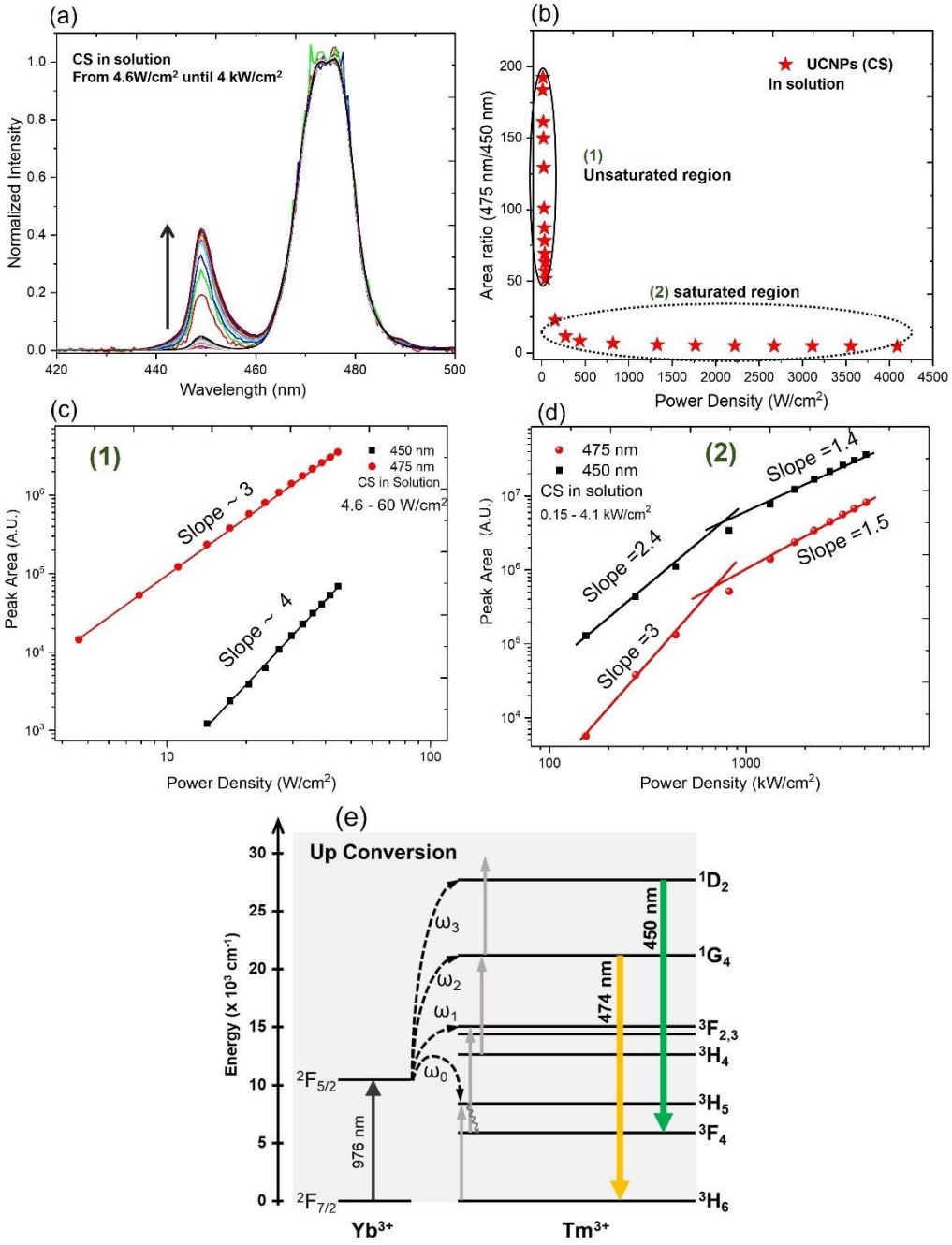

Figure 6. (a) Steady state spectra of core-shell UCNPs in solution, normalized on the 475 nm maximum intensity (At low power density, the spectra are spiky). (b) Calculated area ratio of 475 nm/450 nm in various power densities (0.15 to 4.1 kW/cm^2) (c,d) Power dependence plots corresponding to the unsaturation (c) and saturation (d) regimes at 450 nm and 475 nm. (e) Yb/Tm energy diagram under excitation of 976 nm.

Moreover, the peak area ratios demonstrated the same trends for core particles as for the core-shell UCNPs (Figure 7b). They abruptly decrease with increasing power density, although in a much lower extent (15 to 3 for core vs. 200 to 4 for core-shell particles). This is due to the fact that, when decreasing the excitation power density below a certain

value, the emissivity of the particle is so low that no signal can be measured at 450 nm, and hardly at 475 nm. This is illustrated by the limit case of 17 W/cm² in Figure 7a (black curve), where the signal-to-noise ratio is very poor. Furthermore, power density plots (Figure 7c) exhibit a slope of ~3 at 475 nm, which is equal to the number of photons required for excitation. Figure 7d demonstrated a clear threshold denoted by the breaking in the slope at 475 nm at high excitation power-density (about 7 kW/cm^2) which evidence that the saturation regime is reached. It should thus be noticed that the core particles attain the saturation regime at higher power density than in core-shell particles for 475 nm bands, consistently with the results already reported in the literature. [34] In addition, contrary to core-shell particles, in core particles, 450 nm band does not reach the saturation regime, even at 40 kW/cm^2.

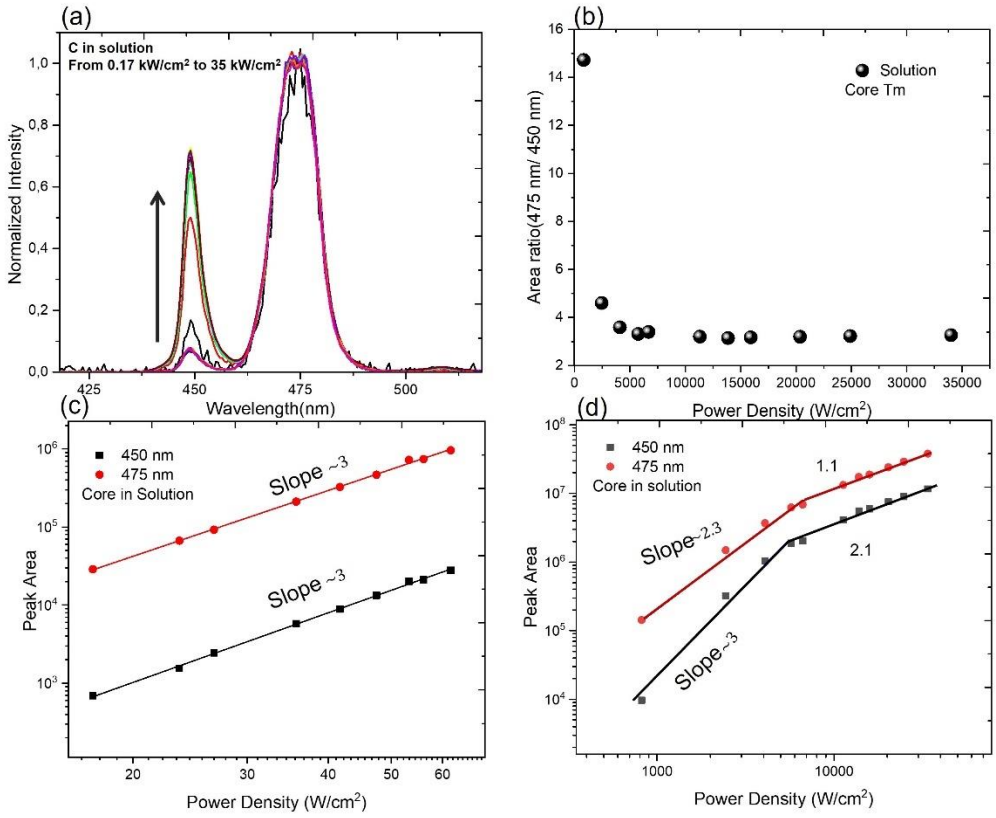

Figure 7. (a) Steady state spectra of core UCNPs in solution, normalized on the 475 nm maximum intensity. (b) Calculated area ratio of 475 nm/450 nm in various power densities (0.17 kW/cm^2 to 35 kW/cm^2) (c,d) Power dependence plots corresponding to the unsaturation (c) and saturation (d) regimes at 450 nm and 475 nm.

The same measurements were performed with the previously introduced confocal microscope setup to provide area ratios and power dependence plots of 450 nm and 475

nm emission bands in the different domains identified in Figures 3a and 4a. In each power density and each region (bright spots, carpet, single particles), 20 emission spectra for various pixels were recorded. As shown in Figure 8a for core-shell particles, bright spots, carpet, and single particles regions demonstrated different area ratios which all tend to converge to the same value at high power density. The area ratios of single particles (region 3 in Figure 4a) are lower than those in other regions, and they exhibit fewer variations through power density changes. On the other hand, the strongest variation through power changes happened in carpet region (Figure 8a, red circles). In addition, by considering the area ratios of ensemble measurements in this curve (Figure 8a, green stars), it can be considered as an average response of bright spots, carpet, and single particles. Also, at high power density (36 kW/cm^2), there is a similarity in the area ratios and steady state spectra of these regions (Figure 8a and b) which makes them quite undistinguishable. Thus, for better revealing the hidden pattern of these multivariate datasets, principal component analysis (PCA) was employed.

The main purpose of PCA is to transfer a set of correlated variables into a set of uncorrelated principal components (PCs) that explain the maximum amount of variation present in the dataset. For the dataset of core-shell particles (Figure 8b) with (60 spectra × 1024 pixels) dimension at highest power (36 kW/cm^2) , which consists of 20 spectra of each region (bright spots, carpet, and single), three PCs accounting for 99.01% of such a variation are selected. As shown in Figure 8c, three distinct clusters are observable for the steady state spectra collected at the highest power density, which highlights the different behaviour between bright spots, carpet, and single particles regions even at the highest power density. The separation of the carpet and single regions clusters from the bright spots cluster might be related to their different behaviour in their assemblies (carpet and single region show a rather spread spatial distribution compared to bright spots as shown in Figure 8c).

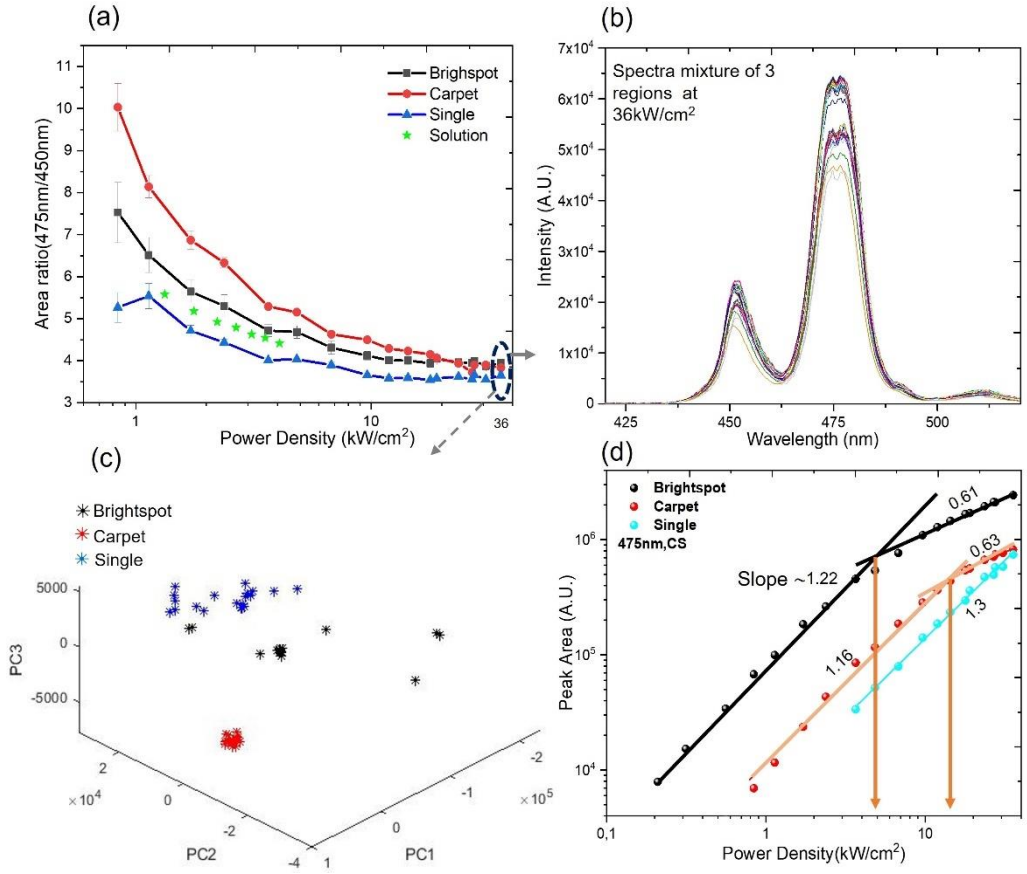

Figure 8. (a) Area ratios of 475 nm to 450 nm bands in various power densities (0.6 to 36 kW.cm^2) for bright spot, carpet, single particle, and solution of core-shell UCNPs. (b) Steady state spectra of each region (bright spot, carpet, single) recorded at 36 kW/cm^2 (c) Score plot stemming from PCA applied to steady state spectra at 36 kW/cm^2. (d) Power dependence plots at 475 nm for bright spots, carpet, and single particles.

Moreover, by performing PCA on the collection of all core-shell datasets, measured at 12 power densities with (720 × 1024) dimension, a clear trend with power was observed for carpet and single regions as shown in Figure 9. This trend displays a minimum and maximum difference for the highest and lowest power density, respectively, which is consistent with area ratio results. On the other hand, in bright spots, the data mainly spread on third direction but some of them adopt the same behaviour as single particle or carpet.

Additionally, as shown in Figure 8d, the slope of the power-dependent plot at 475 nm decreased to below 1 at 8 and 11 kW for bright spot and carpet, respectively. On the other hand, the slope remains 1 for single particles in the high-power range.

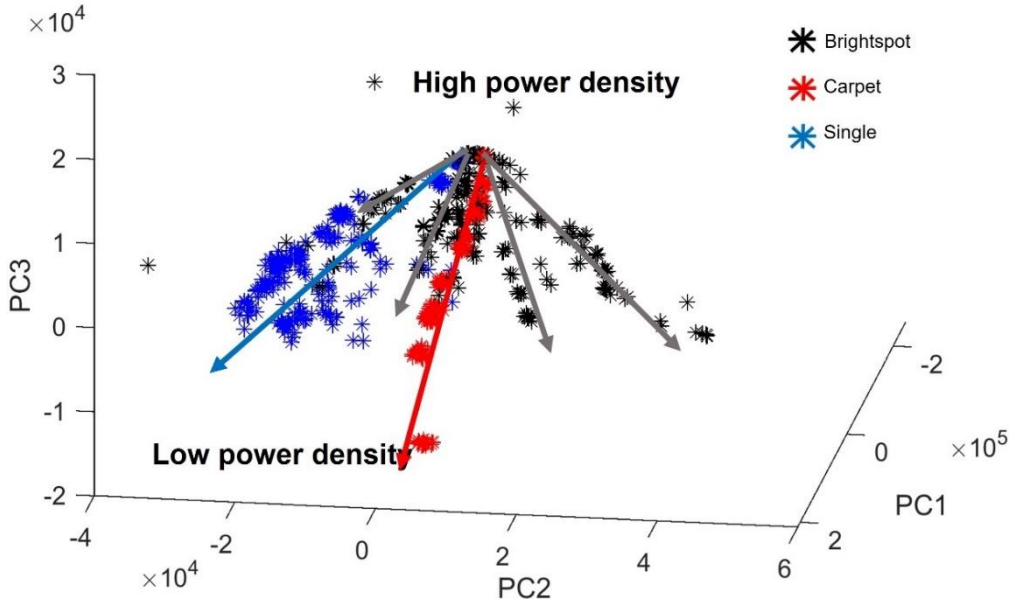

Figure 9. Score plot resulting from PCA applied on all the core-shell dataset at various power densities (0.6 to 36 kW.cm^2) with the dimension (720 × 1024) for bright spots, carpet, and single particle regions.

Unlike the area ratio trends in core-shell particles, core particles demonstrated a different behaviour. As represented in Figure 10a, beside the bright spots region showing the lowest band ratios, there is an area ratio conversion as the power density is reduced. Unlike the bright spot, single particle and carpet demonstrated the same behaviour according to the power change. In solution, area ratio of particles remains almost the same by changing the power. However, its area ratio is completely different from that of other regions. Furthermore, as shown in Figure 10d, after 14 kW/cm2, the slope of the power-dependence plot of the bright spot region becomes one. However, the slope remains constant at all power ranges for carpet and single particles.

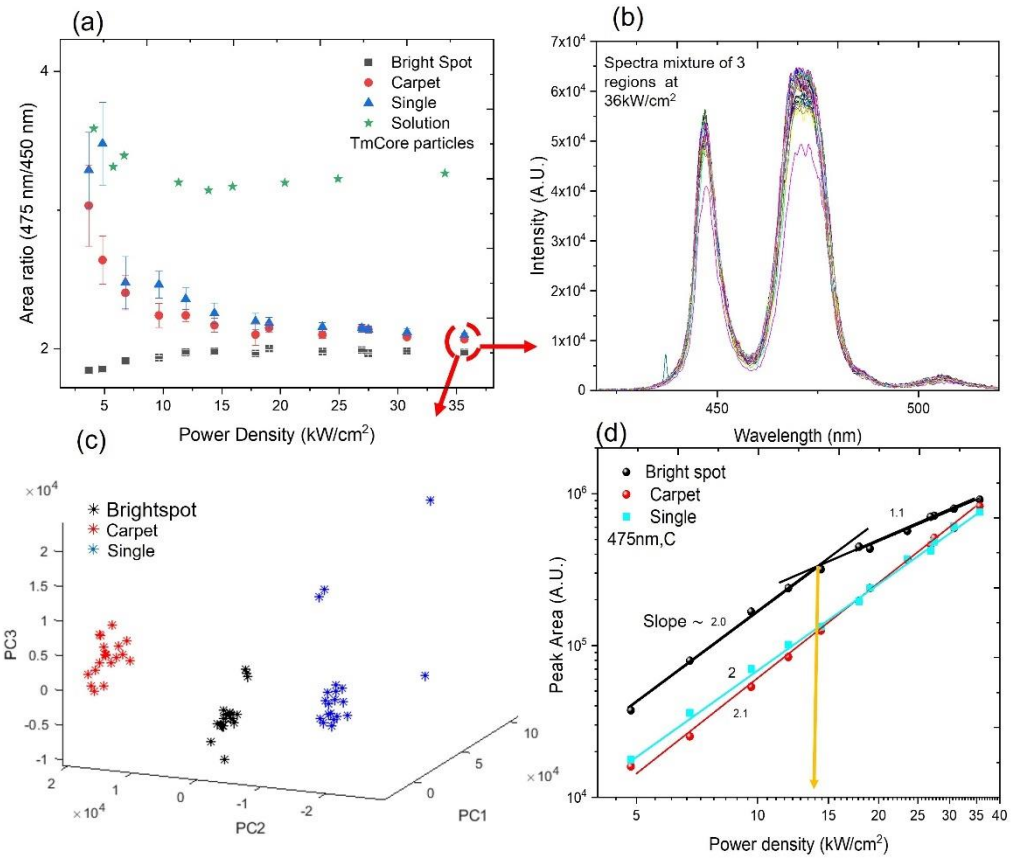

Figure 10. (a) Area ratio at 475 and 450 nm through various power densities (4.6 to 36 kW/cm^2) for bright spot, carpet, single particle, and solution of core particles. (b) Steady state spectra of bright spot, carpet, and single particle regions at high power density (36 kW/cm^2). (c) Score plot with three PCs applied to steady state spectra (b). (d) Power dependence plots at 475 nm for bright spots, carpet, and single particles.

Moreover, at high power density (36 kW/cm^2), because of the low differences among area ratios and steady state spectra (Figure 10a and b), PCA was applied to the core dataset with (60 × 1024) dimension, which consists of 20 spectra of each region (bright spots, carpet, and single). For better demonstration of differences between regions, three PCs accounting for 99.59% of such a variation are selected as illustrated in Figure 10c. The scores of the 3 regions are distributed in three very separated zones, which is significantly different from the result obtained with CS particles. In core-shell particles, bright spot was overlapping with other regions. In addition, by performing PCA on the collection of all core datasets measured at 11 power densities with (660 × 1024) dimension, a clear trend along power density change was observed for core particles (Figure 11). The scores are colocalized for high power density and follow completely different tendencies in the three regions by increasing the power, which is consistent with area ratio results.

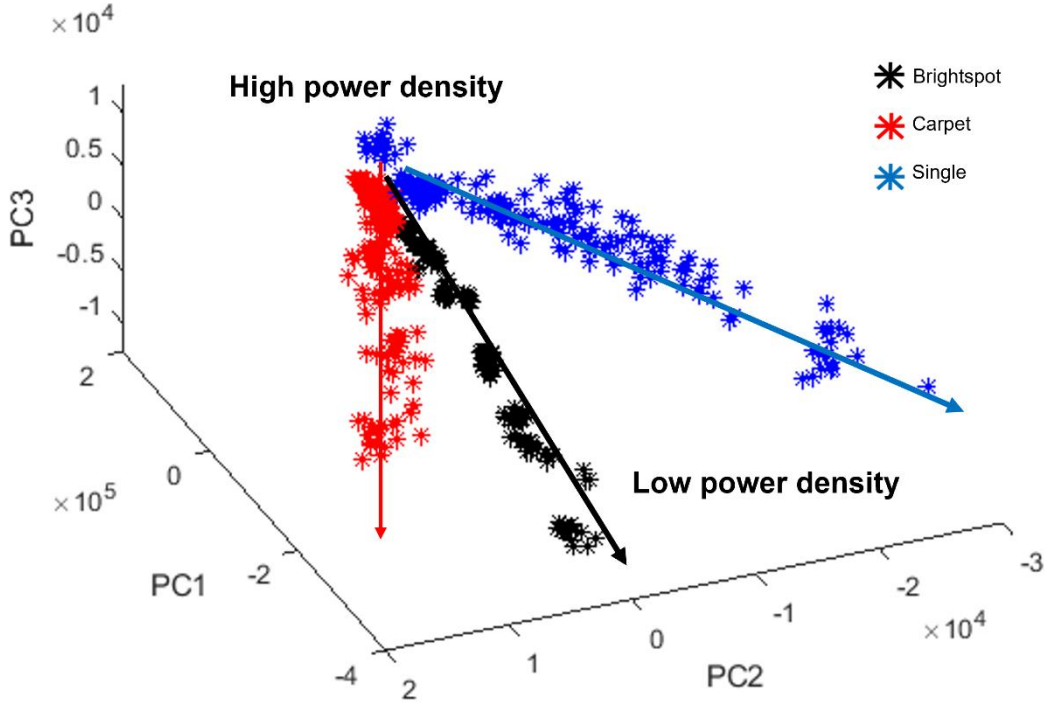

Figure 11. Score plot resulting from PCA applied on all the core dataset with the dimension (660 × 1024) at various power densities (4.6 to 36 kW/cm^2) for bright spot, carpet, and single regions.

In order to investigate the photophysical behaviour of the various assemblies identified in the confocal images (Figure 4a and 5a), we used our new confocal microscopy setup in order to measure steady state spectra of these regions. Power-dependent plots of 450 nm and 475 nm demonstrated different slopes and saturation regimes of these regions, indicating that the photophysical characteristics of these regions are different. Furthermore, the area ratio of 475 nm to 450 nm in core/shell particles reflects the difference between these regions as a function of power density. Additionally, we utilized PCA in order to (i) demonstrate that even in maximum power density, which has the maximum signal overlap, there is still the difference among assemblies, and (ii) display the variance for each power density in relation to each assembly.

By comparing steady sate measurements of core and core-shell particles, the differences among regions for these two kinds of particles are due to the shell: interactions between particles are more feasible in core particles compared to core-shell which results in more discrete clusters in core particles based on their structure of arrangement.[35]

4.5 Time-resolved measurements of 1D, 2D, and 3D assemblies

To further characterize the behaviour of bright spots, carpet, and single particle regions, time-resolved luminescence in various power densities (4.6 to 36 kW/cm^2) were first recorded under 5 ms-square pulse excitation at 976 nm (Figure 12a and b) for core/shell particles.

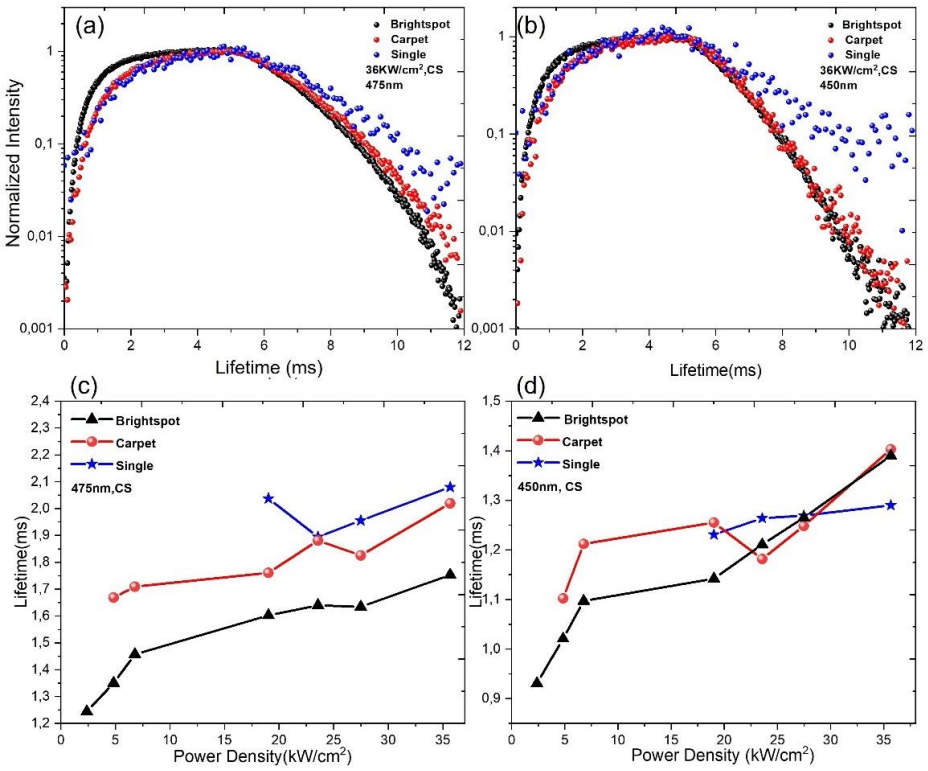

Figure 12. (a, b) Time-resolved emission profiles of the core-shell sample (bright spot, carpet and single particle) with 36 kW/cm^2 excitation power density, at 475 nm (a) and 450 nm (b). (c, d) Calculated decay lifetimes for the three regions (single, carpet and bright spot) in various power densities at 475 nm (c) and 450 nm (d). All time-resolved spectra were measured under square pulse 976 nm irradiation (5 ms irradiation and 7 ms decay).

In core-shell particles, bright spot, carpet, and single particle demonstrate different time-dependent emissions as shown in Figure 12. Contrary to bright spot and carpet, lifetimes of the single particle remain almost unsensitive to power density increase at 450 nm and 475 nm (Figure 12c and d). At 475 nm, bright spot has shorter lifetime than carpet and single particles (by 15% to 20%). At 450 nm, bright spot and carpet have the same lifetime at high power density. Additionally, by increasing the power density, the lifetime values at 450 nm increase to a larger extent than at 475 nm (for carpet: +28% vs. +20% at 450

and 475 nm, respectively; for bright spot: +50% vs. +40% at 450 and 475 nm, respectively). Since the upconversion dynamics depends on the power density,[36] as the power density increases, lifetime increases particularly in the 3D assemblies which have huge amount of activator ions.

Shorter lifetimes obtained in bright spots and carpet are due to more nonradiative processes than in single particles. Indeed, Sevilla et al. demonstrated that interparticle interactions occur in such assemblies.[37] Because of the existence of such UCNP-to-UCNP interactions taking place in all space directions in bright spots (3D aggregates), phonon modes of the crystalline matrix may increase and favour non radiative phonon-assisted relaxation of the activators, leading to the decrease of the measured lifetimes.[38] On the other hand, these inter-particles interactions only occur in the x-y plane in the carpet layout. Thus, carpet is expected to exhibit less phonon-assisted relaxation than bright spots. Hence, phonon-assisted relaxation of the electronically excited states of dopant ions are expected to differently affect the emission properties in the various assemblies.

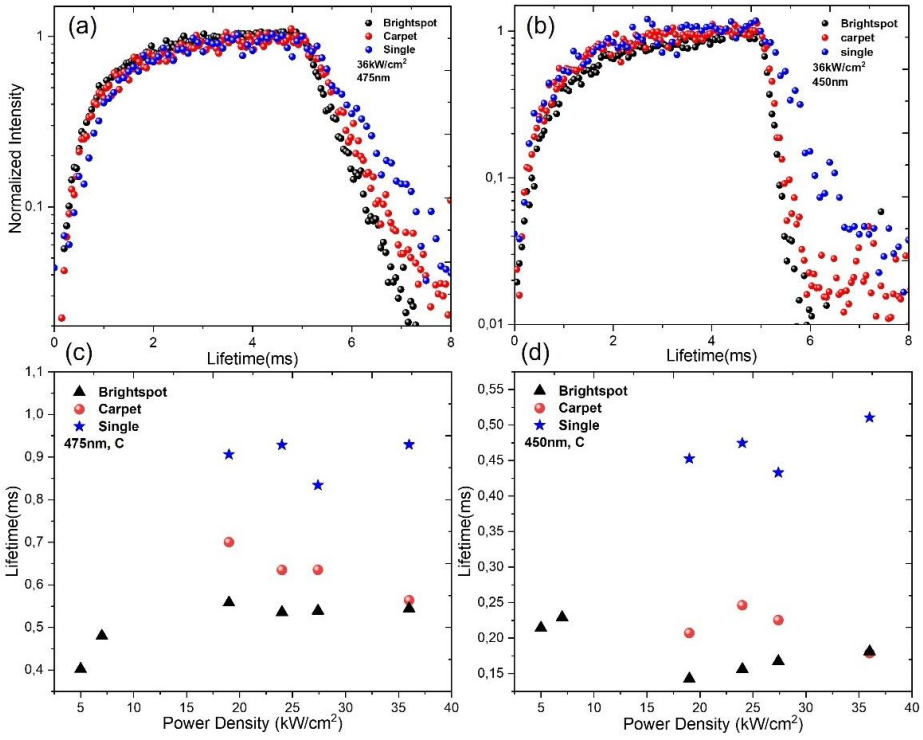

Figure 13. (a, b) Time-resolved emission profiles of the core-only sample (bright spot, carpet and single particle) with 36 kW/cm^2 excitation power density, at 475 nm (a) and 450 nm (b). (c, d) Calculated decay lifetimes for the three regions (single, carpet and bright spot) in various power densities at 475 nm (c) and 450 nm (d). All time-resolved spectra were measured under square pulse 976 nm irradiation (5 ms irradiation and 3 ms decay).

Secondly, the same measurements have been performed for the core-only particles. The trends obtained for the lifetimes in the different regions are different from those of the core-shell particles. As shown in Figure 13c and d, lifetimes in all regions remain approximately unchanged as the power density changes. The lifetimes of bright spot and carpet are significantly lower than the lifetime of single particles at 475 nm and 450 nm at all power densities. In core particles, the absence of shell is expected to induce stronger inter-particles interactions in carpet and bright spots than in the core-shell particles sample, resulting in strong phonon-assisted relaxation and quenching of the activator emission. In this case, regardless of the dimensionality of the arrangement (carpet or bright spot), lifetimes are affected in the same way and quenched more severely than in single particles as presented in Figure 13a and b.

4.6 Conclusion

The optical characterisation of single UCNPs is elevated to a frontier breakthrough of the UCNPs community with respect to the study emphasis of heterogeneous intrinsic structure, distinctive photophysical phenomena, and advanced applications. Therefore, single particle characterization, such as confocal scanning microscope, is a powerful technical approach to exploit the microstructural-dependent spectroscopic characters, which is always compromised in ensemble spectroscopy.

We have developed a new confocal microscope based on a square pulse NIR excitation, from a few µs to ms duration, and an intensified gated CCD camera in order to measure space- and time-resolved emission spectra at single particle level. In order to look at the rising time and interpret it for future analyses, we used squared pulse irradiation.

By measuring the confocal and SEM images, we could show three various assemblies of UCNPs on a clean coverslip: 1) bright spots with multilayer structure, 2) carpets with monolayer structure, and 3) single particles. By measuring steady state spectra under cw irradiation of 976 nm, we calculated band ratio of 475 nm to 450 nm (in different power-density) and power-dependence plot for core-shell and core UCNPs. Analysis of these results revealed that there is a difference in photophysical behaviour among these three regions that also depends on power density. Furthermore, we used PCA method for revealing the hidden spectral pattern among these regions at all power ranges.

In addition, for investigation of photodynamic emission in bright spots, carpet, and single particle regions, time-resolved luminescence in various power densities were recorded under 5ms square pulse excitation at 976 nm. These findings showed lower lifetimes for 3D and 2D assemblies (bright spot and carpet) compared to the single particles which might come from interparticle interactions that increase phonon-assisted relaxation in such assemblies.

4.7 References

1. Naczynski, D., et al., *Rare-earth-doped biological composites as in vivo shortwave infrared reporters.* Nature communications, 2013. **4**(1): p. 1-10.
2. Xu, C.T., et al., *Upconverting nanoparticles for pre-clinical diffuse optical imaging, microscopy and sensing: Current trends and future challenges.* Laser & Photonics Reviews, 2013. **7**(5): p. 663-697.
3. Wang, H.Q., et al., *Rare-earth ion doped up-conversion materials for photovoltaic applications.* Advanced Materials, 2011. **23**(22-23): p. 2675-2680.
4. Zhou, B., et al., *Controlling upconversion nanocrystals for emerging applications.* Nature nanotechnology, 2015. **10**(11): p. 924-936.
5. Ravetz, B.D., et al., *Photoredox catalysis using infrared light via triplet fusion upconversion.* Nature, 2019. **565**(7739): p. 343-346.
6. Li, X., et al., *Energy gap engineering of polymeric carbon nitride nanosheets for matching with NaYF 4: Yb, Tm: enhanced visible-near infrared photocatalytic activity.* Chemical Communications, 2016. **52**(3): p. 453-456.
7. Levy, E.S., et al., *Energy-looping nanoparticles: harnessing excited-state absorption for deep-tissue imaging.* ACS nano, 2016. **10**(9): p. 8423-8433.
8. Chen, G., et al., *(α-NaYbF4: Tm3+)/CaF2 core/shell nanoparticles with efficient near-infrared to near-infrared upconversion for high-contrast deep tissue bioimaging.* ACS nano, 2012. **6**(9): p. 8280-8287.
9. Chen, C., et al., *Multi-photon near-infrared emission saturation nanoscopy using upconversion nanoparticles.* Nature communications, 2018. **9**(1): p. 1-6.
10. Haase, M. and H. Schäfer, *Upconverting nanoparticles.* Angewandte Chemie International Edition, 2011. **50**(26): p. 5808-5829.
11. Auzel, F., *Upconversion and anti-stokes processes with f and d ions in solids.* Chemical reviews, 2004. **104**(1): p. 139-174.
12. Wu, S., et al., *Non-blinking and photostable upconverted luminescence from single lanthanide-doped nanocrystals.* Proceedings of the National Academy of Sciences, 2009. **106**(27): p. 10917-10921.
13. Gnach, A. and A. Bednarkiewicz, *Lanthanide-doped up-converting nanoparticles: merits and challenges.* Nano Today, 2012. **7**(6): p. 532-563.
14. Dong, H., L.-D. Sun, and C.-H. Yan, *Basic understanding of the lanthanide related upconversion emissions.* Nanoscale, 2013. **5**(13): p. 5703-5714.
15. Ma, Q., et al., *Recent progress in time-resolved biosensing and bioimaging based on lanthanide-doped nanoparticles.* Small, 2019. **15**(32): p. 1804969.
16. Würth, C., et al., *Excitation power dependent population pathways and absolute quantum yields of upconversion nanoparticles in different solvents.* Nanoscale, 2017. **9**(12): p. 4283-4294.
17. Chen, G., et al., *Ultrasmall monodisperse NaYF4: Yb3+/Tm3+ nanocrystals with enhanced near-infrared to near-infrared upconversion photoluminescence.* ACS nano, 2010. **4**(6): p. 3163-3168.
18. Kaiser, M., et al., *Power-dependent upconversion quantum yield of NaYF 4: Yb 3+, Er 3+ nano-and micrometer-sized particles–measurements and simulations.* Nanoscale, 2017. **9**(28): p. 10051-10058.
19. Wang, F., et al., *Tuning upconversion through energy migration in core–shell nanoparticles.* Nature materials, 2011. **10**(12): p. 968-973.
20. Johnson, N.J., et al., *Direct evidence for coupled surface and concentration quenching dynamics in lanthanide-doped nanocrystals.* Journal of the American Chemical Society, 2017. **139**(8): p. 3275-3282.
21. Frenzel, F., et al., *Multiband emission from single ß-NaYF4(Yb,Er) nanoparticles at high excitation power densities and comparison to ensemble studies.* Nano Research, 2021. **14**(11): p. 4107-4115.

22. Sedlmeier, A. and H.H. Gorris, *Surface modification and characterization of photon-upconverting nanoparticles for bioanalytical applications.* Chem Soc Rev, 2015. **44**(6): p. 1526-60.
23. Gonell, F., et al., *Aggregation-induced heterogeneities in the emission of upconverting nanoparticles at the submicron scale unfolded by hyperspectral microscopy.* Nanoscale Advances, 2019. **1**(7): p. 2537-2545.
24. Wang, Y., et al., *Critical shell thickness of core/shell upconversion luminescence nanoplatform for FRET application.* The Journal of Physical Chemistry Letters, 2011. **2**(17): p. 2083-2088.
25. Moerner, W., *A dozen years of single-molecule spectroscopy in physics, chemistry, and biophysics*. 2002, ACS Publications. p. 910-927.
26. Dong, H., et al., *Versatile spectral and lifetime multiplexing nanoplatform with excitation orthogonalized upconversion luminescence.* ACS nano, 2017. **11**(3): p. 3289-3297.
27. Gargas, D.J., et al., *Engineering bright sub-10-nm upconverting nanocrystals for single-molecule imaging.* Nature nanotechnology, 2014. **9**(4): p. 300-305.
28. Teitelboim, A., et al., *Energy transfer networks within upconverting nanoparticles are complex systems with collective, robust, and history-dependent dynamics.* The Journal of Physical Chemistry C, 2019. **123**(4): p. 2678-2689.
29. Gorris, H.H. and O.S. Wolfbeis, *Photon-upconverting nanoparticles for optical encoding and multiplexing of cells, biomolecules, and microspheres.* Angewandte Chemie International Edition, 2013. **52**(13): p. 3584-3600.
30. Sedlmeier, A., et al., *Photon upconverting nanoparticles for luminescent sensing of temperature.* Nanoscale, 2012. **4**(22): p. 7090-7096.
31. Fischer, L.H., G.S. Harms, and O.S. Wolfbeis, *Upconverting nanoparticles for nanoscale thermometry.* Angewandte Chemie International Edition, 2011. **50**(20): p. 4546-4551.
32. Maji, S.K., et al. *Towards multiscale reconstruction of perturbated phase from hartmann-shack acquisitions*. in *2012 NASA/ESA Conference on Adaptive Hardware and Systems (AHS)*. 2012. IEEE.
33. Su, Q., et al., *The effect of surface coating on energy migration-mediated upconversion.* J Am Chem Soc, 2012. **134**(51): p. 20849-57.
34. Liu, H., et al., *Balancing power density based quantum yield characterization of upconverting nanoparticles for arbitrary excitation intensities.* Nanoscale, 2013. **5**(11): p. 4770-4775.
35. Wang, J., et al., *Enhancing multiphoton upconversion through energy clustering at sublattice level.* Nat Mater, 2014. **13**(2): p. 157-62.
36. Bergstrand, J., et al., *On the decay time of upconversion luminescence.* Nanoscale, 2019. **11**(11): p. 4959-4969.
37. Rodríguez-Sevilla, P., et al., *Assessing single upconverting nanoparticle luminescence by optical tweezers.* Nano letters, 2015. **15**(8): p. 5068-5074.
38. Liu, G., H. Zhuang, and X. Chen, *Restricted phonon relaxation and anomalous thermalization of rare earth ions in nanocrystals.* Nano Letters, 2002. **2**(5): p. 535-539.

5

Photodynamic investigation of energy transfers from UCNPs (Er and Tm) to Perylene Diimide derivatives

5.1 Introduction

An important part of the production of (opto)electronic devices based on organic materials is the production of thin films containing organic chromophores that conduct charges. These devices include electronic paper, photovoltaic cells, field effect transistors, and light-emitting diodes, among others.[1] Furthermore, perylene diimide derivatives (PDIs, Figure 1a) also have a role to play in this new industrial development, as well as adducts of fullerenes (like PCBMs) and conducting polymer materials (like P3HTs).[2-4] In 1986, Tang developed the first organic solar cell, which contained a perylene dye (3,4:9,10-perylene tetracarboxylic bis-benzimidazole) and a copper phthalocyanine with an efficiency of 1%.[5] PDI are extremely stable organic dyes whose chemistry has been explored in a variety of directions and in a variety of applications. There is a wide range of early applications for these compounds, including car paints, hair-treatment compositions, ink components, and laser dyes.[6-9] In addition, perylene dyes have been reported as N-type materials in organic solar cells in several early studies.[10-13] It is possible to incorporate a wide range of electronic and optical properties into the PDI chromophore by substitution at the so-called bay-positions as shown in Figure 1a.[14] Therefore, it is possible to harvest light from a broad range of wavelengths in the visible spectrum. PDIs are interesting components for electron transfer systems (ultrafast energy and electron transfer cascades in a multichromophoric light harvesting molecular square of nanometric dimensions) and for use in optoelectronic devices because of their ability to accept electrons.[15-18] Nevertheless, the weak absorption in near-infrared (NIR) region limits their further application.[19, 20] As a solution to overcome this shortcoming, UCNPs can be used as donors in FRET-based hybrid materials, since UCNPs emission spectrum well overlaps with the absorption spectrum of the N,N'-Bis(2,6-diisopropylphenyl)perylene-3,4,9,10-tetracarboxylic diimide molecule (Figure 1b).

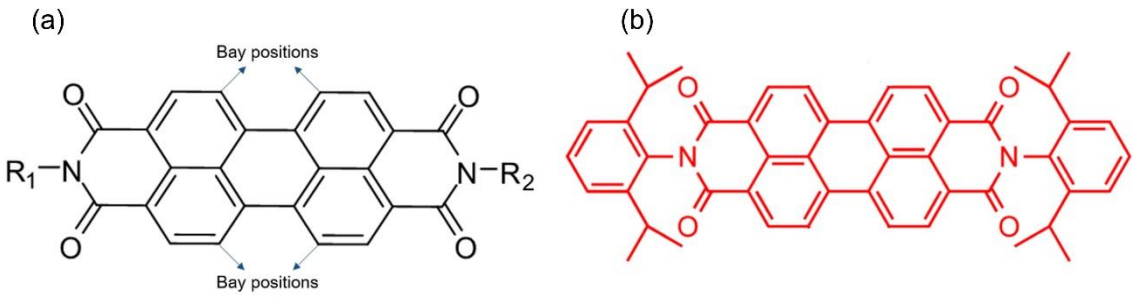

Figure 1. a. General chemical structure of perylene diimide derivatives; b. Molecular structure of N,N'-Bis(2,6-diisopropylphenyl)perylene-3,4,9,10-tetracarboxylic diimide studied in this chapter.

The purpose of this chapter is thus to investigate the possibility of resonance energy transfer under excitation at 976 nm using various UCNPs. We investigated Tm- and Er-based UCNP which show distinct emission spectra upon 976 nm excitation (Figure 2), resulting in different overlapping with the absorption spectra of the considered PDI. Core (C) and coreshell (CS) particles were also examined. Surface modification is indeed expected to provide different energy transfer efficiencies to the PDI. The four considered UCNPs have the following composition:

1) β-$NaYF_4$:20% Yb^{3+}, 2% Tm^{3+} (Core, 12 nm diameter)

2) β-$NaYF_4$:20% Yb^{3+}, 2% Tm^{3+}/$NaYF_4$ (Core-shell , diameter 20 nm, 4 nm-thick shell)

3) β-$NaYF_4$:20% Yb^{3+}, 2% Er^{3+} (Core, 12 nm diameter)

4) β-$NaYF_4$:20% Yb^{3+}, 2% Er^{3+}/$NaYF_4$ (Core-shell, diameter 20 nm, 4 nm-thick shell)

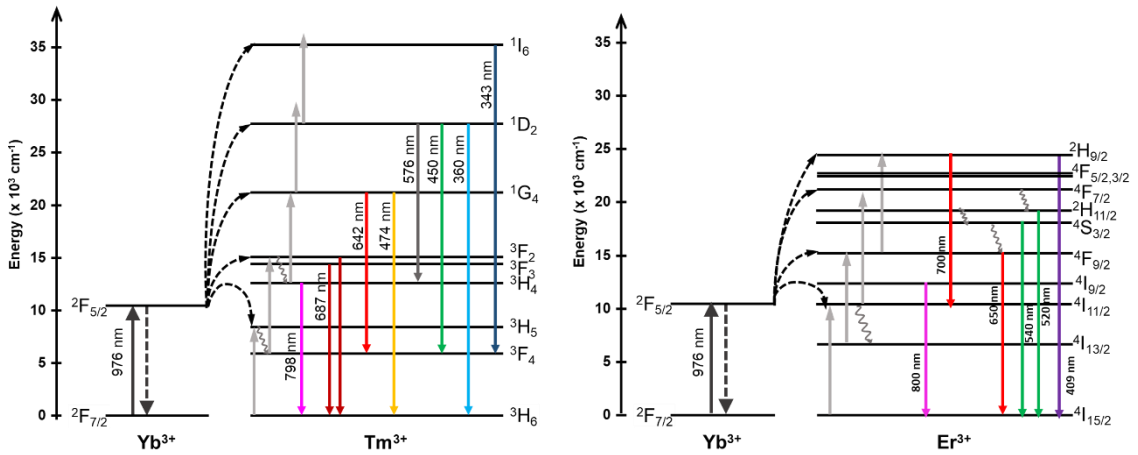

Figure 2. Tm^{3+} (right) and Er^{3+} (left) energy diagram.

PDI was deposited on a UCNP layer adopting two strategies, spin-coating and dropcasting, in order to allow the energy transfer to occur between a single particle UCNP and PDIs. Energy transfer efficiencies were studied using the hyperspectral confocal microscopy setup presented in Chapter 3, for measuring steady state and time-resolved spectra. The obtained results revealed various energy transfer efficiencies depending on

the type of UCNP (Tm or Er, C or CS) and the way of sample preparation (spin-coated or drop-cast PDI molecules).

5.2 Sample preparation

To begin, a dilute solution was prepared from the primary UCNPs solution. For the purpose of achieving single particle level, the primary solution (10mg/mL in Toluene) was diluted 1000 times. 10 µL of UCNPs solution was spin coated on a clean coverslip at 70 × 10^3 rph. All UCNPs samples were processed according to the mentioned procedure.

The PDI solution was prepared by dissolving 1.04 mg of PDI (Mw = 710.87 g/mol) in 4 mL of toluene and obtaining 3.66 × 10^{-4} mol/mL of PDI solution. Then, two different strategies were followed for preparing UCNPs/PDI sample as demonstrated in Figure 2. Our first experiment involved spincoating 20 µL of PDI solution on UCNPs coverslips, and our second experiment involved dropcasting 20 µL of PDI solution on UCNPs coverslips (Figure 3).

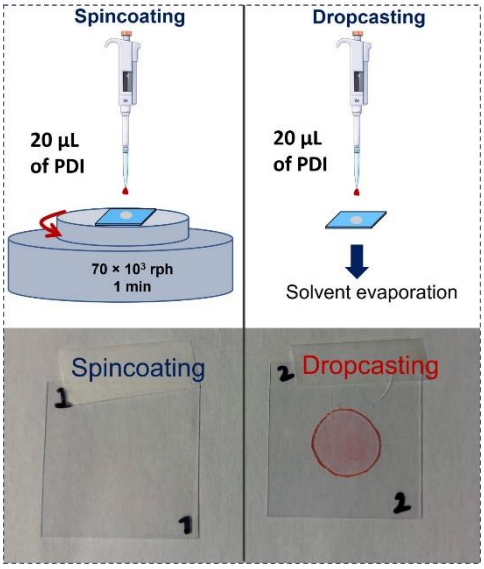

Figure 3. Two preparation methods of PDI/UCNP samples on a microscope coverslip (spincoating and dropcasting).

5.3 Absorption and emission measurements in solution

The absorption and emission spectra of PDI molecules in solution were measured in order to gain a general understanding of how they behave in solution. In this aim, we used double beam Cary 3500 absorption spectrometer (spectral bandwidth of 1 nm and one point every 1 nm) to scan from 400 nm until 600 nm in order to measure PDI absorbance spectrum as demonstrated in Figure 4a. Then, a commercial fluorimeter (Fluoromax-3, Horiba Jobin Yvon) was used to measure the excitation and emission spectra of the same PDI sample in the range of 440 nm to 540 nm and 570 nm to 700 nm, respectively as shown in Figure 4b. For this purpose, a continuous source of light shines onto an excitation monochromator, which selects a band of wavelengths (from 440 nm to 540 nm). This monochromatic excitation light is directed onto a sample, which emits luminescence. The luminescence is directed at 90° into a second, emission monochromator, which selects a band of wavelengths (from 570 nm to 700) and shines them onto a detector.

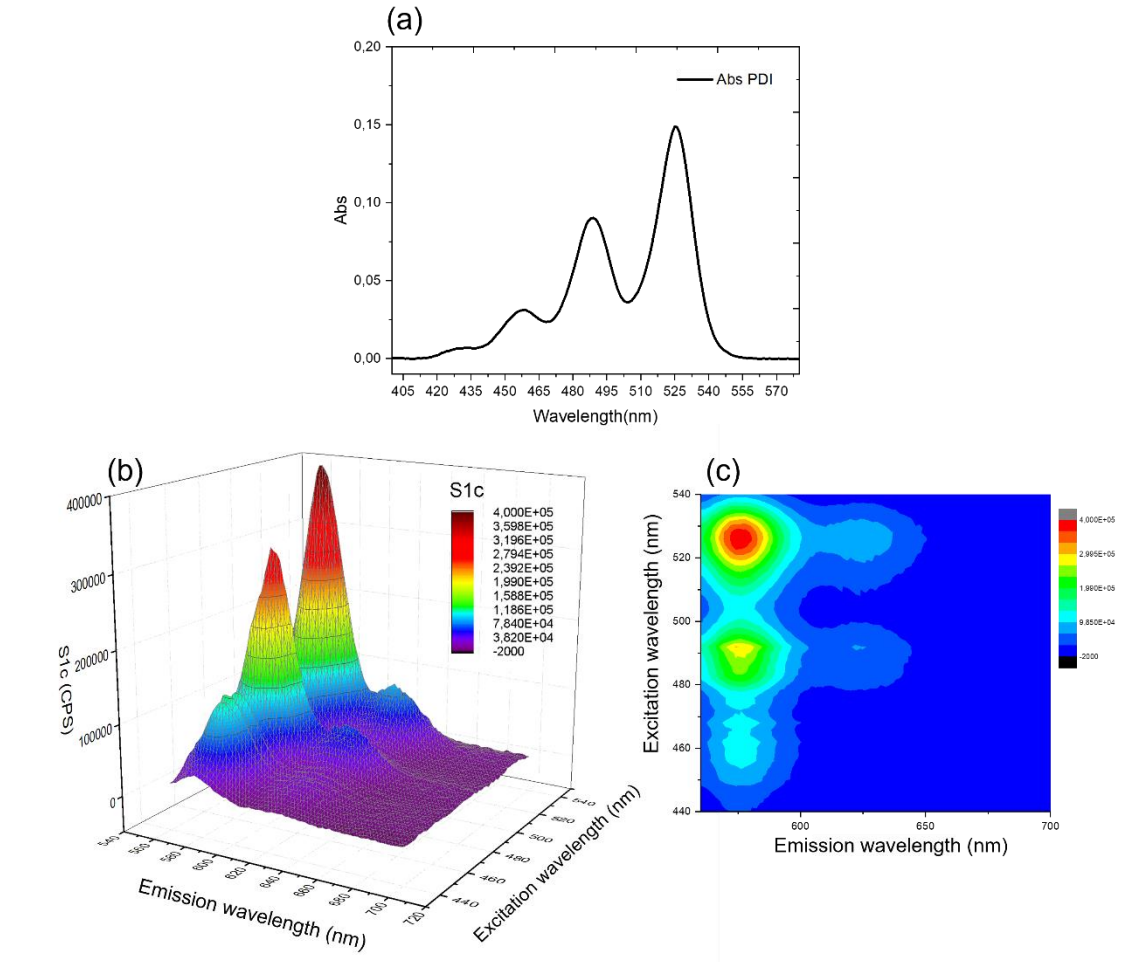

Figure 4. Absorption (a) and excitation-emission spectra (b,c) of PDI in solution.

As presented in Figure 4a, there are three main absorption peaks at 460 nm, 485 nm, and 525 nm in solution. As shown in Figure 4b and c, emission bands in PDI range from 550 nm to 650 nm based on excitation-emission spectra. In addition, as mentioned in Figure 5, there is a good overlap between absorption bands of PDI in solution and emission bands of Tm^{3+} (475 nm and 450 nm which originate form $^1G_4$ and $^1D_2$ states, respectively) and Er^{3+} (520 nm and 540 nm which originate from $^2H_{11/2}$ and $^4S_{3/2}$ states, respectively). Energy transfer is consequently supposed to happen among them. It is however well-known that PDI spectroscopic properties are different whether the molecule is solvated or deposited as a film. This is why these measurements have been then carried out on films (spincoated and dropcast PDI).

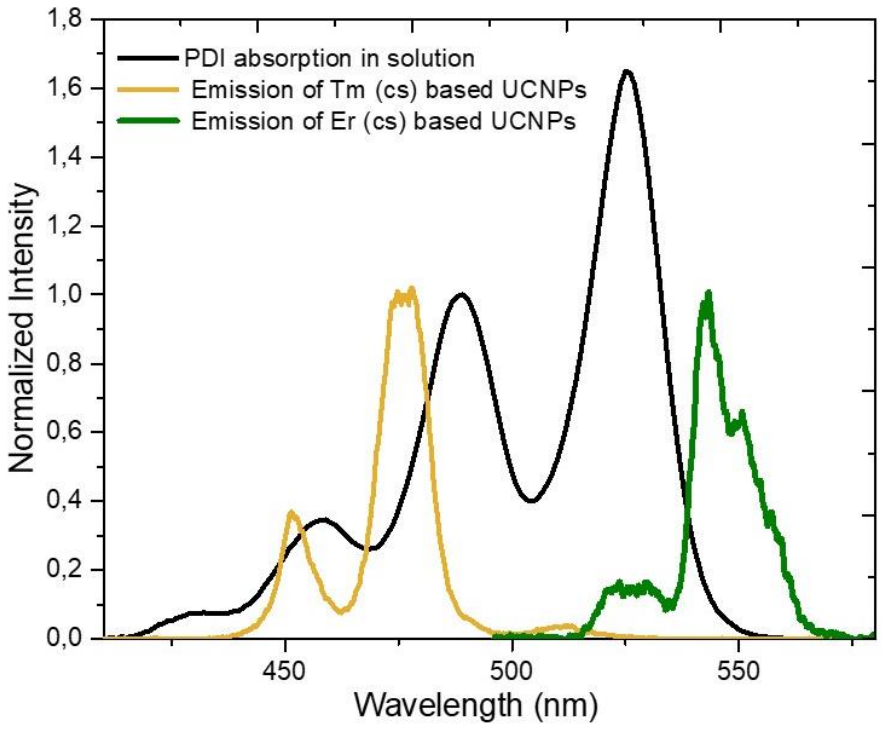

Figure 5. Overlap between PDI absorption in solution and emission bands of Tm^{3+} and Er^{3+}-based UCNPs.

5.4 Photophysical properties of spincoated UCNPs/PDI

5.4.1 Absorption measurements of spincoated UCNPs/PDI

As the PDI solution was spincoated on a clean coverslip, its absorption and excitation-emission spectra were measured on the coverslip. As shown in Figure 6a, its absorption differs from that of PDI in solution, and a red shift can be observed in the absorption of spincoated PDI. In addition, a comparison of the absorption bands with PDI solution also revealed a change in the intensity ratio of absorption bands. The maximum of the emission peaks shift from 560 nm to 630 nm as illustrated in Figure 6b and c. In a study by Williams et al., it has been shown that these differences in absorption can be attributed to the type of aggregation of PDI molecules on the coverslip, which may due to the different assemblies of PDI (J- and H-aggregates).[21] J- and H-aggregates can be identified from the way vibronic coupling in molecules is altered by intermolecular interactions.[22] In many aggregate-forming dye molecules and π-conjugated molecules in general, the main $S_0 \rightarrow S_n$ electronic transitions are coupled to the symmetric vinyl stretching mode (or cluster of modes) with frequencies near 1400 cm^{-1}, resulting in pronounced vibronic progressions in the absorption and photoluminescence (PL) spectra.[23]

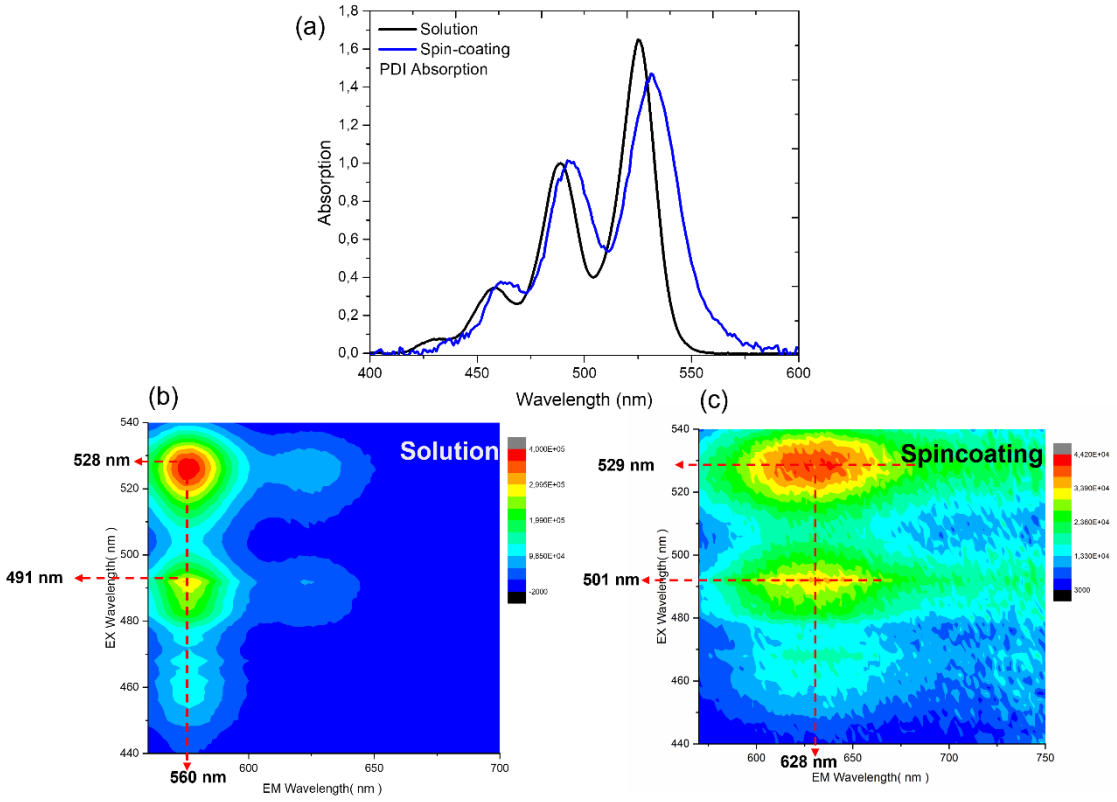

Figure 6. Comparison of absorption (a) and excitation-emission spectra of PDI in solution (b) and spincoated PDI (c).

Red-shift in absorption spectra in spincoated PDI makes a better peak overlap at 525 nm and 540 nm emission, which stem from $^{2}H_{11/2}$ and $^{4}S_{3/2}$ states, of Er^{3+} based UCNPs compared to PDI in solution as represented in Figure 7. On the other hand, the overlap for 450 nm and 475 nm ($^{1}G_{4}$ and $^{1}D_{2}$ states) of Tm^{3+} based UCNPs was slightly reduced.

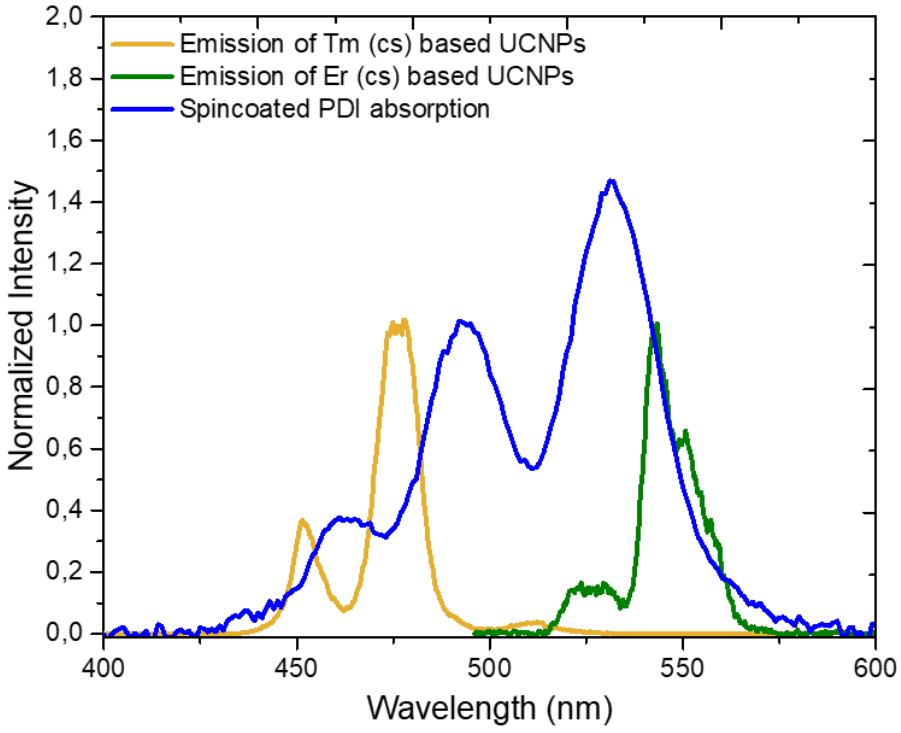

Figure 7. Overlap between PDI absorption in solution and emission bands of Tm^{3+} and Er^{3+} based UCNPs

5.4.2 Steady state measurements of spincoated UCNPs/PDI

All the steady state and time-resolved measurements were performed on the microscopy setup already mentioned in the previous chapter. First, the confocal images of UCNPs and spincoated PDI/UCNPs were measured under cw irradiation at 976 nm with maximum power density (36 kW/cm^2, with a dwell time 6 ms). In Figure 8a, confocal images of Tm coreshell (CS) particles at the single particle level are shown. At the selected image, steady state spectra were measured with intensified CCD camera (1024 × 1024 pixels, PI Max4 Princeton Instruments). All steady state measurements are conducted under the same conditions.

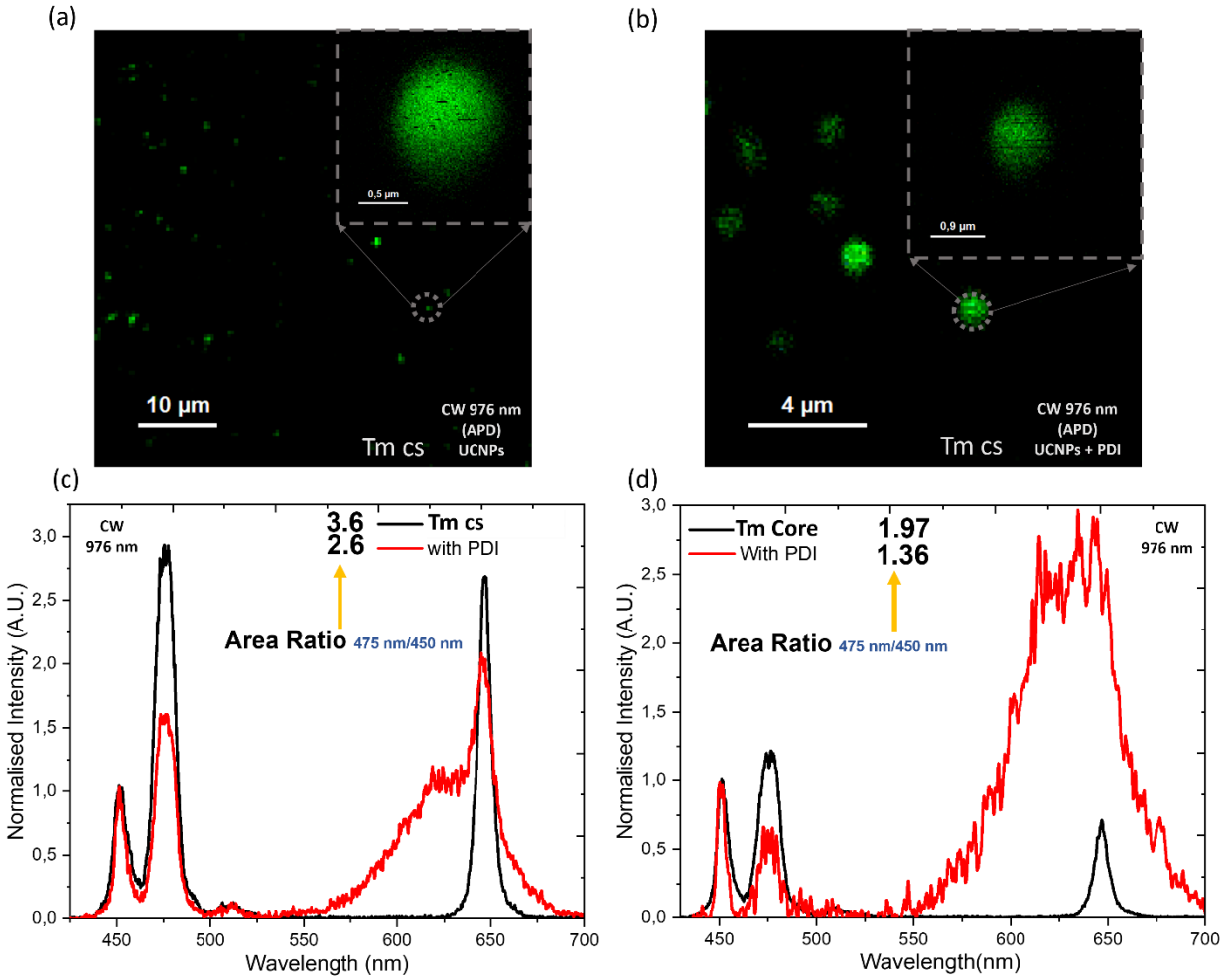

Figure 8. (a) Confocal image of Tm CS particles under 976 nm cw irradiation at maximum power (36 kW/cm^2, 6 ms dwell time). (b) Confocal image of spincoated PDI/Tm CS particles under 976 nm cw irradiation (36 kW/cm^2, 6 ms dwell time). (c) Comparison of steady state spectra of Tm CS particles alone and with PDI. Spectra are normalized on the intensity of the peak at 450 nm. (d) Comparison of steady state spectra of Tm C particles (c) alone and with PDI at 976 nm. Spectra are normalized on the intensity of the peak at 450 nm.

As a first step, we calculated the peak areas for the 450 nm and 475 nm wavelength bands, which correspond to 3 and 4 photon processes in Tm particles (C and CS), respectively.

In Tm CS particles, without PDI coating, the area ratio of 475 nm to 450 nm is around 3.6 as shown in Figure 8c. However, after spincoating the PDI solution, this amount is reduced to 2.6. The changing of this ratio can be attributed to energy transfer from the CS Tm particle to PDI molecules. Moreover, the same results can be seen for the C particles. As well as the area ratio being reduced after spincoating, an inversion of the maximum intensity of the peaks at 475 nm occurs as well.

Dipole-dipole interactions underlie Förster-type energy transfer, which can theoretically be used to convert between molecular spin states. As mentioned in Tm^{3+} ion energy diagram in Figure 2, both emission and energy transfer from 450 nm and 475 nm ($^1D_2 \rightarrow {}^3H_6$ and $^1G_4 \rightarrow {}^3H_6$) are quantum mechanically forbidden due to the selection rules (the difference of spin multiplicity should be zero). It should be noted, however, even in CS particles (with a shell of 4 nm), there is a clear evidence of energy transfer to PDI molecules (as mentioned in Figure 8c and d). In addition, Cravcenco et al. reported that it is possible to transfer excited-state energy through the Förster mechanism without conserving the spin angular momentum.[24] As a result of this idea, the possibility of Förster-type energy transfer has started to be discussed in terms of angular momentum conservation.[25-31] Very important requirement for energy transfer from the triplet excited state of the donor to occur is a finite oscillator strength. This can be achieved by increasing the spin-orbit coupling in the donor. When heavy metals are present, they increase spin-orbit coupling, which causes the selection rules for transitions from singlets to triplets to fall apart.[24]

Similarly, we performed the same measurements on Er^{3+} particles (CS and C, Figure 9). In Er particle, energy transfer to PDI occurs from 545 nm which mostly belongs to $^4S_{3/2}$ state. From a selection rules' point of view, this transition is allowed due to the preservation of the spin multiplicity ($^4S_{3/2} \rightarrow {}^4I_{15/2}$). Then, by calculating the intensity ratio of 540 nm to 650 nm, we could see more reduction of this ratio in CS and C Er particles compared to Tm particles. For example, in Figure 9a, the peak maximum intensity ratio of 540 nm to 650 nm for CS particles without and with PDI are 1.9 and 0.3, respectively. Likewise, this ratio for Er c particles are 1.7 and 0.4 (as shown in Figure 9b). Considering the measured intensity ratio in Er particles, CS particles appear to perform better than c particles.

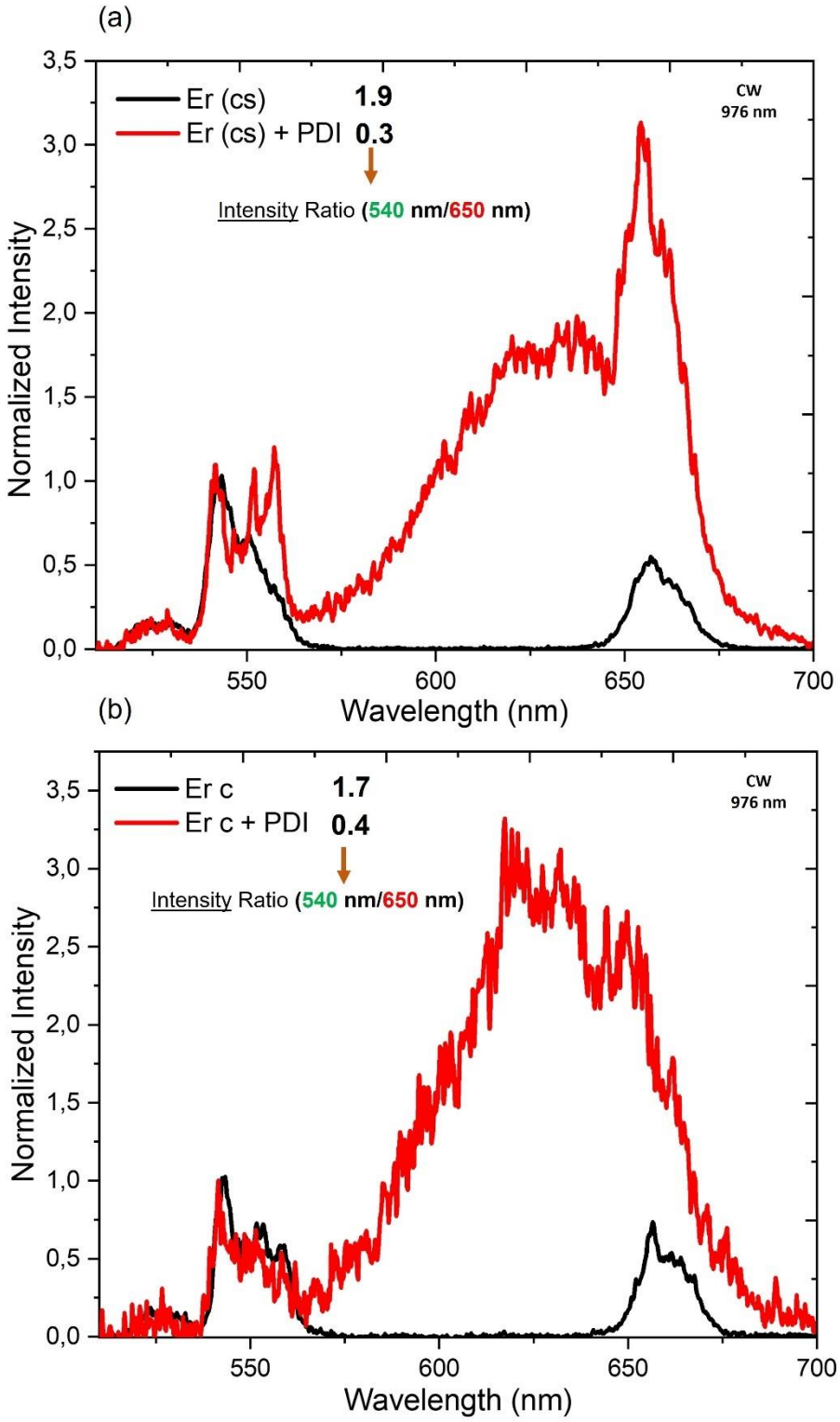

Figure 9. (a) Steady state spectra of Er CS particles without (blackline) and with PDI (redline) under irradiation at 976 nm. (b) Steady state spectra of Er C particles without (blackline) and with PDI (redline) under irradiation at 976 nm. All measurements were performed at maximum power density (36 kW/cm^2).

5.4.3 Time resolved measurements of spincoated of UCNPs/PDI

Time-resolved measurements were performed with our hyperspectral microscopy setup (chapter 3) in order to obtain a more precise estimation of the energy transfer between UCNPs and PDI. As demonstrated in Figure 10a, excitation of UCNPs at 976 nm was performed with square laser pulses. In chapter 3, we discussed how we could produce varying excitation profiles by connecting the Taiko controller (in cw mode) with a delay generator (SRS, model DG535). In total, the sequence period for CS Tm particles is 8 ms, which includes 2 ms for excitation and 6 ms for decay measurement (as shown in Figure 10a). This period for CS Er particles is 2 ms which includes 500 µs for irradiation and 1.5 ms for decay measurement as demonstrated in Figure 11a. A noteworthy point is that time-resolved measurements were made in the same pixels as steady state measurements. All time-resolved measurements were measured by intensified CCD camera (1024 × 1024 pixels, PI Max4 Princeton Instruments). As shown in Figure 10a, time resolved spectra for CS Tm particles at 450 nm and 475 nm were recorded with constant gate width of 50 µs. The first gate time was set to start at 37 ns (insertion delay of the camera) and 160 gates were recorded between 37 ns to 8 ms. In Er CS particles, rising and decays were measured at 540 nm and 650 nm with constant gate width 20 µs. 150 gates were recorded between 37 ns to 2 ms as illustrated in Figure 11a. Despite our best efforts, we were unable to determine the lifetimes of the C particles (Tm and Er) due to a very low signal-to-noise ratio.

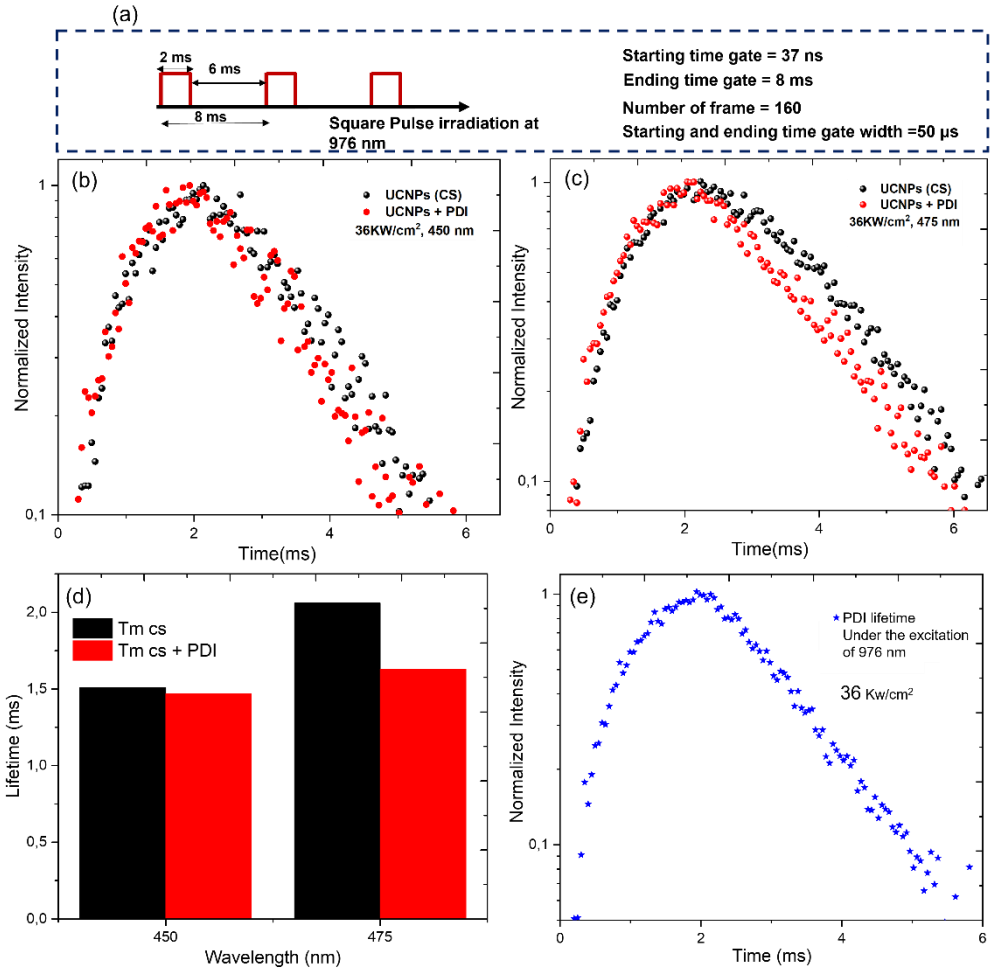

Figure 10. (a) Square pulse excitation sequence used for CS Tm particles samples. (b) and (c) Rising and decay profiles of CS Tm particles at 450 nm (b) and 475 nm (c) under excitation at 36 kW/cm^2. (d) Calculated decay time constants of CS Tm particles at 450 nm and 475 nm. (e) PDI lifetime profile at 625 nm under the 976 nm excitation in the presence of CS Tm particles.

Based on the measured decays at 450 nm and 475 nm (Figures 9b and c), it is completely clear that decay profile at 450 nm remains unchanged after spincoating of PDI. It was also clearly demonstrated by its calculated effective lifetime that remains constant (measured lifetimes are 1.5 ms and 1,47ms for before and after spincoating of PDI, respectively). On the other hand, the measured lifetime at 475 nm reduces 20% after spincoating of PDI (it reduces from 2 ms to 1.6 ms) as shown in Figure 10c and d. This reduction in lifetime can be attributed to the energy transfer that happened between CS Tm particles and PDI molecules which is also in line with steady state results. It

corresponds to FRET efficiency formula $E = 1 - \frac{\tau_{DA}}{\tau_D}$ [32] ($\tau_{DA} \wedge \tau_D$ correspond to the lifetime of donor in the presence and absence of acceptor respectively).

In addition, from the time-resolved measurement it is possible to conclude that the energy transfer happened form 475 nm band that belongs to $^1G_4$ state. Additionally, the lifetime of PDI was measured at 625 nm (under excitation at 976 nm) as shown in Figure 10e. It is estimated that the calculated lifetime, which is approximately 1.2 ms, represents the entire process of upconversion, energy transfer, and possible energy migration through the PDI molecules, as well as the emission of PDI at the end.

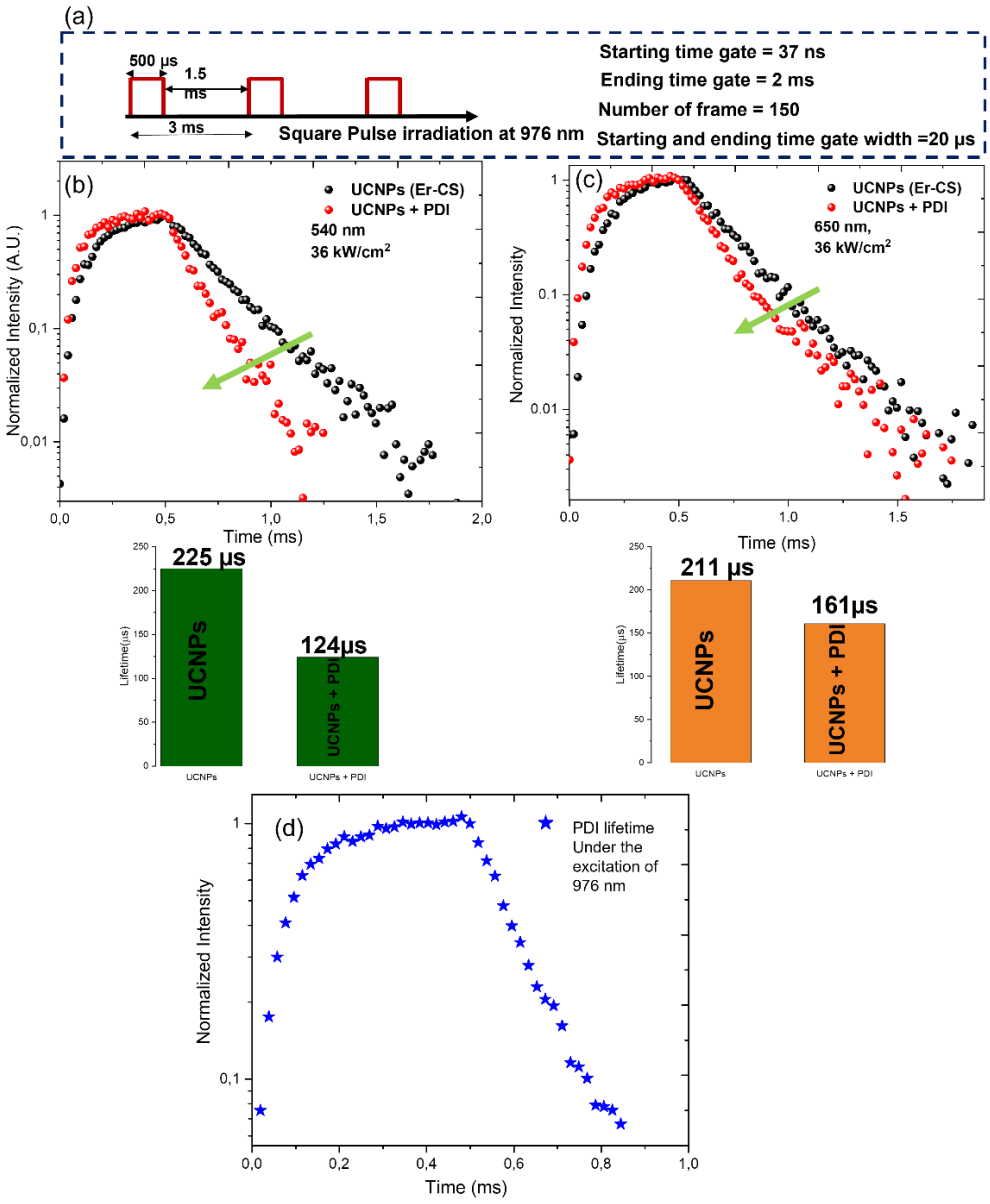

Figure 11. (a) Square pulse excitation sequence used for CS Er particles samples. (b) and (c) Rising and decay profiles of CS Er particles at 540 nm ($^4S_{3/2}$, b) and 650 nm ($^4F_{9/2}$, c) under 976 nm excitation at 36 kW/cm^2. (d) PDI lifetime profile at 625 nm under 976 nm excitation in the presence of CS Er particles.

The lifetime changes of CS Er particles are more sensible than those of CS Tm particles. As demonstrated in Figure 11b and C, calculated lifetime reduced 42% (from 225 µs to 124 µs) and 23% (from 211 µs to 161 µs) at 540 nm ($^4S_{3/2}$) and 650 nm ($^4F_{9/2}$), respectively. These results demonstrated that energy transfer happened from both energy levels ($^4F_{9/2}$, $^4S_{3/2}$) to PDI molecules which is in line with steady state spectra measurements. The difference in the lifetime changes for these bands might be due to the various peak overlap with absorbance of spincoated PDI. It is worth to mention that $^4F_{9/2}$ state has no peak overlap with absorption of PDI. However, as shown in Figure 5b, This state is populated in two ways; first, by energy transfer from Yb and second, by non-radiative depopulation of the 540 nm band. Therefore, if energy transfer occurs at 540 nm, the 650 nm band will also be affected. Moreover, better energy transfer from Er to PDI compared to Tm particles might come from the limitation of selection rules in Tm particles (preservation of spin multiplicity). However, in Er, energy transfer from $^4F_{9/2}$ and $^4S_{3/2}$ states is allowed from spin multiplicity point of view. In general, it can be concluded that the transfer of energy from CS Er particles to PDI is more efficient than that from CS Tm particles.

As spincoating makes difficult the determination of the arrangement of PDI molecules on the clean coverslip (the thickness of coated PDI), we dropcast PDI solution onto the UCNP-coated coverslips. Additionally, dropcasting PDI on the coverslip protects the interlayer PDI molecules (which are in contact with UCNPs) from oxygen in the air. Triplet oxygen can interact with PDI and make singlet oxygen which has higher reactivity and electrophilicity that can cause electron traps on the PDI structure.[33, 34] Therefore, in the following section, we are going to discuss about photophysical properties of dropcast PDI on UCNPs-coated coverslip.

5.5 Photophysical properties of dropcast UCNPs/PDI

5.5.1 Absorption measurements of dropcast UCNPs/PDI

We utilized 20 µL of PDI solution (with the same concentration as used in solution and spincoating, 3.66×10^{-4} mol/mL) for dropcasting it on a UCNPs-coated coverslip. As the PDI solution was dropcast on a clean coverslip, its absorption and excitation-emission spectra were measured on the coverslip. As shown in Figure 12a, its absorption differs

from that of PDI in solution and spincoated PDI, and a red shift can be observed in the absorption of dropcast PDI. In addition, comparison of the absorption bands with PDI solution and spincoated PDI also revealed a change in the intensity ratio of the absorption bands as shown in Figure 12a. According to Figure 12b, this red shift favours more Er particles due to the better overlap between PDI absorption and Er emission at 540 nm. The maximum of the emission peaks shifts from 628 nm (for the spincoated PDI) to 700 nm as illustrated in Figure 12c.

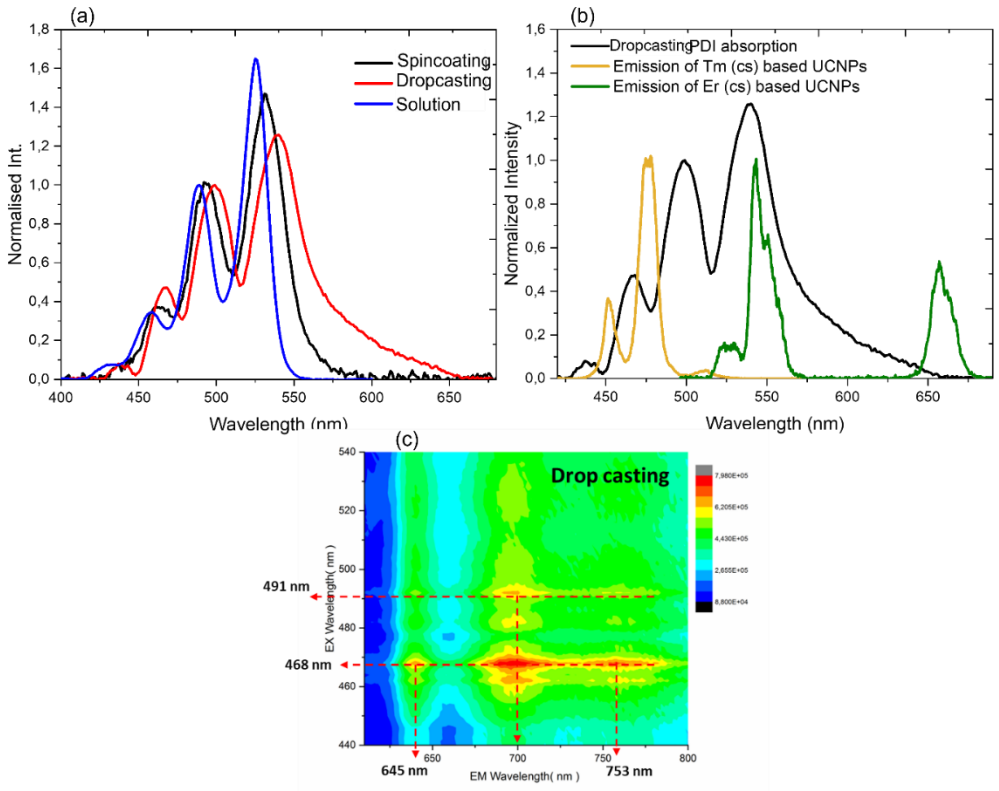

Figure 12. (a) Absorption spectra for PDI in solution, spincoated, and dropcast forms. (b) Peak overlap between absorption of dropcast PDI and emission of CS Tm and Er particles. (c) Excitation and emission spectra of dropcast PDI.

5.5.2 Steady state measurements of dropcast UCNPs/PDI

As c Tm and Er particles have a lower signal-to-noise ratio when compared to CS Tm and Er particles, we have used only CS Tm and Er particles here. As in section 4.4.2, we calculated the peak areas for the 450 nm and 475 nm wavelength bands, which correspond to 3 and 4 photon processes in Tm CS particles. In Tm CS particles, without PDI coating, the area ratio of 475 nm to 450 nm is around 3.6 as shown in Figure 13a. However, after dropcasting, this amount reduced to 3.04. The changing of area ratio can be attributed to

energy transfer from CS Tm particle to PDI molecules. The comparison of PDI emission in Figure 13a and Figure 8b clearly shows stronger signal of PDI emission (at 600 nm) in spincoated PDI compared to dropcast PDI. It has been suggested that this quenching of signals can be attributed to high degree of photon reabsorption of PDI molecules following dropcasting.

As in section 4.4.2, the intensity ratio of 540 nm to 650 nm were measured. In Er particles, energy transfer to PDI occurs form 545 nm which mostly belongs to and $^4S_{3/2}$ state. As previously mentioned, energy transfer from this state is quantum mechanically allowed. Then, by calculating the intensity ratio of 540 nm to 650 nm, we could see less reduction of this ratio in dropcast PDI compared to spincoated one. For example, in Figure 13b, the intensity ratio of 540 nm to 650 nm for CS particles without and with PDI are 1.9 and 1.3, respectively. Due to the peak overlap between the emission of Er particles at 650 nm and the absorption of PDI, the intensity ratio cannot be completely accurate for the energy transfer.

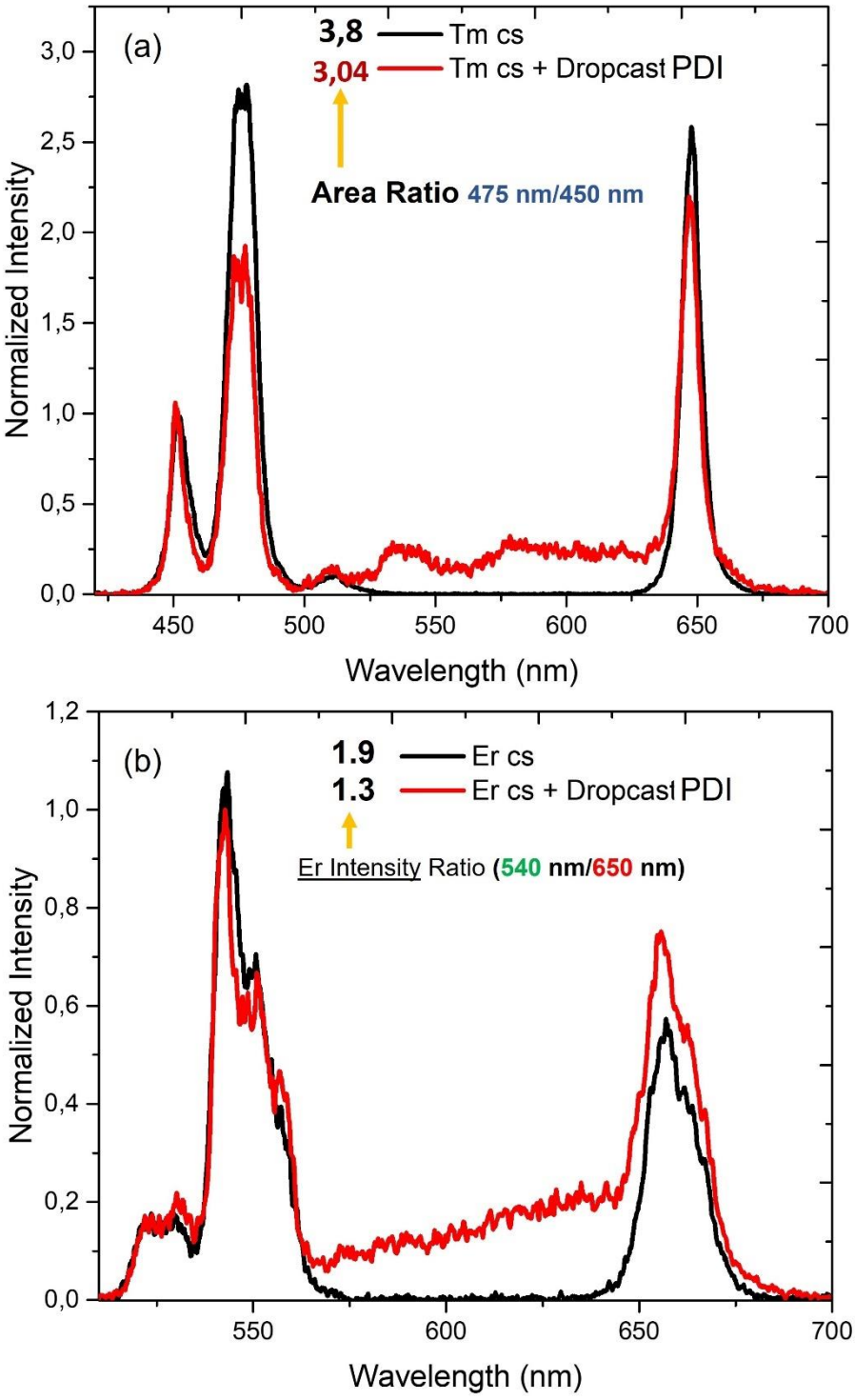

Figure 13. (a) Steady state spectra of CS Tm particle with (redline) and without (blackline) dropcast PDI. (b) Steady state spectra of CS Er particle with (redline) and without (blackline) dropcast PDI. All the steady state spectra were measured 976 nm excitation at maximum power density (36kW/cm^2).

5.5.3 Time-resolved measurements of dropcast UCNPs/PDI

For measuring rising and decay profiles, we used the same setup as in 4.4.3 section. Time-resolved measurements for dropcast PDI/Tm CS particles samples were performed in the same way as for spincoated PDI samples. Figure 14a shows that the sequence period for CS Tm particles is 8 ms, which includes 2 ms excitation and 6 ms decay. In addition, 160 gates were recorded between 37 ns to 8 ms with 50 µs gate constant. In addition, for Tm and Er particles, time-resolved measurements were made in the same pixels as steady state measurements. In dropcast PDI, Tm lifetimes at 450 nm and 475 nm experience more significant changes compared to spincoated one (as demonstrated in Figure 14b and c). Figure 14d show that Tm decay at 450 nm decreases from 1.5 ms to 1.06 ms. Moreover, the decay time at 475 nm experiences a greater decrease than that of the spincoated sample, decreasing from 2.06 ms to 1.4 ms (as shown in Figure 14c).

Logically, each UCNP is better surrounded in dropcasting situation compared to spincoated one. Therefore, it is reasonable to assume that dropcasting of PDI is likely to induces more quenching of Tm ions inside each particle, which occasions stronger decrease of the Tm decay time constants at 450 nm and 475 nm. Figure 14e shows the measured PDI lifetime at 625 nm under 976 nm irradiation. According to the calculated effective lifetime of PDI, it is quite the same amount as before, which is 1.1 ms. PDI lower signal might be due to the photon reabsorption in dropcasting situation.

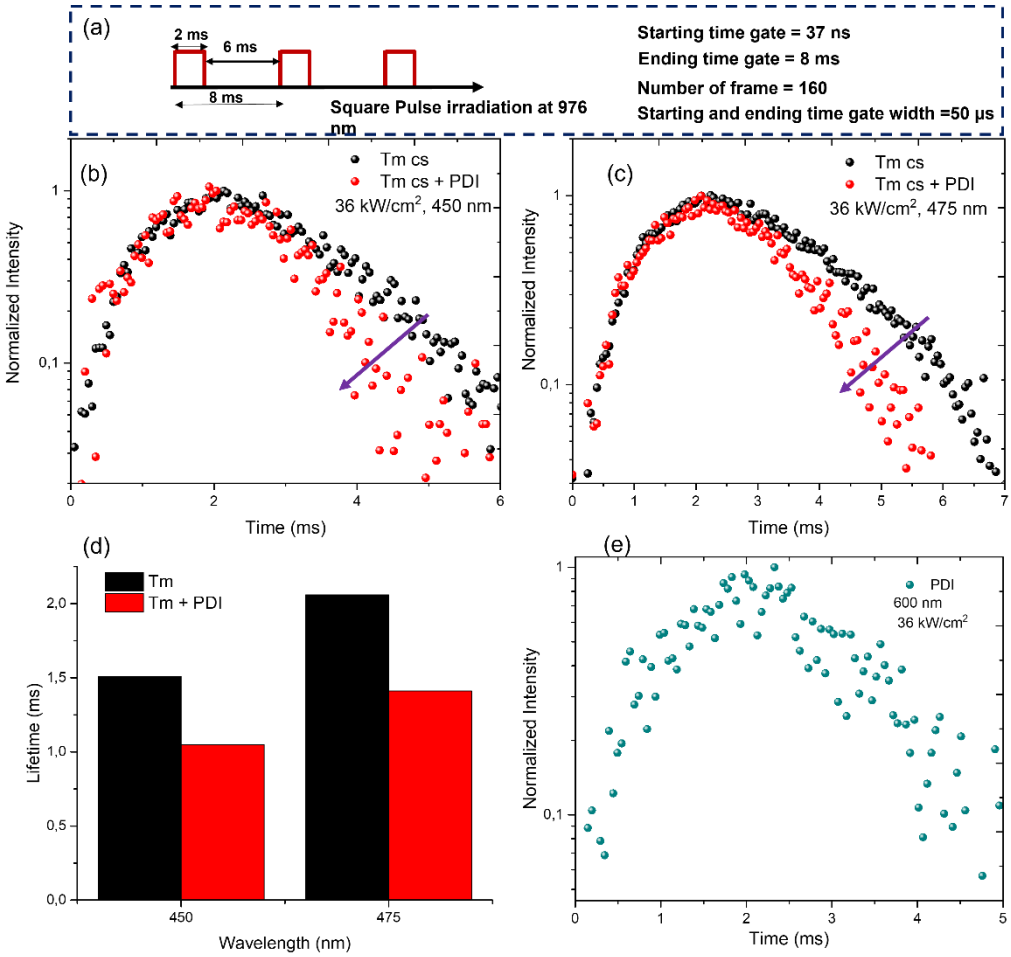

Figure 14. (a) Square pulse excitation of CS Tm particles. It takes 8 ms for each sequence to complete, including 2 ms for excitation and 6 ms for decay. For measuring rising and decay profile, 160 frames were performed between 37 ns and 8 ms with 50 µs gate width constant. (b) and (c) Rising and decay profile of CS Tm particles at 450 nm and 475 nm under the excitation of 976 nm at 36 kW/cm^2. (d) Calculated decay time of CS Tm particles at 450 nm and 475 nm. (e) PDI lifetime profile under the excitation of 976 nm in the presence of CS Tm particles.

There is a slight change in the conditions for time-resolved measurements for Er particles. Due to the lower signal, the excitation duration was increased to 1 ms rather than 0.5 ms (as mentioned in Figure 15a). Lower signal in Er particle clearly demonstrates more quenching of Er ions inside each particle. Therefore, it is possible to point out that in each particle, most of the Er ions, in outer and middle layer, have the chance for energy transfer (as discussed in chapter 2 section 2.2.3). As a result, a few inner Er ions can emit under this condition (dropcast PDI). Although there is a perfect peak overlap between Er emission bands and the absorption of dropcast PDI (Figure 12b), less change in Er lifetime states, at 540 nm and 650 nm, is observable (as shown in Figure 15b, c and d). This is due

to the longer FRET distance between inner Er ions and PDI molecules in the surface. Then it is reasonable to observe less change in Er lifetime.

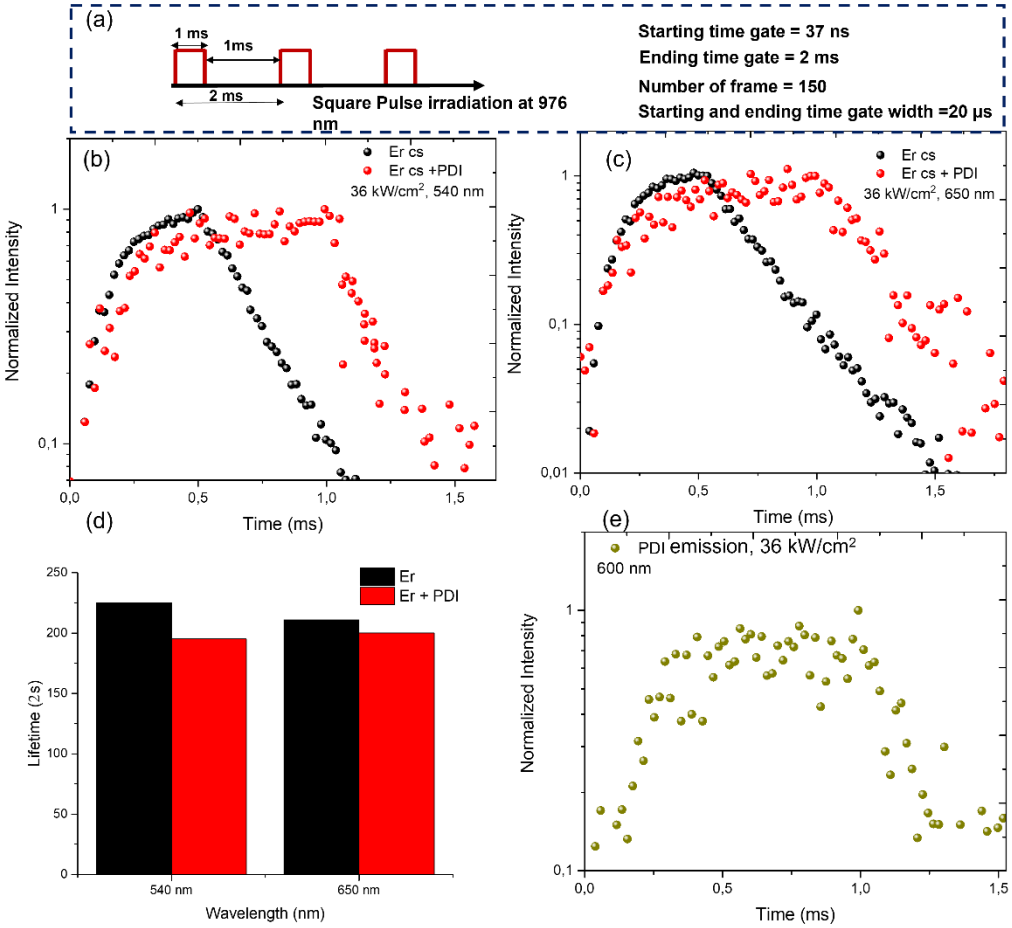

Figure 15. (a) Square pulse excitation of CS Er particles which contains 2 ms for each sequence to complete, including 1 ms for excitation and 1 ms for decay. For measuring rising and decay profile, 150 frames were performed between 37 ns and 2 ms with 20 µs gate width constant. (b) and (c) Rising and decay profile of CS Er particles at 540 nm ($^4S_{3/2}$) and 650 nm ($^4F_{9/2}$) under the excitation of 976 nm at 36 kW/cm^2. (d) Calculated decay time of CS Er particles at 540 nm and 650 nm (e) PDI lifetime profile under the excitation of 976 nm in the presence of CS Er particles.

5.6 Conclusion and outlook

PDI molecules have unique photophysical properties, such as ultrafast energy transfer, however, they are not capable of absorbing light in the near infrared region. Therefore, UCNPs are one of the best options for NIR regions in order to cover this drawback. In this chapter, we investigated the energy transfer process between UCNPs (with Tm and Er emitters) and PDI molecules with confocal microscopy setup for measuring steady state and time-resolved spectra. PDI molecules were not directly attached to the surfaces of UCNPs. Instead, two usual methods, spincoating and dropcasting, were employed. Moreover, since photophysical properties of PDI molecules demonstrated a different behaviour in these two methods, it was necessary to investigate the energy transfer in both methods with various UCNPs.

With spincoating method, for both emitters (Tm and Er) in CS and C architectures, we could see the emission spectra of PDI molecules under the excitation of 976 nm. Based on the time-resolved decays, lifetime of Er CS particles diminished more significantly compared to CS Tm particles, which showed better energy transfer to PDI molecules. On the other hand, in dropcast method, based on the time resolved measurement, it is possible to conclude that both CS Tm and CS Er particles emission was quenched due to the better energy transfer to PDI. It seems that with the dropcasting method, particles were surrounded with enough numbers of PDI molecules. This high number of acceptor molecules makes the energy transfer possible not only from the emitters close to the surface but also from the emitters in the middle layer of a UCNP. However, the drawback of this method is the photon reabsorption of PDI molecules due to their high concentration. Accordingly, dropcast PDI can show a better energy transfer process, but it is necessary to investigate the optimal thickness of dropcast PDI molecules in order to lower the photon reabsorption rate.

For the future analysis, by measuring the quantum yield of the particles, it is possible to have an estimation about FRET distance (R_0). Furthermore, by measuring the band ratio at varying power densities, the effect of power on the band ratio can be determined.

5.7 References

1. Reisch, M.S., *Printing the Right Connections.* CHEMICAL & ENGINEERING NEWS, 2011. **89**(2): p. 20-21.
2. Brabec, C., U. Scherf, and V. Dyakonov, *Organic photovoltaics: materials, device physics, and manufacturing technologies*. 2011: John Wiley & Sons.
3. Dennler, G., M.C. Scharber, and C.J. Brabec, *Polymer-fullerene bulk-heterojunction solar cells.* Advanced materials, 2009. **21**(13): p. 1323-1338.
4. Piliego, C., et al., *High Electron Mobility and Ambient Stability in Solution-Processed Perylene-Based Organic Field-Effect Transistors.* Advanced Materials, 2009. **21**(16): p. 1573-1576.
5. Tang, C.W., *Two-layer organic photovoltaic cell.* Applied physics letters, 1986. **48**(2): p. 183-185.
6. Langhals, H., *Cyclic carboxylic imide structures as structure elements of high stability. Novel developments in perylene dye chemistry*. Heterocycles, 1995. **1**(40): p. 477-500.
7. Schmidt-Mende, L., et al., *Self-organized discotic liquid crystals for high-efficiency organic photovoltaics*. Science, 2001. **293**(5532): p. 1119-1122.
8. Schneider, M., et al., *Novel Electroluminescent Devices Based on Perylene-Doped Sol–Gel Layers.* Advanced Materials, 2000. **12**(5): p. 351-354.
9. Zollinger, H., *Color chemistry: syntheses, properties, and applications of organic dyes and pigments*. 2003: John Wiley & Sons.
10. Ranke, P., et al., *Electroluminescence and electron transport in a perylene dye.* Applied physics letters, 1997. **71**(10): p. 1332-1334.
11. Struijk, C.W., et al., *Liquid crystalline perylene diimides: architecture and charge carrier mobilities.* Journal of the American Chemical Society, 2000. **122**(45): p. 11057-11066.
12. Law, K.Y., *Organic photoconductive materials: recent trends and developments.* Chemical Reviews, 1993. **93**(1): p. 449-486.
13. Dimitrakopoulos, C.D. and P.R. Malenfant, *Organic thin film transistors for large area electronics.* Advanced materials, 2002. **14**(2): p. 99-117.
14. Wang, Z., et al., *Bay Position Substituted Perylene Diimide Derivatives as Cathode Interface Materials for High-Efficient Nonfullerene and Fullerene Organic Photovoltaics.* ACS Applied Energy Materials, 2022.
15. O'Neil, M.P., et al., *Picosecond optical switching based on biphotonic excitation of an electron donor-acceptor-donor molecule.* Science, 1992. **257**(5066): p. 63-65.
16. Mativetsky, J.M., et al., *Self-Assembly of a Donor-Acceptor Dyad Across Multiple Length Scales: Functional Architectures for Organic Electronics.* Advanced Functional Materials, 2009. **19**(15): p. 2486-2494.
17. Gordan, O., et al., *Ellipsometric study of an organic template effect: H2Pc/PTCDA.* Organic electronics, 2006. **7**(6): p. 521-527.
18. Schouwink, P., et al., *The influence of molecular aggregation on the device properties of organic light emitting diodes.* Thin solid films, 2000. **372**(1-2): p. 163-168.
19. Shao, Y., et al., *Engineering of upconverted metal–organic frameworks for near-infrared light-triggered combinational photodynamic/chemo-/immunotherapy against hypoxic tumors.* Journal of the American Chemical Society, 2020. **142**(8): p. 3939-3946.
20. Dong, H., L.-D. Sun, and C.-H. Yan, *Energy transfer in lanthanide upconversion studies for extended optical applications.* Chemical Society Reviews, 2015. **44**(6): p. 1608-1634.
21. Williams, R.M., N.n. Vân Anh, and I.H. van Stokkum, *Triplet formation by charge recombination in thin film blends of perylene red and pyrene: Developing a target model for the photophysics of organic photovoltaic materials.* The Journal of Physical Chemistry B, 2013. **117**(38): p. 11239-11248.
22. Spano, F.C., *The spectral signatures of Frenkel polarons in H-and J-aggregates.* Accounts of chemical research, 2010. **43**(3): p. 429-439.
23. Kistler, K., et al., *Absorption, circular dichroism, and photoluminescence in perylene diimide bichromophores: Polarization-dependent H-and J-aggregate behavior.* The Journal of Physical Chemistry B, 2012. **116**(1): p. 77-86.

24. Cravcenco, A., et al., *Multiplicity conversion based on intramolecular triplet-to-singlet energy transfer.* Science advances, 2019. **5**(9): p. eaaw5978.
25. Skaisgirski, M., X. Guo, and O.S. Wenger, *Electron accumulation on naphthalene diimide photosensitized by [Ru (2, 2'-Bipyridine) 3] 2+*. Inorganic Chemistry, 2017. **56**(5): p. 2432-2439.
26. Chang, Y.L., et al., *Highly efficient warm white organic light-emitting diodes by triplet exciton conversion.* Advanced Functional Materials, 2013. **23**(6): p. 705-712.
27. Chang, Y., et al., *Highly efficient greenish-blue platinum-based phosphorescent organic light-emitting diodes on a high triplet energy platform.* Applied Physics Letters, 2014. **104**(17): p. 64_1.
28. Chang, Y.-L. and Z.-H. Lu, *White organic light-emitting diodes for solid-state lighting.* Journal of Display Technology, 2013. **9**(6): p. 459-468.
29. Cerdán, L., et al., *FRET-assisted laser emission in colloidal suspensions of dye-doped latex nanoparticles.* Nature Photonics, 2012. **6**(9): p. 621-626.
30. Cadranel, A., et al., *Electronic energy transduction from {Ru (py) 4} chromophores to Cr (III) luminophores.* Inorganic Chemistry, 2018. **57**(6): p. 3042-3053.
31. Bonn, A.G. and O.S. Wenger, *Photoinduced charge accumulation by metal ion-coupled electron transfer.* Physical Chemistry Chemical Physics, 2015. **17**(37): p. 24001-24010.
32. Muhr, V., et al., *Particle-size-dependent Forster resonance energy transfer from upconversion nanoparticles to organic dyes.* Analytical chemistry, 2017. **89**(9): p. 4868-4874.
33. Zschieschang, U., et al., *Separating the impact of oxygen and water on the long-term stability of n-channel perylene diimide thin-film transistors.* Organic Electronics, 2015. **26**: p. 340-344.
34. Blacha-Grzechnik, A., et al., *Efficient generation of singlet oxygen by perylene diimide photosensitizers covalently bound to conjugate polymers.* Journal of Photochemistry and Photobiology A: Chemistry, 2020. **388**: p. 112161.

6

Conclusion and future prospects

6.1 Conclusion

After absorption of NIR light (at 976 nm), there are numerous ET pathways in a UCNP. It is convenient to rationalize UCNP luminescence spectra with arrows between atomic energy levels, but in reality, upconverted emission in lanthanide-doped nanoparticles is the result of a complex network of photophysical transitions which arise from a non-linear process. Therefore, understanding the nuances of ET between lanthanide ions is critical to optimize UCNP emissions. In this thesis, we tried to decipher ET pathways in UCNPs by designing spectroscopy and microscopy setups which enabled us to study of dynamic emission of UCNPs.

In the first part of this work, we demonstrated a great enhancement of upconversion luminescence due to the reduction of surface quenching upon addition of an inert shell β-$NaYF_4$ (around 4 nm) to 5 nm Gd_2O_2S:20%Yb,1%Tm by using steady state spectra and time-resolved emission with a ns pulse setup equipped with a time-gated ICCD camera.

Additionally, in order to characterize the dynamics of interactions among dopant ions, temperature cycling method was used to design sub-3 nm particles with a reduced number of emitters inside a UCNP. Therefore, we investigated the photophysical properties of these ultrasmall C UCNPs during the phase transition from α to β polymorphs by measuring their luminescence emission (under cw irradiation at 976 nm) and time-resolved luminescence emission (under ms pulse square excitation at 976 nm). These results enable us to investigate the optimum number of cycles needed for having bright enough particles. In addition, decreasing the size of UCNP down to less than 3 nm inevitably brings strong quenching effects coming from high surface-to-volume ratios but simultaneously reduces the likelihood for activator concentration quenching by cross-relaxation (CR), as the number of Tm^{3+} ions per UCNP is also automatically reduced. We demonstrated that these quenching effects are strongly dependent on the emission bands considered. Ultrasmall C particles, due to their size, have a reduced number of activators (average less than 2), and cross relaxation is thus less efficient and on the other hand, reducing the size of the particle entails an increased influence of surface quenching. However, in bigger particles the effect of cross relation, Yb concentration, and surface coating with a shell on the emission dynamics of the different Tm excited states were addressed by measuring their time-resolved luminescence (under ns pulse excitation at 976 nm) and direct excitation of Tm^{3+} (under ns pulse excitation at 355 nm).

Furthermore, using our confocal setup, we showed the heterogeneity of the photo-physical properties of 1D, 2D and 3D UCNPs layouts. We measured steady state spectra (in cw excitation at 976 nm) and time-resolved profiles (in square pulse irradiation at 976 nm) in the same pixel at various power density for CS and C Tm particles (β-$NaYF_4$:20% Yb^{3+}, 2% Tm^{3+} and β-$NaYF_4$:20% Yb^{3+}, 2% Tm^{3+}/$NaYF_4$) spincoated on a clean coverslip. For better demonstration of the heterogeneity among steady state spectra of UCNPs in the three mentioned arrangements, we utilized principal component analysis (PCA) applied to the spectral data obtained for different power densities. In addition, measured time-resolved luminescence demonstrated lower lifetimes in 3D and 2D assemblies (bright spot and carpet) by comparison to the single particles which might come from inter-particle interactions that increase phonon-assisted relaxation in such assemblies.

In the second application, we investigated the energy transfer process occurring between specific emission bands of UCNPs (with Tm and Er emitters) and perylene diimide (PDI) molecules by using our new confocal setup, measuring steady state spectra and luminescence lifetimes before and after adding PDI molecules. Two reasons have encouraged us for using two emitters. First, they have distinct emission spectra upon 976 nm excitation which brings different spectral overlap with absorption of PDI. Secondly, in contrast to Tm, spin multiplicity is conserved during the transition for Er. Furthermore, PDI molecules were not directly attached to the surfaces of UCNPs. Instead, two usual methods, spincoating and dropcasting, were employed. Based on the obtained results, the efficiency of energy transfer depends on the sample preparation and the type of emitter (Er or Tm). Moreover, we could show that it is possible to transfer excited-state energy through the Förster mechanism without conserving the spin angular momentum in Tm particles.

6.2 Future prospects

Photodynamic study of UNCPs emission with various spectroscopy and microscopy setups presented in this thesis opens up a wide range of novel research directions for the future. I list some major potential research directions that deserve further investigations.

Reaching to ultrasmall size (< 3 nm) with a limited number of emitters is a big step toward the understanding of interactions occurring among dopant ions. However, for characterizing UCNPs with various emitters (one emitter, two emitters, etc.), it is necessary to perform single particle study. With our new confocal microscopy setup, as introduced in fourth chapter, it is possible to study the photodynamics of UCNPs with different emitters in single particle level.

Moreover, photodynamics study of UCNPs with different assemblies (1D, 2D monolayer, and 3D aggregate) can be also examined in various solvents. Various solvents with different polarity can be used to see the effect of solvents and environment on their emission.

Furthermore, study of the energy transfer in UCNPs/deposited PDI film can lead us to investigate multiple cascade energy transfers like for photosynthetic systems [1] by designing a triad that absorbs light in NIR (UCNP) and remotely emits red light with a chosen emitter. UCNP is excited using NIR radiation and acts as a FRET donor to PDI. The PDI film operates as a propagator, an intermediary of energy transfer where PDI molecules propagates an exciton to the surface where a final red emitter dye is fixed (terylene diimide or quantum dot for example). Indeed, emission in the transparent biological windows is foreseen. This kind of triadic material would be of prime importance first for the theoretical study of ET through a heterogeneous material and second, would find applications in light harvesting photonic materials.

Additionally, one of the features of UCNPs is that they are non-blinking luminescent probes. However, it is possible in principle to modulate the emission intensity of UCNPs by FRET using fluorescent dye. One idea I developed during my thesis within a stay in KU Leuven was to use photoswitchable proteins to get reversible switchable materials. Among photoswitchable proteins, rsEGFP2 [2] can be considered as good candidates to perform the modulation of UCNPs emission due to peak overlap with emission of

UCNPs, proteins high absorption cross section, reasonable switching time between on and off states (Figure 1a).

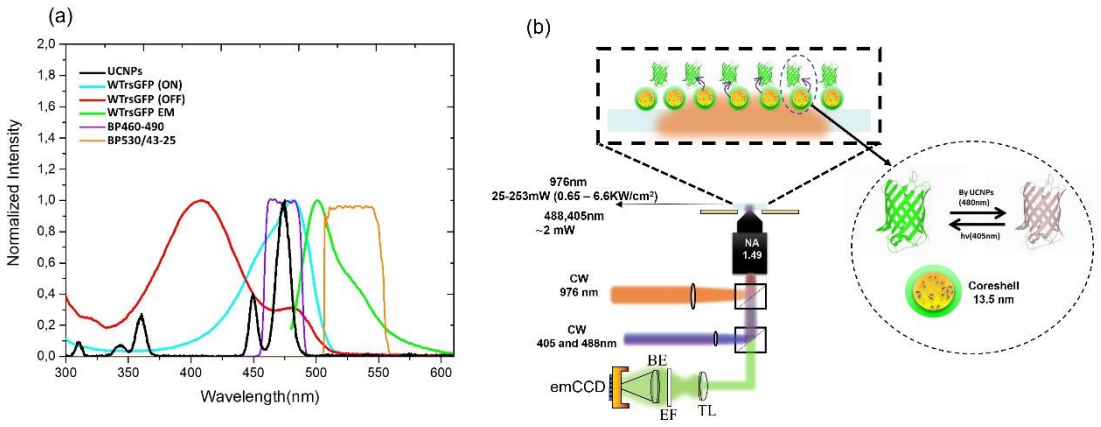

Figure 1. (a) On state (light blue), OFF state (red), and emission of WTrsGFP (green) with emission band of UCNPs (black). (b) Widefield microscopy setup with various excitation of UCNPs (976 nm) and WTrsGFP (405 nm and 488 nm).

In this aim, I performed preliminary experiments by dropcasting crystals of rsEGFP2 on the spincoated UCNPs. By irradiation at 488 nm with a wide-field microscope (figure 1b), rsEGFP2 turns to the OFF state which is not able to absorb emission of UCNPs. Alternately, by irradiating it at 405 nm, it turns ON and is able to absorb the emission from UCNPs. Therefore, as shown in Figure 2a and b, the idea is to put all the rsEGFP2 in the OFF state (by irradiating with 488 nm) and then measure the emission of UCNPs. Afterwards, rsEGFP2 is set in the ON state and the UCNPs emission is recorded. By repeating these sequences, it is possible to modulate UCNPs emission as shown in Figure 1b.

As shown in Figure 2c, we first recorded the emission of UCNPs alone for 1 minute. After dropcasting crystals of rsEGFP2, we applied the 488/405 nm excitation sequence and recorded the emitted light during 80 seconds. We observed some slight fluctuations in UCNPs emission as shown in Figure 2d. There are definitely a number of parameters that should be optimized and the measurement should be reproduced. One of the most critical parameters to investigate first is the physical/chemical attachment of proteins to the surface of UCNPs.[3] However, these very preliminary results pave the way for an innovative study dedicated to the development of NIR-excited photo-commutable hybrids.

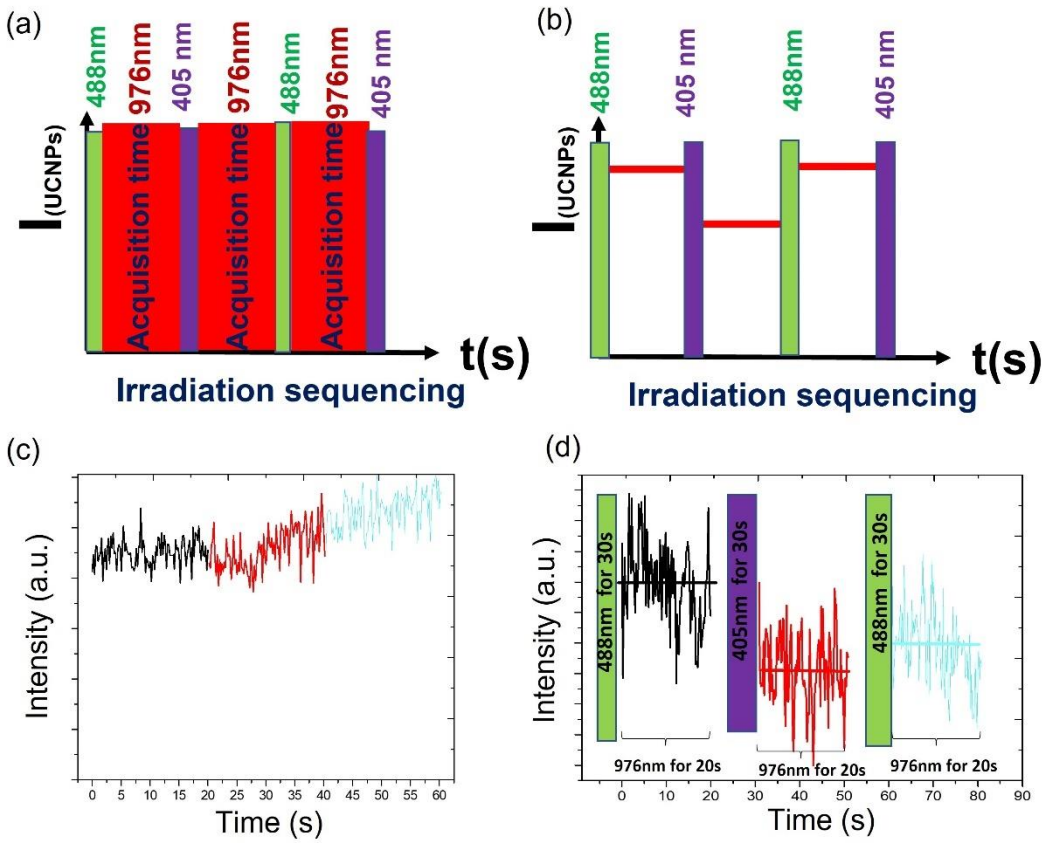

Figure 2. (a) Irradiation sequencing at various excitations wavelengths. (b) Expected UCNPs emission during each acquisition time. UCNPs emission under 976 nm wide field excitation for (c) UCNPs only and (d) UCNPs and photoswitchable rsEGFP2 proteins crystals.

6.3 References

1. Mirkovic, T., et al., *Light absorption and energy transfer in the antenna complexes of photosynthetic organisms.* Chemical reviews, 2017. **117**(2): p. 249-293.
2. Coquelle, N., et al., *Chromophore twisting in the excited state of a photoswitchable fluorescent protein captured by time-resolved serial femtosecond crystallography.* Nature Chemistry, 2018. **10**(1): p. 31-37.
3. Ghosh, S., et al., *Upconversion nanoparticle-mOrange protein FRET nanoprobes for self-ratiometric/ratiometric determination of intracellular pH, and single cell pH imaging.* Biosensors and Bioelectronics, 2020. **155**: p. 112115.

Appendix 1. Table of Poisson distribution

Table A1.1. Calculated Poisson distribution.

	Number of Tm/Np	Poisson 1 Tm for 100 atoms for ideal case	C_1^{20}	C_1^{90}	CS_8^{120}	CS_7^{400}
Poisson Distribution	0 Tm / NP	**37%**	**33%**	**19%**	1%	1%
	1 Tm/NP	**37%**	**27%**	**27%**	2%	3%
	2 Tm/NP	**18%**	**18%**	**23%**	4%	5%
	3 Tm / NP	3%	10%	**15%**	6%	7%
	4 Tm / NP	0.13%	6%	8%	8%	8%
	5 Tm/NP	0.001%	3%	4%	**9.02%**	**9.2%**
	6 Tm/NP	0.000001%	1%	1.9%	**9.59%**	**9.6%**
	7 Tm / NP	0%	1%	0.8%	**9.62%**	**9.5%**
	8 Tm / NP	0%	0%	0.3%	**9.17%**	**8.9%**
	9 Tm/NP	0%	0%	0.2%	8.35%	8.0%
	10 Tm / NP	0%	0%	0.1%	7.29%	6.9%
	11 Tm / NP	0%	0%	0.04%	6.12%	5.8%
	12 Tm/NP	0%	0%	0.02%	4.96%	4.7%
	13 Tm/NP	0%	0%	0.013 %	3.89%	3.6%
	14 Tm / NP	0%	0%	0.008 %	2.95%	2.8%
	15 Tm / NP	0%	0%	0.005 %	2.18%	2.1%
	Sum of Proba k Tm/NP	100%	100%	100%	95%	95%
	P(at least 1 Tm/NP)	63%	67%	81%	99%	99%

Appendix 2: Tables of fitting information for average lifetime calculation

Table A2.1. Pre-exponential factors and time constants obtained from the exponential fitting of time-resolved luminescence decays of C_1^{90} particle at 360, 450, 474 and 798 nm and calculated amplitude average lifetimes.

λ (nm)		**Value**	**Standard error**	**Amplitude-averaged lifetime** (μs)	**Amplitude-averaged lifetime standard error** (μs)
360	A_1	0.82065	0.00676	50.8	1.3
	τ_1 (μs)	44.2415	0.20051		
	A_2	0.10965	0.00695		
	τ_2 (μs)	99.5281	2.3379		
450	A_1	0.93479	0.00215	49.9	2.5
	τ_1 (μs)	45.28333	0.10679		
	A_2	0.04236	0.00230		
	τ_2 (μs)	152.7631	4.69574		
474	A_1	0.35954	0.00229	287.3	0.9
	τ_1 (μs)	110.30759	0.67168		
	A_2	0.59627	0.00234		
	τ_2 (μs)	393.99065	1.15629		
800798	A_1	0.34485	0.0377	74.9	2.8
	τ_1 (μs)	41.05402	2.63449		
	A_2	0.5136	0.0387		
	τ_2 (μs)	97.69484	3.0364		

Table A2.2. Pre-exponential factors and time constants obtained from the exponential fitting of time-resolved luminescence decays of C_1^{20} particle at 360, 450, 474 and 798 nm and calculated amplitude average lifetimes.

λ (nm)		**Value**	**Standard error**	**Amplitude-averaged lifetime** (μs)	**Amplitude-averaged lifetime standard error** (μs)
360	A_1	0.73831	0.00284	77.8	0.5
	τ_1 (μs)	77.79309	0.47539		
450	A_1	0.8236	0.00233	70.1	0.3
	τ_1 (μs)	70.09618	0.30953		
474	A_1	0.54256	0.00617	261.4	10.7
	τ_1 (μs)	146.63741	1.56054		
	A_2	0.18827	0.00577		
	τ_2 (μs)	592.15942	20.44883		
800798	A_1	0.69608	0.00485	172.5	1.7
	τ_1 (μs)	172.52783	1.70007		

Table A2.3. Pre-exponential factors and time constants obtained from the exponential fitting of time-resolved luminescence decays of CS_7^{400} particle at 360, 450, 474 and 798 nm and calculated amplitude average lifetimes.

λ (nm)		**Value**	**Standard error**	**Amplitude-averaged lifetime** (μs)	**Amplitude-averaged lifetime standard error** (μs)
360	A_1	0.82065	0.00676	50.8	1.3
	τ_1 (μs)	44.2415	0.20051		
	A_2	0.10965	0.00695		
	τ_2 (μs)	99.5281	2.3379		
450	A_1	0.93479	0.00215	49.9	2.5
	τ_1 (μs)	45.28333	0.10679		
	A_2	0.04236	0.00230		
	τ_2 (μs)	152.7631	4.69574		
474	A_1	0.35954	0.00229	287.3	0.9
	τ_1 (μs)	110.30759	0.67168		
	A_2	0.59627	0.00234		
	τ_2 (μs)	393.99065	1.15629		
800798	A_1	0.34485	0.0377	74.9	2.8
	τ_1 (μs)	41.05402	2.63449		
	A_2	0.5136	0.0387		
	τ_2 (μs)	97.69484	3.0364		

Table A2.4. Pre-exponential factors and time constants obtained from the exponential fitting of time-resolved luminescence decays of CS_8^{120} particle at 360, 450, 474 and 798 nm and calculated amplitude average lifetimes.

λ (nm)		**Value**	**Standard error**	**Amplitude-averaged lifetime** (μs)	**Amplitude-averaged lifetime standard error** (μs)
360	A_1	0.79933	0.000925	93.4	0.2
	τ_1 (μs)	93.38502	0.15884		
450	A_1	0.6543	0.000635	101.4	18.9
	τ_1 (μs)	87.03887	0.16788		
	A_2	0.01112	0.000392		
	τ_2 (μs)	949.22221	49.30437		
475474	A_1	0.59649	0.00763	400.3	2.7
	τ_1 (μs)	302.29361	1.55322		
	A_2	0.34139	0.00775		
	τ_2 (μs)	571.49192	3.73308		
798	A_1	0.52359	0.000745	131.5	21.1
	τ_1 (μs)	117.68168	0.30598		
	A_2	0.01217	0.000724		
	τ_2 (μs)	727.13230	42.4595		

Table A2.5. Pre-exponential factors and time constants obtained from the exponential fitting of time-resolved luminescence decays of C_{34}^{570} particle at 360, 450, 474 and 798 nm and calculated amplitude average lifetimes.

λ (nm)		**Value**	**Standard error**	**Amplitude-averaged lifetime** (μs)	**Amplitude-averaged lifetime standard error** (μs)
360	A_1	0.72583	0.00275	72.7	0.4
	τ_1 (μs)	72.7043	0.40828		
450	A_1	0.81264	0.00209	66.3	0.3
	τ_1 (μs)	66.2589	0.25055		
475474	A_1	0.60404	0.02189	309.3	51.6
	τ_1 (μs)	199.41213	5.15625		
	A_2	0.16082	0.01924		
	τ_2 (μs)	722.2191	104.38339		
798	A_1	0.57456	0.00536	220.3	3.5
	τ_1 (μs)	220.292	3.50463		

Appendix 3: Python code for calculation of band areas and area ratios

A3.1 Area calculation for all emission bands of Tm^{3+}

```
@author: Alief
"""
import numpy as np
import pandas as pd
import csv
from scipy.integrate import simps
from numpy import trapz
matrix = pd.read_csv(r'M:\FluoroMax\20220405\C.csv')
print(type(matrix))
matrix = matrix.to_numpy()
def matrixcolumns(matrix):
    out = []
    for i in range(len(matrix[0])):
        out.append([])
        for j in matrix:
            out[i].append(j[i])
    return out
A = matrixcolumns(matrix)
C= pd.DataFrame(A)
C=C.transpose()
D=C.iloc[65:107,:]
D = trapz(D.transpose(), dx=0.5)
F=C.iloc[107:143,:]
F= trapz(F.transpose(), dx=0.5)
G=C.iloc[275:316,:]
G= trapz(G.transpose(), dx=0.5)
H=C.iloc[316:396,:]
H= trapz(H.transpose(), dx=0.5)
I=C.iloc[654:730,:]
```

```
I= trapz(I.transpose(), dx=0.5)
J=C.iloc[745:815,:]
J= trapz(J.transpose(), dx=0.5)
K=C.iloc[809:871,:]
K= trapz(K.transpose(), dx=0.5)
L=C.iloc[890:1100,:]
L= trapz(L.transpose(), dx=0.5)
dic = {"343":D,"360":F,"450":G,"475":H,"643":I,"690":J,"720":K,"800":L}
M = pd.DataFrame.from_dict(dic)
M["Power"]=pd.read_csv(r'M:\FluoroMax\20220405\Power2.csv')
import matplotlib.pyplot as plt
y1 = M["343"]
y2 = M["360"]
y3 = M["450"]
y4 = M["475"]
y5 = M["643"]
y6 = M["690"]
y7 = M["720"]
y8 = M["800"]
x = M["Power"]
fig,ax = plt.subplots()
ax.plot(x,y1,color = 'red', label = '1')
ax.plot(x,y2,color = 'red',label = '2')
ax.plot(x,y3,color = 'black',label = '3')
ax.plot(x,y4,color = 'black',label = '3')
ax.plot(x,y5,color = 'black',label = '3')
ax.plot(x,y6,color = 'black',label = '3')
ax.plot(x,y7,color = 'black',label = '3')
ax.plot(x,y8,color = 'black',label = '3')
ax.set_xscale('log')
ax.set_yscale('log')
plt.show()
M.to_csv("M:/FluoroMax/20220405/Cresult.csv")
```

A3.2 Calculation of areas and area ratios of Tm^{3+} at 475 nm and 450 nm

```
import numpy as np
import pandas as pd
import csv
from scipy.integrate import simps
from numpy import trapz
matrix = pd.read_csv(r'C:\Users\Alief\OneDrive\Desktop\PhD\Flouromax\20220404\Core.csv')
print(type(matrix))
matrix = matrix.to_numpy()
def matrixcolumns(matrix):
    out = []
    for i in range(len(matrix[0])):
        out.append([])
        for j in matrix:
            out[i].append(j[i])
    return out
A = matrixcolumns(matrix)
C= pd.DataFrame(A)
C=C.transpose()
G=C.iloc[221:253,:]
G= trapz(G.transpose(), dx=0.5)
H=C.iloc[253:333,:]
H= trapz(H.transpose(), dx=0.5)
dic = {"450":G,"475":H}
Result1 = pd.DataFrame.from_dict(dic)
M1=np.mean(Result1['475']/Result1['450'])
M2=np.std(Result1['475']/Result1['450'])
M=[M1,M2]
M= pd.DataFrame(M)
M.to_csv("C:/Users/Alief/OneDrive/Desktop/PhD/Flouromax/20220404/Results1.csv")
Result1.to_csv("C:/Users/Alief/OneDrive/Desktop/PhD/Flouromax/20220404/Results2.csv")
```

Appendix 4. List of scientific contributions

A4.1 Publications

1. Heterogeneous Oxysulfide@Fluoride Core/Shell Nanocrystals for Upconversion-Based Nanothermometry

ACS Nano **2022**, 16, 8, 12107-12117

https://doi.org/10.1021/acsnano.2c02423

List of authors: Qilin Zou, Cécile Marcelot, Nicolas Ratel-Ramond, Xiaodong Yi, Pierre Roblin, Florian Frenzel, Ute Resch-Genger, Ali Eftekhari, Aude Bouchet, Christophe Coudret, Marc Verelst, Xueyuan Chen,* Robert Mauricot,* and Clément Roux*

A4.2 Contributions to conferences as a presenter

A4.2.1 Oral presentations

1) PhotOnline, young researchers conference of the SP2P subdivision (Photochemistry, Photophysics, Photosciences) of the Physical Chemistry Division (Oral presentation, 15th of October, 2020, online) "Innovative up-converting nanoparticles for nano-bioimaging"

Authors: Ali Eftekhari, Baptiste Amouroux, Clément Roux, Fabienne Gauffre, Mathieu Pasturel, Pierre Roblin, Michel Sliwa, Christophe Coudret, Aude Bouchet

2) 5th Nanosynergetics workshop (Oral presentation, 13th of November, 2020, online) "Innovative up-converting nanoparticles for nano-bioimaging"

Authors: Ali Eftekhari, Baptiste Amouroux, Clément Roux, Fabienne Gauffre, Mathieu Pasturel, Pierre Roblin, Michel Sliwa, Christophe Coudret, Aude Bouchet

3) French-swiss photochemistry symposium (Oral presentation, 21st of January, 2021, online) "Innovative up-converting nanoparticles for nano-bioimaging"

Authors: Ali Eftekhari, Baptiste Amouroux, Clément Roux, Fabienne Gauffre,Mathieu Pasturel, Pierre Roblin, Christophe Coudret ,Michel Sliwa, Aude Bouchet

(Best oral presentation award)

4) LIA Nanosynergetics Graduate students day (Oral presentation, 16th of July, 2021, online) “Innovative up-converting nanoparticles for nano-bioimaging”

Authors: Ali Eftekhari, Baptiste Amouroux, Clément Roux, Fabienne Gauffre, Mathieu Pasturel, Pierre Roblin, Michel Sliwa, Christophe Coudret, Aude Bouchet

A4.2.2 Poster presentations

1) 3rd Conference on Properties, Design, and Applications of Upconversion Nanomaterials (UPCONline2021, Poster, 6th of April, 2021, online) “Investigation of the photophysical propertiesof ultra-small upconverting nanoparticles”

Authors: Ali Eftekhari, Baptiste Amouroux, Clément Roux, Michel Sliwa, Christophe Coudret, Aude Bouchet

(Best poster award)

2) 17th conference on Methods and Applications in Fluorescence (MAF2022, Poster, 11th of September, 2022) “A new tool for time-resolved hyperspectral nano-imaging of upconversion dynamics”

Authors: Ali Eftekhari, Rajesh Komban, Christoph Gimmler, Hikaru Sotome, Syoji Ito, Michel Sliwa, Aude Bouchet